ISBN 978-82-326-3064-6 (printed version)
ISBN 978-82-326-3065-3 (electronic version)
ISSN 1503-8181

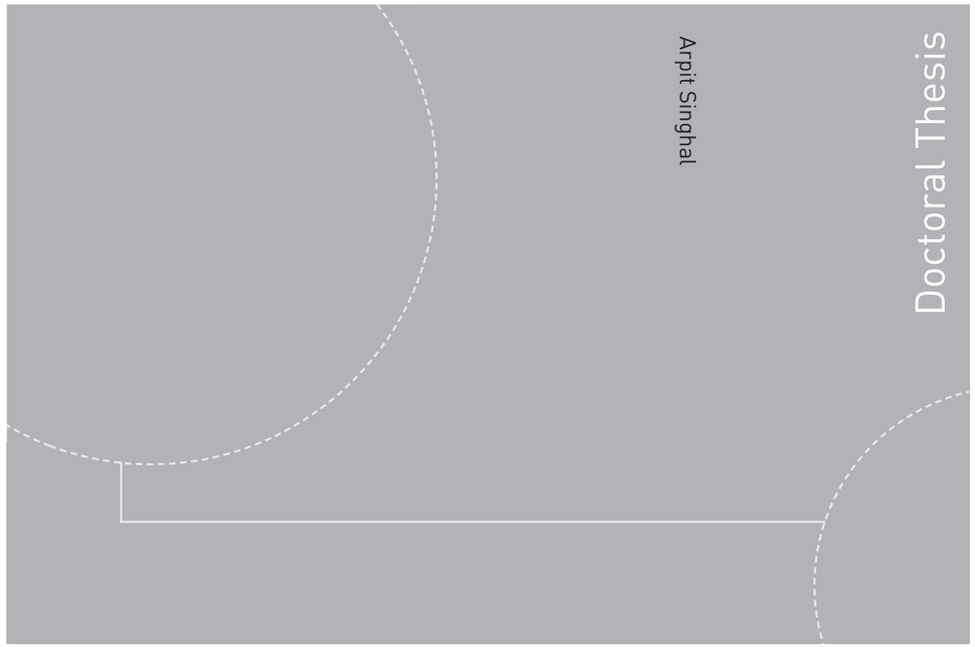

Doctoral theses at NTNU, 2018:137

Arpit Singhal

Heat and mass transfer in gas-solid packed beds

NTNU
Norwegian University of
Science and Technology
Faculty of Engineering
Department of Energy and Process Engineering

NTNU
Norwegian University of
Science and Technology

UNIVERSIDADE DE COIMBRA

Doctoral theses at NTNU, 2018:137

NTNU

NTNU
Norwegian University of
Science and Technology

UNIVERSIDADE DE COIMBRA

Arpit Singhal

Heat and mass transfer in gas-solid packed beds

Thesis for the degree of Philosophiae Doctor

Trondheim, May 2018

Norwegian University of Science and Technology
Faculty of Engineering
Department of Energy and Process Engineering

University of Coimbra
Faculty of Sciences and Technology
Department of Chemical Engineering

NTNU
Norwegian University of
Science and Technology

· U C ·

UNIVERSIDADE DE COIMBRA

NTNU
Norwegian University of Science and Technology

Thesis for the degree of Philosophiae Doctor

Faculty of Engineering
Department of Energy and Process Engineering

University of Coimbra
Faculty of Sciences and Technology Department
of Chemical Engineering

ISBN 978-82-326-3064-6 (printed version)

ISBN 978-82-326-3065-3 (electronic version)
ISSN 1503-8181

Doctoral theses at NTNU, 2018:137

Printed by Skipnes Kommunikasjon as

In the memory of my mother...

'Efficiency is doing things right; effectiveness is doing the right things'

-Anonymous

ABSTRACT

The present thesis probes the heat and mass transfer phenomena in packed bed of particles. The gap in literature for realistically packed dense particle packings is explored, following which a new methodology to study external heat transfer is presented and evaluated with deep sensitivity analysis. The newly developed method is applied to obtain new closure models for external heat and mass transfer in packed beds of mono-disperse spherical particles and cylindrical particles of different aspect ratios. In addition, the obtained data helps refit the new Ergun constant for pressure drop in these dense packings.

A step by step examination for internal mass transfer and reactions depending upon several levels of complexities in literature i.e. different reaction order, multiple reacting species, and gas volume generation/consumption and in practical application of steam methane reforming reveals the need for improvement in industrially viable 1D models. The developed closure models for external heat and mass transfer along with the data from computationally expensive particle-resolved direct numerical simulations (PR-DNS) in dense packings of mono-disperse spherical particles with catalytic reactions inside the porous particles are used to verify and improve the internal mass transfer closures for 1D models through multiscale modelling.

The enhanced 1D model is then used to simulate an industrial scale packed bed chemical looping reforming (PBCLR) reactor. As an application of the work done in this PhD, an alternative to resolved 3D simulation is also presented in this thesis in form of non-resolved Euler Lagrange 3D simulations. The results obtained are documented and discussed in appropriate chapters of this thesis.

Descriptors: Packed bed reactors, Multiscale modelling, CFD-DEM, Gas-solid system, Heat and mass transfer, Direct numerical simulations (DNS), Catalysis

RESUMO

A presente tese estuda os fenómenos de transferência de calor e massa em leito fixo de partículas. A lacuna na literatura no que respeita a leitos fixos de partículas é explorada neste trabalho. Deste estudo resultou uma nova estratégia para análise de transferência de calor externa que é descrita e avaliada através uma análise de sensibilidade minuciosa. O método desenvolvido é aplicado no desenvolvivento de novas correlações para transferência de calor externa e transferência de massa em leitos fixos de partículas esféricas mono-dispersas e partículas cilindricas com diferentes proporções. Para além disso, a informação obtida ajuda também a ajustar novas constantes de Ergun para a queda de pressão em leitos densos.

Uma análise detalhada da literatura no que respeita à transferência de massa interna e reacções químicas dependendo de diferentes níveis de complexidade como diferente ordem de reacção, multiplas espécies reaccionais, volume de gás produzido/consumido e considerando a aplicação no processo de "steam methane reforming" revela a necessidade de melhorar os modelos 1D actualmente usuados a nível indústrial. As correlações desenvolvidas para transferência de calor externa e transferência de massa juntamente com a informação obtida de simulações "particle-resolved direct numerical simulations" (PR-DNS) de elevados custos computacionais em leitos densos de particulas esféricas mono-dispersas com reacções químicas dentro de partículas porosas são usadas para verificar e melhorar as correlações de transferência de massa interna em modelos 1D através de uma metodologia de modelação multiescala.

O modelo 1D melhorado é então usado para simular reactores de leito fixo à escala indústrial para o processo de "chemical looping reforming". O trabalho desenvolvido nesta tese é aplicado em "non-resolved Euler Lagrange 3D simulations" que são uma alternativa às mais complexas "resolved 3D simulations". Os resultados obtidos são descritos e discutidos nos diferentes capítulos desta tese.

Descriptors: Packed bed reactors, Multiscale modelling, CFD-DEM, Gas-solid system, Heat and mass transfer, Direct numerical simulations (DNS), Catalysis

ACKNOWLEDGEMENTS

First of all, I am grateful to The Almighty God and my Parents for establishing me to complete this thesis. This thesis is dedicated to my mother for making me what I am today and my father for his unconditional support in every phrase of my life.

I would like to thank European Research Council for its financial support under Seventh research framework programme (FP7/2007-2013). Additionally, I would like to acknowledge the computational resources used during this project at NTNU provided by NOTUR (http://www.notur.no).

I am deeply grateful to my supervisor Shahriar Amini and my co-supervisor Rosa Quinta-Ferreira for giving me the opportunity to work on this project and guiding me during the PhD. And special thanks to Schalk Cloete for acting as my scientific advisor and sharing his knowledge in guiding and helping me during the course of my PhD. Their patience, guidance and help has been a great learning experience and an ever good memory for life.

My sincere thanks to Stefan Radl (TU Graz) and Pascal Fede (IMFT) for the discussions we had during the project.

Then I like to thank all the other members of EPT and Sintef Flow Technology, where I got a chance to work in a friendly and an international environment. I would like to thank my colleagues: Henri, Karl, Mogahid, Ambrose, Amit, Vipin, Niranjan, Rohan da, Solomon, Tao, Wei, Antoine, Jerol, Ruben, and Alexis for bringing a friendly and creative environment. Special thanks to Shareq and Joana, without them these years during the PhD in office and outside would have not been possible.

I would also like to thank the people outside office in Trondheim (Athul, Pulkit, Jimita and Nakul) for our weekly meetings. Again special thanks to Jimita, Joana and Shareq for being good friends and more importantly good human beings.

Thanks also to the colleagues and peers around the world, who have directly and indirectly helped improve my work. I extend my sincere thanks to my friends, loved ones and their families in and outside India (back home) (especially, Rupika (for bearing with

me), Nikhil, Rahul, Himanshu, Shantanu, Ankit, Raghav, Shobhit, Akshay, Devansh, Aman and Sakshi) for their friendship and support.

Finally, my special gratitude is directed to my Family: for giving me their love, sacrificing for me, encouraging me, and supporting me in every way possible.

I won't say that I always wanted to get a PhD or be in research since my childhood or my engineering days, but I am glad that I have come a long way, and I really would like to continue on this path. It is said that, "*Success is a journey and not a destination"*. So I know my journey has just begin.

Arpit Singhal
Trondheim, Norway

TABLE OF CONTENTS

1 INTRODUCTION 29

1.1 BACKGROUND 30
1.2 PARTICLE RESOLVED DIRECT NUMERICAL SIMULATIONS (PR-DNS) 32
1.3 MULTISCALE MODELLING 32
1.4 RESEARCH OBJECTIVES 33
1.4.1 SCOPE 34
1.4.2 OUTLINE 34

2 RESEARCH REPERTOIRE 37

2.1 INTRODUCTION 39
2.2 METHODOLOGY 41
2.2.1 PARTICLE BED GENERATION (DEM) 41
2.2.2 RANDOM PACKING FROM DEM 42
2.2.3 MESH 43
2.2.4 COMPUTATIONAL FLUID DYNAMICS 43
2.2.5 MODEL EQUATIONS 44
2.2.6 BOUNDARY CONDITIONS 44
2.2.7 SOLVER SETTINGS 45
2.3 VALIDATION FOR A SINGLE PARTICLE 45
2.4 RESULTS AND DISCUSSIONS 46
2.4.1 CASE SETUP 46
2.4.2 HEAT TRANSFER FOR DIFFERENT POROSITIES 47
2.4.3 HEAT TRANSFER PREDICTIONS 50
2.4.4 PERFORMANCE ANALYSIS 51
2.5 SUMMARY AND CONCLUSIONS 53

3 HEAT TRANSFER TO GAS THROUGH MONO-DISPERSE SPHERICAL PARTICLE BED 55

3.1 INTRODUCTION **57**
3.1.1 PREVIOUS HEAT TRANSFER CORRELATIONS 57
3.1.2 MESHING STRATEGIES 59
3.1.3 GOALS 61
3.2 METHODOLOGY **61**
3.2.1 BED GEOMETRY AND MESH GENERATION 61
3.2.2 SIMULATIONS SETUP 63
3.3 RESULTS AND DISCUSSION **65**
3.3.1 GRID DEPENDENCY STUDY 65
3.3.2 STEADY VERSUS TRANSIENT SIMULATION 67
3.3.3 CAPS SIZE STUDY 68
3.3.4 PARTICLE STATISTICS 70
3.3.5 WALL EFFECTS 71
3.3.6 COMPARISON WITH CORRELATIONS FROM LITERATURE 73
3.3.7 A NEW HEAT TRANSFER CORRELATION 75
3.4 CONCLUSION **77**

4 HEAT TRANSFER TO GAS THROUGH PACKED BED OF CYLINDRICAL PARTICLES 79

4.1 INTRODUCTION **81**
4.2 METHODOLOGY **84**
4.2.1 BED GEOMETRY AND MESH DEVELOPMENT 84
4.2.2 SIMULATIONS SETUP 86
4.3 RESULTS AND DISCUSSION **88**
4.3.1 GRID DEPENDENCY STUDY 88
4.3.2 WALL EFFECTS 89
4.3.3 PARTICLE STATISTICS 91
4.3.4 COMPARISON WITH CORRELATIONS FOR HEAT TRANSFER 92
4.3.5 A NEW HEAT TRANSFER CORRELATION 95
4.3.6 PRESSURE DROP CORRECTION 98
4.3.7 HEAT TRANSFER-PRESSURE DROP RELATIONSHIP 100
4.4 CONCLUSION **102**

5 VERIFICATION OF THE CLOSURE MODELS 105

5.1 INTRODUCTION **107**
5.2 METHODOLOGY **110**
5.2.1 THIELE MODULUS AND EFFECTIVENESS FACTOR 110

5.2.2 Conservation equations 111
5.2.3 PR-DNS simulation setup 112
5.2.4 1D packed bed model 117
5.3 Results and Discussion 117
5.3.1 Reaction orders 118
5.3.2 Multiple reactions 120
5.3.3 Reactions with gas volume generation/consumption 124
5.3.4 Combined heat and mass transfer resistance 125
5.3.5 Steam methane reforming reactions 127
5.4 Conclusion 129
5.5 Appendix 130

6 MULTISCALE MODELLING OF A PACKED BED REACTOR 133

6.1 Introduction 134
6.2 Methodology 136
6.2.1 PR-DNS setup 136
6.2.2 1D packed bed model 137
6.3 Results 141
6.3.1 PR-DNS results 141
6.3.2 Comparison of 1D model to PR-DNS results 141
6.3.3 The packed bed chemical looping reforming process 143

7 MULTISCALE MODELLING FOR NON-RESOLVED 3D SIMULATIONS 149

7.1 Introduction 150
7.2 Methodology 151
7.2.1 DEM (particle bed generation) 151
7.2.2 Mesh 152
7.2.3 CFD (DNS) 152
7.2.4 Average procedure 153
7.2.5 Non resolved Eulerian-Lagrangian simulations 154
7.3 Results 155
7.3.1 Heat transfer in randomly arranged packed beds 155
7.3.2 Heat transfer correlations 156
7.3.3 Comparison of the correlations with non-homogenous vs homogenous particle temperature 157
7.3.4 Comparison between resolved and unresolved models 158

7.4 SUMMARY AND CONCLUSIONS 163

8 CONCLUSION AND FUTURE OUTLOOK 165

REFERENCES 169

LIST OF PUBLICATIONS 177

APPENDICES 179

LIST OF TABLES

TABLE 1. THE REACTOR GEOMETRY WITH MESHING DETAILS 42

TABLE 2. DEM PARAMETERS FOR THE NORMAL, TANGENTIAL AND GRAVITY FORCES 43

TABLE 3. FLOW PROPERTIES 45

TABLE 4. COMPARISON OF HEAT TRANSFER COEFFICIENT WITH RANZ-MARSHALL CORRELATION 46

TABLE 5. SCHEMATIC REPRESENTATION OF DIFFERENT PACKED BED SETUPS ACHIEVED BY SHRINKING ... 47

TABLE 6. NUSSELT NUMBER COMPARISON BETWEEN OPENFOAM AND FLUENT 50

TABLE 7. PERFORMANCE TEST (SPRINT RACE FOR 20 S) AND MARATHON 52

TABLE 8: POROSITY RANGE STUDIED BY THE DIFFERENT CORRELATIONS 58

TABLE 9: DEM SIMULATION SETUP 62

TABLE 10: PARAMETRIC FLOW PROPERTIES FOR CFD SIMULATION 64

TABLE 11: FINAL RENDERED GEOMETRY DETAILS USED FOR THE SIMULATION 73

TABLE 12: DEM SIMULATION SETUP FOR CYLINDRICAL PARTICLES OF ASPECT RATIO FOUR IN STAR CCM+ 84

TABLE 13: PARAMETRIC FLOW PROPERTIES FOR CFD SIMULATION. THE FLOW PROPERTIES ARE BASED ON THE RANGE OF DIMENSIONLESS PARAMETERS IN THE PR-DNS STUDY 87

TABLE 14: FINAL RENDERED GEOMETRY DETAILS USED IN THE SIMULATIONS 93

TABLE 15. PACKED BED GEOMETRY AND FLOW SIMULATION PROPERTIES 113

TABLE 16: FLOW PROPERTIES FOR CFD SIMULATION. THE FLOW PROPERTIES ARE BASED ON THE RANGE OF DIMENSIONLESS PARAMETERS (RE, PR, ϕ) IN THE PR-DNS STUDY. 118

TABLE 17: DIFFERENT CATALYTIC REACTIONS WITH THEIR GAS SPECIE PROPERTIES AND LENGTH SCALE 124

TABLE 18: SIMULATION PARAMETERS (PR-DNS) FOR STEAM METHANE REFORMING 131

TABLE 19: KINETIC AND EQUILIBRIUM PARAMETERS FOR REFORMING REACTIONS 131

TABLE 20: ADSORPTION PARAMETERS FOR REFORMING REACTIONS 132

TABLE 21. SIMULATION PARAMETERS FOR PR-DNS 137

TABLE 22. BOUNDARY CONDITIONS EMPLOYED IN THE PBCLR SIMULATION. 144

TABLE 23. MISCELLANEOUS SIMULATION PARAMETERS USED IN THE PBCLR SIMULATION. 144

TABLE 24. DEM SIMULATION SETUP 151

TABLE 25. MESH SIZING DETAILS 152

TABLE 26. REPRESENTATION OF THE CASES SIMULATED 155

LIST OF FIGURES

FIGURE 1.1. THE PICTORIAL REPRESENTATION OF THE SCALE AND THE MEMBER PARTNERS THIS PHD IS DEFINED IN NANOSIM PROJECT UNDER EU-FP7 FRAMEWORK. 30

FIGURE 1.2 TYPICAL SKETCH OF A PACKED BED REACTION [SOURCE: (JAKOBSEN, 2014)] 31

FIGURE 1.3. STRUCTURE OF THE THESIS WITH THE BASIC ESSENCE 35

FIGURE 2.1. FINAL REALISTIC PACKING INSIDE THE REACTOR (LEFT) AND RANDOM PARTICLE BED (RIGHT) GENERATED IN WORKBENCH 42

FIGURE 2.2. PREDICTION OF HEAT TRANSFER COEFFICIENT VARIATION WITH PARTICLE REYNOLDS NUMBERS 46

FIGURE 2.3. REPRESENTATION OF THE REGION OF INTEREST IN THE PACKED BED REGION. 47

FIGURE 2.4. COMPARISON OF HEAT TRANSFER COEFFICIENT WITH THE CORRELATIONS OVER A RANGE OF REYNOLDS NUMBERS AND POROSITY VALUES (OBTAINED BY SHRINKING FACTORS) 49

FIGURE 2.5. COMPARISON OF HEAT TRANSFER COEFFICIENT FOR SHRUNK AND RANDOMLY GENERATED PARTICLE BED 50

FIGURE 2.6. COMPARISON BETWEEN FLUENT AND OPENFOAM 51

FIGURE 2.7. REPRESENTATION OF THE VELOCITY AND TEMPERATURE PROFILE OBTAINED FROM FLUENT AND OPENFOAM (PLANE Y = 0; RE 36; ε = 0.42) 51

FIGURE 3.1. RENDERED FINAL GEOMETRY (RIGHT PANEL) EXTRACTED FROM THE PACKING OF SPHERES CONTAINED IN THE CYLINDRICAL CONTAINER (LEFT). THE COORDINATE SYSTEM SHOWN IS FOLLOWED WHILE EXTRACTING THE GEOMETRY (RENDERED EXTRACT). 63

FIGURE 3.2. GRID INDEPENDENCE FOR HEAT TRANSFER IN ARRAYS OF SPHERICAL PARTICLES AS A FUNCTION OF PARTICLE SURFACE MESH RESOLUTION. VARIATION FOR RANDOM PACKING (ε =0.7) AND RE=144 [LEFT] AND REALISTIC PACKING (ε =0.35) AND RE=144 [RIGHT] RESPECTIVELY. 66

FIGURE 3.3. INCREASE IN THE NUMBER OF CELLS IN THE MESH TO REFINE THE RESOLUTION IN REALISTIC PACKINGS (ε =0.35) AND RE=144. 67

FIGURE 3.4. MAXIMUM VELOCITY (LEFT) AND MINIMUM VELOCITY (RIGHT) VARIATION OF THE FLOW IN THE TRANSIENT DNS SIMULATION THROUGH THE FINAL GEOMETRY (SECTION 3.2.1) AT RE 144 AND BED POROSITY (ε = 0.35)..... 68

FIGURE 3.5. VARIATION OF THE DATA FROM FUNCTION (EQ. (12)) WITH THE AXIAL DISTANCE OF THE PLANES PERPENDICULAR TO THE FLOW FOR COMPUTING THE NUSSELT NUMBER (DEEN ET AL., 2012) (SECTION 3.2.2.2) [LEFT]. NUSSELT NUMBER OBTAINED OVER DIFFERENT FLOW TIME TO MARK THE CONVERGED SOLUTION [RIGHT]. 68

FIGURE 3.6. THE PARTICLE BED GENERATED BY DEM (ABOVE) WITH PROBLEMATIC REGIONS OF CLOSE PROXIMITY REMOVED (BELOW). 69

FIGURE 3.7. VARIATION OF NUSSELT NUMBER WITH THE CYLINDER LENGTH OR CAPS SIZE (LEFT) AND THE EFFECT OF CAPS SIZE ON THE OVERALL PACKED BED POROSITY (RIGHT). 70

FIGURE 3.8. STATISTICALLY AVERAGED NUSSELT NUMBER VARIATION OVER DIFFERENT REYNOLDS NUMBER WITH THE 95% CONFIDENCE INTERVAL..... 71

FIGURE 3.9. LOCAL POROSITY RADIAL PROFILES [LEFT]; LOCAL AXIAL VELOCITY RADIAL PROFILES [RIGHT] IN THE GEOMETRY WITH NUMBER OF PARTICLES EXCLUDED FROM THE WALL (AT RE 144; PR = 1) [ARR1….ARR5 REFER TO DIFFERENT PARTICLE ARRANGEMENTS]. 72

FIGURE 3.10. WALL EFFECTS FOR THE HEAT TRANSFER STUDIED IN THE GEOMETRY WITH THE NUMBER OF PARTICLE DIAMETERS EXCLUDED FROM THE WALL FOR A REYNOLDS NUMBER OF 144 AND PR = 1 [LEFT PANEL; ARR1 … ARR5 REFER TO THE DIFFERENT PARTICLE ARRANGEMENTS STUDIED]. [RIGHT] SLICE THROUGH GEOMETRY OF (ARR2) AT PLANE (Y=0), SHOWING THE SIZE OF THE RADIAL PLANES STUDIED FOR WALL EFFECTS IN THE LEFT PANEL. THE MONODISPERSE PARTICLES ARE CUT UNEQUALLY BY THE PLANE AND THEREFORE APPEAR TO BE OF DIFFERENT SIZES. 72

FIGURE 3.11. VELOCITY DISTRIBUTION (IN M/S) FOR ARR2 AT PLANE (Y=0) AT Re_P = 144 AND PR = 1 IN THE DIRECTION OF FLOW SHOWING THE ADDED VOLUME ON THE WALL. 73

FIGURE 3.12. CONTOUR PLOT OF FLUID VELOCITY (IN M/S) AND STATIC TEMPERATURE (IN K) IN A PLANE PARALLEL TO THE FLOW CUT FROM ONE OF THE ARRANGEMENTS AT RE = 144 AND PR = 1. 74

FIGURE 3.13. HEAT TRANSFER VARIATION (NUSSELT NUMBER) WITH DIFFERENT REYNOLDS NUMBER AVERAGED OVER FIVE PARTICLE ARRANGEMENTS AND COMPARISON WITH THE LITERATURE. THE CORRELATIONS MORE RELEVANT TO THE COMPARISON BECAUSE OF THEIR OVERALL VALIDITY ARE REPRESENTED IN THE LEFT PANEL. 75

FIGURE 3.14. OBSERVED (SIMULATION) VS. PREDICTED (MODEL) VALUES OF THE NUSSELT NUMBER OVER ALL CASES FOR THE MODIFIED GUNN CORRELATION (EQ. (16)) AND THE SIMPLIFIED CORRELATION (EQ. (17)). 76

FIGURE 3.15. THE AVERAGE STANDARD ERROR OVER THE THREE DIFFERENT PRANDTL NUMBERS FOR EACH OF THE SIX REYNOLDS NUMBERS INVESTIGATED IN THIS STUDY. 77

FIGURE 4.1. ILLUSTRATION OF THE RAW PACKING (LEFT PANEL) OF ASPECT RATIO FOUR USED TO EXTRACT A REPRESENTATIVE CYLINDRICAL REGION (CENTER PANEL), AS WELL AS THE RENDERED FINAL GEOMETRY (RIGHT PANEL) USED IN THE FLOW SIMULATIONS. 85

FIGURE 4.2. GRID DEPENDENCE BEHAVIOUR FOR THE VARIATION OF NUSSELT NUMBER IN ARRAYS OF CYLINDRICAL PARTICLES W.R.T. PARTICLE SURFACE MESH RESOLUTION, SIMULATED FOR A CASE AT RE = 144, PR = 1, ε = 0.48 AND *A* = 4. SYMBOLS INDICATE SIMULATION RESULTS AND THE LINE REPRESENTS AN EXPONENTIAL GROWTH FUNCTION : $\boldsymbol{Nu = 20.64 + exp12.16 + 0.785log2dx}$, WHERE $\boldsymbol{dx}$ REPRESENTS THE GRID SPACING ON THE PARTICLE SURFACE. 89

FIGURE 4.3. ILLUSTRATION OF THE SHAPE OF THE PLANES WHEN CONSIDERING A CERTAIN NUMBER OF PARTICLES REMOVED FROM THE WALL (RIGHT PANEL; ALL 25 PLANES EXPLAINED IN SECTION 4.2.2.2 ARE OF THE SAME SIZE REPRESENTABLE IN THE FIGURE). VARIATION OF NUSSELT NUMBER BASED ON THE PARTICLES REMOVED FROM THE WALL (ARR1…ARR5 REPRESENTS THE DIFFERENT PARTICLE ARRANGEMENTS OF *A* = 4) AT RE144 AND PR = 1 (LEFT PANEL). 90

FIGURE 4.4. RADIAL PROFILES OF POROSITY (LEFT PANEL) AND AXIAL VELOCITY (RIGHT PANEL) VERSUS THE PARTICLE REMOVED FROM THE WALL [ARR1…ARR5 REPRESENTS THE PARTICLE ARRANGEMENTS *A* = 4 SIMULATED AT RE = 144 AND PR = 1]. 91

FIGURE 4.5. NUSSELT NUMBER VARIATION (LEFT PANEL) AND PRESSURE GRADIENT (RIGHT PANEL) FOR (ARR1 …ARR5) OF *A* = 4, VERSUS REYNOLDS NUMBER AND FOR A PRANDTL NUMBER *PR* = 1. THE DASHED AND DASHED-DOTTED LINE REPRESENT 95% CONFIDENCE INTERVALS CONSIDERING NO VOID FRACTION VARIATION IN THE AVERAGED QUANTITY. 92

FIGURE 4.6. CONTOUR PLOT OF THE MAGNITUDE OF THE FLUID VELOCITY (IN M/S) (RIGHT PANEL), AS WELL AS THE TEMPERATURE (IN K, LEFT PANEL) IN A PLANE PARALLEL TO THE FLOW (Y = 0, CUT FROM ARRANGEMENT 2, RE = 144, PR = 1, *A* = 2, 4 AND 6 FROM TOP TO BOTTOM). 94

FIGURE 4.7. HEAT TRANSFER RATE (EXPRESSED VIA THE NUSSELT NUMBER) VERSUS REYNOLDS NUMBER AVERAGED OVER FIVE PARTICLE ARRANGEMENTS, INCLUDING A COMPARISON WITH LITERATURE DATA.

THE CORRELATIONS MORE RELEVANT TO THE COMPARISON BECAUSE OF THEIR OVERALL VALIDITY ARE REPRESENTED IN THE RIGHT PANELS ((*A* = 2, 4 AND 6) FROM TOP TO BOTTOM) 95

FIGURE 4.8. LEFT PANEL: OBSERVED VS. PREDICTED VALUES OF THE NUSSELT NUMBER OVER ALL CASES FOR EQ. (29), (30) AND (32). RIGHT PANEL: OBSERVED VS. PREDICTED VALUES OF THE NUSSELT NUMBER OVER ALL CASES INCLUDING SPHERICAL PARTICLES (EQ. (34)). 97

FIGURE 4.9. COMPARISON OF AVERAGE PRESSURE GRADIENT (L.H.S TERM OF EQ. (35)) FOR DIFFERENT PARTICLE ARRANGEMENTS VERSUS REYNOLDS NUMBER (FOR RE 9 - 180). FOR SPHERES (UPPER-LEFT PANEL) THE ARRANGEMENTS ARE PRESENTED IN (SINGHAL ET AL., 2017F) AND FOR CYLINDERS (UPPER-RIGHT AND BOTTOM PANEL) THE PARTICLE ARRANGEMENTS ARE PRESENTED IN SECTION 4.3.3. 99

FIGURE 4.10. OBSERVED VS. PREDICTED VALUES FOR THE ERGUN EQUATION FITTED WITH NEW CONSTANTS WHEN CONSIDERING THE EQUIVALENT PARTICLE DIAMETER (D_E) (RIGHT PANEL) AND THE ACTUAL PARTICLE DIAMETER (D_P) (LEFT PANEL) FOR THE DATA OF PRESSURE GRADIENT OBTAINED FROM ARRANGEMENTS (ARR1…ARR5 OF EACH ASPECT RATIO) OF PACKINGS CONTAINING CYLINDRICAL PARTICLES FOR SIX DIFFERENT REYNOLDS NUMBERS (RE 9-180). 100

FIGURE 4.11. COMPARISON OF THE RATIO OF HEAT TRANSFER RATE TO PRESSURE GRADIENT IN A PACKED BED OF SPHERICAL PARTICLES AND CYLINDRICAL PARTICLES (DATA AVERAGED OVER FIVE ARRANGEMENTS OF EACH ASPECT RATIO (*A* = 2, 4 AND 6), PR = 1). 101

FIGURE 5.1. GRID INDEPENDENCE BEHAVIOUR FOR THE VARIATION OF MASS FRACTION OF SPECIE A (x_A) AT A PLANE PERPENDICULAR TO THE FLOW NEAR THE OUTLET (2 PLANES BELOW THE OUTLET) IN ARRAY OF SPHERICAL PARTICLES W.R.T. PARTICLE SURFACE MESH RESOLUTION, SIMULATED AT dH_{RXN} = -10 KJ/MOL, PR = 1, ε = 0.351, AND ϕ = 10. SYMBOLS REPRESENT THE RESULTS AND THE LINE IS THE EXPONENTIAL FUNCTION: $\boldsymbol{xA = 0.008048 + exp(9.7158 + 1.1035log2(dx))}$, WHERE (DX) IS THE GRID SIZE ON THE PARTICLE SURFACE. 114

FIGURE 5.2. THE CONTOUR PLOTS FOR FLUID TEMPERATURE (K) (AT PLANE Y = 0, THROUGH A BED OF ε = 0.351, RE = 100, PR = 1). [TOP LEFT: (NO MESH) REPRESENTS THE CASE WITHOUT INSIDE PARTICLE MESH (SINGHAL ET AL., 2017F); IN ALL OTHER PLOTS ε_{INSIDE} REPRESENTS THE PARTICLE POROSITY IN EACH CASE.] 116

FIGURE 5.3. NUSSELT NUMBER EXTRACTED ON 25 PLANES BASED ON LOCAL DRIVING FORCE (DEEN ET AL., 2012; DEEN ET AL., 2014; SUN ET AL., 2015; TENNETI ET AL., 2013) VERSUS POROSITY VALUE INSIDE THE PARTICLE. THE COMPARISON IS MADE TO NUSSELT NUMBER FROM THE IDEAL EXTERNAL

HEAT TRANSFER CASE WITHOUT INSIDE PARTICLE MESH. THIS VALUE HAS ALSO BEEN VERIFIED WITH (SINGHAL ET AL., 2017F) HEAT TRANSFER CORRELATION. 116

FIGURE 5.4. PR-DNS RESULTS FOR CONVERSION OF REACTANT (MASS FRACTION OF SPECIE A; x_A) THROUGH A GEOMETRY OF SPHERICAL PARTICLES (AT PLANE Y = 0; ε = 0.352, ϕ = 10, PR = 1) FOR DIFFERENT REACTION ORDERS (0.5^{TH}, 1^{ST}, 2^{ND}) RESPECTIVELY. 119

FIGURE 5.5. COMPARISON OF THE MASS FRACTION (x_A) OF REACTANT CONVERSION (OF SPECIE A) BETWEEN THE TWO APPROACHES (I) PR-DNS (REPRESENTED BY SOLID LINES) (II) 1D MODEL (DASHED LINES) FOR [TOP] THIELE MODULUS (ϕ=10), AND [BOTTOM] ϕ = 5 FOR DIFFERENT REACTION ORDERS (0.5^{TH}, 1^{ST}, 2^{ND}); ALONG THE HEIGHT OF THE REACTOR GEOMETRY. 120

FIGURE 5.6. COMPARISON OF THE MOLE FRACTION OF REACTANT CONCENTRATION (OF SPECIE A AND SPECIE B) FOR THE SIMULATED TWO CASES [TOP] CASE 1, AND [BOTTOM] CASE 2 FROM (I) PR-DNS (REPRESENTED BY SOLID LINES) (II) 1D MODEL CORRECTED (DASHED LINES) ; ALONG THE HEIGHT OF THE REACTOR GEOMETRY. DOTTED LINE IN CASE 1 REPRESENTS THE PREDICTIONS WITHOUT ADJUSTING THE EFFECTIVENESS FACTOR AS: $\boldsymbol{\eta = \eta A - 1 + \eta B - 1 - 1}$ 122

FIGURE 5.7. COMPARISON OF THE MOLE FRACTION OF REACTANT CONCENTRATION (OF SPECIE A AND SPECIE B) FOR THE SIMULATED TWO CASES [TOP] CASE 3, AND [BOTTOM] CASE 4 FROM (I) PR-DNS (REPRESENTED BY SOLID LINES) (II) 1D MODEL CORRECTED (DASHED LINES); (DOTTED LINE) IN CASE 4 REPRESENTS THE PREDICTION INCLUDING A FULL MASS TRANSFER MODEL FOR REACTANT B, WHILE (INTERVAL LINE) REPRESENTS A PREDICTION WITHOUT A MASS TRANSFER MODEL; WHILE IN CASE 3 (DOTTED LINES) REPRESENTS THE PREDICTION WITH INCORRECT THIELE MODULUS. 123

FIGURE 5.8. PR-DNS PREDICTIONS OF THE REACTANT CONCENTRATION (SPECIE A) FOR DIFFERENT REACTIONS (TABLE 17) (AT PLANE Y = 0; ε = 0.352, ϕ = 10, PR = 1) THROUGH A BED OF POROUS SPHERICAL PARTICLES. [NOTE: THE CONTOURS SHOWN ABOVE ARE EXPRESSED ON A SCALE ($-\log_{10}(x_A)$); BLUE SUGGESTS HIGH, WHILE RED MEANS MINIMUM]. 125

FIGURE 5.9. COMPARISON OF MASS FRACTION OF THE REACTANT (SPECIE A) ALONG THE HEIGHT OF THE REACTOR BETWEEN PR-DNS (SOLID LINES), MODIFIED 1D MODEL (DASHED LINES) AND 1D MODEL (DOTTED LINES) FOR DIFFERENT REACTION CASES IN TABLE 17. THE DOTTED LINES REPRESENT THE 1D MODEL PREDICTIONS WITHOUT ACCOUNTING FOR GAS VOLUME GENERATION. THE INLET SPECIE CONCENTRATION IN CASE OF 1D MODEL HAS BEEN ADJUSTED TO ACCOUNT FOR FASTER SPECIE CONVERSION AT THE INLET IN PR-DNS RESULTS. 126

FIGURE 5.10. COMPARISON OF AXIAL SPECIE PROFILES BETWEEN PR-DNS (SOLID LINES) AND 1D SIMULATIONS (DASHED LINES) FOR A PACKED BED OF SPHERICAL PARTICLES AT ($\varepsilon = 0.355$, $Pr = 1$, AND $\phi = 10$) FOR DIFFERENT HEAT OF REACTIONS (dH_{RXN} IN KJ/MOL). 126

FIGURE 5.11. PR-DNS PREDICTIONS OF MOLE FRACTION OF CH4 CONCENTRATION (TOP LEFT], H2 CONCENTRATION [TOP RIGHT] AND FLUID TEMPERATURE (IN K) [BOTTOM] AT (PLANE Y = 0; ε = 0.352) FOR INLET TEMPERATURE 1100 °C, THROUGH A PACKED BED OF POROUS SPHERICAL PARTICLES FOR STEAM METHANE REFORMING PROCESS. 127

FIGURE 5.12. RADIAL PROFILES OF GAS DENSITY AND THE APPROXIMATE REACTION RATE CONSTANT (EQ. (69))) IN A PARTICLE CLOSE TO THE INLET OF THE SIMULATED GEOMETRY. 128

FIGURE 5.13. COMPARISONS OF DIFFERENT 1D MODEL SETUPS AGAINST PR-DNS RESULTS. 130

FIGURE 6.1. MODIFICATION FACTOR FITTED OVER A RANGE OF REYNOLDS NUMBER FOR PACKED BED OF SPHERICAL PARTICLES (WITH PARTICLE VOID FRACTION OF 0.35). 141

FIGURE 6.2. PR-DNS RESULTS FOR MOLAR CONCENTRATION OF CH_4 (LEFT) AND GAS TEMPERATURE (K) VARIATION AT 1000 °C (1273 K) INLET TEMPERATURE. 142

FIGURE 6.3. COMPARISONS OF DIFFERENT 1D MODEL FORMULATIONS TO PR-DNS DATA AT THREE DIFFERENT INLET TEMPERATURES. IN EACH GRAPH, THE CIRCLES REPRESENT THE PR-DNS RESULTS, THE SOLID LINES REPRESENT THE FULL 1D MODEL WITH ALL THE PROPOSED ADJUSTMENTS, THE DASHED LINES REPRESENT THE EXCLUSION OF THE ADJUSTMENT FOR THE VARYING REACTION RATE CONSTANT (EQ. (83)), AND THE DOTTED LINES REPRESENT THE EXCLUSION OF ALL MODEL ADJUSTMENTS (EQS. (82)-(84)). 142

FIGURE 6.4. OUTLET GAS SPECIES COMPOSITION AND TEMPERATURE DURING ONE PBCLR CYCLE. ... 146

FIGURE 6.5. AXIAL PROFILES OF SPECIES AND TEMPERATURE IN THE PBCLR REACTOR AT THE END OF THE OXIDATION STAGE [TOP LEFT – 900 S IN FIGURE 6.4], END OF THE REDUCTION STAGE [TOP RIGHT – 1500 S IN FIGURE 6.4], MIDDLE OF THE REFORMING STAGE [BOTTOM LEFT – 1950 S IN FIGURE 6.4], AND END OF THE REFORMING STAGE [BOTTOM RIGHT – 2400 S IN FIGURE 6.4]. 147

FIGURE 6.6. OUTLET GAS SPECIES COMPOSITION AND TEMPERATURE DURING ONE PBCLR CYCLE WITH 2X HIGHER GAS FEED OVER 4X LARGER PARTICLES THAN FIGURE 6.4. 148

FIGURE 7.1. THE SECTION (Y=0) OF THE REACTOR GEOMETRY WITH CUTCELL MESH 152

FIGURE 7.2. NON-RESOLVED EULER-LAGRANGIAN GRID SETUP 154

FIGURE 7.3. TEMPERATURE DISTRIBUTION PROFILES WITH TEMPERATURE GRADIENTS INSIDE THE PARTICLES AT PLANE Y=0, THROUGH THE REACTOR GEOMETRIES WITH DIFFERENT BED POROSITIES AND REYNOLDS NUMBERS FOR THE CASE WITH A FIXED VOLUMETRIC HEAT SOURCE INSIDE THE PARTICLES. 157

FIGURE 7.4. COMPARISON OF THE HEAT TRANSFER COEFFICIENT IN THE REGION OF INTEREST (NO WALL, INLET AND OUTLET EFFECTS) OVER DIFFERENT POROSITY AND REYNOLDS NUMBER VALUES FOR THE CASE WITH INTEGRATED HEAT SOURCE INSIDE THE PARTICLES. 158

FIGURE 7.5. COMPARISON OF THE PREDICTION OF HEAT TRANSFER FROM THE CORRELATIONS OBTAINED IN THIS WORK. T = CONSTANT TEMPERATURE (HOMOGENOUS PARTICLE SURFACE TEMPERATURE); AND S = INTEGRATED HEAT SOURCE (NON-HOMOGENOUS PARTICLE SURFACE TEMPERATURE. 158

FIGURE 7.6. COMPARISON OF THE PREDICTION OF MEAN PARTICLES SURFACE TEMPERATURE FROM PR-DNS AND NON-RESOLVED SIMULATIONS. (WHERE, FLUENT= PREDICTION FROM PR-DNS; AND CFDEM_AV AND CFDEM_CUP ARE PREDICTIONS FROM NON-RESOLVED SIMULATIONS WITH AVERAGED FLUID TEMPERATURE AND BULK FLUID TEMPERATURE RESPECTIVELY). 160

FIGURE 7.7. TEMPERATURE DISTRIBUTION PROFILES AT PLANE Y=0, THROUGH THE REACTOR GEOMETRIES WITH DIFFERENT AND REYNOLDS NUMBERS FOR THE CASE WITH A FIXED VOLUMETRIC HEAT SOURCE INSIDE THE PARTICLES. FLUENT (ABOVE) AND CFDEM (BELOW). 160

FIGURE 7.8. APPROX. LOCATION OF THE PARTICLES STUDIED FOR THE INTRA PARTICLE TEMPERATURE DISTRIBUTION COMPARISON. 161

FIGURE 7.9. INTRA PARTICLE TEMPERATURE DISTRIBUTION PROFILES AT RE100, RE70, RE40 AND RE10 OBTAINED FROM FLUENT (ASYMMETRIC) AND PARSCALE (SYMMETRIC). [VERTICAL LINE = PREDICTION IN THE DIRECTION OF FLOW (FLUENT), LATERAL LINE= PREDICTION PERPENDICULAR TO THE FLOW (FLUENT); CFDEM_AV AND CFDEM_CUP = PARSCALE PREDICTIONS IN A NON-RESOLVED COUPLED SIMULATION USING DIFFERENT FLUID AVERAGED TEMPERATURES (AVERAGE AND BULK FLUID RESPECTIVELY). 162

FIGURE 7.10. NUSSELT NUMBER VARIATION WITH THE WALL DISTANCE FOR RE100 OBTAINED FROM THE UNRESOLVED SIMULATION APPROACH. 163

LIST OF APPENDICES

APPENDIX 1 COMPARISON OF PARTICLE RESOLVED DIRECT NUMERICAL SIMULATION AND 1D MODELING OF CATALYTIC REACTIONS IN A PACKED BED.

APPENDIX 2 COMPARISON OF PARTICLE RESOLVED DIRECT NUMERICAL SIMULATION AND 1D MODELLING OF CATALYTIC REACTIONS IN A CYLINDRICAL PARTICLE BED.

1 INTRODUCTION

Abstract

This chapter introduces the project under which this PhD work has been completed, then gives the general background of packed bed reactors and their current research. This is followed by a section pertaining to particle resolved direct numerical simulations (PR-DNS), and their application to obtain results with reduced scale simulations in the section on multiscale modelling. The last section of this chapter lays foundation to objectives, scope and outline of the presented work in this thesis.

1.1 Background

This PhD project is a part of the EU FP7 Project: NanoSim (A Multiscale Simulation-Based Design Platform for Cost-Effective CO_2 Capture Processes using Nano-Structured Materials). The aim of NanoSim is to develop an efficient and cost effective multi-scale and multi-dimensional simulation platform using Nano-Structure Materials. A platform named PORTO (NanoSim project) is developed to connect models at different scales ranging from atomistic level, particle, industrial equipment and full plant scale. The model data developed at each scale pass on the data to next subsequent scale at a courser level. To support the scientific coupling and automatic flow of data between the models proper data management and sophisticated software architecture have been developed.

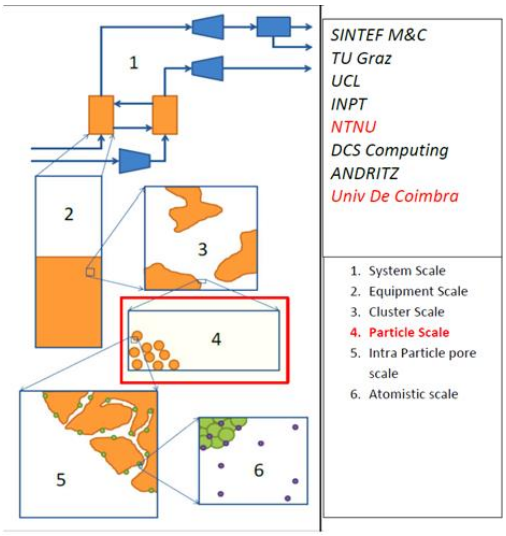

Figure 1.1. The pictorial representation of the scale and the member partners this PhD is defined in NanoSim project under EU-FP7 framework**.**

The Project NanoSim comprises of ten different work packages spread around with eight consortium partners from Europe as shown in Figure 1.1. The consortium partners include SINTEF Materials and Chemistry (Norway), TU Graz (Austria), University of Coimbra (Portugal), University College London (United Kingdom), INPT Toulouse (France), NTNU (Norway), DCS Computing GmbH (Austria), Andritz Energy and Environment GmbH. The current work for the development of "Models for 1D simulations of packed beds" i.e. models for heat and mass transfer in packed bed reactors and "Fully functional

2D axis-symmetric and 3D model for fixed bed reactors" in this PhD are a part of work representing "particle scale" under WP4 and WP5 in NanoSim respectively.

Packed bed reactors are continuous tubular reactors in which the reactive fluid (or gas specie) passes over stationary particles (Jakobsen, 2014). The basic setup of a packed bed reactor can be seen in Figure 1.2. The particle can participate in both catalytic and non-catalytic reactions depending upon the application we are looking into. Packed bed reactors find various applications in chemical and process industry because of their ease of operation and simpler technology. Some different examples where packed beds can be used are separators, filters, dryers, and heat exchangers. A key factor in packed bed reactors is the ability to predict heat transfer inside the bed in order to improve performance and facilitate the proper functionality of the equipment (reactors).

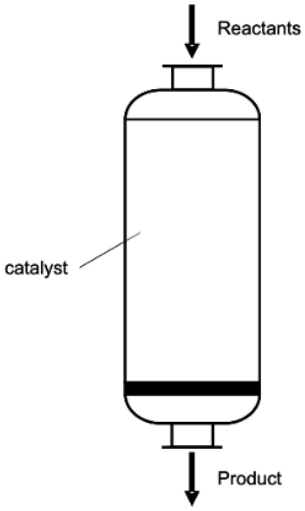

Figure 1.2 Typical sketch of a packed bed reaction [Source: (Jakobsen, 2014)]

Gas-particle heat transfer is one of the most studied topics in the literature for packed bed reactors. Numerous methods and correlations have therefore been suggested for modelling of gas-particle heat transfer (Gupta et al., 1974) (Wakao et al., 1979) (Inaba et al., 1988) (Khan et al., 1991) (Collier et al., 2004) (Scott et al., 2004) (Gnielinski, 1978) (Achenbach, 1995) (Mehrabian et al., 2014) (Gunn, 1978), majorly dependent upon parameters like Reynolds number, Prandtl number, bed porosity, N (Ratio of diameter of reactor to diameter of the particle) value, local flow conditions, and the particles' surface roughness.

Still, the majority of the proposed heat transfer correlations are derived from experimental data, and only recently there have been a number of studies utilizing direct numerical simulations (DNS) (Tavassoli et al., 2015) (Deen et al., 2012; Deen et al., 2014) (Sun et al., 2015; Tenneti et al., 2013) for the prediction of heat transfer rates. Given the uncertainties involved in experimental techniques and their limitation in giving results to a detailed scale to visualize heterogeneities in the bed, these PR-DNS (particle-resolved DNS) methods are proposed as a more accurate framework for deriving closures for gas-solid systems (Dixon, 2017; Dixon and Nijemeisland, 2001).

1.2 Particle resolved direct numerical simulations (PR-DNS)

With the development in terms of computational resources and facilities of supercomputer clusters, the computational fluid dynamics solutions on detailed scale have become possible and more specifically the direct numerical simulations (DNS) have gained limelight. To apply the DNS methodology to packed beds, particle resolved direct numerical simulations are required (PR-DNS). As the current scenario for simulating full scale reactors is still limited by the computational resources, PR-DNS has gained more focus recently, especially because of its capability to give insights into the local phenomena by analyzing a section in the reactors. A small segment of the packed bed simulated using PR-DNS can give more detailed information of the local void fraction and velocities than the information obtained experimentally (Dixon, 2017), and hence these information can be scaled up using the multiscale modelling to be applied to large scale reactors.

PR-DNS requires a realistic packing of particles (packed bed), which is often accomplished using discrete element method (DEM) (Cundall and Strack, 1979). Then the path is either to follow (i) immersed boundary method (Blais et al., 2016; Derksen, 2014; Uhlmann, 2005) or to use (ii) body fitted meshes (Singhal et al., 2017e, f) especially for the non-moving systems, with which higher spatial resolution can be obtained at identical cell count.

1.3 Multiscale modelling

The fundamental understanding of the mass, momentum, heat and specie transfer is the basic necessity for the gas-solid packed bed systems. With the major advancement in

terms of PR-DNS as explained earlier, the fluid flow is resolved around the particles and the data obtained for the particle fluid interactions is interpolated and fitted in form of correlations to represent the phenomena.

With the help of multiscale modelling, these developed correlations for external heat and mass transfer in packed beds are being used as closure relations in unresolved Euler-Lagrange simulations as a coupled simulation between computational fluid dynamics and discrete element method (CFD-DEM), where the size of cells are larger than the particles.

The similar concept of closure relations is used to formulate the Euler-Euler simulations in form of 1D framework, which are used to simulate large industrial scale reactors. Here the appropriate closure relations for external heat and mass transfer along with appropriate models for intra particle diffusion are solved with Eulerian multi-fluid approach on a reduced scale of 1D model.

1.4 Research objectives

The objectives of this PhD is to develop the closure models for external heat and mass transfer in realistically packed bed reactors for gas-solid systems. These closures were then implemented into an open source non resolved Eulerian-Lagrange environment and 1D simulation model to solve large-scale industrially relevant CFD problems. The objectives of the work are summed up as follows:

- Develop a methodology to obtain closures for external heat and mass transfer in densely packed beds.
- Advanced closures for packed bed simulations using the methodology established to capture the effects due to heterogeneities in the particle packings.
- Develop a multi-dimensional Eulerian model for fixed bed reactors.
- Implementation of closures into 1D model framework along with improvements to current internal mass transfer models, such that the resulting modelling tool will be simple and user friendly for use by the industry and has possibility to be coupled to full plant scale simulations.

1.4.1 Scope

- The prediction of heat and mass transfer in realistic packings (porosity(ε) < 0.5) of densely packed particles using PR-DNS, which is generally not the case in the recent correlations in literature (Deen et al., 2012; Deen et al., 2014; Sun et al., 2015; Tavassoli et al., 2015; Tenneti et al., 2013)
- A single correlation valid for external heat and mass transfer in realistically packed bed of either mono disperse spherical particles or cylindrical particles (of different aspect ratios).
- The work points towards the possibility to shift from the conventional resolved-DNS based simulations in packed bed reactors to non-resolved simulations and 1D modelling. These simulations are computationally cheap alternative to resolved DNS simulations.
- The PhD was focussed on development of new models for external heat and mass transfer and improvements to internal mass transfer models with appropriate correction to Ergun constants for pressure drop, while the advanced models for drag and other laws were not the target of this work.
- The verification of the models for internal mass transfer in literature were the final test in the PhD. The closures were tested and improved in the 1D model framework against the PR-DNS data to find the feasibility of using them in industrial scale reactors.

1.4.2 Outline

After discussing the objectives and the scope, an outline of the overall work within this thesis is presented and briefly discussed in this section (also shown in Figure 1.3).

Chapter 2 presents “what not to do” to develop a methodology to study external heat and mass transfer in realistically packed particle beds. It lists the major trends followed in literature to study heat transfer in packed beds and addresses the need to take a closer look in literature to argument their limitations.

In Chapter 3 and 4, followed by the limitations already checked in Chapter 2. A newly developed methodology to correctly deal with the problem of particle overlaps in densely packed beds is detailed and the correct method followed in this thesis to obtain the closure

models for external heat and mass transfer in a packed bed of monodisperse spherical particles and cylindrical particles (aspect ratio = 2, 4 and 6) is presented.

Chapter 5 presents the verification of the heat and mass transfer models for reduced scale 1D model, which can be used for industrial scale simulations. The application of the developed closure models for industrial scale problems through non-resolved and multidimensional approach is demonstrated in Chapter 6 and 7. Finally, Chapter 8 sums up the thesis with conclusion, followed by recommendation for possible future works.

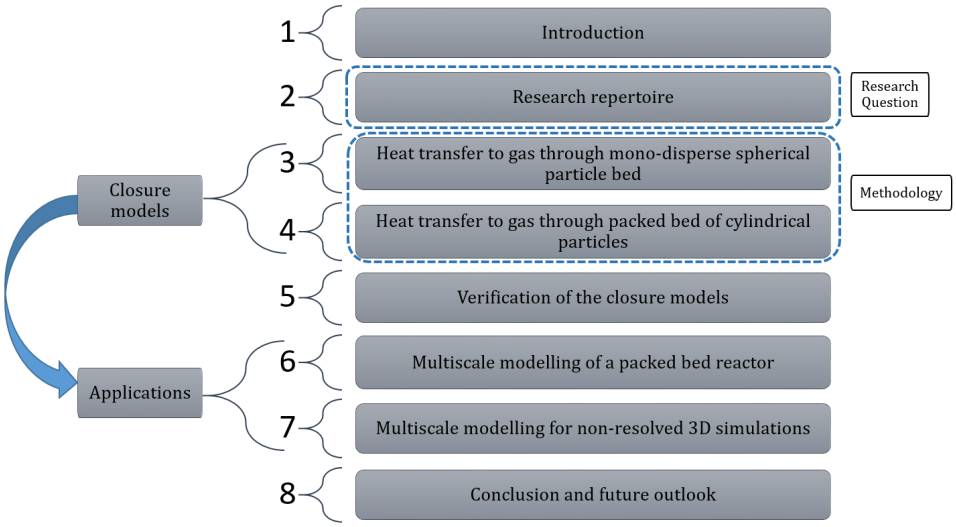

Figure 1.3. Structure of the thesis with the basic essence

2 RESEARCH REPERTOIRE

Abstract

Gas-particle heat transfer rates are investigated using particle-resolved direct numerical simulation (PR-DNS). We utilize a discrete element method (DEM) approach to first obtain a realistic packing of the particles, and then build a computational mesh based on these particle positions for running PR-DNS. A common challenge in such investigations is the region of close proximity or overlap between adjacent particles, which can result in highly skewed cells while meshing. The simplest method for addressing this challenge was investigated in this paper: particle shrinkage. We investigated the hypothesis that the void fraction variations caused by particle shrinkage could be tolerated when using a correlation with void fraction dependence. However, this hypothesis was proved false because the particle assembly created by shrinking all particles was evenly spaced and not random, resulting in an over prediction of heat transfer relative to existing correlations. When a random particle arrangement was simulated, however, results matched well with correlations. In addition, we find that DNS results using the commercial CFD code ANSYS FLUENT and the open-source code OpenFOAM® return very similar results. The computational performance was similar, with (i) OpenFOAM being faster for a fixed number of iterations, and (ii) ANSYS FLUENT requiring a smaller number of iterations to find convergence. [i]

[i] This chapter is based on Arpit Singhal, S. Cloete, S. Radl, R.Q. Ferreira, S. Amini., CFD-DEM predictions of heat transfer in packed beds using commercial and open source codes, *MAYFEB Journal of Chemistry and Chemical Engineering*, 1 (2016), pp. 10-26

Nomenclature

Symbols

Re	Reynolds number
Nu	Nusselt number
Pr	Prandtl number
d_p	Diameter of the particle (m)
D	Diameter of the reactor (m)
j	Number of particles
K_f	Thermal Conductivity of fluid (W/ m K)
m_P	Mass of the particle (kg)
C_p	Specific Heat Capacity of fluid (J/Kg K)
h	Heat transfer coefficient (W/m^{2}K)
T_{bulk}	Bulk fluid temperature (K)
T_P	Particle surface temperature (K)
T	Temperature of the fluid (K)
e_z	Unit vector in z-direction
u	Superficial velocity of the fluid (m/s)
v	Velocity of the particles for DEM (m/s)
u_z	Velocity of the fluid in Z-direction (m/s)
N	Ratio of diameter of reactor to diameter of the particle
dV	Volume in the region of interest
g	Gravity (m/s^2)

Greek

ε	Porosity (void fraction)
ρ	Density of fluid (kg/m^3)
μ	Viscosity of fluid (kg/ m s)
$\varphi_{f\rightarrow P}$	Heat flux from fluid to particles (W/m^2)

Vectors:

$\vec{u}$	Fluid velocity (m/s)
$\vec{g}$	Gravity (m/s^2)

Subscripts:

P	particle
f	fluid
n	normal
t	Tangential

Operators:

$\boldsymbol{\nabla}$ Gradient operator (m^{-1})

$\nabla.$ Divergence operator (m^{-1})

∇^2 Laplace operator (m^{-2})

$\frac{d}{dt}$ time derivative (s^{-1})

2.1 Introduction

Gas-particle heat transfer is one of the most studied topics in the literature for packed bed reactors. Numerous methods and correlations have therefore been suggested in the literature for modelling of gas-particle heat transfer. Still, the majority of the proposed heat transfer correlations are derived from experimental data, and only recently, there have been a number of studies utilizing direct numerical simulations (DNS) for the prediction of heat transfer rates. Given the experimental uncertainties involved in existing correlations, these PR-DNS (particle-resolved DNS) methods are proposed as a more accurate framework for deriving gas-particle heat transfer models.

PR-DNS for the derivation of accurate heat transfer correlations in realistically packed particle assemblies is therefore an important research question and has not been published yet in our knowledge. A single complete empirical correlation for heat and mass transfer in packed beds, fluidised beds and single particle, valid for both analytical and experimental conditions, was first introduced by (Gunn, 1978). The correlation was valid for a wide range of porosity ($0.35<\varepsilon<1$), Reynolds number and Prandtl number. However, a modelling study by (Tavassoli et al., 2015) has recently suggested that the correlation is only accurate for rather dilute systems ($\varepsilon>0.7$). This hints to a possible shortcoming of the parameters in the Gunn correlation to predict heat (and mass) transfer rates in dense systems.

(Deen et al., 2014) used DNS to refit the model from (Gunn, 1978) to improve the accuracy for porosities ranging from 0.5 to 1, and a variety of Reynolds numbers for monodisperse particles. Most important, the simulations of Deen et al. were performed in laterally-periodic, but rather thing slaps of particles. Similar work using PR-DNS was done by (Sun et al., 2015) however, in fully periodic domains. Both studies suggested an improved empirical correlation for heat and mass transfer in packed beds, utilizing the concept of a cup-mixing (bulk) temperature for the fluid. This cup-mixing temperature

was calculated using the planes in the direction perpendicular to the flow direction. We note in passing, that this cup-mixing temperature is not available in simulations on a coarser length scale (e.g., two-fluid model simulations, TFM). Hence, a correction needs to be applied when using the average fluid temperature in TFM-based simulations as noted by (Sun et al., 2015).

The major problem associated with developing a realistic packed bed particle arrangement through DEM is the particle-particle and particle-wall overlap. This overlap leads to highly skewed cells in the proximity regions of particle-particle and particle-wall contacts. Such highly skewed cells should be avoided because they can decrease the convergence and accuracy of the solution.

There are many solutions to this overlapping problem suggested in the literature. (Kuroki et al., 2009) introduced a method to join the particles by a cylinder if the distance between the particles decreases a predefined value. This method accounts for the pressure drop correctly but the overall porosity of the bed gets highly affected. (Eppinger et al., 2011) described a method to flatten the particle surfaces locally in order to avoid the overlap. The above methods are classified as local modification methods.

(Guardo et al., 2004) suggested to increase the particle size by a certain value, in this way the contact points become contact areas and consequently decreases the skewed cells in the geometry. The most common method available to deal with the overlapping problem is to shrink the particles in the packed bed by certain values, and hence to avoid the overlap. Such a methods is classified under the category of and overall modification, because it affects the overall structure of the packed bed. Many publications using different shrinkage factors have used this method to deal with the particle-particle and particle-wall contacts. This is an easy method to implement but it strongly affects the porosity of the bed. (Bai et al., 2009) used the particle bed with 1% shrinking, (Atmakidis and Kenig, 2009) preferred to shrink the particles by 2%, (Lopes and Quinta-Ferreira, 2009) used a shrinking of 3% for the bed, while, (Dixon and Nijemeisland, 2001) firstly presented the work with shrinking by a factor of 1% and then in (Dixon et al., 2007) reduced the particles by 0.5% to avoid contact. (Calis et al., 2001) used 1% shrinkage factor after generating the bed, both 2% and 1% shrinkage was checked for the change in friction factors from the pressure drop simulations to check the validity of 1% shrinkage. Similar trend was followed by (Reddy and Joshi, 2008) by a shrinkage of bed by 1% to avoid overlap. The influence of the shrinking factors on the heat transfer and fluid velocity

was investigated by (Romkes et al., 2003), different shrinking factors 1%, 2% and 5% were compared and it was decided that the 1% shrinkage is representative of the full contact of particles, given a 5% relative error corridor is acceptable.

A review of all the methods available to deal with the problem was given by (Dixon et al., 2013) They suggested two types of changes in the bed: a local modification, and an overall modification of the packed bed. The suggestion was leaned towards using local modification of the bed than the overall modification, with a better approximation for porosity and pressure drop using caps and bridge method.

Numerous methods for generating the particle bed have also been investigated in the literature. (Jafari et al., 2008; Soleymani et al., 2007) generated a packed bed with non-overlapping particles with an unknown random arrangement. (Gunjal et al., 2005) utilized a periodic box setup with particles arranged at a distance of 1mm from each other. (Lee et al., 2007) utilized a body centered cubical (BCC) and face centered cubical (FCC) arrangement with distance of 1mm between the particles for their heat transfer study with large eddy simulations (LES). (Deen et al., 2012; Deen et al., 2014) used a Monte-Carlo method to generate the random packed bed, and to avoid the overlap for their DNS.

In this paper, the overall modification methods are dealt with in detail for the heat transfer problems. The main focus of this work is to test the validity of shrinking the particles in packed beds for heat transfer calculations and to highlight whether such packings can be considered realistic or random. The effect of shrinking is studied in detail by comparing the results of heat transfer with the heat transfer correlations valid for random packings (Sun et al. and Deen et al.). (Deen et al., 2014; Sun et al., 2015) The effects caused by shrinking are reported and documented. In addition, this work compares heat transfer predictions in packed beds by using both commercial (ANSYS FLUENT) and open source (OpenFOAM) software.

2.2 Methodology

2.2.1 Particle bed generation (DEM)

DEM (Discrete Element Method) using Ansys FLUENT 17.2 is used to generate the packed bed in this work. The particles are injected in a cylindrical geometry with gravity force and when the particles get settled the packed bed is obtained. More details about the

particle arrangement and the DEM setup used to obtain the packing are given in Table 1 and Table 2.

The particle bed generated through DEM has particle and particle overlaps which will be removed by shrinking the particles as discussed in the last Section 2.1. Different shrinking factors are considered later in this work and their effects are then documented.

Table 1. The reactor geometry with meshing details

Parameters	Value
Number of particles	100
Diameter of the particles (d_p) (m)	5e-3
Diameter of the reactor (D) (m)	0.03
N value of the reactor	6
The cell size of surface mesh on the particles (m)	1e-4
Maximum face size for the mesh (m)	1e-3
Resolution of mesh on particles for DNS	d_p/50
Growth rate of mesh	1.2

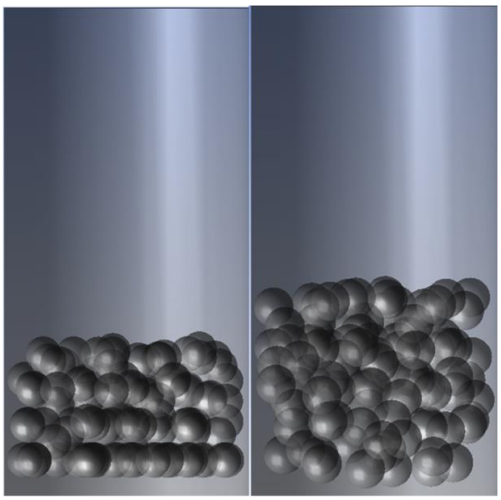

Figure 2.1. Final realistic packing inside the reactor (left) and random particle bed (right) generated in Workbench

2.2.2 Random packing from DEM

To generate a random particle arrangement of higher porosities, particles are injected into the reactor geometry as explained in Section 2.2.1 without the gravity force. Initially, there is a significant degree of overlap between the injected particles, thus creating large repulsive forces which accelerate the particles in different directions. As a result, particles move around and collide in a random fashion. After 20s of this random particle translation

and collision, the simulation is stopped and the resulting random particle positions are exported as described before. The resulting geometry is shown in Figure 2.1.

Table 2. DEM parameters for the normal, tangential and gravity forces

Parameters	Law	Value
Particle normal force Spring Dashpot for DEM	Spring dashpot	*K* = 250 *Eta* = 0.9
Particle tangential force parameter for DEM	Friction-dshf	*mu-stick* = 0.5 *mu-slide* = 0.2 *mu-limit* = 0.1
Gravity force		-9.81 m/s^2

2.2.3 Mesh

The obtained geometry given in Figure 2.1 is then meshed using ANSYS Meshing. There are different mesh types available for the complicated geometries of the packed beds. Tetrahedral cells form the most basic form of unstructured mesh, but large meshes are required to obtain the same level of accuracy as compared with Polyhedral and Cutcell and therefore tetrahedral is not used in this work. Polyhedral meshing is difficult to obtain directly in ANSYS Meshing and has to be converted using Fluent which makes it inconvenient for export to OpenFOAM for the comparison done in this work. The structured hexahedral mesh created using the cutcell method can limit the number of cells required and can also be conveniently exported to OpenFoam®. It is therefore selected for this study with the details shown in Table 1.

The reactor geometry is meshed with the refinement near the particle surfaces and in the proximity region between the two particles using cutcell mesh. The particles are to be resolved for the Direct Numerical Simulation (DNS); therefore the resolution of $d_p/50$ is used on the particle surfaces. This degree of resolution is sufficient to resolve the heat transfer around individual particles in the packed beds.

2.2.4 Computational fluid dynamics

The meshed geometry is solved under steady state conditions since transient effects in the packed bed region can be assumed to negligible at operating low Reynolds numbers. Transient effects are stronger in the regions above the packed bed but the focus of this work was working on heat transfer in the packed bed region to compute the Nusselt

number for the particle to fluid heat transfer. Therefore, the steady state simulations provide a computationally cheaper solution to the heat transfer problems.

2.2.5 Model equations

The conservation equations of continuity, momentum, and energy for the incompressible, steady state, Newtonian fluid solved for the DNS are given by

$$\nabla.\vec{u} = 0 \quad (1)$$

$$\nabla.(\rho\vec{u}\vec{u}) = -\nabla p + \mu\nabla^2\vec{u} + \rho\vec{g} \quad (2)$$

$$\rho C_p \nabla.(T\vec{u}) = K_f \nabla^2 T \quad (3)$$

The particle equation of motion solved in the DEM simulations is given below. Rotational particle motion was not solved as this was not necessary to obtain a randomly dispersed particle array.

$$m_p \frac{dv}{dt} = m_p g + \sum_{i=1}^{j} (F_{p,i,n} + F_{p,i,t}) \quad (4)$$

2.2.6 Boundary conditions

The particles maintained at a temperature of 573 K are cooled by a flowing fluid (air in this work) at 473 K. Table 3 shows the flow properties used in the simulations.

The cylindrical reactor geometry contains a velocity inlet and a pressure outlet. The reactor wall is modelled with a no-slip boundary condition, and with zero heat flux. The heat transfer coefficient in the bed is calculated with the help of the heat flux through the particle surfaces from Eq. (5). The bulk fluid temperature is calculated using Eq. (6), i.e., the flux-averaged fluid temperature was computed. This is similar to the cup-mixing temperature used in literature. The values of the heat transfer coefficient are computed in the region of interest as described later in Section 2.4.1.

Table 3. Flow properties

Parameter	Value
Diameter of the particle (d_P) (m)	5e-3
Density (ρ) (kg/m^3)	1.225
Viscosity (μ) (kg/m s)	1.789e^{-5}
Thermal conductivity (k) (W/m K)	0.0242
Specific Heat capacity (C_p) (J/kg K)	1006
Prandtl number	0.744
Temperature of Inlet (K)	473
Temperature of particles surface (K)	573

$$\varphi_{P\to f} = h\,(T_P - T_{bulk}) \tag{5}$$

$$T_{bulk} = \frac{\int (u.e_z)T\,dV}{\int (u.e_z)\,dV} \tag{6}$$

2.2.7 Solver settings

ANSYS FLUENT is used to solve the heat and fluid flow around the particles in the bed. The phase-coupled SIMPLE algorithm with 2nd order spatial discretization schemes for pressure-velocity coupling are used to obtain the solution.

2.3 Validation for a single particle

This section of the paper validates the method outlined in Section 2.2 for a single particle before it is applied for more complex case simulations.

The heat transfer coefficient (Nusselt Number) and drag coefficient calculated from single particle surface immersed in fluid domain is computed for several particle Reynolds numbers varying between 20 and 400. The results for the convective heat transfer were compared to the experimental correlation from Ranz-Marshall,(W. E. Ranz and W. R. Marshall, 1952). The comparison of heat transfer from the simulation and the experimental correlation is represented in Table 4 and Figure 2.2. It is seen that the comparison of results is good, and the relative error exceeds 5% only at very low Reynolds numbers which are not of interest for packed bed operation.

Table 4. Comparison of heat transfer coefficient with Ranz-marshall correlation

Re	h_Ranz-Marshall (W/m²K)	simulation (W/m²K)	% (relative difference)
20	21.44	20.22	-6.099
40	26.32	25.35	-3.861
60	30.06	29.28	-2.695
80	33.22	32.50	-2.200
100	35.10	35.34	-1.871
200	46.90	46.83	-0.152
400	62.31	62.87	0.881

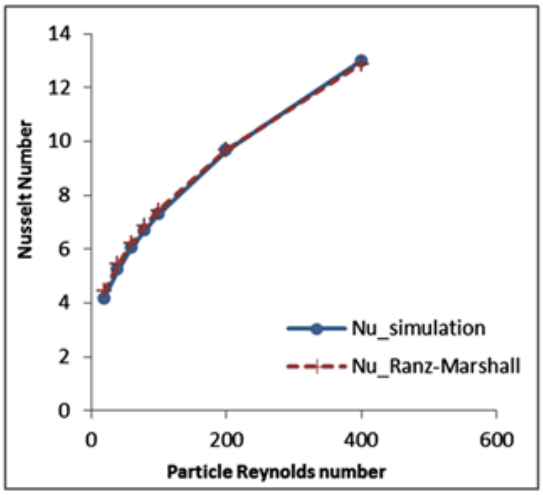

Figure 2.2. Prediction of heat transfer coefficient variation with particle Reynolds numbers

2.4 Results and Discussions

This section compares the effect of different shrinking factors on the packed bed and checks whether the packed bed after shrinking can still be accounted under realistic packing or even random packings. The accuracy of the results from the different codes is validated, and the performance of commercial and open source codes is compared.

2.4.1 Case setup

A reactor with an N value (ratio of reactor diameter to particle diameter) greater than 4 can be assumed to be less sensitive to the wall effects (Dixon, 1997). Similar findings were presented by (Smirnov et al., 2003) for N > 3.5. The reactor in this work is with $N = 6$. To be sure that the wall effects, inlet effects and outlet effects do not affect the heat

transfer calculations strongly, a region of interest is considered (Figure 2.3) thus minimizing these effects. The data for the bed porosity and the convective heat transfer is calculated inside this region of interest.

Various degrees of shrinkage were applied to the particle bed in order to avoid overlap and a change of the bed porosity. The five cases to be discussed in the next section are outlined in Table 5. Each of these five cases was simulated at four different particle Reynolds Numbers ranging between 36 and 144.

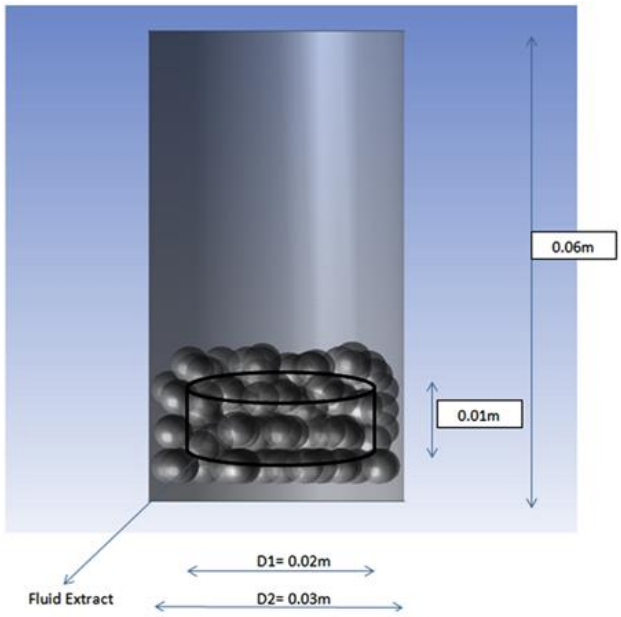

Figure 2.3. Representation of the region of interest in the packed bed region.

Table 5. Schematic representation of different packed bed setups achieved by shrinking

Shrinkage (%)	Particle Diameter [mm]	Bed Porosity (Fluid Extract Region)
1.5 %	4.925	0.425
4 %	4.8	0.4755
10 %	4.5	0.5535
20 %	4.0	0.7256

2.4.2 Heat transfer for different porosities

The comparison study for the spherical particle packed bed generated through shrinking is obtained by analysing the results of convective heat transfer coefficient from ANSYS

FLUENT and then benchmarking the results against the experimental correlation results by (Gunn, 1978) as well as two recent correlations derived from DNS results (Deen et al. and Sun et al.).(Deen et al., 2014; Sun et al., 2015).

The plots for the convective heat transfer from the particle surfaces in the region of interest for various porosities and different particle Reynolds numbers are shown in Figure 2.4. It can be seen that for porosity ($\varepsilon = 0.42$), i.e., the closest to realistic packing, the heat transfer is under-predicting to the correlation results. This is not in good comparison and can be because of the validity of (Sun et al., 2015) is for porosity ($0.5< \varepsilon <1$) i.e. random packings and not realistic packings. The comparison is similar for the correlation of (Deen et al., 2014) which agrees closely with the results from (Sun et al., 2015) The validity of (Gunn, 1978) has already been discussed by (Tavassoli et al., 2015) suggesting that is only valid for dilute systems with porosity ($\varepsilon>0.7$).

For the higher porosity values ($\varepsilon= 0.47$, 0.55 and 0.72) which are achieved by shrinking the particles, the predicted heat transfer coefficients steadily increase when compared to the correlation values. Eventually, results from this study over predict all the experimental correlation values at porosity ($\varepsilon = 0.72$).

The reason for this trend is that a particle bed created by a large degree of particle shrinkage can be considered as neither a realistic nor a random packing. Particles in this kind of arrangement are equally spaced from each other, thus maximizing the degree of gas-particle contact. In contrast, in a random packing (for which the various published correlations are valid), particles may shield each other. We speculate that this results in regions of relatively high voidage, where the gas slips past the particles, and hence heat transfer is limited. Our speculations are supported by a set of simulations in which a different packing was considered. Specifically, heat transfer in the random packing shown in Figure 2.1 with the same setup for geometry, meshing and solution as mentioned in Table 1 and Table 3, was analyzed. Therefore, this new random packing with a porosity of $\varepsilon = 0.62$ was generated, and compared to a bed with the same porosity but prepared by shrinking our old packing from section on 2.2.1 up by a factor of 13%.

A variety of flow situations characterized by Reynolds numbers between 36 and 144 were analyzed for both packings. Figure 2.5 illustrates that our results using a random packing are in close agreement with the DNS results from (Deen et al., 2014; Sun et al., 2015)

within a 5% error corridor. This result serves as a validation of our simulation methodology against previous DNS results for random packings of higher void fractions. Most important, this result highlights the limitation in the method of varying the packing porosity by shrinking the particles.

Furthermore, this result serves as a validation of this method against previous DNS results for random packings of higher void fractions. This reemphasizes the result for the lowest porosity case shown in Figure 2.4 where the DNS results from this study returned substantially lower heat transfer than all the correlations. This apparent inaccuracy of existing correlations in realistic packed bed packings is recommended for closer examination in future works.

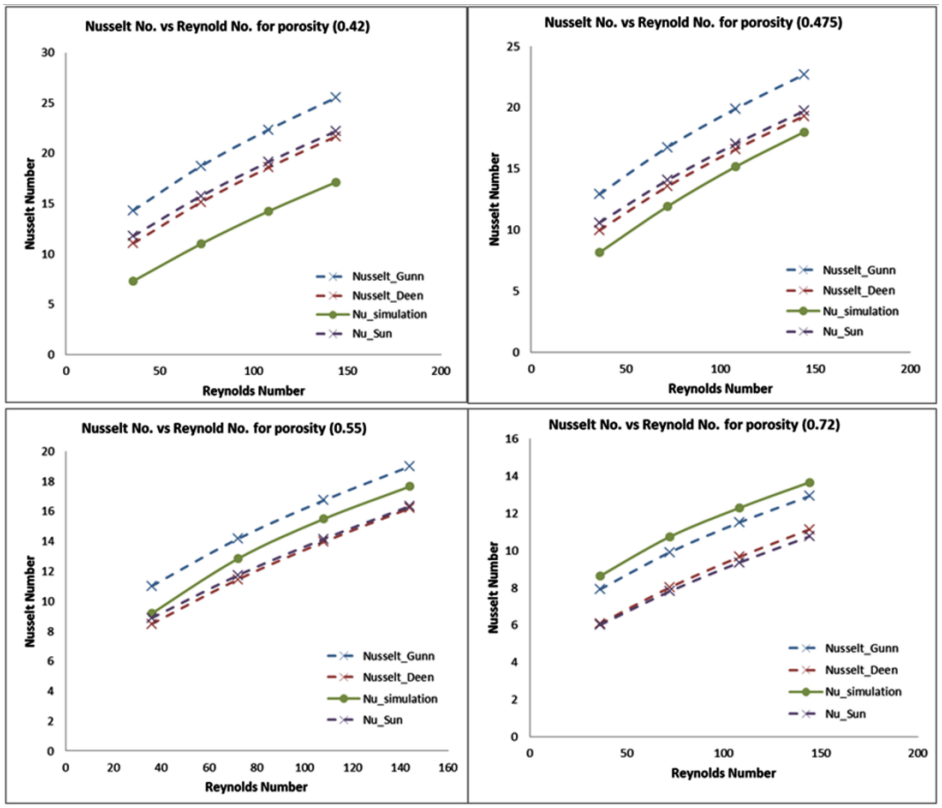

Figure 2.4. Comparison of heat transfer coefficient with the correlations over a range of Reynolds numbers and porosity values (obtained by shrinking factors)

Table 6. Nusselt number comparison between OpenFOAM and Fluent

Porosity (ε)	Reynolds number	Code	Nusselt number	Difference (%)
0.42	36	FLUENT	7.327	0.398
		OF	7.357	
	144	FLUENT	17.141	-0.405
		OF	17.072	
0.72	36	FLUENT	8.634	1.640
		OF	8.776	
	144	FLUENT	13.662	1.630
		OF	13.885	

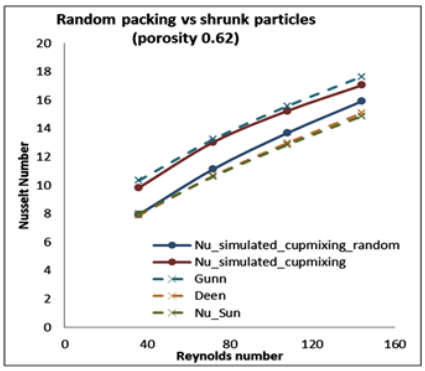

Figure 2.5. Comparison of heat transfer coefficient for shrunk and randomly generated particle bed

2.4.3 Heat transfer predictions

To verify the accuracy of the open source code OpenFOAM and the commercial code ANSYS FLUENT for the heat transfer calculations, a comparison from the results for the heat transfer coefficient over four (4) different cases is studied.

To validate the trend observed in the results obtained with FLUENT, 4 different cases as shown in Table 6 are simulated in OpenFOAM. To ensure a fair comparison, an identical setup is used for both codes when predicting the heat transfer rate as mentioned in previous sections (particle bed generation, random packing for DEM and case setup). The results obtained from OpenFOAM and FLUENT match quite well within a 2% error corridor for $\varepsilon = 0.72$, and within 1% for $\varepsilon = 0.42$ (see Table 6 and Figure 2.6). The typical velocity profile (Figure 2.7) in realistic packing ($\varepsilon = 0.42$) shows similar detailed flow and temperature profiles being resolved by both codes, thus verifying the similar quantitative predictions given in Table 6.

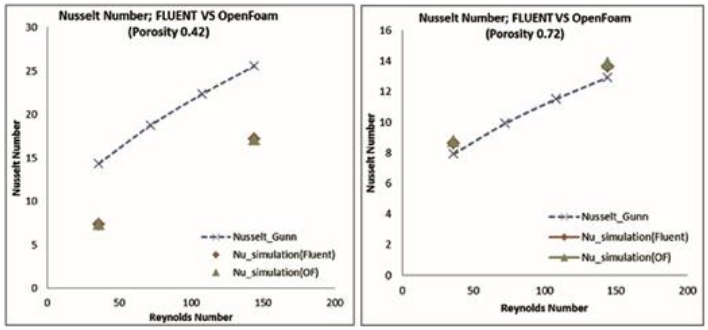

Figure 2.6. Comparison between FLUENT and OpenFOAM

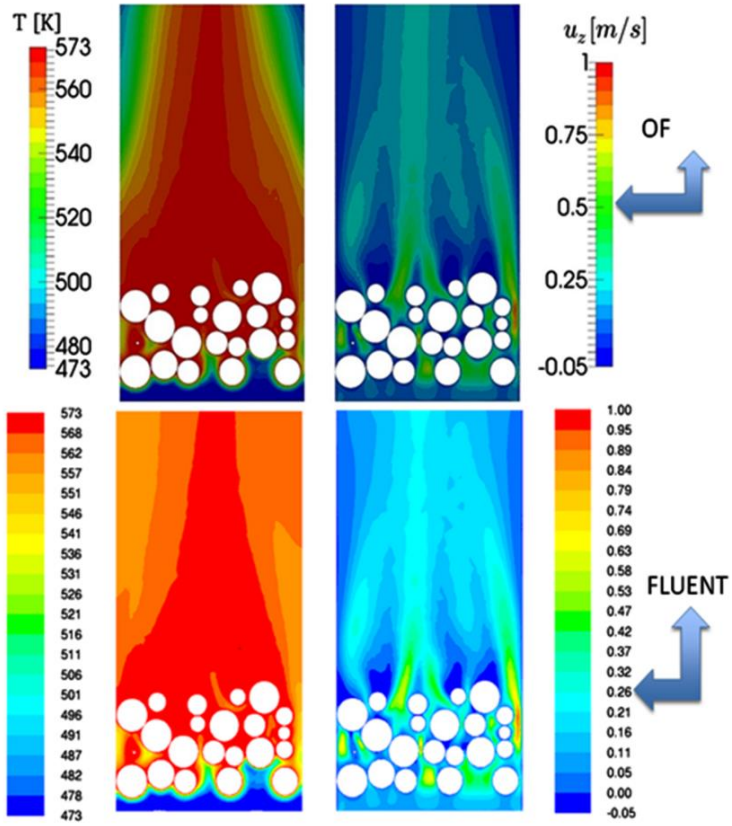

Figure 2.7. Representation of the velocity and temperature profile obtained from FLUENT and OpenFOAM (plane y = 0; Re 36; ε = 0.42)

2.4.4 Performance analysis

Two performance tests are studied using 20% shrinkage (ε = 0.72) and Reynolds number (Re = 36):

Sprint race: In this test the simulation for ε = 0.72 and Re = 36 is run using both codes for 20 iterations using eight cores of similar clock speed and with the same under relaxation factors for energy, pressure and momentum. The difference of the wall time at the end of iteration 21 and at the end iteration 1 is then computed. The time between the end of iteration 1 and end of iteration 21 is considered. This is because the time overhead due to matrix assembling is excluded in the computation time, which is negligibly small in a typical solution. The results from the sprint test are shown in Table 7, it is seen that for the same solver settings (Multigrid Solver) OpenFOAM takes a lesser time per iteration (15.25 s) when compared with the per iteration time (19.9 s) consumed by ANSYS FLUENT.

Marathon: For the second performance test both the codes (software) running the same simulation are run until convergence. Convergence is monitored considering the residual parameters of the continuity, velocity and energy transport equation. An additional parameter described by the area weighted average of heat flux from the particle surfaces in the region of interest (Figure 2.3) is also monitored. The parameters are monitored to reach the convergence of level 10^{-5} in both codes. It can be seen in Table 7 that the total number of iteration to convergence taken by FLUENT is only 46.8% of that consumed by OpenFOAM. The solver used by FLUENT simulations is AMG (Algebraic multigrid). When working with OpenFOAM the multigrid solver (GAMG) is only available for pressure, not temperature. Therefore to reach the degree of accuracy DILUPBiCG (Diagonal Incomplete LU preconditioned Biconjugate gradient) was used.

Table 7. Performance test (Sprint race for 20 s) and marathon

Code	Time (s)	Solver	Per iteration time (s)
FLUENT	398	AMG	19.9
OpenFOAM	305	GAMG	15.25

Code	No. of iterations	Solver
FLUENT	1083	AMG
OpenFOAM	2312	DILUPBiCG

2.5 Summary and conclusions

The research problem targeted by this paper is the derivation of heat transfer correlations from PR-DNS for realistic packings of spherical particles. PR-DNS is commonly used for deriving heat transfer correlations at higher void fractions using random particle assemblies, but this flow situation is more suitable to fluidized beds than packed beds. Since particles in packed beds are about one order of magnitude larger than particles in fluidized beds, gas-particle heat transfer is a much more important limiting phenomenon in packed beds than fluidized beds.

For this reason, this work presents a method for conducting PR-DNS heat transfer studies in realistic packings of spherical particles. The most important challenge posed by this method is the regions of close proximity/overlap between particles, which result in highly skewed cells when the geometry is meshed. This study investigates the effect of overcoming this challenge by shrinking of particles in the bed. Comparison with heat transfer correlations available in the literature showed that particle shrinkage is not an attractive method to generate different porosity beds. The bed of particles (when shrunk) leads to a packing of equally spaced particles at a higher overall void fraction, which is neither a random nor a realistic packing. This packing over predicts the degree of gas-particle contact, and therefore also the degree of heat transfer relative to a random particle arrangement.

The correlations from (Deen et al., 2014; Sun et al., 2015) are valid for random packings ($0.5 < \varepsilon < 1$). Our results for a random packing with a porosity of $\varepsilon = 0.62$ are in close agreement with these correlations. However, our DNS results for heat transfer in more dense (i.e., $\varepsilon = 0.42$) and wall-bounded packings differ significantly from Sun et al.'s and Deen et al.'s correlations for random packings. Thus, the question arises on the validity of these correlations for wall-bounded packings, and under denser particle concentrations. The presented method with shrinking the particles improves on other works in that it can generate realistic packings. However, the accuracy of heat transfer predictions from this methodology is not sufficient for the derivation of reliable packed bed heat transfer correlations. Other more complex methods such as creating small gaps or bridges between adjacent particles will therefore be investigated in future works.

In addition an attempt is made to study the prediction of gas-particle heat transfer rates with the commercial code (FLUENT) and open source code (OpenFOAM) suggesting

similar predictions. Computational performance of the two codes was also similar. On one hand the sprint race shows that OpenFOAM is clearly faster, when per iteration time is concerned. On the other hand the marathon test shows FLUENT gives the result in a smaller number of iterations. The origin of this difference is unclear, since a detailed documentation of FLUENT's algorithms is not available.

Author Contributions: *Arpit, Schalk & Stefan conceived the idea. Arpit designed, and performed the simulations; Rosa Quinta-Ferreira and Shahriar Amini supervised the work; Arpit Singhal wrote the paper.*

Arpit Singhal (Sign)

3 HEAT TRANSFER TO GAS THROUGH MONO-DISPERSE SPHERICAL PARTICLE BED

Abstract

Particle-resolved direct numerical simulation (PR-DNS) has emerged as a promising method to improve gas-particle heat transfer closure models. To date, this method has been applied in random and regular particle assemblies at comparably high void fractions. This paper presents a new methodology for deriving heat transfer correlations from PR-DNS of very dense particle packings relevant for packed bed applications. First particle packings were generated using the discrete element method (DEM). After geometric modifications in regions of close particle-particle proximity, a fine mesh with low cell skewness was created for PR-DNS. Grid independence and the effect of the geometry modification were thoroughly investigated. It was also established that steady state simulations are accurate for PR-DNS in this case. Simulations carried out in different assemblies of ~100 particles showed significant variation of local transfer rates, implying that it is important to specify a confidence interval when reporting correlations derived from PR-DNS. A newly developed Nusselt number correlation predicts values in the lower range of predictions from literature correlations. This implies that the use of the currently available correlations may over-predict heat transfer in densely packed beds. [i]

[i] This chapter is based on Arpit Singhal, S. Cloete, S. Radl, R.Q. Ferreira, S. Amini, Heat transfer to a gas from densely packed beds of monodisperse spherical particles, *Chemical Engineering Journal*, 314 (2017), pp. 27-37

Nomenclature

Symbols

C_p	Specific Heat Capacity of fluid (J/Kg K)
d_p	Diameter of the particle (m)
D	Diameter of the reactor (m)
e_z	Vector in Z-direction
g	Gravity (m/s^2)
h	Heat transfer coefficient (W/m^{2}K)
j	Number of particles
K	Spring constant in the normal contact force law
K_f	Thermal Conductivity of fluid (W/ m K)
m_p	Mass of the particle (kg)
N	Ratio of diameter of reactor to diameter of the particle (D/d_p)
Nu	Nusselt number (hd_p/K_f)
Pr	Prandtl number $(\mu C_p/K_f)$
Re	Reynolds number $(\rho u_s d_p/\mu)$
T	Static temperature of the fluid (K)
T_p	Particle surface temperature (K)
T_{bulk}	Bulk fluid temperature (K)
u_s	Superficial velocity of the fluid (m/s)
u_z	Velocity of the fluid in Z-direction (m/s)
v	Velocity of the particles for DEM (m/s)
dV	Volume in the region of interest (m^3)

Greek

ε	Porosity (void fraction)
η	Dashpot term in the normal contact force law
$\left.\begin{matrix}\mu_{glide}\\ \mu_{limit}\\ \mu_{stick}\end{matrix}\right\}$	Friction coefficients in the tangential contact force law
ρ	Density of fluid (kg/m^3)
μ	Viscosity of fluid (kg/ m s)
$\varphi_{p\to f}$	Heat flux from fluid to particles (W/m^2)

Vectors:

$\vec{\boldsymbol{u}}$	Fluid velocity (m/s)
$\vec{g}$	Gravity (m/s^2)

Subscripts:

p	particle

f fluid

n normal

t tangential

Operators:

$\boldsymbol{\nabla}$ Gradient operator (m^{-1})

$\nabla.$ Divergence operator (m^{-1})

∇^2 Laplace operator (m^{-2})

$\frac{d}{dt}$ time derivative (s^{-1})

3.1 Introduction

Packed bed reactors find various applications in chemical and process industry. Some different examples where packed beds can be used are separators, filters, dryers, chemical reactors and heat exchangers. One important factor for packed bed reactors is the ability to predict heat transfer inside the bed in order to facilitate the proper functionality of the equipment (reactors). Therefore, heat transfer in packed beds is an extensively studied subject in the literature. There are several different correlations to predict heat transfer in the packed bed reactors in the current state of the art.

3.1.1 Previous Heat Transfer Correlations

(Gupta et al., 1974) reported a non-linear relationship between the heat transfer coefficient and the influence parameters, i.e., the Reynolds number and the void fraction of the bed. An expression based on experimental data depending on Prandtl number and Reynolds number with an asymptotic solution in the limit of $Re \rightarrow 0$ was suggested by (Wakao et al., 1979). The effect of porosity for the calculation of heat transfer was not considered in (Wakao et al., 1979).

(Inaba et al., 1988) studied the transient characteristics of cold air flowing over a heated packed bed. It was shown that the heat transfer coefficient depends on the ratio of particle diameter and reactor as well as on the flow rate. This model is only valid over a small range of porosity ($0.310<\varepsilon<0.475$).

A correlation was derived by (Khan et al., 1991) for superheated steam drying in a packed bed using both experimental and computational methods. The model has the capability to

predict condensation before drying begins for the initial heating of the bed. The model is even reliable for the superheated steam drying of the packed bed. The limitation of the model lies in the computation of the Nusselt number which will compute no heat transfer for $Re \rightarrow 0$.

(Collier et al., 2004) and (Scott et al., 2004) calculated the heat transfer coefficient in a packed or fluidized bed utilizing heat transfer from a single particle to the ambient particle bed. The limitation of this study was to not account for the porosity of the bed.

(Gnielinski, 1978) introduced a semi empirical relation to predict the Nusselt number in the packed bed with an asymptotic solution of 2 for $Re \rightarrow 0$. It was validated for experimental results up to Reynolds number ($Re/\varepsilon = 2 \cdot 10^4$), and over a wide range of porosities ($0.26<\varepsilon<0.935$) and Prandtl numbers ($0.7<Pr<10^4$). An improvement to this model was proposed by (Achenbach, 1995) to extend the range of the Reynolds number to $Re/\varepsilon = 7.7 \cdot 10^5$ and fix prediction at low Reynolds numbers. (Achenbach, 1995) suggested that porosity and the tube diameter to particle diameter ratio are the major factor influencing the heat transfer rate.

Table 8: Porosity range studied by the different correlations

Publication (Author)	Porosity range
Inaba et al. (Inaba et al., 1988)	$0.310 < \varepsilon < 0.475$
Gnielinski (Gnielinski, 1978)	$0.26 < \varepsilon < 0.935$
Achenbach (Achenbach, 1995)	$0.26 < \varepsilon < 0.935$
Gunn (Gunn, 1978)	$0.35 < \varepsilon < 1$
Deen et al. (Deen et al., 2014)	$0.5 < \varepsilon < 1$
Sun et al. (Sun et al., 2015)	$0.5 < \varepsilon < 1$
Wakao (Wakao et al., 1979)	$\varepsilon = 0.4$

The different parameters on which the forced convection can depend upon are (i) the Reynolds number, (ii) the Prandtl number, (iii) bed porosity, (iv) N (Ratio of diameter of reactor to diameter of the particle) value, (v) local flow conditions, and (vi) the particles' surface roughness. The above mentioned experimental correlations available show variation from each other which was demonstrated in the work of (Mehrabian et al., 2014). It was suggested that the reason for the variation in the results depicted by different correlations was due to the non-uniformities arising because of the variation of the

porosity in the bed. It was hence suggested that the semi empirical relations by Gnielinski and Achenbach given in (Achenbach, 1995; Gnielinski, 1978) were the most successful method to predict heat transfer.

An empirical relation for computation of heat transfer in packed beds was given by (Gunn, 1978) which was valid for a wide range of Reynolds number, Prandtl number and also for the porosity ($0.35<\varepsilon<1$). This work suggested that, at low Reynolds numbers, assuming an asymptotic solution cannot be supported by analysis or experiments. (Gunn, 1978) introduced a single equation for heat and mass transfer valid for packed beds, fluidized beds and single particles agreeing over both analytical and experimental conditions. A limitation of the Gunn correlation (Gunn, 1978) was identified by (Tavassoli et al., 2015), namely that the model is accurate only for rather dilute systems ($\varepsilon>0.7$).

A modification to Gunn (Gunn, 1978) to improve the accuracy was suggested by Deen et al. (Deen et al., 2012; Deen et al., 2014) and more recently by Sun et al. (Sun et al., 2015; Tenneti et al., 2013). These recent studies considered refitting the (Gunn, 1978) model using results of direct numerical simulation (PR-DNS) for monodisperse particle beds. Semi-periodic box setups were used to extract Nusselt numbers over a wide range of porosities for Reynolds numbers up to 100. Random particle arrangements inside the periodic boxes were used for the particle resolved DNS.

3.1.2 Meshing Strategies

The PR-DNS setup requires a three-dimensional particle packing, which (i) has to be meshed with sufficiently small body-fitted computational cells, or (ii) which requires the usage of some flavor of the immersed boundary method (Blais et al., 2016; Derksen, 2014; Uhlmann, 2005). The former route (i.e., the generation of a body-fitted mesh) is often preferred in non-moving systems. This is due to the fact that a higher spatial resolution can be realized at identical cell count. Consequently, in what follows we exclusively focus on such a “body-fitted” approach.

The first step in such an approach is the generation of a realistic particle arrangement which can be used in the PR-DNS. This is often accomplished using the Discrete Element Method (DEM), originally introduced by (Cundall and Strack, 1979). Generating a packed bed using DEM results in many instances of very close proximity or slight overlap

of particles with each other or with the walls of the reactor. This is not a favorable phenomenon, leading to very acute angles in regions of very close proximity or slight overlap. Such acute angles lead to skewed cells causing convergence problems. In literature many methods have been introduced to overcome this problem.

The most common method available to deal with the particle proximity problem is to shrink the particles in the packed bed by a certain value and hence reduce the degree of proximity between particles. For example, (Bai et al., 2009) used the particle bed with 1% shrinking, (Atmakidis and Kenig, 2009) preferred to shrink the particles by 2%, while (Dixon et al., 2007) reduced the particles by 0.5% to avoid contact. This is an easy method, but significantly affects the porosity of the bed.

The method suggested by (Guardo et al., 2004) involved increasing the particle size by a certain value. This converts the contact points to contact areas, which is a way to decrease the skewed cells. This method then requires accounting for the change in the porosity and pressure drop. (Kuroki et al., 2009) suggested a method to join the particles by a cylinder if the distance between the particles decreases a predefined value. This method accounts for the correct prediction of pressure drop; however, the overall porosity of the bed becomes affected. This would have a smaller effect on porosity than shrinking or enlarging the entire particle.

(Eppinger et al., 2011) described a method to avoid the problems due to close proximity and overlapping of particles and particle-wall: the particle surfaces can be flattened locally in case the distance between the surfaces is below a predefined value. The surface flattening is done by moving the vertices of the elements of particle surface meshes in close proximity following the strict order that the predefined minimum distance is maintained. The method avoids the problem of skewed cells while minimizing the effect on the bed porosity, but is more complex to implement than other methods.

An overview comparison for the change in porosity and pressure drop was conducted by (Dixon et al., 2013) for all contact point modification methods available in literature. Local modification of the bed was preferred over overall modification, with a better approximation for porosity and pressure drop using the caps and bridge methods.

Maestri et al. (Rebughini et al., 2016) suggested that, out of the two local modification methods available for the packed bed according to (Dixon et al., 2013), the bridge method

was more accurate. It depicts better porosity approximation, pressure drop, and heat transfer in random packed beds.

3.1.3 Goals

The methodology presented in our current contribution can avoid problems due to close proximity and overlapping of particles. Our methodology can be applied to either the caps or bridge method described in (Dixon et al., 2013), depending on whether small cylindrical volumes are subtracted or added in regions of close proximity or slight overlap between adjacent particles. The method implemented by us is different from (Eppinger et al., 2011), and is simpler in application, since the particle-particle and particle-wall contact is removed before meshing the geometry unlike the latter in which the treatment is dependent on moving the nodes of the mesh to create a gap. This work validates the caps method part (Section 3.3.3) of the local bed modification for the change in porosity and heat transfer in realistic packings of spherical particles.

The grid independence in these packing is depicted in this work (Section 3.3.1). Also, to gain confidence in the model, multiple arrangements of the packed bed are simulated, and the statistics (i.e., mean and variance) of the heat transfer coefficient are studied. The validity of the available model correlations for heat transfer in the literature is tested and documented for the solution of realistic packed bed of mono-disperse particles.

3.2 Methodology

3.2.1 Bed Geometry and Mesh Generation

The particle bed is generated using the DEM (Discrete Element Method) using the commercial CFD package ANSYS FLUENT and Design Modeller. The particles are injected at the top of the cylindrical container where they start accelerating downwards under gravity. After 25 s of motion due to particle-particle collisions, particle-wall collisions and gravity, the particles reach an equilibrium position with relative velocity between them approximately zero. Subsequent to the DEM simulation, the locations of the settled particles are exported from ANSYS FLUENT. Then, with the help of a Python script, the particle locations are converted into a complete geometrical description in

Design Modeler. More details related to the DEM-based simulations are given in Section 3.2.2.1 and Table 9.

Table 9: DEM simulation setup

Parameters	Value
Number of particles	1,800
Diameter of the particles (d_p) (m)	0.001
Particle normal force Spring Dashpot for DEM	K = 250 η = 0.9
Particle tangential force parameter for DEM ("friction-dshf" model in FLUENT (ANSYS, November 2013))	μ_{stick}= 0.5 μ_{glide}=0.2 μ_{limit}= 0.1
Time step (s)	$5 \cdot 10^{-5}$
Gravity (m/s^2)	-9.81

The final geometry as extracted from the DEM-based simulation is shown in Figure 3.1. In this way, the effects on the DEM packing due to the container walls can be reduced (Boccardo et al., 2015). A small gap (Figure 3.6) is created between particles which are overlapping or in close proximity in order to prevent highly skewed cells. The effect of this geometry modification is thoroughly investigated in Section 3.3.3. In addition, a small volume (thickness of $d_p/12.5$) as shown in Figure 3.1 is added around the extracted region in order to avoid sharp angles between sliced particles and the walls of the extracted geometry. The presence of possible wall effects in the final geometry are discussed in detail in Section 3.3.5.

Ideally, the PR-DNS simulations would be carried out in a geometry with periodic boundary conditions instead of walls. However, given the lack of wall effects demonstrated in Section 3.3.5, the presented method is preferred because it conveniently allows for the creation of a high quality body-fitted mesh over the realistically packed spherical particles. A body-fitted mesh allows for local refinement on the particle surfaces and in regions of close particle proximity – an important advantage given the very small cell sizes required to achieve grid independent solutions in a realistically packed particle assembly (see Section 3.3.1). This method also avoids the computational overheads associated with fictitious domain or immersed boundary methods that are considered suitable for fully periodic PR-DNS simulations. For these reasons, the cylindrical cut-out geometry is preferred over a fully periodic domain for this study.

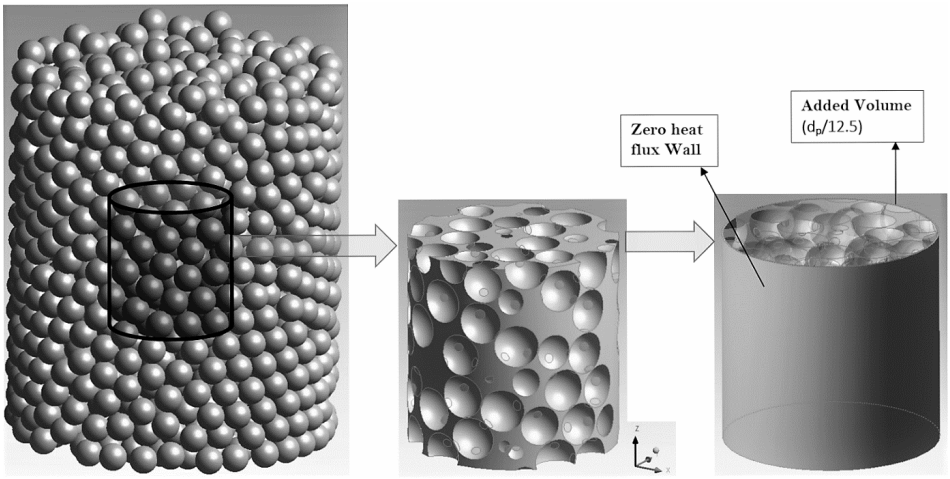

Figure 3.1. Rendered final geometry (right panel) extracted from the packing of spheres contained in the cylindrical container (left). The coordinate system shown is followed while extracting the geometry (Rendered extract).

The resulting fluid geometry is meshed with tetrahedral elements using ANSYS Meshing. Flow around the particles is to be resolved for the Direct Numerical Simulation (DNS); therefore a grid resolution of $d_p/60$ is used on the particle surfaces, while a 20% cell growth rate is allowed away from these surfaces. A grid independence study is presented in Section 3.3.1.

3.2.2 Simulations Setup

3.2.2.1 Model equations

The conservation equations of continuity, momentum, and energy for steady-state flow of an incompressible Newtonian fluid are as follows:

$$\nabla \cdot \vec{u} = 0 \tag{7}$$

$$\nabla \cdot (\rho \vec{u}\vec{u}) = -\nabla p - \mu \nabla^2 \vec{u} \tag{8}$$

$$\nabla \cdot (T\vec{u}) = K_f / (\rho C_p) \nabla^2 T \tag{9}$$

Steady DNS was accurate in this case since no transient fluctuations occur in flow in between the particles in the packed bed (this is discussed in more detail in Section 3.3.2). Therefore, the steady state assumption provides a computationally cheaper solution to the heat transfer problems. ANSYS FLUENT is used to solve the heat and fluid flow around

the particles in the bed. The phase-coupled SIMPLE algorithm with 2nd order spatial discretization schemes are used to obtain the solution.

Newton's equation of translational motion was solved when performing the DEM-based simulations as shown below. Rotational particle motion was not considered in the present work, however, tangential forces have been considered in the force balance.

$$m_p \frac{dv}{dt} = m_p g + \sum_{i=1}^{j} (F_{p,i,n} + F_{p,i,t}) \quad (10)$$

3.2.2.2 Boundary conditions and Simulation Parameters

The cylindrical rendered geometry contains a velocity inlet and a pressure outlet. A no-slip wall boundary condition with zero heat flux is implemented as shown in Figure 3.1. Thus, we consider a cylindrical sub-region of a packed bed with "rough" cylindrical walls, and do not allow for in- or outflow across the cylinder side walls. The no-slip condition was selected to limit flow in the small regions between the sliced particles and the wall, thus limiting unphysical heat transfer from the sliced particle surfaces. Table 10 summarizes all the flow properties used for the CFD simulations.

Table 10: Parametric flow properties for CFD simulation

Parameter	Value
Dynamic Viscosity (μ) (kg/ m s)	$1 \cdot 10^{-5}$
Density of the fluid (ρ) (kg/m^3)	1
Thermal conductivity (k) (W/m K)	0.01
Range of Prandtl numbers	1; 0.75; 0.50
Range of Reynolds numbers	9-180
Temperature of Inlet (K)	473
Temperature of particles surface (K)	573

The method of computing the local fluid temperature is important because it directly affects the calculated heat transfer coefficient. The correct way of calculating the heat transfer coefficient is to compute the fluid temperature over several surface planes in the direction perpendicular to the flow as described by Deen et al. and Sun et al. (Deen et al., 2012; Deen et al., 2014; Sun et al., 2015; Tenneti et al., 2013). We have used in total of 25 surface planes (distance of $d_p/5$ between planes) in a way that the results are

independent of the number of planes (e.g., left panel in Figure 3.5). The average heat transfer coefficient (h) in the bed is calculated based on the local driving force F_{ln} (Eq. (12)) and the particle surface area per unit volume ($a_p = 1- 6\cdot\varepsilon/d_p$) calculated based on the average porosity (ε) over all planes as shown in Eq. (11). The expression $d(F_{ln})/dx$ ((Eq. (11)) is computed as the gradient of the linear decrease in the driving force (F_{ln}) with the axial coordinate of each plane as shown in Figure 3.5 (left). To remove any possible inlet and outlet effects, two planes from the inlet and also from outlet are neglected in the calculations. The average bulk fluid temperature used in Eq. (12) is calculated from Eq. (13) according to the cup-mixing assumption (Deen et al., 2012; Deen et al., 2014). Subsequently, the average Nusselt number in the cylindrical region can be computed following Eq. (14).

$$h = \frac{\frac{d(F_{ln})}{dx}}{a_p} \cdot u_s \rho C_p \qquad (11)$$

$$F_{ln} = ln\left[\frac{(T_p - av.(T))}{(T_p - av.(T_0))}\right] \qquad (12)$$

$$T_{bulk} = av.(T) = \frac{\int (u.e_z) T \, dA}{\int (u.e_z) \, dA} \qquad (13)$$

$$Nu = h \cdot d_p / K_f \qquad (14)$$

3.3 Results and Discussion

The steps followed to verify the accuracy of the proposed method are listed in this section and the major findings obtained are elaborated as well.

3.3.1 Grid Dependency Study

To obtain a grid-independent solution for heat transfer in the geometry shown in Figure 3.1 a thorough study was conducted. Simulations were carried out at the highest Reynolds number considered (i.e., $Re_p = 144$) with Prandtl number Pr = 1, since this case is expected to require the finest mesh.

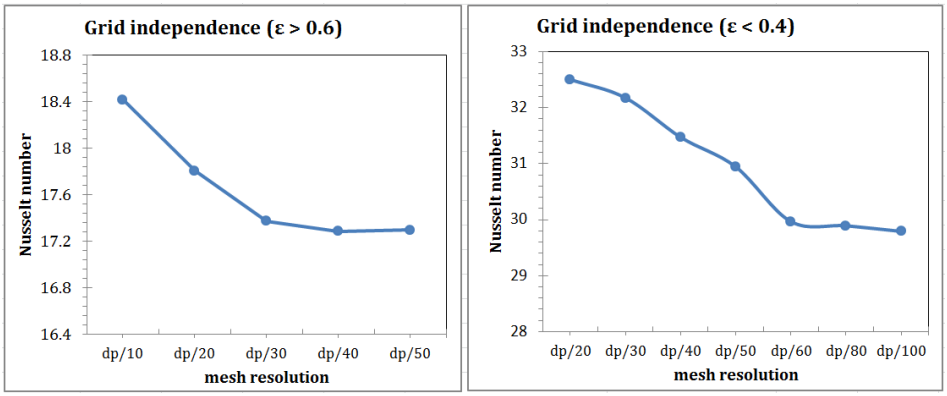

Figure 3.2. Grid independence for heat transfer in arrays of spherical particles as a function of particle surface mesh resolution. Variation for random packing (ε =0.7) and Re=144 [left] and realistic packing (ε =0.35) and Re=144 [right] respectively.

Figure 3.2 shows the variation of Nusselt number with particle surface mesh resolutions for the heat transfer in static arrays of spherical particles. Most important, always random particle arrays with $\varepsilon > 0.6$ were studied in the previous works of Deen et al. and Sun et al. (Deen et al., 2012; Deen et al., 2014; Sun et al., 2015; Tenneti et al., 2013) for obtaining their correlations. Figure 3.2 suggests that grid independence for such packing can be achieved quite easily, and a resolution of approximately $d_p/30$ is enough to approach the infinite-resolution asymptote. It is evident from Figure 3.2 that the grid independence for denser packings ($\varepsilon < 0.4$) is achieved on a much finer grid. Thus, these more dense packings required a $d_p/60$ mesh resolution to produce grid independent results. This rather fine grid resolution is used for the following work in this paper.

Figure 3.3 shows the associated cost of refinement in terms of number of cells for grid independence in realistic packings. We speculate that the reason for this difference in grid independence is the development of a rather thick fluid layer around the particles that is in thermal equilibrium with the particles in beds with a porosity $\varepsilon > 0.6$. This thick layer is rather easy to resolve, and hence a grid independent solution can be obtained quite easily. On the contrary, when dealing with denser packings (i.e., $\varepsilon < 0.4$), such a thick boundary layer cannot develop due to locally high fluid velocities, and the (in general) smaller size of the voids.

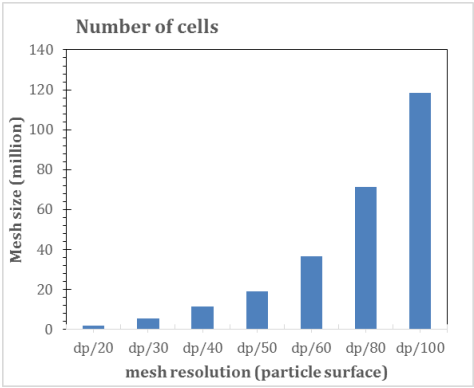

Figure 3.3. Increase in the number of cells in the mesh to refine the resolution in realistic packings (ε =0.35) and Re=144.

3.3.2 Steady versus Transient Simulation

Transient DNS are an extremely costly method to obtain the solution for heat transfer problems. Therefore, for the geometry of packed bed studied, we investigated to find the presence of transient effects and thus have Steady DNS as an alternative.

The meshed geometry with mesh resolution ($d_p/60$) (Section 3.2.1; Section 3.3.1) is simulated with the setup given in Table 10 at a Reynolds number of $Re_p = 144$ and Prandtl number of Pr = 1. Transient DNS with time step ($1.05e^{-06}$ s) to maintain a Courant number (< 1) was simulated for 0.025s i.e. $36 \cdot d_p/u_s$ in terms of characteristic flow time, and the maximum velocity of the flow through the packing was monitored to see if any transient velocity fluctuations are present. Figure 3.4 shows that the flow becomes steady after 0.005s in the flow time and the transient effects can be considered negligible in the studied geometry.

The Nusselt number was also calculated periodically over the simulation time to show that no transient variations in heat transfer are observed (Figure 3.5). The Nusselt number from the transient simulation was within 1% from the steady state simulation.

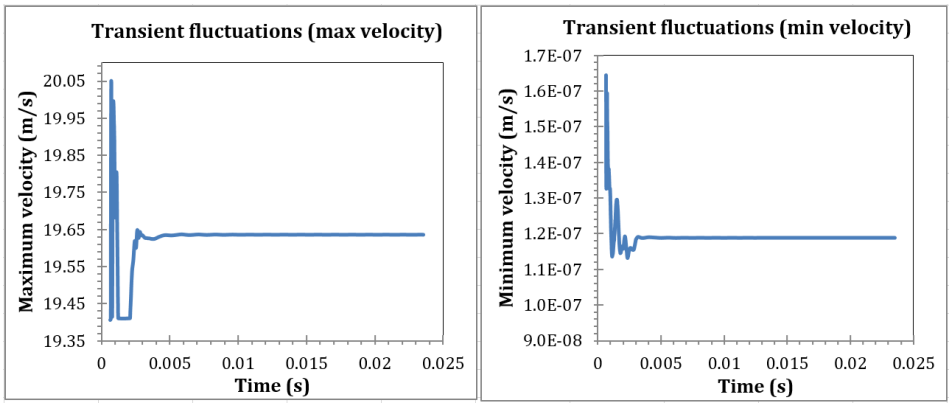

Figure 3.4. Maximum velocity (left) and minimum velocity (right) variation of the flow in the Transient DNS simulation through the final geometry (Section 3.2.1) at Re 144 and bed porosity (ε = 0.35)

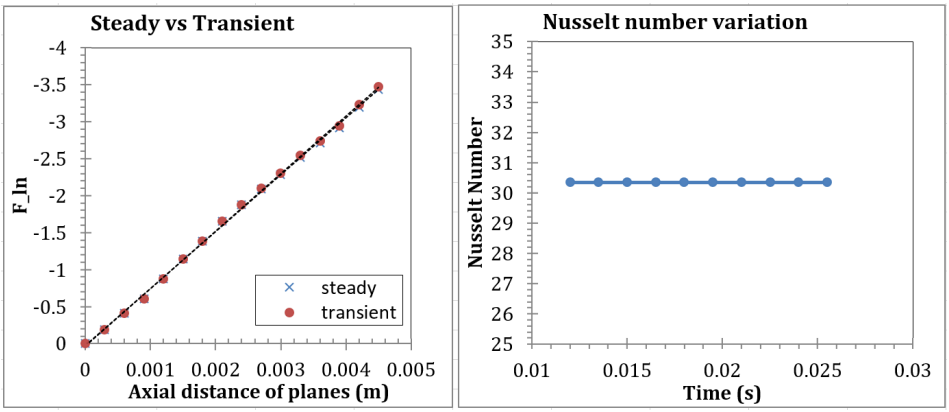

Figure 3.5. Variation of the data from function (Eq. (12)) with the axial distance of the planes perpendicular to the flow for computing the Nusselt number (Deen et al., 2012) (Section 3.2.2.2) [Left]. Nusselt number obtained over different flow time to mark the converged solution [Right].

3.3.3 Caps size study

Generating packed bed by DEM (Section 3.2.1) results in many instances of close proximity between particles as shown in Figure 3.6. To overcome this problem, a small cylindrical geometry is used to cut the particles at the point of contact in order to avoid regions of close proximity or slight overlap with minimal impact on the overall geometry (volume error of 0.05%). A Matlab code is used to identify particle pairs which are located sufficiently close together to create meshing problems. A cylinder aligned with a straight

line connecting the two particle centres is then specified (diameter, height and orientation) for each of these particle pairs. Figure 3.6 shows a typical result from this operation.

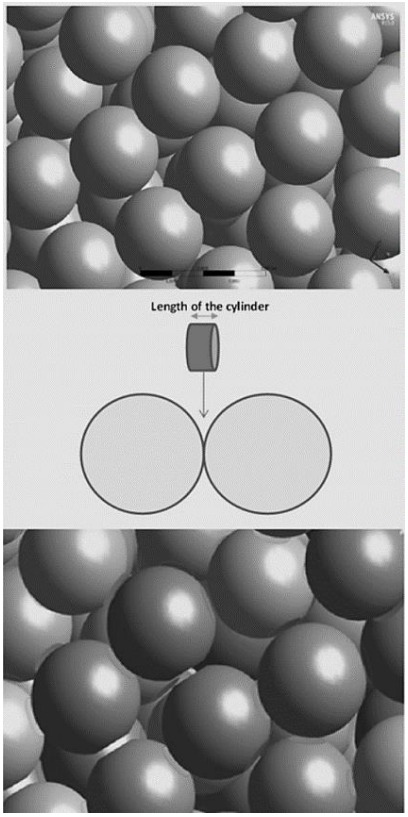

Figure 3.6. The particle bed generated by DEM (above) with problematic regions of close proximity removed (below).

The length of the cylinder is chosen to allow for easy meshing of the geometry while minimizing effects on the packing porosity. As shown in Figure 3.7, the effect of the cylinder length on bed porosity is negligible when the length is smaller than $d_p/50$. Figure 3.7 also shows that model predictions of heat transfer rate (Nu) are sufficiently accurate for a cylinder length of $d_p/50$ (within 2%). A small change in the Nusselt number is still observed when reducing the cylinder length to $d_p/66.6$. However, the mesh quality started to decrease significantly for these very small gap sizes.

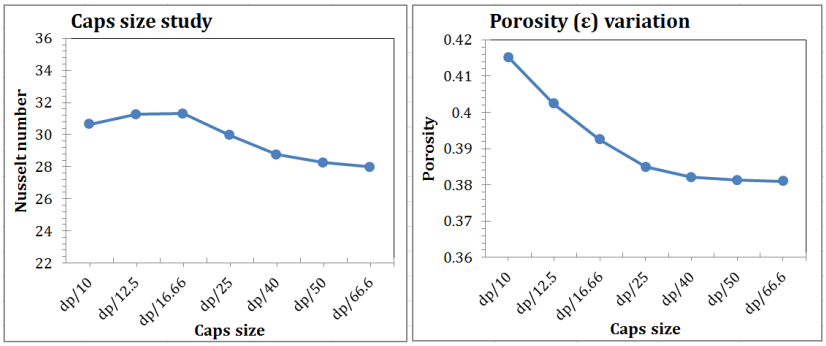

Figure 3.7. Variation of Nusselt number with the cylinder length or caps size (left) and the effect of caps size on the overall packed bed porosity (right).

3.3.4 Particle statistics

It is possible that 100 particles are insufficient to obtain a reliable measure of the heat transfer coefficient in an infinitely large packed bed. For this reason, four additional arrangements of 100 particles were extracted from the initial settled particle array (i.e., from the left panel of Figure 3.1) to quantify the variation of the Nusselt number extracted from different particle arrays. Simulations were carried out over a range of Reynolds numbers for all five geometries and the mean and 95% confidence intervals were calculated for each Reynolds number. 95% confidence intervals (mean ± 1 standard deviation) were calculated from the standard error (SE) as follows:

$$SE = 2.776\frac{SD}{\sqrt{n}} \qquad (15)$$

Here, SD is the sample standard deviation and n is the number of samples (5 in this case). The mean Nusselt number and 95% confidence intervals over a range of Reynolds numbers are represented in Figure 3.8. It is clear that a significant level of variation in the calculated Nusselt number between the different particle arrangements exists. It is therefore important to quantify this uncertainty, something which has not been considered in previous PR-DNS studies.

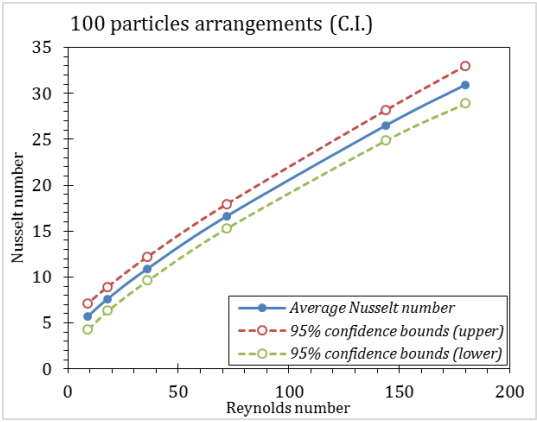

Figure 3.8. Statistically averaged Nusselt number variation over different Reynolds number with the 95% confidence interval.

3.3.5 Wall Effects

Reactors with a small value of N (ratio of reactor diameter to particle diameter (D/d_p)) are believed to be dominated by the wall effects which can affect the heat transfer rate. Therefore, the development of consistent correlations for heat transfer becomes more difficult. (Dixon, 1997) suggested that wall effects are significant when N is smaller than 4. As discussed in Section 3.2.1, the geometry used in the present contribution is a small sub-region extracted from a much larger DEM-generated packed bed in order to avoid the effects due to the reactor walls. Most importantly, the extracted geometry will avoid the significant fluctuations of the void fraction close to the walls of a regular packed bed. As a result, the final geometries will have uniform radial porosity as presented in Figure 3.9 (left). Also, Figure 3.9 (right) shows no clear influence of the boundary conditions at the cylinder wall on the velocity field. However, some wall effects may still be present because the flow is constrained at the walls of the extracted geometry and a small volume (thickness of $d_p/12.5$) is added on the outside of this geometry to avoid highly skewed cells. These effects were investigated by excluding increasing fractions of the domain from the walls inwards in the calculation of the Nusselt number (Figure 3.10 (right)). In practice, this implied progressively smaller diameters of the planes (perpendicular to the flow) on which the cup-mixing temperature is calculated (Deen et al., 2012) (Section 3.2.2.2).

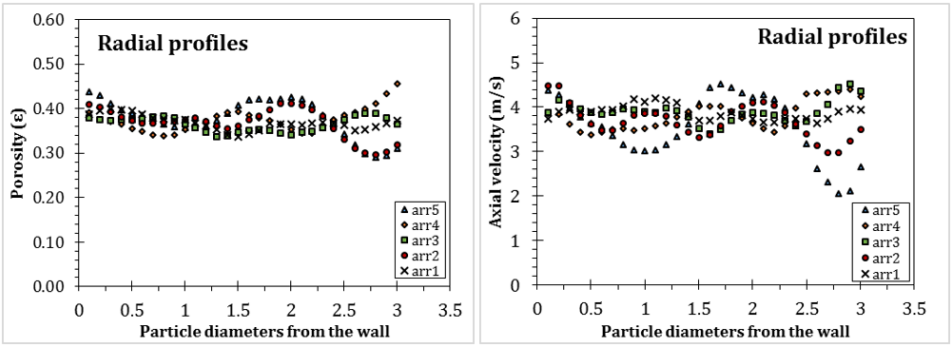

Figure 3.9. Local porosity radial profiles [Left]; Local axial velocity radial profiles [Right] in the geometry with number of particles excluded from the wall (at Re 144; Pr = 1) [arr1….arr5 refer to different particle arrangements].

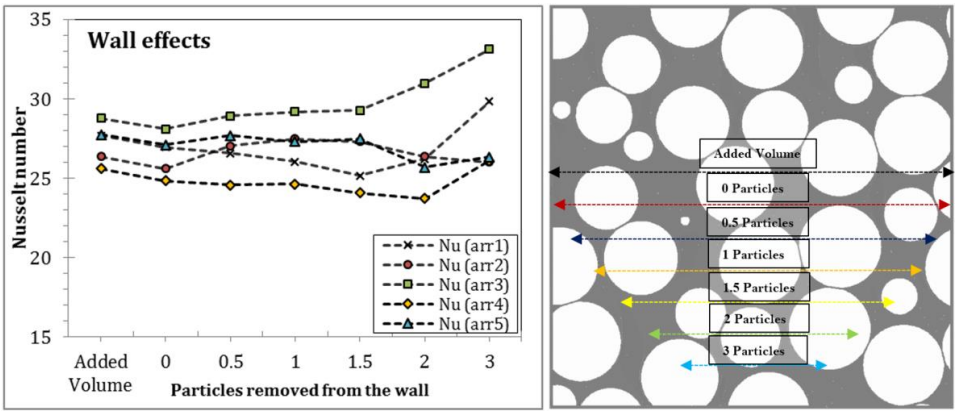

Figure 3.10. Wall effects for the heat transfer studied in the geometry with the number of particle diameters excluded from the wall for a Reynolds number of 144 and Pr = 1 [left panel; arr1 … arr5 refer to the different particle arrangements studied]. [Right] Slice through geometry of (arr2) at plane (y=0), showing the size of the radial planes studied for wall effects in the left panel. The monodisperse particles are cut unequally by the plane and therefore appear to be of different sizes.

The first insight from Figure 3.11 is that the added volume is small enough to minimize seepage of the gas past the sliced particles. Figure 3.10 (right) represents the approx. sizes of the radial planes studied for wall effects in terms of the number of particles removed from the wall. The left-hand side of Figure 3.10 also shows a relatively small influence on the Nusselt number when excluding the added volume from the calculation. More importantly, however, the Nusselt number variation with the wall distance (particle

diameters) removed from the wall is different for each individual arrangement, making it evident that there is no systematic trend for wall effects. Thus, after removing the added volume part of the geometry for heat transfer calculations, the wall effects can be considered negligible. It is also clear that the variation between the five particle arrangements increases significantly as more volume is excluded from the calculation. For this reason, it is favorable to include multiple particle arrangements when developing Nusselt number correlations. This is to minimize uncertainty related to variation in the Nusselt number between different particle arrangements. Alternatively, one could simply use larger domains. However, this strategy requires wider (not longer) domains, since the temperature field approaches the particle temperature in the flow direction, again adding uncertainty when extracting the heat transfer coefficients.

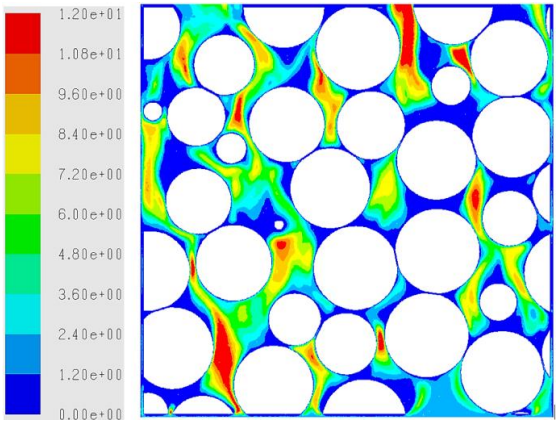

Figure 3.11. Velocity distribution (in m/s) for arr2 at plane (y=0) at Re_p = 144 and Pr = 1 in the direction of flow showing the added volume on the wall.

3.3.6 Comparison with Correlations from Literature

The arrangements mentioned in Section 3.3.4 considering the grid independence (Section 3.3.1), caps-size (Section 3.3.3) and the wall effects (Section 3.3.5) are simulated using the simulation setup given in Table 10 and Table 11 with the steady state DNS over a range of Reynolds numbers (Re 9-180) and Prandtl number (Pr = 1). A typical fluid velocity (in the direction of flow) and Temperature distribution contour for one of the simulated arrangements is shown in Figure 3.12.

Table 11: Final rendered geometry details used for the simulation

Parameter	Value

Number of particles	100 (approx.)
Diameter of particles (d_p) (m)	$1 \cdot 10^{-3}$
Diameter of the geometry (m)	$4.8 \cdot 10^{-3}$
Height of the geometry (m)	$4.8 \cdot 10^{-3}$
Mesh resolution (particle surfaces)	$d_p/60$
Caps size	$d_p/50$
Average porosity of the bed (ε)	0.355

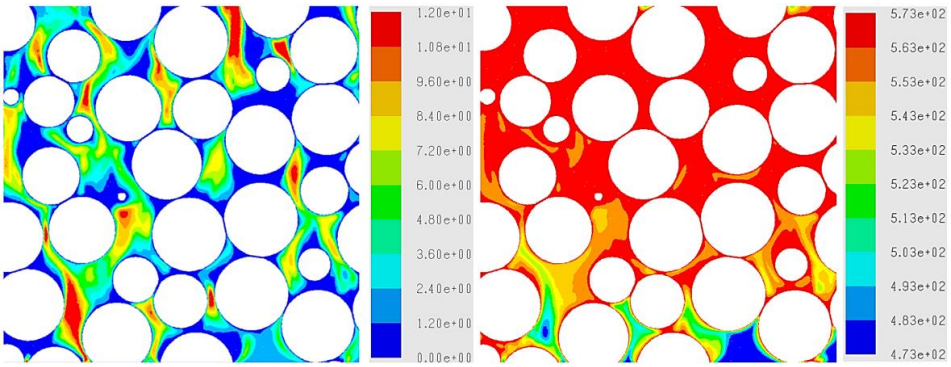

Figure 3.12. Contour plot of fluid velocity (in m/s) and static Temperature (in K) in a plane parallel to the flow cut from one of the arrangements at Re = 144 and Pr = 1.

The correlations most relevant to the comparison because of their nature of development, i.e. using the PR-DNS, are by Deen et al. and Sun et al. (Deen et al., 2012; Deen et al., 2014; Sun et al., 2015; Tenneti et al., 2013). Figure 3.13 shows in general good agreement of the present simulation data with literature results. Results from this study are in the lower range of correlations from literature derived with experiments (Figure 3.13) (left). This result therefore suggests that heat transfer in rather dense packings (i.e., for which $\varepsilon<0.4$) is slower than that predicted by correlations which are more suited to more dilute packings (i.e., for which $\varepsilon>0.6$). The confidence intervals in this log-log plot also shows that the uncertainty related to variations between different particle arrangements increases substantially when decreasing the Reynolds number (in relative terms, i.e. percentage variation around the mean). In absolute terms, the variation in the Nusselt number decreases slightly with decreasing Reynolds number (see Figure 3.8 which is not plotted on a log scale).

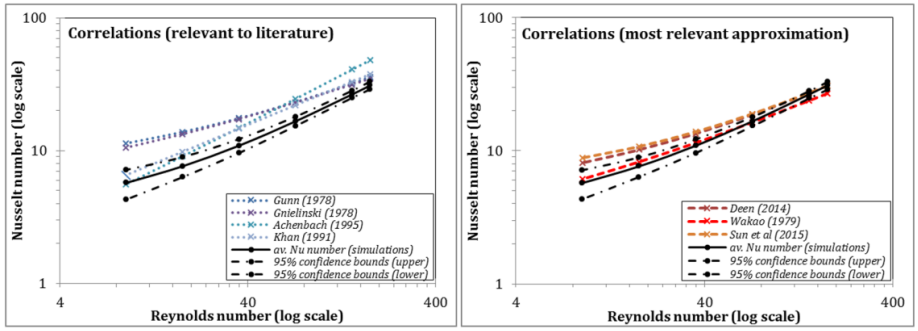

Figure 3.13. Heat transfer variation (Nusselt number) with different Reynolds number averaged over five particle arrangements and comparison with the literature. The correlations more relevant to the comparison because of their overall validity are represented in the left panel.

3.3.7 A New Heat Transfer Correlation

Finally, simulations were run for all five different particle arrangements over six different Reynolds numbers (Re 9-180) and three different Prandtl numbers (Pr 0.5-1). These results were subsequently fitted in the form of the classical Gunn correlation (Eq. (16)). No void fraction dependency was included since very little variation in the void fraction exists in realistic packings of monodisperse spheres: the void fractions of the five particle arrangements considered in the present study varied over a range of 0.351-0.367 only. In order to capitalize on the generality of the Gunn correlation with respect to variations in Re and Pr, the coefficients (2.84 and 0.62) in front of the second and third terms of Eq. (16) were directly calculated from the original Gunn correlation at the average void fraction of the five particle arrangements (ε = 0.359). Two model coefficients (-2.15 and 1.01 in Eq. (16)) were then fitted to the data. Since the second fitted coefficient is essentially equal to unity, it can be concluded that the Re and Pr dependency of the original Gunn correlation gives a good fit to the present data.

$$Nu = -2.15(\pm 1.48) + 1.01\left(2.84Re^{0.2}Pr^{1/3} + 0.62Re^{0.7}Pr^{1/3}\right) \quad (16)$$

$$Nu = 2.67(\pm 1.48) + 0.53Re^{0.77}Pr^{0.53} \quad (17)$$

Even though the correlation in Eq. (16) should benefit from the generality of the established Gunn correlation, two problems can be identified with extrapolating this correlation beyond the range of Re and Pr covered in this study. Firstly, as shown in

Figure 3.14, this correlation shows a small systematic deviation from the simulation results, i.e., an under-prediction at low and high Nusselt numbers and a slight over-prediction at intermediate Nusselt numbers. Secondly, Eq. (16) indicates an unphysical limit for Re approaching zero, i.e., a negative heat transfer coefficient. Both of these issues imply that any use of this correlation outside the range of Reynolds and Prandtl numbers covered in this study may lead to significant errors.

In response to these challenges with Eq. (16), a simplified heat transfer correlation was fitted in Eq. (17). This correlation produced an almost perfect fit to the simulation data (Figure 3.14) and achieved a physical limit for Re approaching zero. It is therefore recommended for use within or close to the range of Re and Pr covered in this study (typical gas-solid packed bed reactors), but cannot be recommended for conditions far outside this range (e.g., gas-liquid packed beds).

The bracketed term in Eq. (16) and Eq. (17) represents the 95% confidence bound of this correlation (see Section 3.3.4). This confidence interval was calculated as the average of the standard errors from all 90 cases studied based on three different particle arrangements. The standard error was independent of the Prandtl number, but, as shown in Figure 3.15, it may be weakly dependent on the Reynolds number. However, this dependence is not strong enough to merit a more complex non-linear representation of the 95% confidence bounds.

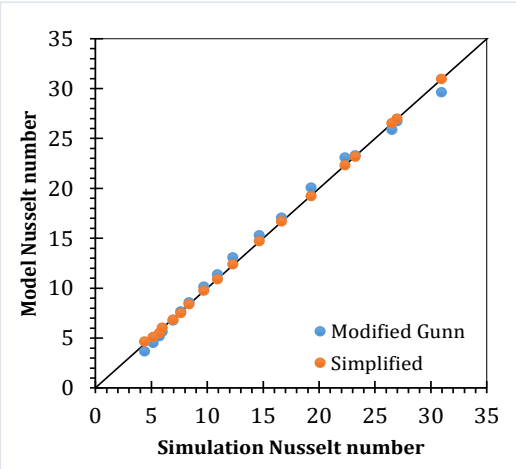

Figure 3.14. Observed (simulation) vs. predicted (model) values of the Nusselt number over all cases for the modified Gunn correlation (Eq. (16)) and the simplified correlation (Eq. (17)).

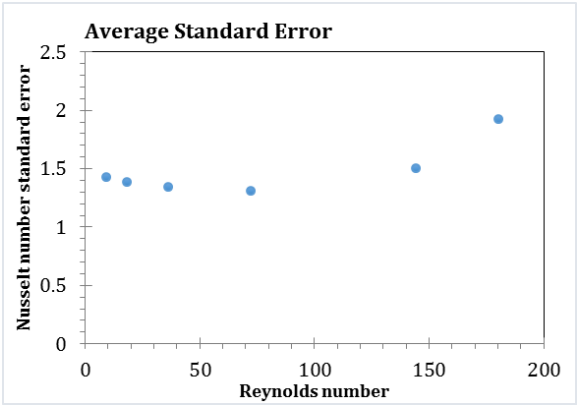

Figure 3.15. The average standard error over the three different Prandtl numbers for each of the six Reynolds numbers investigated in this study.

3.4 Conclusion

Previous particle-resolved simulation studies considered arrays of randomly positioned particles, or regular particle arrays. Most important, these existing PR-DNS studies did not consider very dense particle ensembles, i.e., that having a porosity of less than 0.4. The results of these previous studies are therefore more applicable to fluidized bed applications than packed bed applications. This is an important limitation because, due to the larger particle size, gas-particle heat transfer is typically a much more important limiting factor in packed beds than in fluidized beds. This study therefore presents a methodology and heat transfer correlation focussing on densely packed beds of monodisperse spherical particles.

The proposed methodology consists of the following steps: 1) the generation of a large realistic particle packing using the discrete element method (DEM), 2) extraction of a limited number of particles from the centre of the DEM packing to avoid wall effects and ensure randomness, 3) generation of a modified geometry accounting for small particle-particle and particle-wall gaps, 5) generating a sufficiently fine body-fitted computational mesh of high quality (i.e., low skewness), 6) conducting PR-DNS simulations over a range of important parameters, 7) processing the results to extract the Nusselt number for each simulation, and 8) fitting an improved heat transfer correlation.

This method of extracting a number of particles from the centre of a large DEM packing is preferred over the conventional periodic box approach in order to facilitate the use of

a high quality body-fitted mesh. A body-fitted mesh allows for local refinement on the particle surfaces (greatly reducing the required number of computational cells) and also avoids the computational overhead associated with fictitious domain and immersed boundary methods that are better suited to periodic box simulations. Given that the wall boundary conditions of the extracted cylindrical geometry were proven not to impact the calculated Nusselt number, this method is preferred over the periodic box approach in this study.

Great care has been taken to ensure the validity of the methodology. A grid independence study revealed that the realistic packing required a much finer grid (i.e., $d_p/60$) than a random particle array at higher void fraction (i.e., $d_p/30$). The introduction of a gap of $d_p/50$ between all particles was found to be sufficient to ensure a high quality mesh, while showing almost no effect on the bed porosity and calculated Nusselt number. It was also confirmed that no transient velocity fluctuations took place within the narrow channels created by the realistic packing, thus allowing the use of much less computationally costly steady-state simulations.

Results also showed that significant differences in Nusselt number exist between different particle assemblies (~100 particles) extracted from the large realistic DEM packing. It is therefore important to quantify this uncertainty when deriving correlations as demonstrated in the present contribution. The average Nusselt numbers calculated in the present study fall in the lower range of existing correlations with only the lower 95% confidence interval falling below all previous correlations. Most important, we find that a different exponent to the Prandtl number (compared to that of Gunn) leads to a substantially better fit of our data for systems in which $0.5 < Pr < 1$.

Specifically, we propose the following correlation for heat transfer from monodisperse particles in densely packed beds where the fluid phase is a gas (the bracketed term represents the 95 % confidence bounds) $Nu = 2.67(\pm 1.48) + 0.53Re^{0.77}Pr^{0.53}$. Further work is required to extend this correlation to liquid-solid systems.

Author Contributions: *Arpit, Schalk & Stefan conceived the idea. Arpit designed, and performed the simulations; Rosa Quinta-Ferreira and Shahriar Amini supervised the work; Arpit Singhal wrote the paper.*

Arpit Singhal (Sign)

4 HEAT TRANSFER TO GAS THROUGH PACKED BED OF CYLINDRICAL PARTICLES

Abstract

Particle resolved direct numerical simulation (PR-DNS) has been used extensively to obtain closures for heat transfer from static particle arrays. However, most of the currently available closure models are valid for packings of spherical particles only. We present closure models for momentum and heat transfer in densely packed cylindrical particle assemblies of different aspect ratios (2, 4 and 6). Our packings are generated using the Discrete Element Method (DEM). Subsequently, the void space is meshed with a high quality computational grid, and steady-state DNS simulations are completed to provide insight into the local heat transfer and pressure drop characteristics. The variation observed in the values for the local heat transfer rates from our PR-DNS study implies the necessity of specifying confidence intervals when reporting a correlation for the corresponding Nusselt number. Our newly developed correlations are applicable to densely packed beds of cylindrical particles in the porosity range ($0.405 < \varepsilon < 0.539$), and allow the estimation of the variability of the Nusselt number.

[i] This chapter is based on Arpit Singhal, S. Cloete, S. Radl, R.Q. Ferreira, S. Amini, Heat transfer to a gas from densely packed beds of cylindrical particles, *Chemical Engineering Science*, 172 (2017), pp. 1-12

Nomenclature

Symbols

a	Cylindrical particle aspect ratio (L_p/d_p)
a_p	particle-fluid heat transfer surface per unit volume (a_p = ((2 + 4 a) · (1 - ε)/(d_p a)) (1/m)
C_p	Specific heat capacity of fluid (J/kg K)
d_e	Equivalent diameter of the particle (m)
d_p	Diameter of the cylindrical particle (m)
D	Diameter of the reactor (m)
e_z	Vector in z-direction
g	Gravity (m/s^2)
h	Heat transfer coefficient (W/m^{2}K)
I_p	Moment of Inertia (kg · m^2)
j	Particle index
K_f	Thermal conductivity of fluid (W/ m K)
K_n	Normal spring stiffness (N/m)
K_t	Tangential spring stiffness (N/m)
L_p	Length of the Cylindrical Particle
m_p	Mass of the particle (kg)
N	Ratio of diameter of reactor to diameter of the particle (D/d_e)
Nu	Nusselt number
ΔP	Pressure drop across the packed bed (Pa)
Pr	Prandtl number ($\mu\ C_p/K_f$)
r	Rolling resistance coefficient
Re	Reynolds number ($\rho\ u_s\ d_e/\mu$)
T	Static temperature of the fluid (K)
T_p	Particle surface temperature (K)
T_{bulk}	Bulk fluid temperature (K)
u_s	Superficial velocity of the fluid (m/s)
u_z	Velocity of the fluid in Z-direction (m/s)
v	Velocity of the particles for DEM (m/s)
dV	Volume in the region of interest (m^3)

Greek

ε	Porosity (void fraction)
$\left.\begin{matrix}\mu_f\\ e_n\\ e_t\end{matrix}\right\}$	DEM contact model parameters

ρ Density of fluid (kg/m^3)

ω_p Angular velocity (rad/s)

τ Torque force (N · m)

μ Viscosity of fluid (kg/ m · s)

$\varphi_{p\to f}$ Heat flux from fluid to particles (W/m^2)

Vectors:

$\vec{u}$ Fluid velocity (m/s)

$\vec{g}$ Gravity (m/s^2)

Subscripts:

p particle

f fluid

n normal

t tangential

Operators:

∇ Gradient operator (m^{-1})

$\nabla.$ Divergence operator (m^{-1})

∇^2 Laplace operator (m^{-2})

$\frac{d}{dt}$ time derivative (s^{-1})

4.1 Introduction

There are multiple applications in the chemical and process industry of packed bed reactors, ranging from separators to heat exchangers. Therefore, it would not be difficult to find extensive research devoted to study heat and momentum exchange in packed bed reactors. However, the majority of the available literature for heat transfer in packed beds is concerned with particles spherical in shape. Unfortunately, this is often problematic: it has been established that in some applications like biomass combustion the shape of the particles is a major factor influencing the combustion process (Bonefacic et al., 2015). Similarly, in pharmaceutical applications or heterogeneous catalytic reactors, non-spherical particles (often cylindrical in shape) are preferred.

There are studies available in literature to evaluate the correct pressure drop in the cylindrical packed beds. The Carman-Kozeny (Carman, 1956) approximation laid the foundation towards the use of an effective diameter when calculating the pressure drop using the Ergun equation (Ergun, 1952). Following the work of (Carman, 1956), (Nemec

and Levec, 2005) concluded that the constants of the Ergun equation should be modified as a function of the particle size rather than just using the effective diameter. (Dorai et al., 2015) recently corrected the prediction of (Nemec and Levec, 2005) for viscous flows (stokes regimes). Similarly, the drag force exerted on a single particle has also been evaluated extensively for non-spherical particles. An evaluation of the methods available to compute drag were presented in (Chhabra et al., 1999), suggesting the model by (Ganser, 1993) to be the most accurate one to calculate drag in cylindrical particles. More recently, the work of (Oschmann et al., 2014) combined the works of (Ergun, 1952)/(Wen and Yu, 1966) with the model of (Hölzer and Sommerfeld, 2009) for isolated particles. This study, however, only applied a drag correlation, to establish or check accuracy.

To predict the heat transfer rate in packed beds, there exist several correlations in literature. To our knowledge, the most appropriate closure models are based on experimental and analytical data, as proposed by, (Handley and Heggs, 1968), (Wakao et al., 1979), (Khan et al., 1991), (Gnielinski, 1978), (Achenbach, 1995) and (Gunn, 1978). (Mehrabian et al., 2014) demonstrated the variation of these experimental correlations relative to each other based on the parameters that affect forced convection namely (i) Prandtl number, (ii) Reynolds number, (iii) N value, (iv) porosity of the bed, (v) surface roughness (particles'), and (vi) local flow conditions.

The effect of packing structure on heat transfer and pressure drop predictions was first observed by (Handley and Heggs, 1968). Further, (Romkes et al., 2003) and (Calis et al., 2001) studied heat transfer in structured packings of spherical particles. (Yang et al., 2010) reported that the heat transfer in structured packed beds can be improved tremendously by selecting appropriate particle shape and packing structure. These studies indicate that the heat transfer characteristics are strongly affected by the flow structure around the particles, thus the particle shape and orientation can strongly affect the heat transfer rate.

With the development in the field of Direct Numerical Simulations (DNS), PR-DNS (Particle Resolved DNS) has become an attractive method to improve predictions of flow, heat transfer and reactions in packed beds. The most straight-forward application of PR-DNS directly simulates a small region within the process at a single operating point, often considering reactions (Eppinger et al., 2016; Karthik and Buwa, 2017; Maestri and Cuoci, 2013; Nijemeisland et al., 2004; Partopour and Dixon, 2017; Wehinger et al., 2015;

Wehinger et al., 2017). Somewhat more elaborate studies (Mirhashemi and Hashemabadi, 2012; Mirhashemi et al., 2011; Motlagh and Hashemabadi, 2008; Zare and Hashemabadi, 2013) considered orderly stacked cylindrical particles, which are, however, less relevant for industrial applications that typically involve randomly-packed particles. In summary, these previous studies are (i) less helpful to establish closures that are valid over a larger parameter range, and (ii) provide only limited insight in what affects, e.g., local heat transfer rates in real-world dense packed beds of cylindrical particles, which motivates the presented work.

Therefore, the ultimate goal is to derive closures based on a sound theoretical understanding and an appropriately large set of experimental or computational data. Studies following such an idea, and that focus on wall and shape effects, have a long tradition and date back to the early work of (Dixon, 1988). More recently, a modification to Gunn's correlation (Gunn, 1978) (which is valid for dilute systems with $\varepsilon > 0.7$ as reported by (Tavassoli et al., 2015)) has been suggested by (Deen et al., 2012; Deen et al., 2014), as well as by (Sun et al., 2015; Tenneti et al., 2013). These recent developments used PR-DNS using monodisperse spherical particles to refit the constants in Gunn's correlation to improve the accuracy of the correlation. The validity of these correlations is limited to packed and fluidized beds with a rather large porosity (i.e., $\varepsilon > 0.5$). Hence, a new PR-DNS-based correlation valid for denser (and hence more realistic) packed beds has been suggested in our previous work that considered spherical particles (Singhal et al., 2017f).

To the best of our knowledge, the only systematic PR-DNS study that focussed on establishing a rigorous heat transfer closure for non-spherical packings is that of (Tavassoli et al., 2015). They used PR-DNS to study the flow and temperature fields in a bed of spherocylinder particles and computed the average heat transfer coefficient as a function of Reynolds number, porosity and particle shape (Tavassoli et al., 2015). These authors suggested that their work is applicable to fluidized bed as the particles are not in contact with each other like in the case of denser (i.e., more realistic) packed beds.

Therefore, our present study is the only one focussed on systematically exploring shape effect on heat transfer rates in realistic, densely packed beds of cylindrical particles. Specifically, we have structured our present contribution as follows: in Section 4.2 we summarize our research methodology, including the bed geometry and the simulation

setup. A grid independence study considering cylindrical packings is discussed in Section 4.3.1. In Sections 4.3.2 to 4.3.4 we then work towards validation of our simulation results. Then, and in order to present an accurate model, multiple arrangements of the cylindrical packings are simulated similar to the last work (Singhal et al., 2017f) to obtain the statistically (i.e. mean and variance) averaged heat transfer coefficient. Sections 4.3.5 to 4.3.7 of our manuscript document new findings for pressure drop, and Nusselt number. Finally, we conclude in Section 4.4.

4.2 Methodology

4.2.1 Bed Geometry and Mesh Development

The cylindrical particle bed is generated using the commercial DEM (Discrete Element Method) package integrated in the software tool "STAR CCM+ 11.02". The particles settle under gravity with the relative velocity between them approx. zero after 60 s of the random motion due to particle-particle and particle-wall collisions. Following the DEM simulation, the settled particle locations are exported from Star CCM+ and regenerated as a complete geometrical depiction in the tool "ANSYS DesignModeler" to ascend the established methodology portrayed in our previous work (Singhal et al., 2017f). Star CCM+ is used because of its validated DEM capabilities to generate cylindrical packings, while ANSYS FLUENT is only capable of performing DEM-based simulations with spherical particles. This step of the transformation from Star CCM+ to ANSYS DesignModeler is attainable with the help of a python script.

The dimensions of the cylindrical particles are obtained for aspect ratio ($a = L_p/d_p$) of 2, 4 and 6 by preserving the effective diameter (d_e) as $1 \cdot 10^{-3}$ m. The effective diameter (d_e) is defined as the diameter of the spherical particle (Singhal et al., 2017f) with the same volume as the cylindrical particle (Doraia et al., 2012; Tavassoli et al., 2015). The details of the setup for the DEM simulations are given in Section 4.2.2.1 and Table 12.

Table 12: DEM simulation setup for cylindrical particles of aspect ratio four in Star CCM+

Parameters	Description	Value
Number of Particles		2,017
Particle Dimensions (m)	Length of the Cylindrical Particle (L_p)	$2.201 \cdot 10^{-3}$
	Diameter of the Cylindrical Particle (d_p)	$5.503 \cdot 10^{-4}$
	Effective Diameter of the particles (d_e)	$1 \cdot 10^{-3}$
Aspect Ratio of a cylindrical		4

particle (L_p/d_p)		
DEM Contact Model (Linear Spring)	Static Friction Coeff. Normal Restitution Coeff. Tangential Restitution Coeff. Normal Spring Stiffness Tangential Spring Stiffness	μ_f = 0.4 e_n = 0.8 e_t = 0.8 K_n = 300,000 N/m K_t = 300,000 N/m
DEM Rolling Resistance	Force Proportional	r = 0.001
Time step (s)		$1 \cdot 10^{-4}$
Gravity (m/s^2)		-9.81

The final rendered geometry as shown in Figure 4.1 is obtained from the central region of the DEM generated packed bed. The effects of the container walls can be effectively reduced and we obtain the bulk packing in this way (Boccardo et al., 2015; Caulkin et al., 2009). The DEM contact model parameters in Star CCM+ as shown in Table 12 are kept at an extremely high value to avoid any possible overlap between the cylindrical particles. A small volume (thickness $d_e/12.5$) is added around the rendered geometry to avoid sharp angles between the sliced particles and the walls of the rendered geometry as shown in Figure 4.1. Wall effects in such an extracted geometry have been found to be negligible (Section 4.3.2 for details).

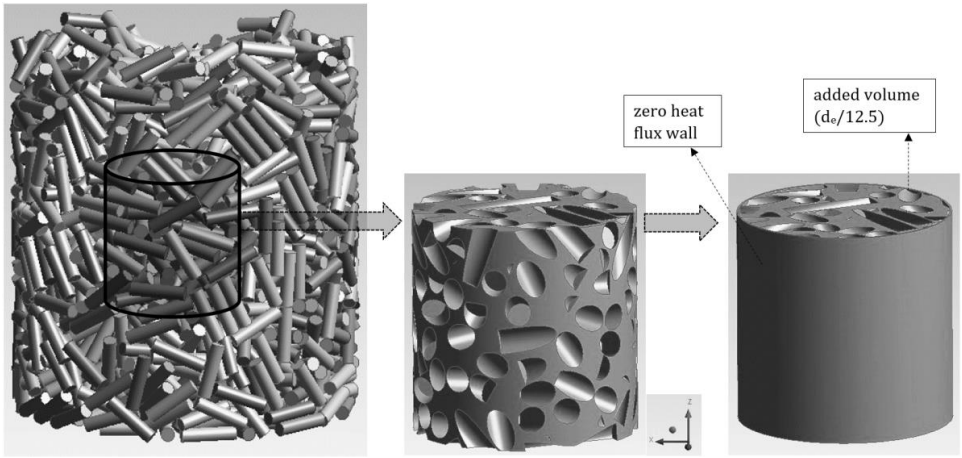

Figure 4.1. Illustration of the raw packing (left panel) of aspect ratio four used to extract a representative cylindrical region (center panel), as well as the rendered final geometry (right panel) used in the flow simulations**.**

Three dimensional particle packings when used in PR-DNS studies require either (i) a geometry to be meshed with sufficiently resolved body fitted cells, or (ii) to utilize the immersed boundary method (Blais et al., 2016; Derksen, 2014; Uhlmann, 2005). In our present contribution, we have focused on the body fitted mesh with high spatial resolution of tetrahedral elements using ANSYS Meshing tool. In this way, the cell count is minimized through local grid refinement and the added computational overhead associated with the usage of immersed boundary methods is avoided.

Specifically, direct Numerical Simulation (DNS) for the obtained rendered geometry requires the mesh to be resolved with at least $d_e/60$ resolution on the particle surfaces to obtain a sufficiently grid independent result for heat transfer problems (see Section 4.3.1 for details). A cell growth rate of 20% is followed subsequently from the particle surfaces to resolve the flow in the void space around them.

4.2.2 Simulations Setup

4.2.2.1 Model equations

The steady-state conservation equations for the conservation of mass, momentum, and energy considering an incompressible Newtonian fluid are represented by following set of equations (Eq. (18)-(20):

$$\nabla \cdot \vec{u} = 0 \tag{18}$$

$$\nabla \cdot (\rho \vec{u}\vec{u}) = -\nabla p - \mu \nabla^2 \vec{u} + \rho \vec{g} \tag{19}$$

$$\nabla \cdot (T\vec{u}) = K_f / (\rho C_p) \nabla^2 T \tag{20}$$

As suggested in our previous work (Singhal et al., 2017f), steady state-DNS is found to be accurate for the geometries extracted by the method explained previously in Section 4.2.1 and Figure 4.1 and the considered flow conditions. Thus, Steady DNS is used as a much cheaper alternative to transient DNS for the solution to heat transfer problems. The phase coupled SIMPLE algorithm with 2nd order spatial discretisation scheme implemented in ANSYS FLUENT is used to solve the heat and fluid flow around the particles in the geometry studied.

The DEM simulations are based on Newton's equation of motion, and consider both normal and tangential forces as shown in Eq. (21). Rotational particle motion is considered as well, and the corresponding evolution equation for the angular momentum $I_p\omega_p$ is given by Eq. (22).

$$m_p \frac{dv}{dt} = m_p g + \sum_{i=1}^{j} (F_{p,i,n} + F_{p,i,t}) \quad (21)$$

$$\frac{d(I_p\omega_p)}{dt} = \sum_{i=1}^{j} (\tau_{p,i}) \quad (22)$$

4.2.2.2 Boundary conditions and Simulation Parameters

The cylindrical geometry incorporates a velocity inlet, a pressure outlet and a non-slip wall with zero heat flux to eliminate outflow across the cylindrical geometry wall as shown in Figure 4.1. The non-slip condition on the wall benefits in restricting the flow in a thin, ring-shaped region between the sliced particles and the wall (denoted as "added volume" in the right panel of Figure 4.1). In this way, we consider a cylindrical subsection or the bulk packing (Caulkin et al., 2009) of the bed with a uniform void fraction distribution in the radial direction as obtained from the DEM-generated packed bed. Moreover, our setup limits any unphysical heat transfer from the sliced particle surfaces. At the surface of the particles, a non-slip boundary condition with a fixed temperature of 573 K is applied. The flow properties used in the CFD simulations are summarised in Table 13.

Table 13: Parametric flow properties for CFD simulation. The flow properties are based on the range of dimensionless parameters in the PR-DNS study.

Parameter	Value
Dynamic Viscosity (μ) (kg/m · s)	$1 \cdot 10^{-5}$
Density of fluid (ρ) (kg/m^3)	1
Thermal conductivity (k) (W/m K)	0.01
Range of Prandtl numbers	1; 0.75; 0.50
Range of Reynolds numbers	9-180
Temperature of Inlet (K)	473
Temperature of particles surface (K)	573

Obtaining a suitable method for calculating the fluid temperature is important as it impacts directly the prediction of heat transfer rate. The correct method used in calculating the local fluid temperature on planes perpendicular to the flow, and subsequently the heat transfer coefficient, is described by (Deen et al., 2012; Deen et al., 2014; Sun et al., 2015; Tenneti et al., 2013). In total, 25 surface planes (with a distance of $d_e/5$ between the planes) are used following a similar methodology we have used in our previous work on monodisperse spherical particles (Singhal et al., 2017f). Two planes from the inlet as well as from the outlet are neglected in our present calculations to avoid inlet and outlet effects. The calculation of the average heat transfer coefficient (h) using the local driving temperature difference F_{ln} (Eq. (23)) and specific particle-fluid heat transfer surface (a_p) has been explicitly presented in earlier work (Singhal et al., 2017f). The average bulk fluid temperature represented by the cup-mixing assumption (Deen et al., 2014; Sun et al., 2015) is calculated from Eq. (25), and the average Nusselt number can be subsequently obtained from Eq. (26).

$$h = \frac{\frac{d(F_{ln})}{dx}}{a_p}\, u_s \rho C_p \tag{23}$$

$$F_{ln} = ln\left[\frac{(T_p - av\,(T))}{(T_p - av\,(T_0))}\right] \tag{24}$$

$$T_{bulk} = av(T) = \frac{\int (u \cdot e_z) T\, dA}{\int (u \cdot e_z)\, dA} \tag{25}$$

$$Nu = h\, d_e / K_f \tag{26}$$

4.3 Results and Discussion

4.3.1 Grid dependency study

Grid dependence behaviour was studied by completing simulations with different grid resolutions at high value of Reynolds number (where grid dependencies are expected to be greatest). As shown in Figure 4.2, the results show the expected behaviour where the change in solution increases exponentially with each doubling of the cell size. Extrapolation of the fitted exponential growth function to an infinitesimally small cell size results in a Nusselt number of 20.64. This is 3.1% smaller than the Nusselt number

on the smallest cell size deemed affordable for completing the large number of simulations in this study ($d_e/60$). It is therefore important to note that results presented in this paper may over-predict heat transfer by up to 3.1% due to grid dependencies.

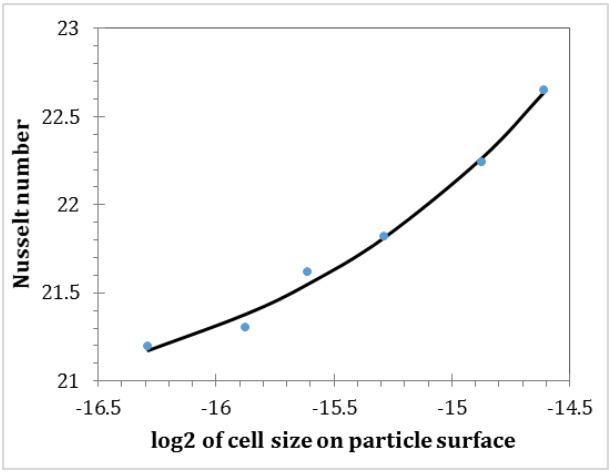

Figure 4.2. Grid dependence behaviour for the variation of Nusselt number in arrays of cylindrical particles w.r.t. particle surface mesh resolution, simulated for a case at Re = 144, Pr = 1, ε = 0.48 and a = 4. Symbols indicate simulation results and the line represents an exponential growth function : $\boldsymbol{Nu = 20.64 + exp\left(12.16 + 0.785 log_2(dx)\right)}$, where $(\boldsymbol{dx})$ represents the grid spacing on the particle surface**.**

4.3.2 Wall effects

The geometry shown in Figure 4.1 is considered to have negligible wall effects. This was already proved in the previous paper (Singhal et al., 2017f), nevertheless this needs to be established again for the cylindrical packings. Therefore, all the five particle arrangements for aspect ratio (a = 4) described in Section 4.3.3 (see below) are simulated with Re = 144 and Pr = 1 for a setup described in Table 13 and Table 14. To observe any specific trend in the prediction of heat transfer (which might be due to wall effects), the Nusselt number is calculated on the circular planes (which are decreased systematically in diameter as shown in Figure 4.3). These planes are the ones described in Section 4.2.2.2, on which the local fluid temperature is computed (bulk fluid temperature (T_{bulk})). In addition, the radial profiles of the porosity and axial velocity in each of the arrangements is determined based on the number of equivalent particle diameters (d_e) from the wall.

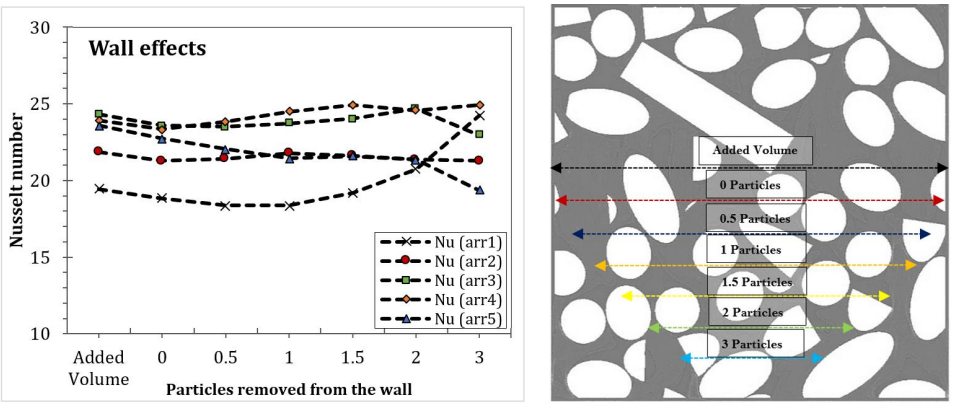

Figure 4.3. Illustration of the shape of the planes when considering a certain number of particles removed from the wall (right panel; all 25 planes explained in Section 4.2.2.2 are of the same size representable in the figure). Variation of Nusselt number based on the particles removed from the wall (arr1…arr5 represents the different particle arrangements of a = 4) at Re144 and Pr = 1 (left panel).

Figure 4.3 (left) shows the wall effects based on the number of equivalent particle diameters (d_e) from the wall that are excluded from the calculation. It can be seen that there is no systematic trend in the variation of Nusselt number, which was also concluded for the spherical particle packings in our previous work (Singhal et al., 2017f). Therefore, to be consistent with the methodology, we remove the added volume from the planes for calculating the Nusselt number. A similar observation can be made for the radial profiles of porosity (Figure 4.4 left panel) and axial velocity (Figure 4.4 right panel): the porosity is nearly uniform and so is the axial velocity. This suggests that the effects due to the imposed cylindrical wall are minimal. The spread towards the right of the graph is caused by the reduced size of the surfaces over which the velocity values are collected (in the centre of the geometry), thus creating more variance between the different packings.

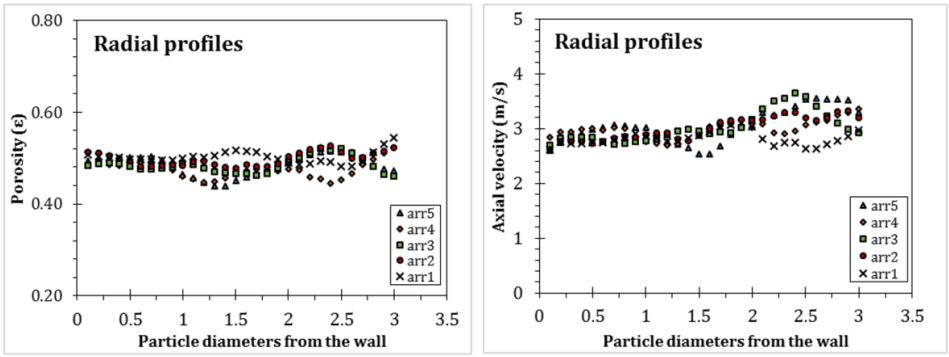

Figure 4.4. Radial profiles of porosity (left panel) and axial velocity (right panel) versus the particle removed from the wall [arr1…arr5 represents the particle arrangements a = 4 simulated at Re = 144 and Pr = 1].

4.3.3 Particle statistics

It is known that heat and mass transfer phenomena in a packed bed can vary significantly as a function of location within the packing (Guo and Thompson, 2001). We therefore assess whether ~100 particles in a packed bed geometry of cylindrical particles are sufficient to predict a reliable value for the heat transfer coefficient. Five different arrangements of aspect ratio (a = 4) are extracted following a similar strategy as demonstrated in Figure 4.1 in order to measure any possible variation in the Nusselt number, or pressure drop prediction. The solution obtained with all these arrangements is observed to be grid independent (as discussed in Section 4.3.1) and the wall effects are negligible (see Section 4.3.2). Steady-state PR-DNS simulations are performed over a range of different Reynolds number (Re 9-180) with the parameters given in Table 13 for five different geometries with porosity of the bed varying between (ε = 0.468-0.501). The mean Nusselt number over five different geometries is averaged for Prandtl number (Pr = 1) and 95% confidence intervals (C.I.) are computed. The 95% C.I. are calculated based on the definition of a standard error (Eq. (27)), which is dependent on standard deviation (SD) of the samples (n = 5, in this case) (calculated by Eq. (28)), where ($\bar{x}$) is the mean of the samples.

$$SE = 2.776\frac{SD}{\sqrt{n}} \qquad (27)$$

$$SD = \sqrt{\frac{\sum(x - \bar{x})^2}{(n-1)}} \tag{28}$$

The mean value of the Nusselt number and the pressure gradient is plotted in Figure 4.5 along with the corresponding 95% confidence intervals. It can be seen that the C.I. is quite widespread signifying that there is considerable level of variation in the values and therefore need to be quantified in the calculation.

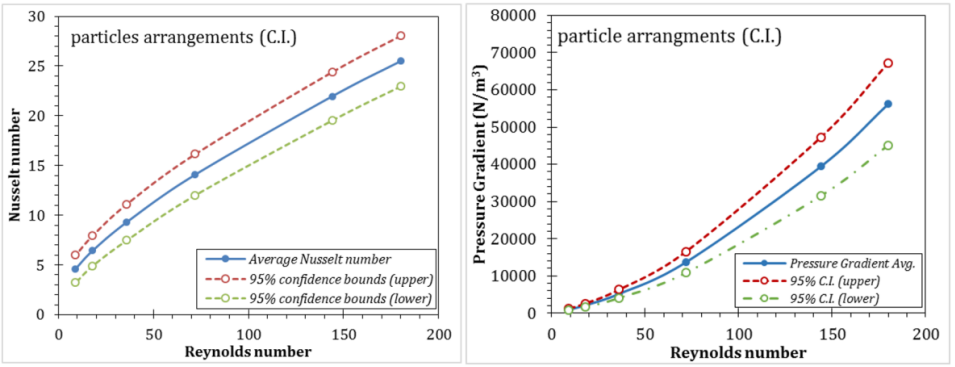

Figure 4.5. Nusselt number variation (left panel) and pressure gradient (right panel) for (arr1 …arr5) of a = 4, versus Reynolds number and for a Prandtl number Pr = 1. The dashed and dashed-dotted line represent 95% confidence intervals considering no void fraction variation in the averaged quantity**.**

4.3.4 Comparison with correlations for heat transfer

The computed heat transfer rates for each aspect ratio (a = 2-6) along with its 95% confidence interval bounds (see Section 4.3.3) over a range of Reynolds numbers (Re 9-180) at Prandtl number (Pr = 1) is compared with existing correlations. The setup of the simulation is given in Table 13 and Table 14. The contour plot for typical axial velocity and static temperature variation through the simulated arrangements (arr2: through plane y = 0) is shown in Figure 4.6.

The heat transfer correlations for packed beds in literature have been predominantly obtained with spherical particle packings. A typical comparison of the value of Nusselt numbers (averaged) with the 95% C.I. compared with the correlations for spherical packings in literature, based on experimental studies in spherical particle beds is shown in Figure 4.7 (left-panels). Secondly, the results were compared with the correlations based on PR-DNS in spherical particle beds (Figure 4.7, right-panels) including a

comparison with the predictions of (Tavassoli et al., 2015). Tavassoli et al. suggested that the prediction of heat transfer rate in non-spherical packings can be obtained with their correlation for spherical particles, and in case the particle diameter (d_p) is used instead of the equivalent particle diameter (d_e) when computing the Reynolds and Nusselt number.

Table 14: Final rendered geometry details used in the simulations

Parameter	Value
Number of particles	100 (approx.)
Eq. Diameter of particles (d_e) (m)	$1 \cdot 10^{-3}$
Diameter of the geometry (m)	$4.8 \cdot 10^{-3}$
Height of the geometry (m)	$4.8 \cdot 10^{-3}$
Mesh resolution (particle surfaces)	$d_e/60$
Porosity range (ε) for a = 2	0.405-0.432; 0.418 (avg.)
Porosity range (ε) for a = 4	0.468-0.501; 0.483 (avg.)
Porosity range (ε) for a = 6	0.514-0.0.539; 0.526 (avg.)

The suggestions by (Tavassoli et al., 2015) (with particle diameter (d_p)), were found to be not valid for the realistic packed beds of cylindrical particles (in porosity range $0.405 < \varepsilon < 0.539$) when compared with the simulated data. When the equivalent particle diameter (d_e) definition is used, a better comparison to previous work of (Tavassoli et al., 2015) and (Singhal et al., 2017f) (valid for dense spherical particle packings) is achieved, although both correlations sometimes fall outside the 95% confidence intervals of the data (Figure 4.7 (right-panels). The good performance of our previous correlation for spherical particles is particularly interesting, suggesting that it should be possible to derive a correlation based on the equivalent particle diameter that is valid for spheres and cylinders of different aspect ratios.

It should be noted that the confidence interval (C.I.) presented in Figure 4.7 is at the maximum size for aspect ratio four because of one arrangement (arr1) that returned a significantly lower Nusselt number than the mean (Figure 4.3, left panel). This arrangement was thoroughly investigated, but no reason could be found to discard it as an outlier. It is therefore retained as a representation of the natural heat transfer variability in a densely packed bed of cylindrical particles.

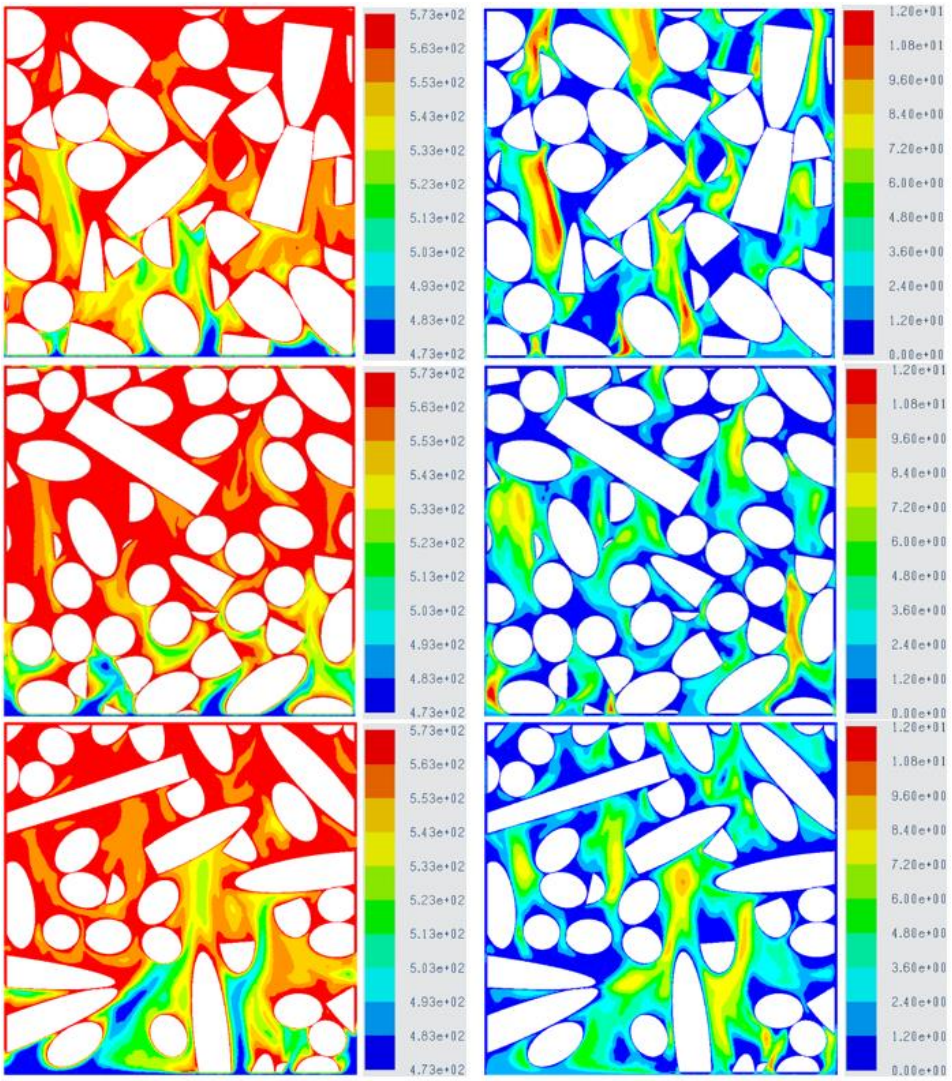

Figure 4.6. Contour plot of the magnitude of the fluid velocity (in m/s) (right panel), as well as the temperature (in K, left panel) in a plane parallel to the flow (y = 0, cut from arrangement 2, Re = 144, Pr = 1, *a* = 2, 4 and 6 from top to bottom).

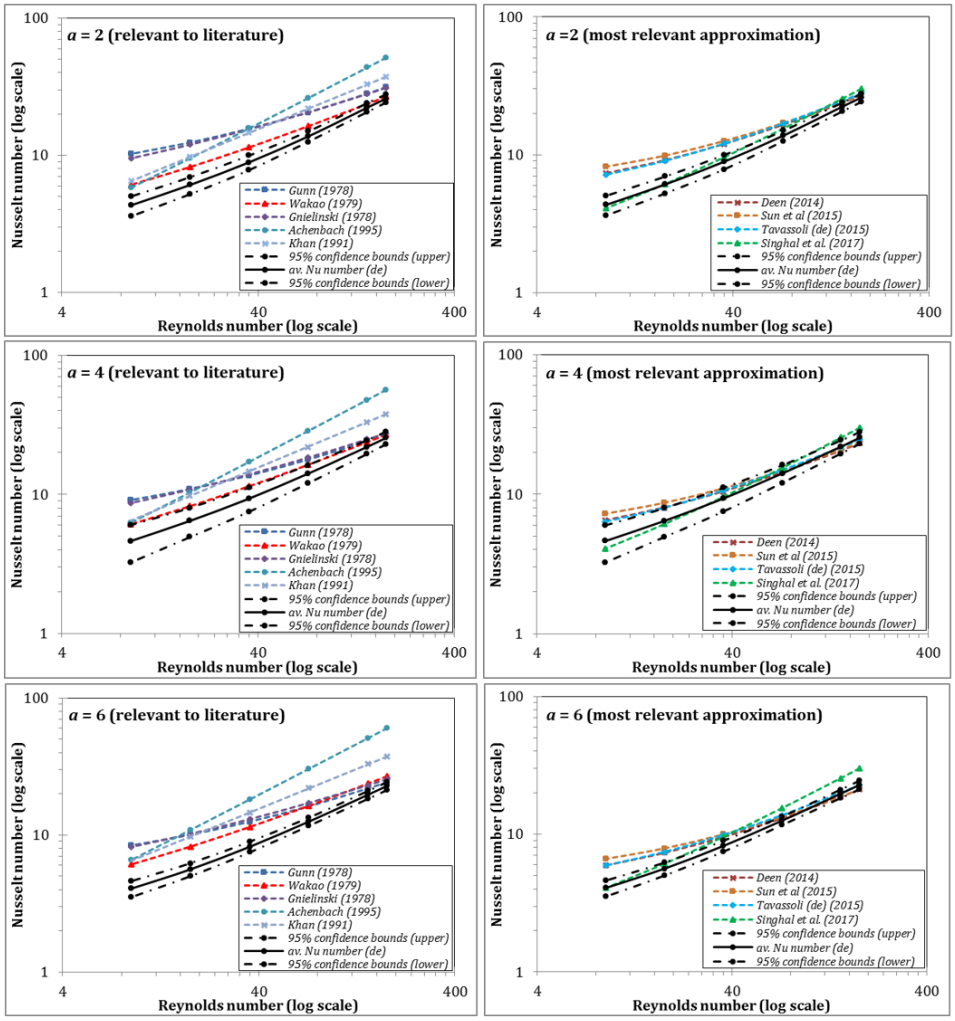

Figure 4.7. Heat transfer rate (expressed via the Nusselt number) versus Reynolds number averaged over five particle arrangements, including a comparison with literature data. The correlations more relevant to the comparison because of their overall validity are represented in the right panels ((a = 2, 4 and 6) from top to bottom)

4.3.5 A New Heat Transfer Correlation

This section presents generalized heat transfer correlations derived from results for all five particle arrangements of each aspect ratio (a =2, 4 and 6) over six Reynolds numbers (Re 9-180) and three Prandtl numbers (Pr 0.5-1). For each combination of Re, Pr and a, steady state PR-DNS simulations were completed for different packings of ~100 particles, requiring 270 simulations in total.

Packings of cylindrical particles show a natural increase in void fraction with an increase in aspect ratio. In fact, the data on the three different aspect ratios spanned a void fraction range of 0.405-0.539. To account for the possible void fraction dependency, the first fit was completed in the form of the classic Gunn correlation. The void fraction, Re and Pr dependencies of the Gunn correlation were retained and two model coefficients were adjusted to result in Eq. (29) with R^2 = 0.956. As observed in the previous work on spherical particles (Singhal et al., 2017f), the Gunn correlation shape resulted in an unphysical negative Nusselt number when Re approaches zero. This can be seen from the first model coefficient (-1.76). The second coefficient (1.04) is close to unity, implying that the void, Re and Pr dependencies in the data are generally well captured by the coefficients of the Gunn correlation.

$$Nu = -1.76(\pm 1.81) + 1.04\left(0.7(7 - 10\varepsilon + 5\varepsilon^2)Re^{0.2}Pr^{1/3} + (1.33 - 2.4\varepsilon + 1.2\varepsilon^2)Re^{0.7}Pr^{1/3}\right) \quad (29)$$

The bracketed number in the first term represents the average 95% confidence intervals that quantify the uncertainty related to the variation in the five different particle arrangements simulated for each combination of Re, Pr and void fraction (ε).

The previous work ((Singhal et al., 2017f)) found that a simplified correlation form avoided the unphysical limit as Re approaches zero and also resulted in a better fit to the data. Eq. (30) and (31) show the same equation form presented in the aforementioned work, refitted to all the data for the three different aspect ratio cylinders using Nu and Re data for the equivalent (Nu_e ; Re_e) and actual particle diameter (Nu_d ; Re_d) respectively. The fit using the actual particle diameter produced was slightly better (R^2 = 0.982) than the fit using the equivalent diameter (R^2 = 0.976).

$$Nu_e = 1.65(\pm 1.41) + 0.34\varepsilon^{-0.59}Re_e^{0.73}Pr^{0.50} \quad (30)$$

$$Nu_d = 0.73(\pm 0.75) + 0.23\varepsilon^{-1.10}Re_d^{0.70}Pr^{0.49} \quad (31)$$

Further improvement in the fit can be achieved by including the aspect ratio as a variable. This produced Eq. (32) and (33) with R^2 = 0.986 for the equivalent diameter case (Re_e) and R^2 = 0.988 for the actual diameter case (Re_d). Inclusion of the aspect ratio (a) as a variable therefore made the quality of the fit almost identical between the two representations of the particle diameter.

$$Nu_e = 1.46(\pm 1.07) + 0.031\varepsilon^{-2.99} Re_e^{0.71} Pr^{0.49} a^{0.53} \quad (32)$$

$$Nu_d = 0.74(\pm 0.64) + 0.041\varepsilon^{-2.76} Re_d^{0.70} Pr^{0.49} a^{0.37} \quad (33)$$

The most important difference in the model coefficients with the introduction of the aspect ratio as a parameter is a substantially larger coefficient for the void fraction. This data suggests that the introduction of the aspect ratio as a variable allows the void fraction coefficient to only explain the dependency of the Nusselt number on the void fraction within a given aspect ratio, whereas the void fraction coefficient must explain the effect of both aspect ratio and void fraction in Eq. (30) and (31).

The plot of observed vs. predicted values for the three fits based on the equivalent particle diameter are displayed in Figure 4.8 (left-panel). It is clear that all fits are good and do not show any clear outliers.

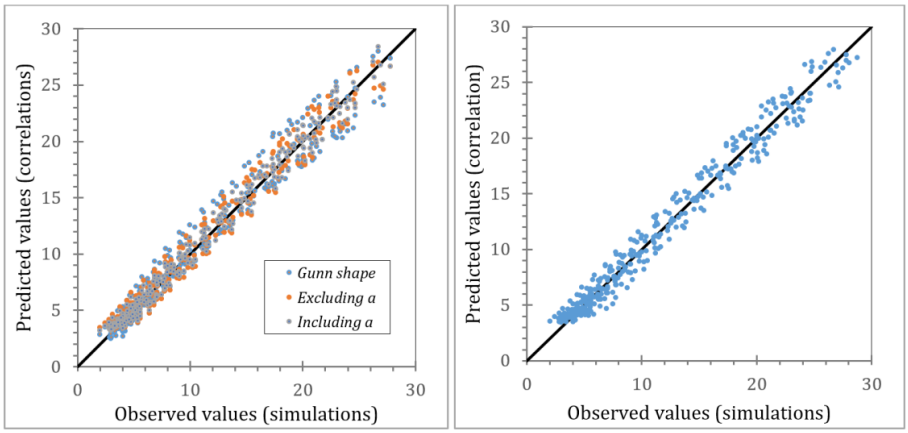

Figure 4.8. Left panel: Observed vs. predicted values of the Nusselt number over all cases for Eq. (29), (30) and (32). Right panel: Observed vs. predicted values of the Nusselt number over all cases including spherical particles (Eq. (34)).

Finally, the equivalent diameter fit in Eq. (30) was repeated when also including the data from the spherical particles investigated in a previous work (Singhal et al., 2017f). The following equation was fitted with $R^2 = 0.978$:

$$Nu = 1.77(\pm 1.39) + 0.29\varepsilon^{-0.81} Re^{0.73} Pr^{0.50} \quad (34)$$

It is clear that the quality of the fit is just as good as for Eq. (30) even though both spheres and cylinders are now represented. Eq. (34) can therefore be used as a generalized correlation for heat transfer from spherical or cylindrical particles in gas-particle realistic

packed beds as suggested in the discussion of Figure 4.7. The performance of this fit is visualized in Figure 4.8 (right-panel).

4.3.6 Pressure drop correction

The pressure drop through the packed bed is often explained by Forchheimer effect, which suggests the dependence of pressure drop on frictional losses (Nemec and Levec, 2005). In general, it can be said that the bed porosity tends to increase as we deviate from the spherical shaped particles. Even a minimal change in porosity greatly influences the pressure drop. (Ergun, 1952) presented the values for the Blake-Kozeny-Carman constant A (i.e., the viscous term) and the Burke-Plummer constant B (i.e., the inertial term) to be 150 and 1.75 respectively in Eq. (35). These values suggest that the Ergun equation is a widely accepted model for predicting the pressure drop in packed beds, if the shape of the particles can be more closely approximated to spheres and in the absence of wall effects.

First, the foundation in prediction of pressure drop in our rendered geometry (obtained from a DEM packed bed (Figure 4.1)) is laid by comparing the results of pressure gradient across the bed from the simulations of arrangements analysed in the previous work (with mono-disperse spherical particles) (Singhal et al., 2017f) with Ergun equation (Ergun, 1952).

$$\frac{\Delta P}{L} = \left[\frac{A\mu}{{d_p}^2}\cdot\frac{(1-\varepsilon)^2}{\varepsilon^3}\cdot u_s + \frac{B\rho}{d_p}\cdot\frac{(1-\varepsilon)}{\varepsilon^3}\cdot {u_s}^2\right] \qquad (35)$$

The pressure gradient across the packed bed geometry is obtained from a linear fit of the static pressure in planes perpendicular to the flow (see Section 4.2.2.2). The average pressure gradient over a range of Reynolds number (Re 9-180) and arrangements (arr1…arr5) from spherical packings (Singhal et al., 2017f) with its 95% C.I. (obtained as explained in Section 4.3.3) is shown in Figure 4.9 (upper-left). It is observed that the predictions from simulations are within the 95% C.I. bounds of Ergun equation (Ergun, 1952). Thus, suggesting confidence in the pressure drop predictions from our rendered geometry (Figure 4.1).

The pressure gradient obtained from the arrangements on cylindrical particles are compared against the predictions from the Ergun equation (Eq. (35) with the constants (A = 150; B = 1.75)) and the equivalent diameter (d_e) instead of particle diameter (d_p) as

suggested by (Carman, 1956). Figure 4.9 (upper-right and bottom) clearly suggests the results from Ergun with (d_e) to be out of the bounds of our current DNS simulations. Considering the current dimensions of the cylindrical particles ($L_p/d_p = a$ = 2, 4 and 6), the constant values for A and B can be approximated from the model suggested by (Nemec and Levec, 2005) (for $L_p/d_p > 1$). It is seen that the prediction with the Ergun constants (A; B) proposed by (Nemec and Levec, 2005) becomes acceptable in the C.I. of the current simulations as the aspect ratio of the cylindrical particles is increased. However, further modifications to the Ergun constants will be required to achieve a good fit to the simulation data from this study

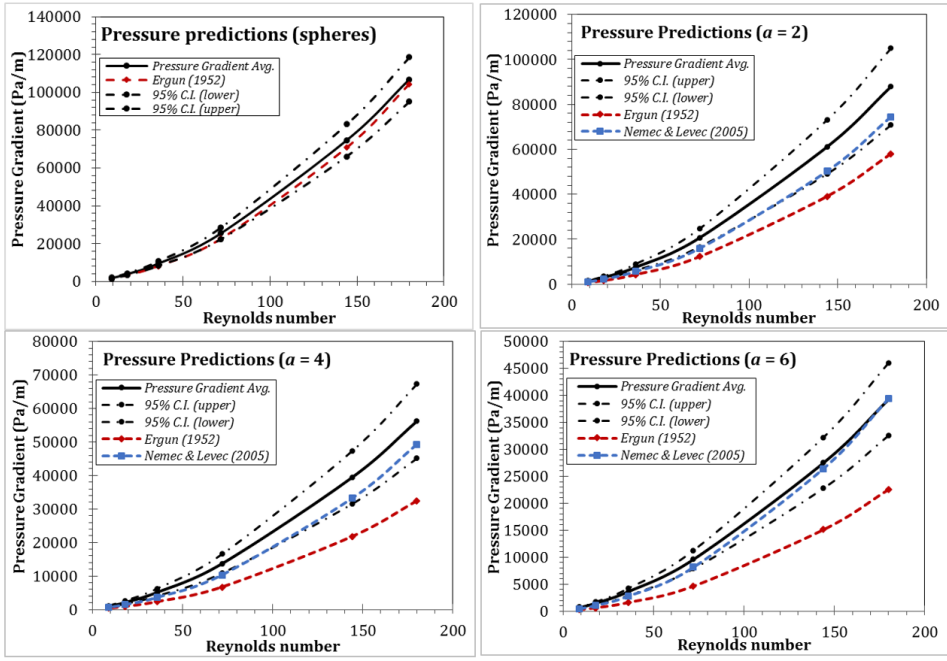

Figure 4.9. Comparison of average Pressure gradient (L.H.S term of Eq. (35)) for different particle arrangements versus Reynolds number (for Re 9 - 180). For spheres (upper-left panel) the arrangements are presented in (Singhal et al., 2017f) and for cylinders (upper-right and bottom panel) the particle arrangements are presented in Section 4.3.3**.**

Therefore, to present the correct values for the constants in the Ergun equation (Eq. (35)), we analyzed and re-fitted the data (Figure 4.10 for the resulting parity plot) for all three aspect ratios. The fits were completed using both the equivalent (d_e) and actual particle diameters (d_p).

The equivalent particle diameter (d_e) yielded Ergun coefficients of A = 284 and B = 2.67 with R^2 = 0.982, while the coefficients for the actual diameter (d_p) were A = 91 and B = 1.75 with R^2 = 0.968. Use of the equivalent particle diameter therefore yielded a better fit for all the combinations of Re and aspect ratio covered in this study.

When the actual particle diameter was used, clearly different trends in the plot of observed vs. predicted values were observed for the different aspect ratios. This systematic inconsistency was largely corrected by using the equivalent particle diameter as illustrated in Figure 4.10. The correlation using the equivalent particle diameter is therefore recommended for general use in packed beds with cylindrical particles.

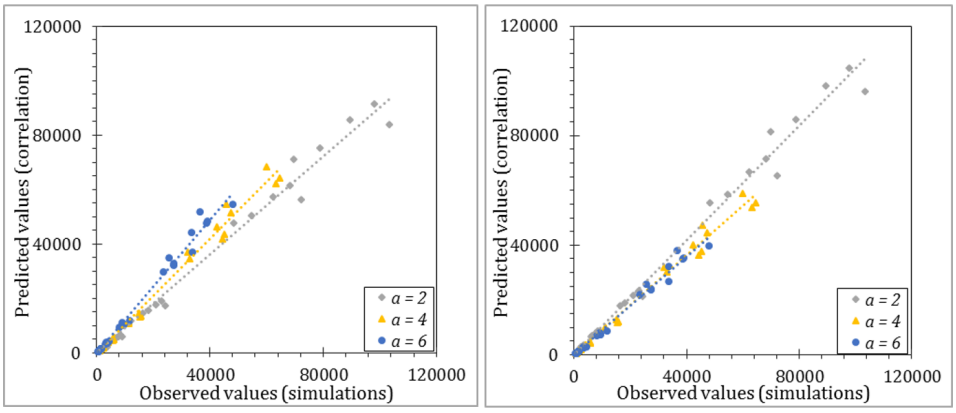

Figure 4.10. Observed vs. predicted values for the Ergun equation fitted with new constants when considering the equivalent particle diameter (d_e) (right panel) and the actual particle diameter (d_p) (left panel) for the data of pressure gradient obtained from arrangements (arr1…arr5 of each aspect ratio) of packings containing cylindrical particles for six different Reynolds numbers (Re 9-180)**.**

It was also attempted to fit new Ergun constants using data from both the simulations of spherical and cylindrical particles, but the pressure drop characteristics of the bed with spherical particles was very different from the beds with cylindrical particles. A pressure drop correlation applicable to both spherical and cylindrical particles is therefore not presented.

4.3.7 Heat transfer-pressure drop relationship

A high pressure drop through the packed bed is undesirable because of the energy and equipment costs required to pressurize the incoming gases to overcome the pressure drop. Simultaneously, it is desired to have a high rate of heat (and mass) exchange between the

gas and particles in the packed bed in order to minimize the size of the reactor. In a packed bed operation it is thus preferred to have a high ratio of the heat transfer rate to pressure drop in the bed.

Using the data obtained for heat transfer and pressure gradient in spherical packings (previous work (Singhal et al., 2017f); see Section 4.3.6) and cylindrical packings (see Section 4.3.5 and Section 4.3.6), the ratio of a volumetric heat transfer coefficient (W/m^3K) and the pressure gradient (N/m^3) is computed. The volumetric heat transfer coefficient is calculated as the heat transfer coefficient times the particle-fluid heat transfer surface per unit volume (a_p). For a packed bed of a given volume, the ratio therefore represents the heat transfer potential (W/K) over the force required to push the gas through the bed (N).

The corresponding data for all five arrangements of each aspect ratio and Reynolds numbers (18-180) is shown in Figure 4.11. It is seen that the packed bed with cylindrical particles ($a \geq 4$) has almost twice the ratio for heat transfer to pressure drop compared to the bed with spherical particles. This difference is primarily due to the higher void fraction in packed beds of cylindrical particles and the higher surface area / volume ratio of cylinders relative to spheres. This suggests that the cylindrical particles are more efficient for heat transfer, and have potential to curb high pressure drops in packed beds.

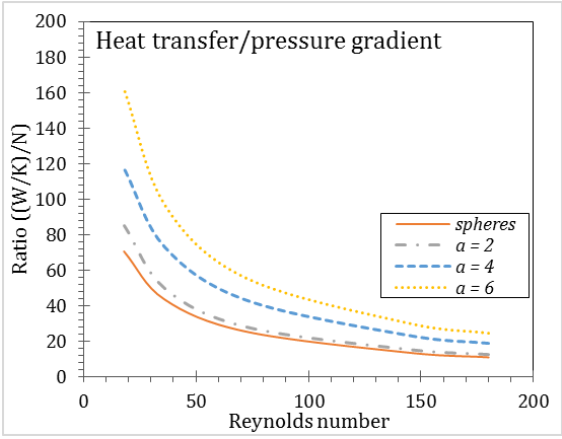

Figure 4.11. Comparison of the ratio of heat transfer rate to pressure gradient in a packed bed of spherical particles and cylindrical particles (data averaged over five arrangements of each aspect ratio (a = 2, 4 and 6), Pr = 1).

4.4 Conclusion

The presented study is an extension of the previous methodology presented for dense mono-disperse spherical particle packings (Singhal et al., 2017f). In this study, we have presented heat transfer predictions for dense packings of cylindrical particles (a = 2, 4 and 6) in porosity range ($0.405 < \varepsilon < 0.539$) for gas-solid systems. Previous heat transfer studies with PR-DNS have been mainly focussed on spherical particles with the exception of (Tavassoli et al., 2015), which focussed on fluidized bed applications, i.e., more dilute conditions. Hence, this study presents the first analysis of heat transfer phenomena in dense cylindrical particle packings.

We generated a large cylindrical particle packed bed using DEM, then the geometry representing the cylindrical packing is extracted from the large particle bed. This step of transformation helps in avoiding wall effects and obtaining a uniform radial profile of porosity. The rendered geometry obtained is meshed with tetrahedral elements to create a high quality body-fitted mesh. Then, using PR-DNS to obtain the simulation results, the heat transfer rate and pressure gradient is extracted from each simulation and fitted to obtain (i) a new heat transfer correlation, and (ii) to obtain new Ergun constants for predicting the pressure drop in particle beds of cylindrical particles.

The methodology is consistent with the previous work, and the grid independence is found at a resolution of $d_e/60$ for dense cylindrical packings. Wall effects were found to be negligible for computing heat transfer rate, supporting our choice for representing the bed geometry. The results for computing the Nusselt number showed significant variation between individual arrangements consisting of ~100 cylindrical particles each. This was quantified by using 95% confidence bounds in deriving the relation to approximate the calculated heat transfer rates.

In addition, we introduced new values for the Ergun constants (i.e., A = 284 and B = 2.67), refitted in a way such that with the equivalent particle diameter (d_e), a good fit over all aspect ratios is achieved for cylindrical particles. We find that relating Nusselt number (predicted from different arrangements) on aspect ratio (a) as a parameter in the correlations leads to a better fit of data for the system with $0.50 < Pr < 1$. We also find the ratio of heat transfer to pressure drop in packed bed of cylindrical particles to be more favorable than that in beds of spherical particles.

To sum up, we establish a new simple correlation applicable for heat transfer from a densely packed bed of either spherical particles or cylindrical particles (valid for $\varepsilon \approx 0.35$ for spherical particles; $0.405 < \varepsilon < 0.539$ for cylindrical particles, and in gas-solid system). The proposed correlation uses Nu and Re based on the equivalent particle diameter (d_e): $Nu = 1.77(\pm 1.39) + 0.29\varepsilon^{-0.81} Re^{0.73} Pr^{0.50}$. In this correlation, the bracketed term represents the 95% confidence bounds.

Author Contributions: *Arpit, Schalk & Stefan conceived the idea. Arpit designed, and performed the simulations; Rosa Quinta-Ferreira and Shahriar Amini supervised the work; Arpit Singhal wrote the paper.*

Arpit Singhal (Sign)

5 VERIFICATION OF THE CLOSURE MODELS

Abstract

Particle resolved direct numerical simulation (PR-DNS) is known to provide an accurate detailed insight into the local flow phenomena in static particle arrays. Most PR-DNS studies in literature do not account for reactions taking place inside the porous particles. In this study, PR-DNS is performed for catalytic reactions inside the particles using the mutifluid approach where all heat and mass transfer phenomena are directly resolved both inside and outside the particles. These simulation results are then used to verify existing 1D model closures over a number of different reaction parameters including different reaction orders, multiple reactions and reactants, interacting reactions, and reactions involving gas volume generation/consumption inside the particle. Results clearly showed that several modifications to existing 1D model closures are required to reproduce PR-DNS results. The resulting enhanced 1D model was then used to accurately simulate steam methane reforming, which includes all of the aforementioned reaction complexities. The effect of multiple reactants was found to be the most influential in this case. [i]

[i] This chapter is based on Arpit Singhal, S. Cloete, R.Q. Ferreira, S. Amini, Verification of heat and mass transfer closures for industrial scale packed bed reactor simulations, *Energies*, Vol 11(4), 805

Nomenclature

Symbols

$\boldsymbol{a}$	Characteristic length of spherical particle ($d_p/6$)
a_p	Spherical particle-fluid heat transfer surface per unit volume ($a_p = 6 \cdot (1 - \varepsilon)/d_p$) (1/m)
c_A	Concentration of species A (kmol/m^3)
c_{As}	Concentration of species A on particle surface (kmol/m^3)
C_p	Specific heat capacity of fluid (J/kg K)
d_p	Diameter of the spherical particle (m)
dA	Area of the axial plane (m^2)
D	Molecular diffusivity of gas (m^2/s)
e_z	Vector in z-direction
E_a	Activation energy (J/mol)
g	Gravity (m/s^2)
h	Enthalpy (J/kg)
h_e	Heat transfer coefficient (W/m^{2}K)
J	Diffusive flux (kg/(m^2.s))
k	Reaction rate constant (mol^{1-n} m^{3n-2}/s)
k_0	Arrhenius constant (1/s)
K	Thermal conductivity of gas (W/ m K)
K_x	Adsorption constant for species (x = CH_4, CO, H_2,H_2O)
K_{pg}	Interphase momentum exchange coefficient (kg/(m^3.s))
m_p	Mass of the particle (kg)
N	Ratio of diameter of reactor to diameter of the particle
Nu	Nusselt number
p	Partial pressure of the specie (bar)
P	Pressure (Pa)
Pr	Prandtl number ($\mu\ C_p/K_g$)
r	Reaction rate (mol/m^3.s)
R	Gas constant (8.314 J/mol/K)
Re	Reynolds number ($\rho\ u_s\ d_p/\mu$)
S	Source term
Sc	Schmidt number ($\mu/\rho\ D$)
t	Tortuosity
T	Static temperature of the fluid (K)
T_p	Particle surface temperature (K)
T_{bulk}	Bulk fluid temperature (K)

u_s Superficial velocity of the fluid (m/s)

u_z Velocity of the fluid in Z-direction (m/s)

v Velocity of the particles for Dem (m/s)

dV Volume in the region of interest (m^3)

Y Species concentration (mass or molar fraction)

y Species mole fraction

x Species mass fraction

Greek

α Volume fraction

ε Porosity (void fraction)

ϕ Thiele modulus

ρ Density (kg/m^3)

η Effectiveness factor

$\bar{\bar{\tau}}$ Stress tensor ($kg/(m.s^2)$)

μ Viscosity of fluid (kg/ m · s)

Vectors:

$\vec{u}$ velocity (m/s)

$\vec{g}$ Gravity (m/s^2)

Subscripts:

p particle

g gas

e effective

n reaction order

i species i

j Reaction and particle index

Operators:

∇ Gradient operator (m^{-1})

$\nabla.$ Divergence operator (m^{-1})

$\frac{d}{dt}$ time derivative (s^{-1})

5.1 Introduction

Packed bed gas-solid reacting systems are widely used in the chemical and process industry. Due to this industrial importance, modelling and simulation of packed bed reactors have been an important research and industrial priority for several decades.

With the development in computational resources it is now possible to perform resolved 3D simulations of fluid flow as well as heat and mass transfer phenomena in realistic particle packings. The advantages of such resolved simulations, commonly referred to as particle-resolved direct numerical simulations (PR-DNS), have been pointed out by (Dixon and Nijemeisland, 2001). Due to the homogenous average voidage in a typical packed bed, the resolved simulation of a small segment of the bed can give valuable insight into the local transport phenomena, applicable to the whole packed bed. This is especially helpful in evaluating and improving industrially affordable 1D models without uncertainties associated with experiments, which motivates the current work.

A complete evaluation of 1D model performance requires full resolution of all transfer phenomena, both inside and outside the particles. However, the vast majority of PR-DNS studies involves studying pressure drop, particle-fluid heat transfer and dispersion only on the fluid region outside the particles (Atmakidis and Kenig, 2009; Bai et al., 2009; Deen et al., 2014; Eppinger et al., 2011; Eppinger et al., 2016; Jafari et al., 2008; Karthik and Buwa, 2017; Lee et al., 2007; Maestri and Cuoci, 2013; Mirhashemi and Hashemabadi, 2012; Mirhashemi et al., 2011; Motlagh and Hashemabadi, 2008; Nijemeisland et al., 2004; Partopour and Dixon, 2017; Romkes et al., 2003; Singhal et al., 2017e, f; Sun et al., 2015; Tavassoli et al., 2015; Wehinger et al., 2017; Zare and Hashemabadi, 2013) either on an orderly or randomly packed bed of spherical or cylindrical particles.

Analyzing the intra particle transfer phenomena requires the particles to be meshed, which increases the computational overhead and also complicates the mesh generation. There have been several works including the intra particle heat transfer for the non-reactive cases (Augier et al., 2010; Dixon et al., 2003; Nijemeisland et al., 2004; Singhal et al., 2016b; Wehinger et al., 2016). The complexity intensifies as the reactions are considered, with most of the available CFD solvers not allowing chemical species inside the porous catalyst (Dixon, 2017). They consider the particle as solid regions (Dixon, 2017). To model reacting resolved systems some authors have constrained the parameters studied or simplified the geometries. (Mousazadeh et al., 2013) used a 2D model to study the ethylene oxidation, while (Zhou et al., 2013a) choose to use 3D spherical particle bed, without considering intraparticle effects to analyze isopropanol-acetone-hydrogen heat pump module.

Particle resolved simulations for intra particle reactive systems of steam methane reforming with catalyst particle as porous mediums was first presented by (Dixon et al., 2010) for spherical particles and by (Dixon et al., 2012) for cylindrical particles. They developed an approach in Fluent® to use user defined parameters to be defined inside the solid particles and thus help in extracting correct heat and mass transfer at particle surfaces.

Recently, (Dixon, 2017) presented a study for 3D simulations of heterogeneous catalytic reactions in packed beds of N = 5.96 with reactions happening inside the porous particle and not confined to the particle surface. They suggested that, in order to understand the transport phenomena and reaction engineering inside the packed bed, it is essential to have a particle bed long enough to obtain the developed flow properties.

Previous studies from the authors have used PR-DNS to study the intra particle heat and mass transfer applied to reacting systems with both spherical (Singhal et al., 2017c; Singhal et al., 2017d) and cylindrical particles (Singhal et al., 2017a). In these works, the geometry simulated is extracted from a large realistic packing in order to minimize wall, inlet and outlet effects (Singhal et al., 2017e, f).

The objective of the current work is to use the conceptually more correct PR-DNS for a geometry of monodisperse spherical particles with solid catalyzed reactions taking place inside the porous catalyst particle. The main purpose of this study is to evaluate the validity of mass and heat transfer closures commonly used in industrial scale 1D models against the PR-DNS data. Moreover, our study is the only one focused on investigating and suggesting modification to 1D model for simulating steam methane reforming process compared with results from detailed scale of PR-DNS.

The work is presented as follows: in Section 5.2 we have explained the methodology, grid independence, closure models and simulation set ups. Section 5.3 documents the major findings of the paper with the investigation based on (i) reaction orders (ii) multiple reactions (iii) gas volume (iv) steam methane reforming reactions. Then finally we conclude in Section 5.4.

5.2 Methodology

5.2.1 Thiele modulus and effectiveness factor

Intra particle diffusion resistances are important in describing the actual reaction rate inside the catalyst pellet. The effectiveness factor (η) is defined by Eq. (36) and quantifies the effect intra particle diffusion resistance has on reaction rate (Ishida and Wen, 1968; Levenspiel, 1999; Rawlings, 2002; Yang et al., 2016).

$$\eta = \frac{actual\ reaction\ rate}{reaction\ rate\ without\ diffusion\ limitations} \tag{36}$$

The concept of effectiveness factor (η) in heterogeneous catalytic reactions for porous particle is given by (Levenspiel, 1999). Meanwhile, (Thiele, 1939) added the plots of effectiveness factor vs Thiele modulus for simple reaction orders. Thiele modulus (ϕ) is dimensionless number dependent upon reaction rates, effective diffusivities, and concentration of the reactant in the fluid surrounding the particle (Eq. (37)).

$$\phi = \frac{reaction\ rate}{diffusion\ rate} \tag{37}$$

The effectiveness factor (η) and Thiele modulus (ϕ) definitions for spherical particles (given in Eq. (38) and (39)) are according to the general definitions of these parameters given in (Rawlings, 2002) for a n[th] order generic catalytic reaction $\left(A \xrightarrow{k} B\right), where\ r = kc_A^n$. Thus, for heterogeneous catalytic reaction system, effectiveness factor can be defined as a function of Thiele modulus. For the spherical particles studied in this work, $a = r_p/3$.

$$\phi = \sqrt{\frac{n+1}{2}\frac{kc_A^{n-1}a^2}{D_e}} \tag{38}$$

$$\eta = \frac{1}{\phi}\left[\frac{1}{tanh\phi} - \frac{1}{3\phi}\right] \tag{39}$$

$$D_e = \frac{D\varepsilon}{t} \tag{40}$$

5.2.2 Conservation equations

The steady state incompressible conservation equations for continuity, momentum, species transfer and energy for both 3D and 1D framework in Newtonian flow are given by Eulerian multifluid approach, which assumes the gas phase and solid phase to be interpenetrating continua. Both the phases operate with separate set of equations. The conservation of equations for each phase (k) are given in Eqns. (41) - (44). The momentum equation is not solved for the solid phase as the velocities of solid phase is fixed to zero, being a packed bed. In addition, species are only conserved for the gas phase because the solid acts only as a catalyst and does not undergo any reaction.

$$\nabla \cdot (\alpha_k \rho_k \vec{u}_k) = 0 \tag{41}$$

$$\nabla \cdot \left(\alpha_g \rho_g \vec{u}_g \vec{u}_g\right) = -\alpha_g \nabla p + \nabla \cdot \bar{\bar{\tau}}_g + \alpha_g \rho_g \vec{g} + K_{pg}\left(\vec{u}_p - \vec{u}_g\right) \tag{42}$$

$$\nabla \cdot \left(\alpha_g \rho_g g Y_{g,i}\right) = \nabla \cdot \alpha_g \vec{J}_{g,i} + \alpha_g S_{g,i} \tag{43}$$

$$\nabla \cdot (\alpha_k \rho_k \vec{u}_k h_k) = \bar{\bar{\tau}}_k : \nabla \vec{u}_k + Q_k + \nabla \cdot \left(\sum_j h_{k,j} J_{k,j}\right) \tag{44}$$

The Ergun equation (Ergun, 1952) is used to account for drag in Eq. (42) (last term). Interphase heat exchange term (Q_k) in Eq. (44) is modelled according to our previous work (Singhal et al., 2017f). The rightmost term in Eq. (43) accounts for the heterogeneous catalytic reactions implemented. The parametric studies presented in this study utilize a hypothetical reaction to allow for easy interpretation of results, but an example with real steam methane reforming reactions is also presented. These reactions are detailed later in the paper.

To be consistent with the previous works (Singhal et al., 2017e, f), with the similar way to obtain the geometry (Section 5.2.3.1), steady state DNS (and hence Eqns. (41) - (44)) in ANSYS Fluent with phase couple SIMPLE algorithm and 2nd order spatial discretization for all other equations is used.

For the DEM simulation only Newton's translation motion equation with tangential forces included is solved to obtain the packed bed (Eq. (45)).

$$m_p \frac{dv}{dt} = m_p g + \sum_{i=1}^{j} (F_{p,i,n} + F_{p,i,t}) \quad (45)$$

5.2.3 PR-DNS simulation setup

5.2.3.1 Geometry and mesh development

The spherical particle bed is generated using discrete element method (DEM) in ANSYS Fluent. The methodology of generating the particle bed, extracting and creating the rendered geometry from this large bed for the simulations is exactly similar to the previous work with monodisperse spherical particles (Section 3.2.1 of Chapter 3).

The overlap between the spherical particles in our realistically packed bed geometry is dealt by caps method with the cylinder cap size of $d_p/50$. This is consistent with the detailed study done in Section 3.3.3 of Chapter 3.

Following the creation of the geometry, the rendered geometry is meshed with polyhedral elements both inside and outside the particles using the Fluent Meshing tool with resolution $d_p/60$ (Section 5.2.3.3). This allows for directly simulating mass and heat transfer phenomena both inside and outside the porous particle.

The rendered geometry used for simulations in this study is considered to be free from wall effects as proven for external heat transfer in our previous work (Singhal et al., 2017f). This was found to be consistent even for this work, we found negligible wall effects for species conversion.

5.2.3.2 Boundary conditions and simulation parameters

The simulated geometries contain a velocity inlet, pressure outlet, and a non-slip zero heat flux reactor wall (Singhal et al., 2017f). The grain diameter inside the porous particles is set to $1e^{-7}$ m. This small diameter results in essentially instantaneous momentum and heat transfer to prevent any flow through the particle and to ensure thermal equilibrium between the gas and the solid phase, especially with the high particle porosity employed in this work. As discussed later in Section 5.2.3.4, the particle porosity in the PR-DNS simulations had to be set close to unity in order to ensure accurate simulation of external heat transfer. A particle porosity of 0.993 was chosen, resulting in a 100 times lower solid concentration than a conventional particle with a porosity of 0.3.

This implies that the volumetric reaction rate and particle thermal conductivity had to be increased by a factor of 100 to replicate the behaviour of a regular particle with a porosity of 0.3.

Similar to our previous work (Singhal et al., 2017f), the method of calculating the bulk fluid temperature on number of planes (in total 25 planes with gap of $d_p/5$ between each plane) perpendicular to the flow is followed now, in order to extract bulk species concentrations (Y_{bulk}). In this way, the species concentrations are calculated locally on each plane by Eq. (46), (where *Y*, is the mass or mole fraction of the reacting species). The resulting axial profiles of bulk temperature and species are suitable for direct comparisons to 1D model results.

$$Y_{bulk} = \frac{\int (u.e_z) Y dA}{\int (u.e_z) dA} \tag{46}$$

5.2.3.3 Mesh dependence

The simulation for mesh independence study involved a hypothetical heterogeneous first order catalytic reaction (Eq. (47)). The reaction takes place inside the porous solid particle (by grain model (Szekely, 1976)). The simulation is carried out at Reynolds number (Re = 100), Prandtl number (Pr = 1), and Thiele module (ϕ = 10) with inlet reactant mass fraction (x_A = 0.1). Eqn. (48) presents the reaction rate for an exothermic reaction (dH_{rxn} = -10 kJ/mol) i.e. Eq. (47), with pre exponential factor in Eq. (49) calculated to result in the reaction constant of 10000 1/s at an inlet temperature of 1000K. The solid particle, and particle bed properties are given in Table 15.

Table 15. Packed bed geometry and flow simulation properties

Parameter	Value
Particle size (m)	$1 \cdot 10^{-3}$
Bed porosity (ε)	0.352
Particle inside volume fraction (α_p)	0.007
Number of particles	100 (approx.)
Diameter of the geometry (m)	$4.8 \cdot 10^{-3}$
Height of the geometry (m)	$4.8 \cdot 10^{-3}$
Mesh resolution (particle surface)	$d_p/60$
Pre-exponential factor (k_0) (1/s)	1.674×10^9

Activation energy (J/mol)	100000
Thermal conductivity of solid (W/ m K)	500

$$A\,(g) + (solid) \rightarrow B\,(g) + (solid) \tag{47}$$

$$r_{cat} = \alpha_p k c_A \tag{48}$$

$$k = k_0\, e^{\left(\frac{-E}{RT}\right)} \tag{49}$$

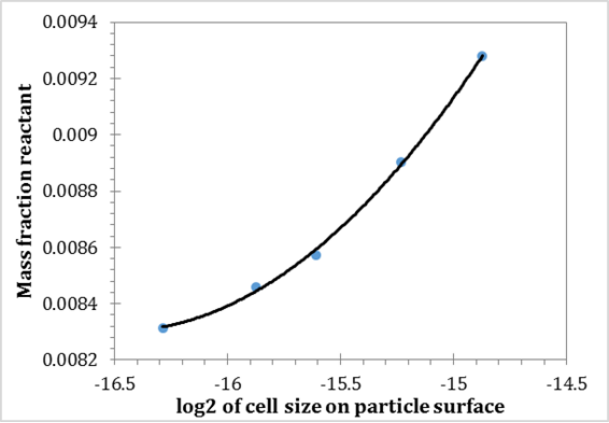

Figure 5.1. Grid independence behaviour for the variation of mass fraction of species A (x_A) at a plane perpendicular to the flow near the outlet (2 planes below the outlet) in array of spherical particles w.r.t. particle surface mesh resolution, simulated at dH_{rxn} = -10 kJ/mol, Pr = 1, ε = 0.351, and ϕ = 10. Symbols represent the results and the line is the exponential function: $\boldsymbol{x_A = 0.008048 + exp\,(9.7158 + 1.1035 log_2(dx))}$, where (dx) is the grid size on the particle surface.

The mesh independence study is completed at an exothermic reaction (dHrxn = -10 kJ/mol) because the external heat transfer becomes the controlling phenomenon in this case and therefore the grid size becomes important. The mass fraction of species A (x_A) at 2 planes (Section 5.2.3.2) below the outlet is analysed to explore the conversion of x_A through the geometry on different grid sizes. Figure 5.1 shows that the overall conversion increases with each doubling of the grid size when fitted with an exponential function. This is because larger cell sizes over predict the external heat transfer, allowing more of the heat generated by the exothermic reaction to leave the particle, in turn resulting in a cooler particle and a lower reaction rate. The difference between the value at $d_p/60$ and

the infinitesimally small cell size results in the difference of 4.8%. Thus the cell size of $d_p/60$ is used in this work. Subsequently, the growth rate of 20% is followed to fill the voids for fluid and solid sections.

5.2.3.4 Void fraction inside the particle

The solid catalyst particles are defined as fluid regions in FLUENT using the multifluid approach and then a specific solid volume fraction value is patched into this region. This enables direct simulation of heat and mass transfer including gas density gradients inside the solid particle (as would be the case when the reaction creates or consumes gas volume).

Before proceeding with the intra particle transfer, the ability of Ansys FLUENT to predict external heat transfer with the Eulerian multifluid approach is verified. The external heat transfer simulations on a geometry of spherical particles ($\varepsilon = 0.352$) are performed for Re = 100, Pr = 1, T_{inlet} = 473 K, and T_p = 573K. The comparison is made over a range of particle porosity values (ε_{inside} = 0.05-0.993) and an ideal external heat transfer case, where the particle surface is defined as a wall without any inside mesh (Singhal et al., 2017f). Figure 5.2 shows that as the particle porosity (ε_{inside}) value increases (or particle volume fraction (α_p) decreases), the fluid temperature relates more closely to the ideal external heat transfer case.

This effect is quantified in Figure 5.3, when the Nusselt number (with the methodology explained in Section 3.2.2.2 of Chapter 3) is extracted from all the cases shown in Figure 5.3. It is seen that Nusselt number value for external heat transfer from particle surface to fluid approaches the ideal value as the particle porosity (ε_{inside}) is increased, with almost the same Nusselt number prediction at ε_{inside} = 0.993 or α_p = 0.007. This sensitivity is related to the multifluid assumption creating numerical errors on the edge of the particles where there is a step change in volume fraction.

Based on this result, the value (ε_{inside} = 0.993) is used in the PR-DNS simulations and the reaction rate constant is increased by a factor 100 to mimic the more realistic case where ε_{inside} = 0.3.

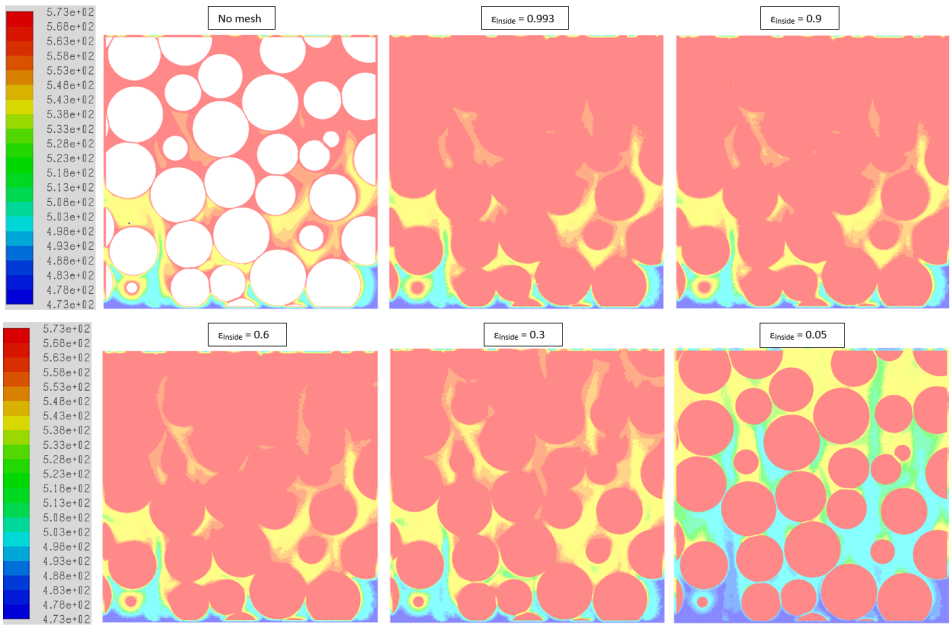

Figure 5.2. The contour plots for fluid temperature (K) (at plane y = 0, through a bed of ε = 0.351, Re = 100, Pr = 1). [Top left: (No mesh) represents the case without inside particle mesh (Singhal et al., 2017f); In all other plots ε_{inside} represents the particle porosity in each case.]

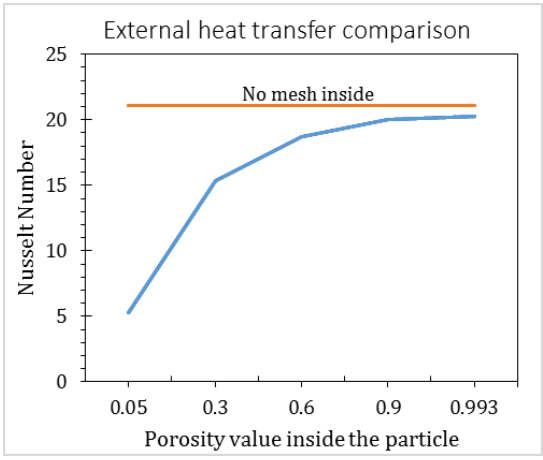

Figure 5.3. Nusselt number extracted on 25 planes based on local driving force (Deen et al., 2012; Deen et al., 2014; Sun et al., 2015; Tenneti et al., 2013) versus porosity value inside the particle. The comparison is made to Nusselt number from the ideal external heat transfer case without inside particle mesh. This value has also been verified with (Singhal et al., 2017f) heat transfer correlation.

5.2.4 1D packed bed model

As outlined in Section 5.2.2, the 1D model is also based on the Eulerian multifluid approach. Only in this case, the void fraction is constant in all cells and the geometry is meshed only in one direction. More details can be found in the previous work of the authors (Cloete et al., 2016), and the applications in (Singhal et al., 2017c; Singhal et al., 2017d). The domain is discretized into 100 cells, with the length of the geometry equal to the PR-DNS geometry as given in Table 15. The 1D model is solved with similar simulation setup and boundary condition of respective PR-DNS cases. The primary difference is that the particles are assumed to have a realistic void fraction of 0.3 (as opposed to $\varepsilon_{inside} = 0.993$ used in the PR-DNS as outlined in the previous section), so no adjustment to the reaction rate is required.

This work focuses on closure models to account for external heat and mass transfer and intra particle diffusion that are required to model the phenomenal that are directly resolved in PR-DNS. The models to define intra particle diffusion (Levenspiel, 1999; Rawlings, 2002) are given in Eqns. (38), (39), and (40). While the closures for external heat and mass transfer are given in Eq. (50) and (51). These models are based on our previous work with mono disperse spherical particle (Singhal et al., 2017f) and are integrated to calculate the effective reaction rate in 1D model.

$$Nu = 2.67 + 0.53Re^{0,77}Pr^{0,53} \tag{50}$$

$$Sh = 2.67 + 0.53Re^{0,77}Sc^{0,53} \tag{51}$$

The mean solid volume fraction (α) in 1D model is fixed as a product of particle bed volume fraction ($1-\varepsilon$) times the inside particle volume fraction ($\alpha_p = 0.7$). Also, the heat of reaction (dH_{rxn}) as suggested in previous work (Singhal et al., 2017d) is assigned to the solid phase unlike the PR-DNS (in which it is assigned as an enthalpy term to gas phase).

5.3 Results and Discussion

In this section, the comparison of 1D model with PR-DNS is discussed based on different levels of complexity in the reactant behaviour.

5.3.1 Reaction orders

The ability of 1D models to predict correct reactant conversion with different reaction orders is studied in this section. For the hypothetical catalytic reaction in Eq. (47), both the PR-DNS and 1D models are simulated with the properties given in Table 16. The molecular diffusivity (D) and thermal conductivity (k) of the gas is calculated based on the values (ϕ = 10; Pr =1; Re = 100 and Sc ≈ 0.7).

In order to have uniformity in the predictions of reactant concentration (x_A) with different reaction orders, the temperature influence on reaction rate in this validation is eliminated. First, the effective diffusivity (D_e) of the gas inside the particle is calculated for the first order reaction with reaction rate constant of 10000 1/s (for ϕ = 10 and ϕ = 5) (using Eq. (38)). Here, we assume that $D_e = D/5$ to account for a realistic particle porosity and tortuosity. Following this, using the rearranged Eq. (38) for a fixed inlet concentration (c_A = 10 mol/m^3), the reaction rate constant (k; Eq. (53) and Eq. (38)) for each reaction order is calculated in Eq. (52). This practice ensures that the ratio of reaction rate to diffusion rate at the start of the geometry is identical between cases with different reaction orders.

$$k = \frac{2\phi^2 D_e}{(n+1)c_A^{n-1}a^2} \tag{52}$$

$$r_n = \alpha_p k_n c_A^n \tag{53}$$

The reaction rate for each reaction order (namely 0.5th, 1st, and 2nd) is defined using Eq. (53). The PR-DNS results of species conversion of reactant (A) for inlet mass fraction (x_A) at ϕ = 10, simulated for the setup and flow properties in Table 16 is shown in Figure 5.4. The reaction rate resistances increases with increase in reaction order, which is reflected in Figure 5.4. Thus, the reactant concentration (x_A) gets consumed fastest at 0.5th order reaction. The reaction rate at the inlet is similar between cases, but slows down in the remainder of the domain in the cases with a higher reaction order as the reactant is consumed.

Table 16: Flow properties for CFD simulation. The flow properties are based on the range of dimensionless parameters (Re, Pr, ϕ) in the PR-DNS study**.**

Parameter	Value
Prandtl number	1

Reynolds number	100	
Thiele modulus	10; 5	
Temperature of Inlet (K)	1000	
Inlet mass fraction (species A)	0.1	
Heat of reaction (kJ/mol)	0	
Operating pressure (bar)	1	
Thiele modulus	ϕ = 10	ϕ = 5
Molecular diffusivity (m^2/s)	$1.38889 \cdot 10^{-5}$	$5.55556 \cdot 10^{-5}$
Reaction rate constants		
• 0.5^{th} order	$4.22 \cdot 10^{4}$	
• 1^{st} order	$1.00 \cdot 10^{4}$	
• 2^{nd} order	$6.67 \cdot 10^{2}$	
	Gases	**Particles**
Dynamic Viscosity (μ) (kg/m · s)	$1 \cdot 10^{-5}$	
Density (ρ) (kg/m^3)	1	2500
Thermal conductivity (W/m K)	0.01	500
Molecular weight (kg/kg mol)	10	10
Specific heat (C_p) (J/kg K)	1000	1000

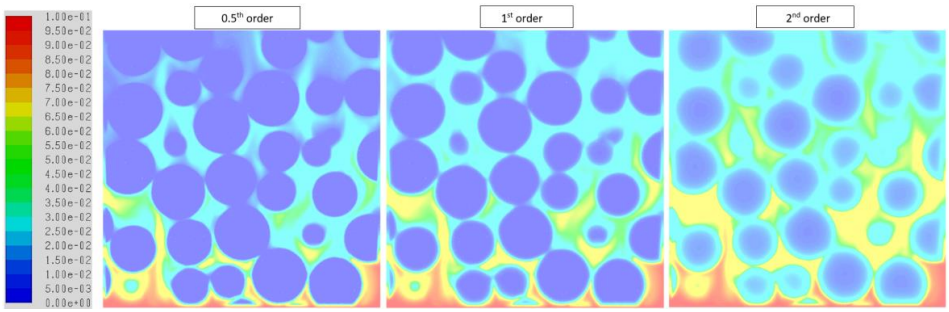

Figure 5.4. PR-DNS results for conversion of reactant (mass fraction of species A; x_A) through a geometry of spherical particles (at plane y = 0; ε = 0.352, ϕ = 10, Pr = 1) for different reaction orders (0.5^{th}, 1^{st}, 2^{nd}) respectively.

The results of reactant conversion through the reactor from 1D model and PR-DNS compared for two different Thiele modulus values (ϕ = 10, 5) over three different reaction orders is shown in Figure 5.5. Overall, the 1D model compares well with the PR-DNS simulations (with only a mild deviation for the 2^{nd} order reaction). The change in reaction order is well captured by the 1D model, with overall reactant conversion decreasing with increased reaction order.

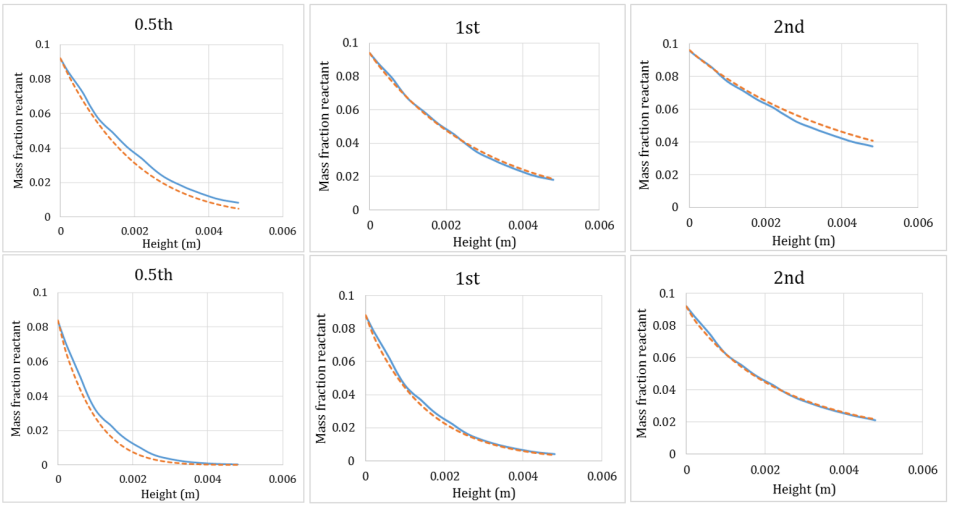

Figure 5.5. Comparison of the mass fraction (x_A) of reactant conversion (of species A) between the two approaches (i) PR-DNS (represented by solid lines) (ii) 1D model (dashed lines) for [Top] Thiele modulus (ϕ=10), and [Bottom] ϕ = 5 for different reaction orders (0.5^{th}, 1^{st}, 2^{nd}); along the height of the reactor geometry.

5.3.2 Multiple reactions

Chemical reaction systems often consist of multiple reactions or reactions with multiple reactants. This leads to interactions between species reaction and diffusion phenomena in the particle and could result in significant errors when using a single component mass transfer model. This section will therefore evaluate a number of different cases with multiple reactions/reactants to quantify the uncertainties that such reaction systems introduce to 1D packed bed modelling. The four investigated cases are briefly described below:

1. A single catalytic reaction with two reactants (Case 1, Eq. (54))
2. Two reactions with one independent reactant each (Case 2, Eq. (55))
3. Two reactions consuming the same reactant at different rates (Case 3, Eq. (57), parallel reactions)
4. Two reactions where the product of the first reaction is the reactant of the second (Case 4, Eq. (58), sequential reactions)

In order to simplify the comparison between cases 1 and 2, the inlet reactant ratio (of A and B i.e. $y_{A:B}$ = 1:2) is kept same, and simulated for ϕ = 10, with flow properties for all

the reacting species [(Case 1 (Eq. (54)) and Case 2 (Eq. (55))] similar and given in Table 16. The reaction rate constant (k_2) for case 2 (Eq. (55)) is offset to 1000 1/s. The reaction rate constant (k_1) for case 1 is defined based on the fixed reaction rate constant of case 2 (Eq. (56)), by assuming the overall reaction rate from both cases to be equal at the reactor inlet.

$$A\,(g) + B\,(g) + solid \rightarrow C\,(g) + D\,(g) + solid$$

$$r_A = \alpha_p k_1\, c_A\, c_B \tag{54}$$

$$A\,(g) + solid \rightarrow C\,(g) + solid;\ r_A = \alpha_p k_2 c_A$$

$$B\,(g) + solid \rightarrow D\,(g) + solid;\ r_B = \alpha_p k_2 c_B \tag{55}$$

As may be expected, Figure 5.6 shows that the two independent reactions in Case 2 are well captured by the 1D model without any adjustment. For the multiple reactants in Case 1, however, an adjustment was required to define the overall effectiveness factor as($\eta = (\eta_A^{-1} + \eta_B^{-1})^{-1}$) using the effectiveness factor definition for individual species in (Eq. (39)). If the effectiveness factor is defined according to the diffusion of only one reactant, Figure 5.6 shows that the 1D model significantly overpredicts the effective reaction rate.

$$k_1 = \frac{k_2(c_{A,in} + c_{B,in})}{(c_{A,in}\, c_{B,in})} \tag{56}$$

For cases 3 and 4, the inlet reactant mole fraction y_A is set to 1. The reaction rate expressions simulated in these two cases are shown in Eq. (57) and (58).

$$A\,(g) + solid \rightarrow B\,(g) + solid;\ r = \alpha_p \frac{2}{3} k_2 c_A$$

$$A\,(g) + solid \rightarrow C\,(g) + solid;\ r = \alpha_p \frac{1}{3} k_2 c_A \tag{57}$$

In case 3 (Eq. (57)), the Thiele modulus value (Eq. (38)) for both the reactions must be calculated from the overall rate at which reactant A reacts. In other words, the Thiele modulus must be calculated according to the sum of the two reaction rates given in Eq. (57) ($r = \alpha_p k_2 c_A$). Figure 5.7 shows that calculating the Thiele modulus from the lower reaction rate of each individual reaction results in an under prediction of the mass transfer limitation and an over prediction of the overall reactant conversion.

$$A\,(g) + solid \rightarrow B\,(g) + solid;\ r_A = \alpha_p k_2 c_A$$

$$B\,(g) + solid \rightarrow C\,(g) + solid;\ r_B = \alpha_p k_2 c_B \tag{58}$$

Case 4 (Eq. (58)), where the product of the first reaction is the reactant of the second, is more complex. As shown in Figure 5.7, simulating the B ➔ C reaction according to the standard mass transfer model greatly under predicts the reaction rate, leading to a large over prediction in the mole fraction of B. This is simply because the A ➔ B reaction releases species B directly inside the particle so that no mass transfer limitation is present. However, Figure 5.7 also shows that, when the mass transfer limitation is completely removed, the B ➔ C reaction rate is over predicted. This suggests that some of the reactant B is consumed directly as it is formed inside the particle, but some must enter from outside the particle.

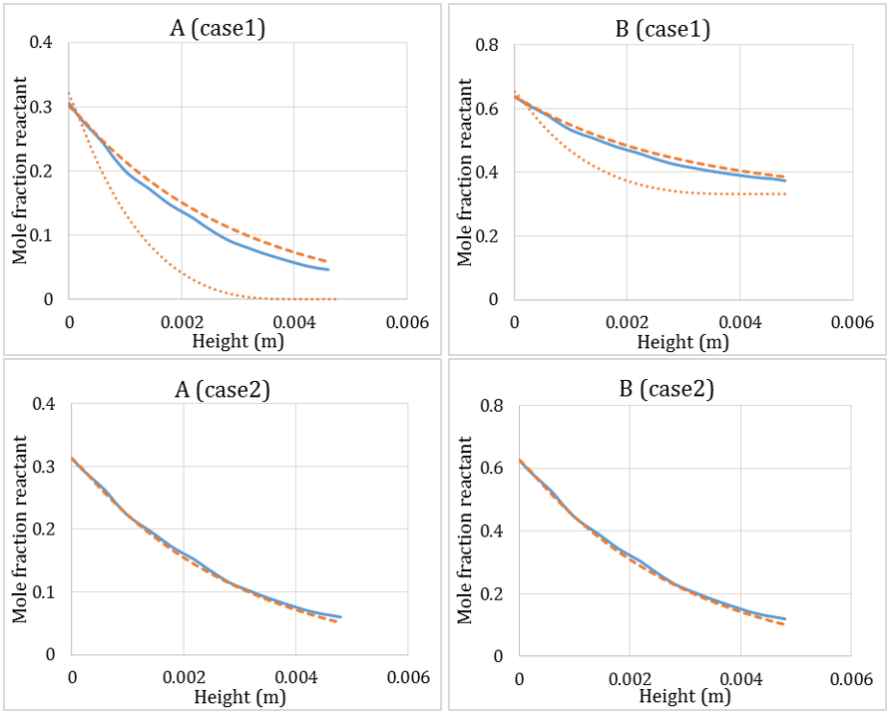

Figure 5.6. Comparison of the mole fraction of reactant concentration (of species A and species B) for the simulated two cases [Top] case 1, and [Bottom] case 2 from (i) PR-DNS (represented by solid lines) (ii) 1D model corrected (dashed lines) ; along the height of the reactor geometry. Dotted line in Case 1 represents the predictions without adjusting the effectiveness factor as: $\boldsymbol{\eta = \left(\eta_A^{-1} + \eta_B^{-1}\right)^{-1}}$.

As such, a simple blended model is proposed for this case, respecting the limits that 1) when $r_B \ll r_A$ in Eq. (58) the concentration of species B will be higher inside the particle

than outside and can be approximated as c_B/η_A, and 2) when $r_B \gg r_A$ the B ➔ C reaction will experience full mass transfer limitation (all reactant must come from outside the particle). Hence, the concentration of species B is divided into two parts (Eq. (59)): a part that is released inside the particle ($c_{B,in}$) experiencing no mass transfer resistance, and a part that resides outside the particle ($c_{B,out}$) experiencing the full mass transfer resistance. The reaction rate r_B in Eq. (58) is thus split into two reactions using the concentrations $c_{B,in}$ and $c_{B,out}$ where the former is simulated with no mass transfer limitations and the latter with complete mass transfer limitations. As shown in Figure 5.7, this blended model returns a reasonable prediction if $C = 5$ in Eq. (59).

$$c_{B,in} = \frac{c_B}{\eta_A + C\dfrac{r_B}{r_A}}$$
$$c_{B,out} = \max(c_B - c_{B,in}, 0) \tag{59}$$

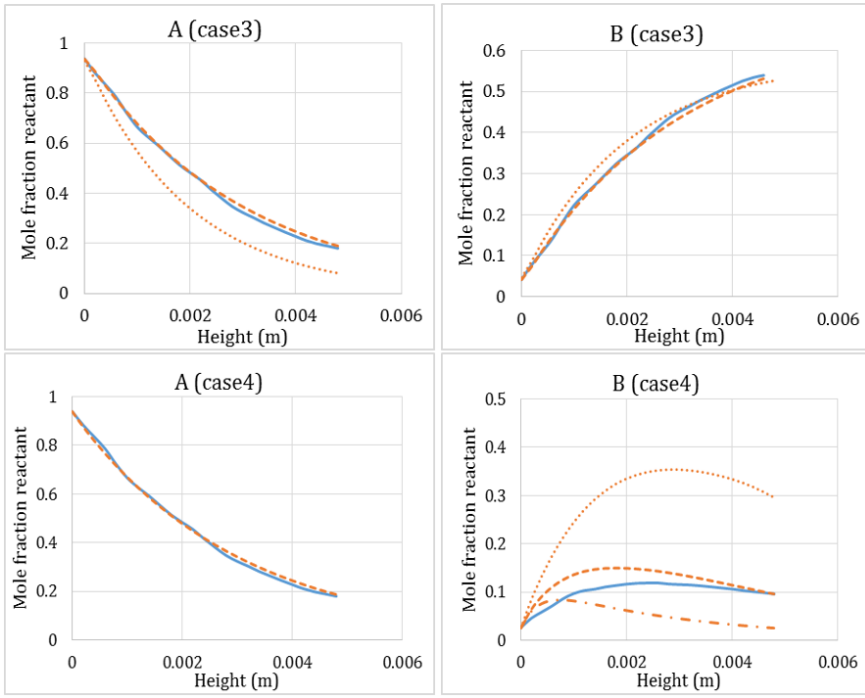

Figure 5.7. Comparison of the mole fraction of reactant concentration (of species A and species B) for the simulated two cases [Top] case 3, and [Bottom] Case 4 from (i) PR-DNS (represented by solid lines) (ii) 1D model corrected (dashed lines); (dotted line) in Case 4 represents the prediction including a full mass transfer model for reactant B, while

(interval line) represents a prediction without a mass transfer model; while in Case 3 (dotted lines) represents the prediction with incorrect Thiele modulus.

5.3.3 Reactions with gas volume generation/consumption

Catalytic reactions that generate or consume gas volume without adding or removing mass create a gas density gradient in the particle. This gradient affects the flux at which gaseous reactants can diffuse into the particle$\left(D_e \rho_g \nabla x_i\right)$. For gas generation, the gas density decreases towards the center of the particle, reducing the diffusive flux of reactant into the particle. As a result, the effective diffusivity used in the Thiele modulus calculation must be reduced in order to accurately model the resulting mass transfer resistance. Through the same mechanism, reactions that consume gas volume will enhance mass transfer into the particle and the effective diffusivity should be corrected in a similar manner.

Simulations are carried out under similar conditions to previous Section 5.3.1 for a first order reaction with inlet reactant mass fraction now ($x_A = 1$), to emphasize the effect of gas consumption or generation. To facilitate gas volume generation or consumption, the reaction stoichiometry as well as the gas species density and molecular weight are changed as outlined in Table 17. Five reactions are simulated: gas volume generation [(i) (b); (iii) (b)], gas volume consumption [(i) (a); (iii) (a)] and a base case (ii). Table 17 shows that the cases are set up to change the gas volume by a factor of 5 or 2 upon reaction.

As expected Figure 5.8 (right), shows significantly lower overall reactant conversion for gas volume generation than for gas volume consumption (Figure 5.8 (left)). This is quantified in Figure 5.9.

Table 17: Different catalytic reactions with their gas specie properties and length scale

Reactions	**Molecular weight (kg/kmol)**		**Density (kg/m3)**	
Analogous cases	***A***	***B***	***A***	***B***
(i) (a) A + (solid) → 0.2B + (solid)	10	50	1	5
(b) A + (solid) → 5B + (solid)	10	2	1	0.2
(ii) A + (solid) → B + (solid)	10	10	1	1
(iii) (a) A + (solid) → 0.5B + (solid)	10	20	1	2

(b) A + (solid) → 2B + (solid)	10	5	1	0.5

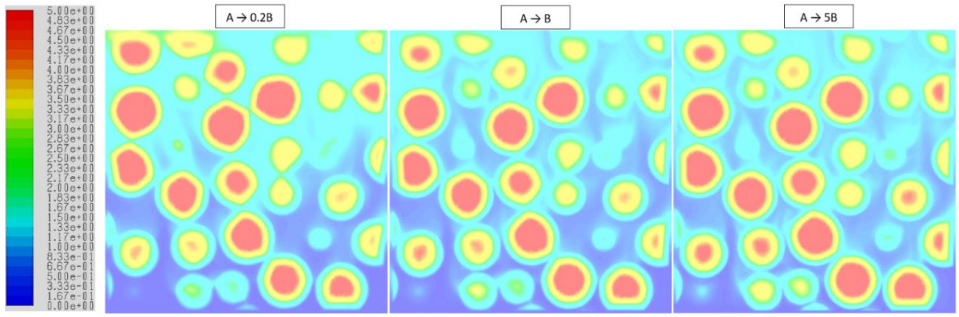

Figure 5.8. PR-DNS predictions of the reactant concentration (species A) for different reactions (Table 17) (at plane y = 0; ε = 0.352, ϕ = 10, Pr = 1) through a bed of porous spherical particles. [Note: The contours shown above are expressed on a scale ($-\log_{10}(x_A)$); Blue suggests high, while Red means minimum].

It was found that this effect could be accounted for by simply multiplying the effective diffusivity (Eq. (40)) by the ratio between the densities of the products and the reactants. If the products are lighter than the reactants (e.g., Cases (i) (b) and (iii) (b) in Table 17), this ratio will be smaller than 1, leading to a lower effective diffusivity, a higher Thiele modulus and a larger mass transfer resistance. Reactions where the products are heavier than the reactants will experience the opposite effect. Thus, the effective diffusivity is redefined as follows:

$$D_e = \frac{D\varepsilon}{t}\frac{\rho_{products}}{\rho_{reactants}} \tag{60}$$

As illustrated in Figure 5.9, this simple adjustment to the intra-particle mass transfer model successfully captures the effect of gas volume generation/consumption over all the cases considered.

5.3.4 Combined heat and mass transfer resistance

In the previous sections, only the effect of mass transfer was considered. Therefore, in this section, the combined effect of heat and mass transfer limitations is presented. The first order reaction (Section 5.3.1) is simulated for the case at Thiele modulus (ϕ = 10) and Prandtl number (Pr = 1) with properties given in Table 15. The effect of reaction enthalpies or heat of reaction on specie conversion is detailed using two different

endothermic (with dH_{rxn} = 10 and 100 kJ/mol), one exothermic reaction (dH_{rxn} = -10 kJ/mol) and an isothermal case with (dH_{rxn} = 0 kJ/mol).

The case with Pr = 1 and ϕ = 10 involves large external heat and mass transfer limitations. Figure 5.10 showcases the ability of 1D model to predict similar results for reactant conversions with PR-DNS for these combined heat and mass transfer limited cases without any additional modifications to the model.

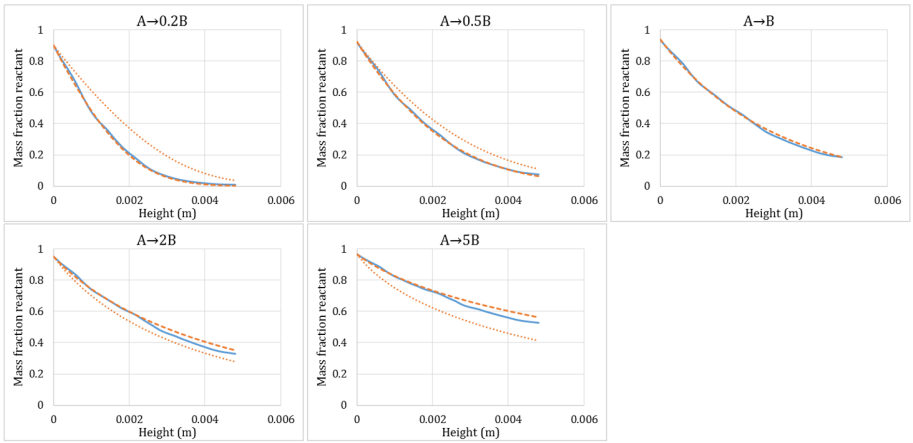

Figure 5.9. Comparison of mass fraction of the reactant (species A) along the height of the reactor between PR-DNS (solid lines), modified 1D model (dashed lines) and 1D model (dotted lines) for different reaction cases in Table 17. The dotted lines represent the 1D model predictions without accounting for gas volume generation. The inlet specie concentration in case of 1D model has been adjusted to account for faster specie conversion at the inlet in PR-DNS results.

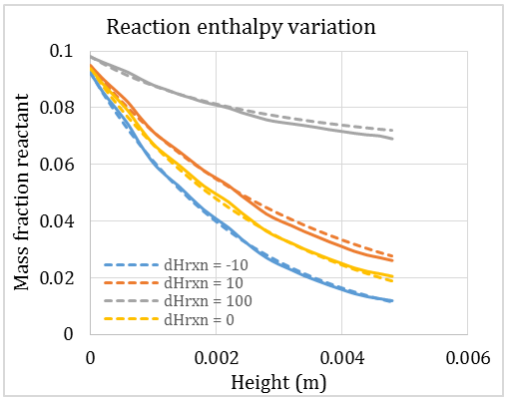

Figure 5.10. Comparison of axial species profiles between PR-DNS (solid lines) and 1D simulations (dashed lines) for a packed bed of spherical particles at (ε = 0.355, Pr = 1, and ϕ = 10) for different heat of reactions (dH_{rxn} in kJ/mol).

5.3.5 Steam methane reforming reactions

After verifying the 1D model on hypothetical conditions for (i) different reaction orders (Section 5.3.1), (ii) multiple reacting species (Section 5.3.2) and (iii) gas volume influence (Section 5.3.3), a realistic test case can be explored. Steam methane reforming (SMR) reactions are considered in this section to detail the performance of 1D models in a realistic packed bed process when compared with PR-DNS. The reaction rate expressions used in this case are outlined in detail in the appendix.

PR-DNS results for the steam methane reforming process can be seen in Figure 5.11. The gradients in the CH_4 conversion (Figure 5.11 (top-left)) suggest the mass transfer limitations encountered by the reactant to diffuse inside the particle, while the constant concentration of H_2 (Figure 5.11 (top-right)) inside the particles suggest limited resistance to product diffusion out of the particle (H_2 has a high molecular diffusivity relative to other gases). Figure 5.11 (bottom) shows significant external heat transfer limitations.

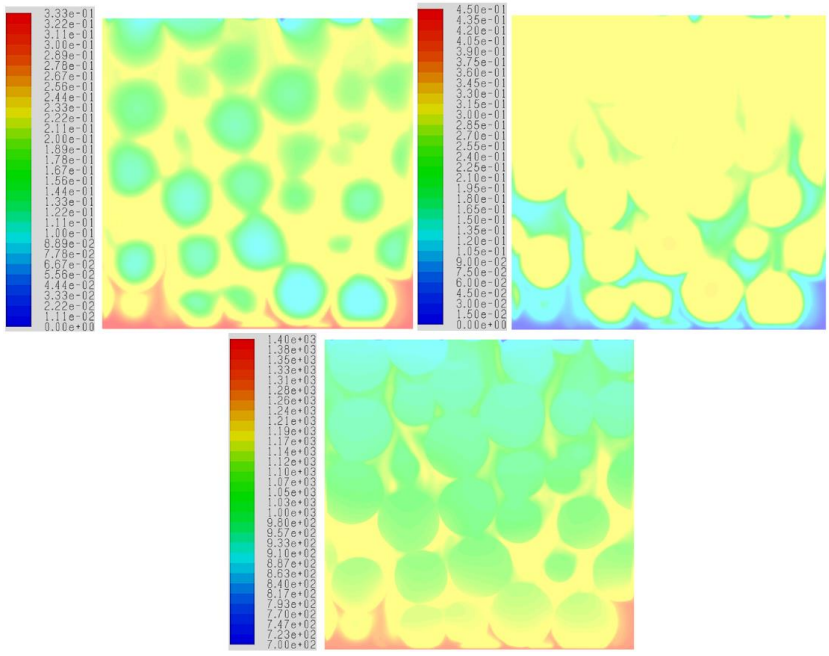

Figure 5.11. PR-DNS predictions of mole fraction of CH4 concentration (Top left], H2 concentration [Top right] and fluid temperature (in K) [Bottom] at (plane y = 0; ε = 0.352) for inlet temperature 1100 ◦C, through a packed bed of porous spherical particles for steam methane reforming process.

To gain further insight into the intra-particle mass transfer phenomena in this steam methane reforming reaction system, radial profiles were extracted from a particle close to the inlet. Figure 5.12 shows the two most important insights from the radial particle profile. Firstly, it can be seen that, even though the SMR reaction system generates gas volume, the density inside the particle is essentially constant. This is primarily the result of the high diffusivity of H_2 relative to the other gases in the system (~3x higher). In practice, this means that the adjustment for gas volume generation (Eq. (60)) is not required.

Secondly, Figure 5.12 reveals a new challenge introduced by this equilibrium reaction system: no clear reaction order exists. The intra-particle mass transfer modelling discussed in this paper is based on the analytical solution of a simple first order reaction and relies on the assumption that the reaction rate constant used in the calculation of the Thiele modulus (Eq. (38)) remains constant in an isothermal particle. However, it is clear from Figure 5.12 that the approximate reaction rate constant defined according to Eq. (69) is not constant inside the particle. This is primarily due to the sharp increase in the reaction rate of the overall steam methane reforming reaction at low H_2 concentrations (due to $p_{H_2}^{3.5}$ in the denominator of Eq. (67)) and could be corrected by adjusting the effective diffusivity (Eq. (40)) as follows:

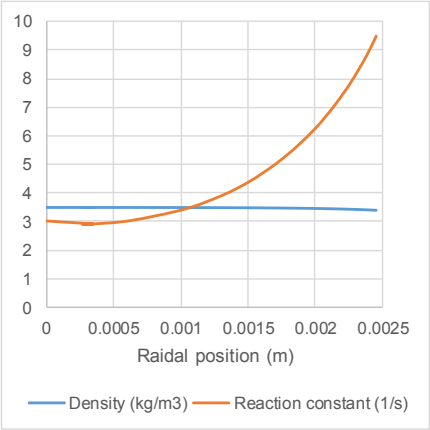

Figure 5.12. Radial profiles of gas density and the approximate reaction rate constant (Eq. (69))) in a particle close to the inlet of the simulated geometry.

$$D_e = \frac{D\varepsilon}{\tau} min\left(y_{H_2}/0.2\,,1\right) \tag{61}$$

Following these insights, the 1D model was run in comparison to the PR-DNS results for five different cases:

1. Inclusion of all available model adjustments including multiple reactants (Eq. (54)), reactions consuming the same reactant (Eq. (57)), reactions consuming the products of other reactions (Eq. (58)), and the effect of a varying reaction rate constant (Eq. (61)).
2. Deactivation of the adjustment for the varying reaction rate constant relative to Case 1.
3. Deactivation of the adjustment for reactions consuming the products of other reactions relative to Case 2.
4. Deactivation of the adjustment for reactions consuming the same reactant relative to Case 3.
5. Deactivation of the adjustment for multiple reactants relative to Case 4.

Figure 5.13 shows that only the adjustment for multiple reactants (difference between Cases 4 and 5) had a large impact on the 1D model performance. Cases 1-4 that included this effect all compare well to PR-DNS results. Close inspection also shows that the adjustment for the varying reaction rate constant (difference between Cases 1 and 2) had a minor effect close to the inlet where the overall steam methane reforming reaction is very fast. The interacting effects between the different reactions were insignificant because the overall steam methane reforming reaction (Eq. (64)) was much faster than the other two reactions in this case.

5.4 Conclusion

This work presented a verification study of computationally efficient 1D packed bed models against data from computationally expensive, but highly accurate particle resolved direct numerical simulations (PR-DNS). The ability of the 1D model to account for several complexities such as different reaction orders, multiple reactions and reactants, interacting reactions and gas volume generation/consumption from reactions was evaluated.

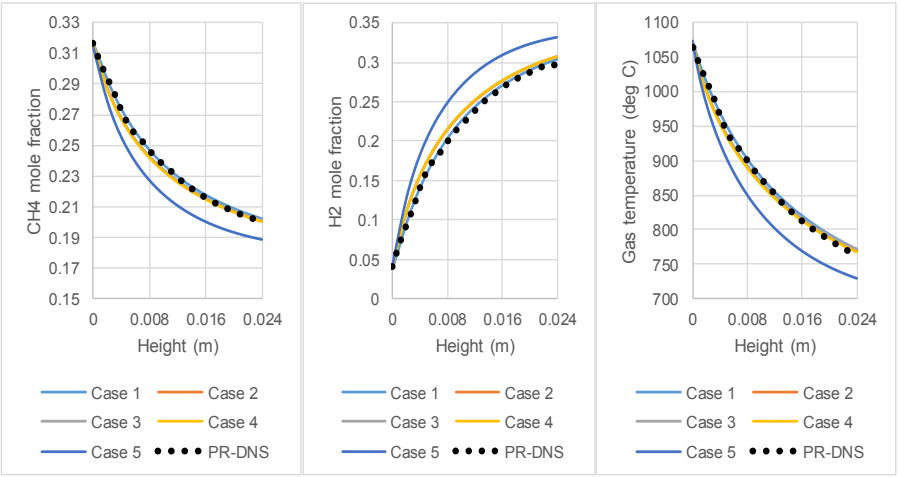

Figure 5.13. Comparisons of different 1D model setups against PR-DNS results.

Results showed that 1D modelling with conventional mass and heat transfer closures can accurately reproduce different reaction orders and multiple non-interacting reactions. However, model adjustments are required for reactions with multiple reactants, interacting reactions and reactions involving gas generation/consumption in the particle. Based on these results, enhancements were proposed, leading to substantial improvements in the 1D model performance.

The resulting enhanced model was then used to simulate a steam methane reforming reaction system. Comparisons between PR-DNS and 1D modelling showed that only the adjustment for multiple reactants was important in this particular case. Following this enhancement, the highly computationally efficient 1D model could accurately reproduce results from computationally expensive PR-DNS.

5.5 Appendix

The steam methane reforming (SMR) reactions Eq. (62)-(64) are modelled with reaction inside the particle as summarized in Table 18.

$$CH_4 + H_2O \leftrightarrow CO + 3H_2 \quad Rx1 \tag{62}$$

$$CO + H_2O \leftrightarrow CO_2 + H_2 \quad Rx2 \tag{63}$$

$$CH_4 + 2H_2O \leftrightarrow CO_2 + 4H_2 \quad Rx3 \tag{64}$$

The reactions are modelled according to the kinetic model (Eq. (65)-(67)) of Langmuir-Hinshelwood (Oliveira et al., 2010; Xu and Froment, 1989) with the appropriate kinetic and equilibrium constants (k_j and K_j) adapted from (Francisco Morgado et al., 2016; Ortiz et al., 2012; Zhou et al., 2013b) as outlined in Table 19.

$$r_1 = \frac{k_1}{p_{H_2}^{2.5}}\left(p_{CH_4}p_{H_2O} - \frac{p_{H_2}^3 p_{CO}}{K_1}\right)/(DEN)^2 \quad (65)$$

$$r_2 = \frac{k_2}{p_{H_2}}\left(p_{CO}p_{H_2O} - \frac{p_{H_2}^4 p_{CO_2}}{K_2}\right)/(DEN)^2 \quad (66)$$

$$r_3 = \frac{k_3}{p_{H_2}^{3.5}}\left(p_{CH_4}p_{H_2O}^2 - \frac{p_{H_2}^4 p_{CO_2}}{K_3}\right)/(DEN)^2 \quad (67)$$

$$DEN = 1 + K_{CO}p_{CO} + K_{H_2}p_{H_2} + K_{CH_4}p_{CH_4} + K_{H_2O}p_{H_2O}/p_{H_2} \quad (68)$$

Table 18: Simulation parameters (PR-DNS) for steam methane reforming

Parameters	Value
Particle diameter (d_p) (m)	0.005
Packed bed voidage (ε)	0.352
Particle volume fraction (α_p)	0.007
Density (solid) (kg/m^3)	2500
Fluid velocity (m/s)	0.5
Inlet mole fraction ratio (CH_4:H_20)	1:2
Specific heat capacity (C_p) (solid) (J/kg/k)	1200
Inlet temperature (°C)	1100
Operating pressure (bar)	20

The adsorption coefficients (K_{CO}, K_{H_2}, K_{CH_4}, *and* K_{H_2O}) of the gases are defined in in Table 20 (Oliveira et al., 2010). The particle thermal conductivity is kept to a high value (500 W/m.K; due to high assumed porosity of the particle), such that there are no considerable gradients for temperature inside the particles. The thermal conductivity and molecular diffusivity are calculated according to the kinetic theory of gases.

Table 19: Kinetic and equilibrium parameters for reforming reactions

	Kinetic parameters		Equilibrium parameters	
Reactions	$k_{0,j}$	E_a	$K_{0,j}$	E_a

Steam methane reforming (Rx1)	5.83×10^{11}	218.55×10^{3}	1.2×10^{13}	223.08×10^{3}
Water gas shift (Rx2)	2.51×10^{4}	73.523×10^{3}	1.77×10^{-2}	-36.58×10^{3}
Overall steam methane reforming (Rx3)	4.67×10^{13}	236.85×10^{3}	2.124×10^{11}	186×10^{3}

Table 20: Adsorption parameters for reforming reactions

	Adsorption parameters	
Specie	$k_{0,i}$	E_a
CH_4	6.66×10^{-4}	-38.28×10^{3}
CO	8.25×10^{-5}	-70.65×10^{3}
H_2	6.15×10^{-9}	-82.90×10^{3}
H_2O	1.77×10^{5}	$88.68\ 10^{3}$

In order to determine the Thiele modulus for the SMR reactions, the reaction order must be identified. All the reactants are approximately first order, except for the H_2O in Eq. (64), which is approximately second order according to Eq. (67). In addition, it was assumed that the reactions are controlled by reactant diffusion into the particle, and not by product diffusion out of the particle. This is a reasonable assumption given that the diffusivities of the species are similar, except for the product H_2, which has a much higher diffusivity than the other species.

Hence, the Thiele moduli for the different reactants were calculated as in the following example for the overall SMR reaction (Eqs. (64) and (67)):

$$\phi_{CH_4} = \sqrt{\frac{ka^2}{D_{CH_4}}}, k = \frac{r_3}{c_{CH_4}} \tag{69}$$

$$\phi_{H_2O} = \sqrt{\frac{3}{2}\frac{kc_{H_2O}a^2}{D_{H_2O}}}, k = \frac{2r_3}{c_{H_2O}^2} \tag{70}$$

Author Contributions: *Arpit, and Schalk conceived the idea. Arpit designed, and performed the simulations; Rosa Quinta-Ferreira and Shahriar Amini supervised the work; Arpit Singhal wrote the paper.*

Arpit Singhal (Sign)

6 MULTISCALE MODELLING OF A PACKED BED REACTOR

Abstract

Packed bed reactors are broadly used in industry and are under consideration for novel reactor concepts such as packed bed chemical looping reforming (PBCLR). Mass and heat transfer limitations in and around the particles in packed bed reactors strongly affect the behaviour of these units. This study employs a multiscale modelling methodology to simulate a PBCLR reactor. Specifically, small-scale particle-resolved direct numerical simulation is utilized to improve large-scale mass transfer models for use in an industrial scale 1D model. Existing intra-particle mass transfer models perform well for simple first order reactions, but several model enhancements were required to model the more complex steam methane reforming reaction system. Three specific aspects required enhanced modelling: the generation of additional gas volume by the reforming reactions, the lack of clear reaction orders in the equilibrium reactions, and the diffusion of multiple reactant species into the particle. Large-scale simulations of the PBCLR reactor with the enhanced 1D model showed that the highly reactive Ni-based catalyst / oxygen carrier employed allows for the use of large particle sizes and high gas flowrates, offering potential for process intensification. [i]

[i] This chapter is based on

Arpit Singhal, S. Cloete, R.Q. Ferreira, S. Amini, Multiscale modelling of a packed bed chemical looping reforming (PBCLR) reactor, *Energies,* Vol 10 (12), 2056.

Arpit Singhal, S. Cloete, R.Q. Ferreira, S. Amini, Multiscale modelling of a packed bed chemical looping reforming, *Energy procedia,* Vol 136, pp. 349-355

Nomenclature

Greek Symbols

α	Volume fraction
ε	Void fraction
φ	Thiele modulus (Th)
η	Effectiveness factor
ρ	Density (kg/m^3)

Latin Symbols

a	Characteristic length of spherical particle (r_p/3)
C_p	Specific heat capacity of gas [J/kg·K]
E_a	Activation energy [J/mol]
h_e	effective heat transfer coefficient [W/m^2·K]
k_0	Arrhenius constant [1/s]
k_g	Thermal conductivity of gas [W/m·K]
Nu	Nusselt number ($h\ d_p/k_g$)
P	Pressure [Pa], 1 bar = 101,325 Pa
Pr	Prandtl number ($\mu\ C_p/k_g$)
R	Gas constant [8.314 J/mol/K]
r	Radius [m]
Re	Reynolds number ($\rho\ u_s\ d_p/\mu$)
Sc	Schmidt number ($\mu/\rho\ D$)
T	Temperature [K]
u_s	Superficial velocity of the gas [m/s]
x_i	Mass fraction of species *i*
y_i	Mole fraction of species *i*

Sub/superscripts

g	Gas
p	Particle

6.1 Introduction

Packed beds are broadly deployed in the chemical and process industry, with a wide variety of uses in adsorption, heat exchangers, chemical reforming, etc. Gas-solid reaction systems in packed beds can be classified under heterogeneous catalytic and/or non-catalytic reactions. Packed beds generally use relatively large particles to minimize

pressure drop over the reactor. These large particles result in significant mass and heat transfer limitations affecting the reactor performance. Significant research efforts have been invested over several decades to correctly model these limitations in catalytic and non-catalytic reactions, the latter being more complex as the solid is altered in the reactions (Ramachandran and Doraiswamy, 1982).

With the development in the field of computational resources, it is now possible to obtain resolved 3D CFD simulations of flow around arrays of packed particles to directly simulate these mass and heat transfer limitations. Particle resolved direct numerical simulations (PR-DNS) provides insight into the local phenomena of velocities and void fractions in packed beds, which cannot be obtained from experiments. There have been several studies on intra particle diffusion, but most of these studies used the particles as the porous regions (Augier et al., 2010; Dixon et al., 2003; Karthik and Buwa, 2017; Magnico, 2009; Nijemeisland et al., 2004). A detailed review of several studies on intra particle diffusion is given by (Dixon, 2017) in a recent work with 3D CFD simulations for heterogeneous catalytic reactions in a tube packed bed ($3 \leq N \leq 10$). (Dixon, 2017) included reactions inside the catalytic particle for the endothermic steam methane reforming (SMR) reaction.

The objective of the current work is to utilize multiscale modelling to improve the accuracy of 1D models for a packed bed process running SMR reactions. Firstly, PR-DNS is used on a geometry of ~100 densely packed mono-disperse spherical particles ($\varepsilon = 0.355$) extracted according to the methodology outlined in our previous works (Singhal et al., 2017d, e, f). Secondly, the PR-DNS results are used to improve a computationally affordable 1D packed bed model (Cloete et al., 2016; Singhal et al., 2017a, c; Singhal et al., 2017d) which is based on appropriate models for effectiveness factor (Levenspiel, 1999) and external heat and mass transfer (Singhal et al., 2017f). This method does not resolve any gradients inside the particles as is done in the models utilizing the colocation method (Dixon, 2017; Yang et al., 2016). As a result, the model is very fast so that it can be conveniently used for large-scale transient simulations of processes such as the packed bed chemical looping reforming (PBCLR) reactor investigated in this work.

In essence, the PBCLR concept is an SMR reactor where the catalyst also acts as an oxygen carrier used in a typical chemical looping combustion reactor. The oxygen carrier

material can be reduced by fuel and subsequently oxidized by air to facilitate fuel combustion without any direct contact between N_2 and CO_2. In this way, the PBCLR process supplies heat to the endothermic SMR reactions by combusting fuel with integrated CO_2 capture. Given that the heat is directly stored in the catalyst / oxygen carrier particles, the process also achieves perfect heat transfer from fuel combustion to the SMR reactions.

The process configuration incorporating the PBCLR reactors will be similar to the gas switching reforming (GSR) reactor concept previously investigated by the authors (Francisco Morgado et al., 2016; Wassie et al., 2017), with the main difference being the use of packed beds instead of fluidized beds. As in the GSR concept, a cluster of several dynamically operated PBCLR reactors will be required to create a steady state process unit. The efficient GSR process configuration for pure hydrogen production can also utilize PBCLR reactors. Specifically, process efficiency is maximized by feeding the off-gas fuel from the pressure swing adsorption (PSA) unit back to the fuel stage of the PBCLR reactors, thus ensuring complete fuel conversion and CO_2 capture with no direct energy penalty.

6.2 Methodology

6.2.1 PR-DNS setup

The realistically packed bed geometry of monodisperse spherical particles ($\varepsilon = 0.355$) is generated using the discrete element method (DEM) in ANSYS FLUENT as explained in detail in our previous works (Singhal et al., 2017e, f). The geometry is meshed with polyhedral elements using FLUENT Meshing both inside and outside the particles with a cell size of $d_p/30$ on the particle surfaces. A growth rate of 20% is used to propagate the mesh into the domain. More detail can be obtained from previous work of the authors (Singhal et al., 2017a, c; Singhal et al., 2017d, e, f).

The SMR reaction takes place inside the porous particles (grain model (Szekely, 1976)) according to Eq. (71)-(73). The simulation parameters used are given in Table 21. The reactions were modelled using the kinetic model of Langmuir-Hinshelwood proposed by Xu and Froment (Xu and Froment, 1989) with appropriate kinetic and equilibrium constants from (Oliveira et al., 2010). Simulations are completed for three different values

for inlet temperature (Table 21). The molecular diffusivity and gas thermal conductivity are obtained according to the kinetic theory of gases.

$$CH_4 + H_2O \leftrightarrow CO + 3H_2 \quad \text{R x 1} \tag{71}$$

$$CO + H_2O \leftrightarrow CO_2 + H_2 \quad \text{R x 2} \tag{72}$$

$$CH_4 + 2H_2O \leftrightarrow CO_2 + 4H_2 \quad \text{R x 3} \tag{73}$$

Table 21. Simulation parameters for PR-DNS

Parameter	Value	Parameter	Value
Particle diameter (d_p) (m)	0.005	Inlet mole fraction ratio (CH_4:H_20)	1:2
Packed bed voidage	0.355	Specific heat capacity (C_p) (solid) (J/kg/k)	1200
Particle void fraction (internal)	0.3	Thermal conductivity (solid) (W/m.K)	1.0
Density (solid) (kg/m^3)	2500	Operating pressure (bar)	20
Gas velocity (m/s)	0.5	Inlet temperature (°C)	1100,1000,900

6.2.2 1D packed bed model

The 1D model setup used is developed considering 100 cells in one direction with solid phase velocity fixed to zero in all these cells. The model is consistent with the previous work of the authors (Cloete et al., 2016; Singhal et al., 2017a; Singhal et al., 2017d). The closures (Levenspiel, 1999; Singhal et al., 2017f) represented in Eqns. (74)-(77) are used in conjunction with the same reaction kinetics and boundary conditions as the PR-DNS simulation. The Thiele modulus (ϕ) represents the ratio of kinetic rate to diffusion rate, so higher values represent greater mass transfer limitation. The effective diffusivity (D_e) is composed of the molecular diffusivity (D), the internal void fraction of porous particles ($\varepsilon = 0.3$) and the tortuosity ($\tau = 1$). In realistic cases, tortuosity will be greater than 1, but, since tortuosity cannot be directly resolved in PR-DNS, it was omitted by setting $\tau = 1$. A more realistic tortuosity of $\tau = 3$ was used in the large scale simulations of the PBCLR reactor presented at the end of the paper.

$$Nu = 2.67 + 0.53Re^{0.77}Pr^{0.53} \tag{74}$$

$$\phi = a\sqrt{\frac{n+1}{2}\frac{kc^{n-1}}{D_e}} \tag{75}$$

$$\eta = \frac{1}{\phi}\left(\frac{1}{\tanh(3\phi)} - \frac{1}{3\phi}\right) \tag{76}$$

$$D_e = \frac{D\varepsilon}{\tau} \tag{77}$$

In comparison to the previous work (Singhal et al., 2017a; Singhal et al., 2017d), four important complications are introduced: multiple reactions, multiple reactants per reaction, the generation of gas volume during the reaction, and reactions without a clear reaction order. However, the effect of multiple reactions is not so important because the overall steam methane reforming (OSMR) (Rx3) reaction is much faster than the others. Comparisons between the PR-DNS and 1D modelling showed that the remaining three effects required adjustments to the 1D model to yield accurate results. In this way, results from the PR-DNS scale were used to propose model improvements to increase the accuracy of large scale 1D simulations. The resulting enhanced 1D model was then used to simulate a large scale packed bed chemical looping reforming (PBCLR) reactor.

The complexity of the catalytic SMR reactions involving gas volume generation and reactions without a clear reaction order posed the most important challenge. The standard intra-particle mass transfer model (Eq. (76)), was derived for a simple first order reaction without any gas volume generation, and significant adjustments were necessary to achieve accurate results in the more complex SMR reaction system. The reaction rate expression for the OSMR reaction, which is about an order of magnitude faster than the others, is given below as an example (Xu and Froment, 1989).

$$r_{OSMR} = \frac{k_{OSMR}}{p_{H_2}^{3.5}}\left(p_{CH_4}p_{H_2O}^2 - \frac{p_{H_2}^4 p_{CO_2}}{K_{OSMR}}\right)/(DEN)^2 \tag{78}$$

$$DEN = 1 + K_{CO}p_{CO} + K_{H_2}p_{H_2} + K_{CH_4}p_{CH_4} + K_{H_2O}p_{H_2O}/p_{H_2} \tag{79}$$

The OSMR reaction can be viewed as approximately first order with respect to CH_4 and second order with respect to H_2O. With this in mind, Thiele moduli (i.e. Eq. (75)) can be

calculated from approximate reaction rate constants defined by dividing the reaction rate by the appropriate reactant species concentrations:

$$\phi_{CH_4} = a\sqrt{\frac{k}{D_{e,CH_4}}}, k = \frac{r_{OSMR}}{c_{CH_4}} \tag{80}$$

$$\phi_{H_2O} = a\sqrt{\frac{3}{2}\frac{kc_{H_2O}}{D_{e,H_2O}}}, k = \frac{2r_{OSMR}}{c_{H_2O}^2} \tag{81}$$

The challenge posed by this practice is that the reaction rate constants, k, defined in this manner vary with the species concentration, especially when the hydrogen partial pressure (p_{H_2} in Eq. (78)), is low (due to $p_{H_2}^{3.5}$ in the denominator). As a result, this approximation of the reaction rate constant will generally decrease towards the centre of the particle as more H_2 is formed by CH_4 and H_2O diffusing into the particle. The mass transfer model (Eq. (76)) assumes a reaction rate constant that actually remains constant with changing reactant concentrations (in an isothermal particle) and will therefore over predict the effective reaction rate in this case.

This reaction rate over prediction is further augmented by the generation of additional gas volume by the SMR (Eq. (71)) and OSMR (Eq. (73)) reactions. Additional volume of lighter gases will create a density gradient inside the particle with lower densities in the particle centre. A gradual decrease in gas density within the particle slows down the diffusive flux $\left(D\rho_g\nabla x_i\right)$ of the incoming reactants. This effect is not accounted for in the standard mass transfer model (Eq. (76)) and will therefore lead to further over predictions of the effective reaction rate.

Comparisons between PR-DNS and 1D model results revealed that these effective reaction rate over predictions can be accurately accounted for by adjusting the effective diffusivity (D_e) for use in the calculation of the Thiele modulus (Eq. (75)). To account for the gas volume generation, dedicated PR-DNS simulations revealed that the effective diffusivity simply needs to be multiplied by the ratio of the gas density of reaction products to reactants. For example, the ratio is 0.5 for the SMR reaction (2 moles of reactants yield 4 moles of products) and 0.6 for the OSMR reaction (3 moles of reactants yield 5 moles of products). This adjustment (Eq. (82)) will lower the effective diffusivity in reactions with gas volume generation, leading to a higher Thiele modulus and a lower effectiveness factor.

$$D_e = \frac{D\varepsilon}{\tau}\frac{\rho_{products}}{\rho_{reactants}} \tag{82}$$

The sensitivity of the approximated reaction rate constant to reactant concentrations at low values of p_{H_2} required a similar adjustment. In this case, it was found that an almost perfect match to PR-DNS data could be achieved if the effective diffusivity in the OSMR reaction is adjusted by the factor $min\left(y_{H_2}/\alpha\,,1\right)$, thus increasing the effective mass transfer resistance at low values of p_{H_2} where the reaction rate constants defined in Eqs. (80) & (81) will decrease rapidly towards the inside of the particle. Thus, the effective diffusivity in the OSMR reaction is defined as follows:

$$D_e = \frac{D\varepsilon}{\tau}\frac{\rho_{products}}{\rho_{reactants}} min\left(\mathrm{y}_{H_2}/0.2\,,1\right) \tag{83}$$

Finally, PR-DNS results revealed that it is important to account for the intra-particle diffusion resistance of multiple reacting species. This could be accomplished by simply treating the effectiveness factors calculated for individual reactants via Eq. (76) as parallel resistances:

$$\frac{1}{\eta} = \frac{1}{\eta_1} + \frac{1}{\eta_2} \tag{84}$$

Experience also showed that the heat transfer rate (described by Eq. (74)) had to be multiplied by a factor ($\beta < 1$) to match well with PR-DNS results. The modification factor (β) becomes necessary because of the multifluid approach followed in the simulations. The multifluid approach is a convenient method for this problem, but it models the solid and fluid phase as interpenetrating continua and can therefore lead to numerical inaccuracies when the volume fraction field changes abruptly (as is the case on the surface of the particles).

Because of this numerical challenge, the external heat transfer rate was significantly under predicted by the PR-DNS simulations using the multifluid approach relative to a PR-DNS simulation where particle surfaces are designated as walls (Singhal et al., 2017e, f). This required the use of the factor, β, when comparing the PR-DNS and 1D simulation results. The generalised correlation for obtaining the modification factor based on the Reynolds number is fitted as shown in Figure 6.1 represented by $\beta = 5.8582 \times 10^{-6} Re^2 -$

$2.8859 \times 10^{-3} Re + 9.5924 \times 10^{-1}$. The equation is valid up to Reynolds number (Re < 200) and for the packed bed with particle void fraction (~0.35), used in this work.

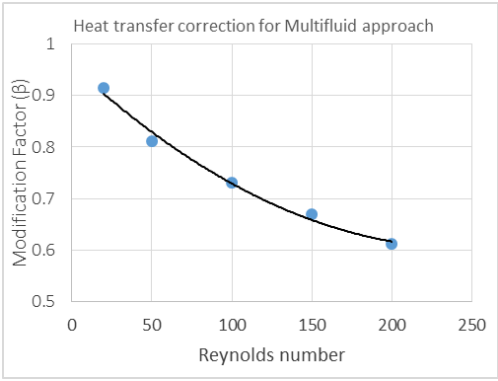

Figure 6.1. Modification factor fitted over a range of Reynolds number for packed bed of spherical particles (with particle void fraction of 0.35).

6.3 Results

6.3.1 PR-DNS results

Contour plots for methane mole fraction and temperature are shown in Figure 6.2. The effects of heat and mass transfer limitations are clearly visible. A gradual species concentration gradient is visible inside the particles (Figure 6.2, left) signifying an internal mass transfer limitation. However, the temperature inside the particles is relatively uniform (Figure 6.2, right), implying that external heat transfer limitations dominate.

6.3.2 Comparison of 1D model to PR-DNS results

Figure 6.3 illustrates the influence of the 1D model adjustments proposed from PR-DNS through this multiscale modelling exercise. Clearly, use of the standard intra-particle mass transfer model (Eqs. (75)-(77)) results in substantial over predictions of the effective reaction rate. This is evident from the dotted lines in Figure 6.3 showing that methane is consumed and hydrogen is produced too rapidly. The temperature also drops too rapidly due to the over prediction of the endothermic reaction rate.

When the effect of gas volume generation Eq. (82) is included and the effectiveness factor is calculated from the parallel mass transfer resistances (Eq. (84)) instead of only the reactant with the highest Thiele modulus, the solution improves markedly. The dashed lines in Figure 6.3 show that these adjustments still show significant deviations in the slopes of the curves at the start of the domain, while the slopes become similar further away from the inlet. This implies that the reaction rate close to the inlet remains too high.

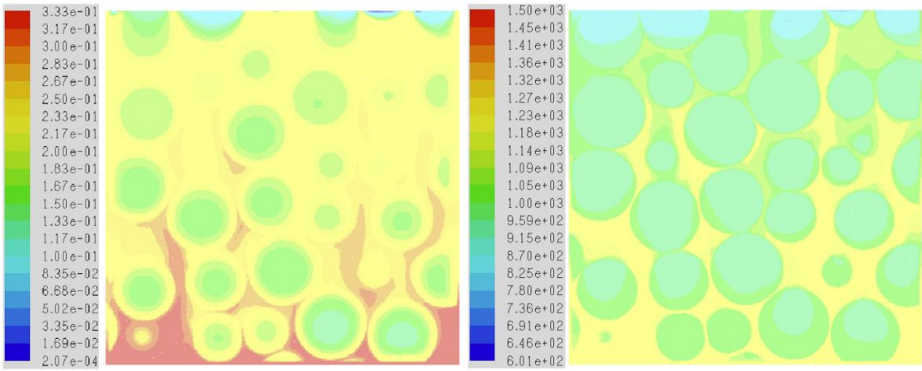

Figure 6.2. PR-DNS results for molar concentration of CH_4 (left) and gas temperature (K) variation at 1000 °C (1273 K) inlet temperature.

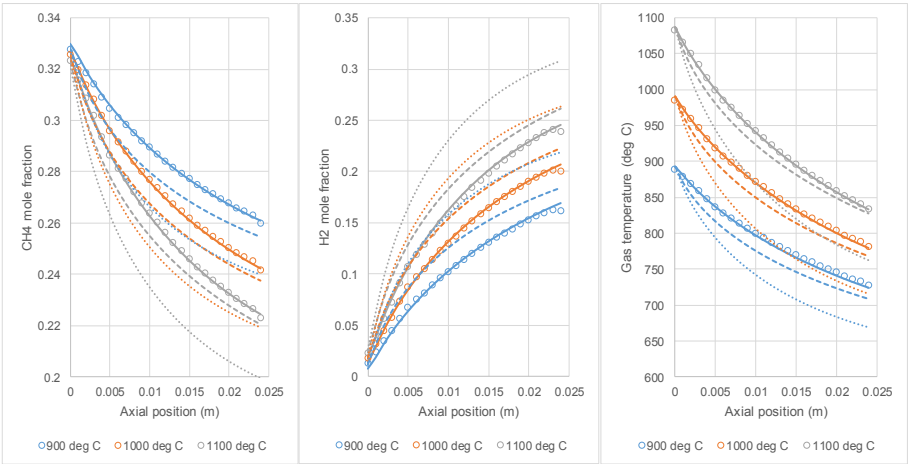

Figure 6.3. Comparisons of different 1D model formulations to PR-DNS data at three different inlet temperatures. In each graph, the circles represent the PR-DNS results, the solid lines represent the full 1D model with all the proposed adjustments, the dashed lines represent the exclusion of the adjustment for the varying reaction rate constant (Eq. (83)), and the dotted lines represent the exclusion of all model adjustments (Eqs. (82)-(84)).

In this region, the hydrogen mole fraction is low, emphasizing the effect of the varying reaction rate constant as defined in Eqs. (80) & (81). The solid lines in Figure 6.3 show that the adjustment to the effective diffusivity proposed in Eq. (83) with the model coefficient α set to 0.2 resulted in an excellent match to the PR-DNS results. These results show that this fully adjusted model is generally accurate over a wide range of temperatures and gas species concentrations. The Thiele moduli (Eq. (75)) and effectiveness factors (Eq. (76)) in the three cases varied over wide ranges ($\phi = 0.5$ to 90 and $\eta = 0.006$ to 1) proving that the model accurately describes a broad range of intra-particle mass transfer resistances in the SMR reaction system.

6.3.3 The packed bed chemical looping reforming process

The mass transfer model from the previous sections (solid lines in Figure 6.3) is employed to simulate the behaviour of an industrial scale packed bed chemical looping reforming (PBCLR) reactor. One important difference from the small scale comparison in the previous section is that the tortuosity was set to a more realistic value of 3 to increase the mass transfer resistance simulated in the PBCLR reactor. As mentioned in the discussion of Figure 6.3, the proposed model enhancements perform well over a wide range of Thiele moduli and effectiveness factors. Good accuracy can therefore also be expected in this case where the Thiele modulus would be moderately increased by a factor of $\sqrt{3}$ by increasing the tortuosity from 1 to 3 in Eq. (77). In addition, the modification to the heat transfer correlation that was required only for comparison to the PR-DNS results (Figure 6.1) is not included in this large scale simulation.

As outlined in the introduction, the PBCLR process consists of three stages: oxidation with air, reduction with residual fuel from the PSA unit, and reforming of methane with steam. The PBCLR process is very similar in nature to the packed bed chemical looping combustion (PBCLC) process (Cloete et al., 2016; Noorman et al., 2007). The primary difference between PBCLR and PBCLC is that the heat from fuel combustion is used for the endothermic reforming reaction (PBCLR) instead of driving a gas turbine for power production (PBCLC).

Heterogeneous reactions occurring in the oxidation and reduction stages are described by the kinetics for Ni40Al-FG oxygen carrier given in Abad et al (Abad et al., 2007). These extremely fast reactions are moderated by the mass transfer limitation model presented in

Yang et al (Yang et al., 2016). Even with this mass transfer limitation, the overall reaction rate of this highly active oxygen carrier remained very high and had to be lowered by an additional order of magnitude to allow for reasonably large time steps in the simulation with 5 mm particles (Figure 6.4 and Figure 6.5). This artificial lowering of the reaction rate did not have a significant influence on the results because the reactions remained fast enough to create almost perfect plug-flow behaviour of the reactor during these two stages. Note that this artificial modification was not required for the final simulation with 20 mm particles (Figure 6.6) due to the larger mass transfer limitation in this case.

Boundary conditions for the reactor simulation are given in Table 22. Gas flow rates were selected to keep the maximum reactor pressure drop below 1 bar (the classic Ergun pressure drop equation (Ergun, 1952) was employed). Other important simulation information is summarized in Table 23. In addition, the effective thermal conductivity model of (Tsotsas and Martin, 1987) was implemented and that the heat capacities of Ni, NiO and Al_2O_3 were implemented as functions of temperature based on data from Robie et al. (Robie and Hemingway, 1995).

Table 22. Boundary conditions employed in the PBCLR simulation.

Stream	Stage time (s)	Inlet velocity (m/s)	Inlet temperature (°C)	Composition (mole fraction)	
Compressed air to oxidation stage	900	0.4	420	O_2	0.21
				N_2	0.79
PSA off-gas fuel to reduction stage	600	0.2	350	H_2	0.150
				CO	0.150
				CH_4	0.175
				H_2O	0.025
				CO_2	0.500
Methane and steam to the reforming stage	900	0.25	200	CH_4	0.333
				H_2O	0.667

Table 23. Miscellaneous simulation parameters used in the PBCLR simulation.

Parameter	Value
Bed length	10 m
Active content (fully reduced)	20% Ni

Oxygen carrier density	2500 kg/m^3
Reactor void fraction	0.4
Particle void fraction	0.3
Particle tortuosity	3
Particle diameter	5 mm
Reactor outlet pressure	18 bar

Transient outlet gas stream composition and temperature from one cycle of oxidation, reduction and reforming stages are shown in Figure 6.4. The first 900 s of the cycle is the oxidation stage where all the oxygen in the incoming air is consumed and only nitrogen exits the reactor. Even though a lot of heat is released from the exothermic oxidation reaction, the outlet gas temperature remains relatively low due to the plug-flow nature of the PBCLR reactor.

The reduction stage takes place during the next 600 s of the cycle. All the incoming fuel gases are converted to CO_2 and H_2O during this stage and the heat generated during the preceding oxidation stage starts to exit the reactor.

Finally, the reforming stage takes place in the final 900 s of the cycle. As shown just after 1500 s in Figure 6.4, the first few seconds of the reforming stage still yields combustion products (CO_2 and H_2O) because the oxygen carrier was not fully reduced at the end of the preceding reduction stage. Full reduction of the oxygen carrier in the reduction stage can lead to some fuel slip that will reduce process efficiency and reduce CO_2 purity. During the remainder of the reforming stage, the oxygen carrier is fully reduced and catalyses the steam methane reforming reactions.

The temperature close to the reactor outlet primarily influences the outlet gas composition during the reforming stage. During the first ~600 s of the reforming stage, the temperature in this region of the reactor is high, leading to almost complete methane conversion and high hydrogen yield. However, the last ~300 s of the reforming stage sees a substantial drop in the temperature close to the reactor outlet, leading to much lower methane conversion. Ideally, the reforming stage would be stopped before this drop in conversion occurs, but the reactor must be cooled down before the next oxidation stage to prevent overheating of the oxygen carrier. Fortunately, the PBCLR process can afford a

substantial amount of fuel slip during reforming because the unconverted methane is returned to the reduction stage of the PBCLR reactor from the PSA unit.

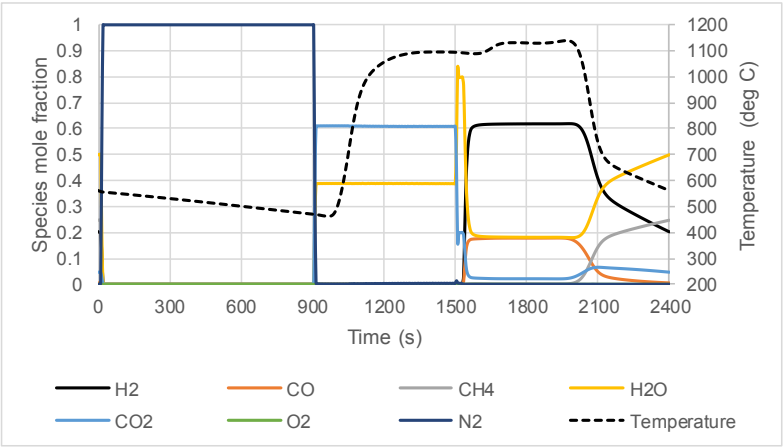

Figure 6.4. Outlet gas species composition and temperature during one PBCLR cycle.

For more insight into the reactor behaviour, Figure 6.5 shows axial reactor profiles at various points in the cycle. As outlined earlier, most of the reactor is hot at the end of the oxidation stage, but the heat generated during the reaction has not yet reached the reactor outlet. At the end of the reduction stage, the axial profiles show that catalytic reactions take place in the part of the reactor that is fully reduced (<8 m) and the resulting reformed fuel gases react rapidly in a narrow reaction front just after 8 m.

During the reforming stage, the gas composition closely tracks the local oxygen carrier temperature. Higher temperatures lead to a higher equilibrium conversion and more heat consumption by the endothermic reforming reactions. As a result, the reactor is cooled down by the reforming reactions in a plug-flow manner. However, Figure 6.5 shows that the temperature gradient developing in the bed during the reforming stage is not very sharp. This causes the large amount of unconverted methane shown at the end of the cycle in Figure 6.4 as the reforming stage must be continued until the end of the reactor is at a low enough temperate to accommodate the large temperature rise in the subsequent oxidation stage.

Another clear feature from Figure 6.5 is that, despite the significant mass transfer limitations implemented, the reforming reactions are generally fast enough to get very

close to the equilibrium conversion at all points in the reactor. This can be observed from the very strong correlation between the hydrogen mole fraction and the temperature. For this reason, the PBCLR reactor can be designed with substantially larger particles, allowing for a larger gas flowrate. To investigate this possibility, the simulation was repeated with gas feed rates double the values given in Table 22 and a particle size that is quadruple the value given in Table 23 (20 mm). This modification allows the pressure drop to stay roughly constant. In addition, the stage times in Table 22 were halved to accommodate the doubling in the gas feed rates.

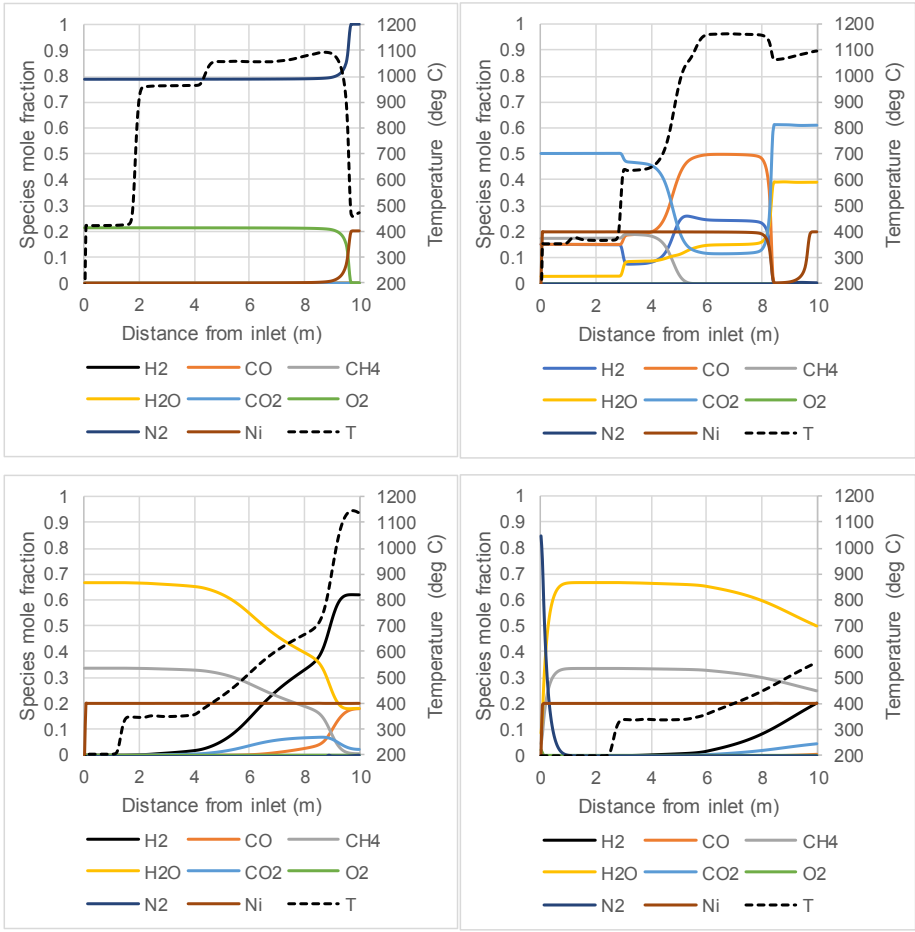

Figure 6.5. Axial profiles of species and temperature in the PBCLR reactor at the end of the oxidation stage [**top left** – 900 s in Figure 6.4], end of the reduction stage [**top right** – 1500 s in Figure 6.4], middle of the reforming stage [**bottom left** – 1950 s in Figure 6.4], and end of the reforming stage [**bottom right** – 2400 s in Figure 6.4].

The resulting outlet gas composition and temperature profiles are plotted in Figure 6.6. In comparison to Figure 6.4, the very fast redox reactions ensure that the oxidation and reduction stages are almost unchanged, aside from a slight increase in the average outlet temperature. This increased temperature is the result of less reaction occurring in the reforming stage to consume heat.

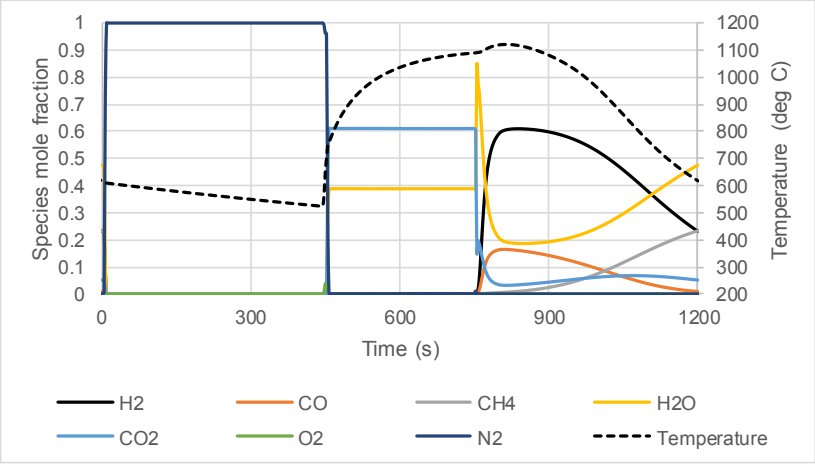

Figure 6.6. Outlet gas species composition and temperature during one PBCLR cycle with 2x higher gas feed over 4x larger particles than Figure 6.4.

The increased mass transfer limitations in the reforming stage are more clearly visible. In general, methane slip starts significantly earlier than was the case in Figure 6.4, and the maximum rate of change in species and temperature outlet profiles is smaller. However, even with such very large particles, the reaction rate remains quite high, allowing for good conversion of the incoming fuel. PBCLR using a highly reactive Ni-based oxygen carrier can therefore benefit from significant process intensification via high gas throughput rates and, possibly, shorter reactors.

Author Contributions: *Arpit, and Schalk conceived the idea. Arpit and Schalk designed, and performed the simulations, Schalk did the PBCLR simulations; Rosa Quinta-Ferreira and Shahriar Amini supervised the work; Arpit and Schalk wrote the paper.*

Arpit Singhal (Sign)

7 MULTISCALE MODELLING FOR NON-RESOLVED 3D SIMULATIONS

Abstract

This work presents a modelling study of gas-particle heat transfer on two distinct scales. Firstly direct numerical simulations (DNS) are conducted in a geometry of spherical particles generated via the discrete element method (DEM). Simulations are completed on random particle arrays ranging from a void fraction of 0.9 to maximum packing over a range of Reynolds number. The geometry is meshed with a fine Cartesian cutcell mesh both inside and outside the particles. These DNS results are then used to provide improved heat transfer closures to an unresolved Lagrangian modelling approach which can be used to simulate much larger particle beds. The unresolved Lagrangian approach also incorporates a 1D heat conduction model to directly simulate heat transfer inside the particles. This model is then verified against DNS data in geometries where wall effects and intra-particle heat transfer, both of which are directly accounted for by the Lagrangian approach, are important. These new heat transfer closures derived are applicable to infinitely large beds. The CFDEM simulations adjust these 1D closures for narrow geometries with a low D/d ratio. Minor differences in results are discussed and the achievable computational speedup by this approach is quantified. [i]

[i] This chapter is based on Arpit Singhal, S. Cloete, S. Radl, S. Amini, Multiscale modelling of heat transfer from arrays of spherical particles, *in proceedings of 9th International conference on Multiphase flows (ICMF) 2016,* Firenze, Italy.

7.1 Introduction

Packed and fluidized bed reactors are broadly deployed in chemical, petrochemical and pharmaceutical industry. The prediction of transport parameters in such reactors is not an easy task and has been a central research topic for many decades.

Recently, DNS (Direct numerical simulation) for a coupled concept of CFD-DEM has emerged as a useful tool to obtain reliable predictions of heat transfer, considering the uncertainties involved in the experimental correlations. There are several correlations in the literature for heat transfer predictions utilising this concept of PR-DNS (particle resolved DNS).

An empirical correlation valid in both packed and fluidized beds over a range of porosity, Reynolds numbers and Prandtl numbers for heat and mass transfer was presented by (Gunn, 1978). The study by (Tavassoli et al., 2015) recently recommended the Gunn correlation (Gunn, 1978) only for dilute systems with porosity ($\varepsilon>0.7$).

DNS is used to improve the accuracy of the model from (Gunn, 1978) for monodisperse particles by increasing the range of porosity and Reynolds numbers (Deen et al., 2012; Deen et al., 2014). The concept of using PR-DNS to obtain a similar observation like (Deen et al., 2014) was introduced by (Sun et al., 2015; Tenneti et al., 2013). These models suggested an empirical correlation for packed beds with better prediction for heat and mass transfer.

Generally, a constant particle surface temperature is considered when modelling arrays of particles for deriving heat transfer correlations. This approach neglects the effects of intra particle temperature gradients which can lead to inhomogeneous particle surface temperatures. The only complete model to consider the conduction in packed beds is introduced by (Oschmann et al., 2016) hence representing the temperature distribution inside particles in a packed bed.

In this work, the goal is to develop correlations for heat transfer based on the non-homogenous temperature distribution via a constant heat source implemented in all particles. These results can then be compared with correlations derived from simulations with a fixed particle temperature. The comparison between the correlations to predict heat

transfer with non-homogenous and homogenous particle surface temperatures is documented.

Then the verification of the correlation with homogenous surface temperatures is obtained by utilizing the correlation to predict the heat transfer in an unresolved Euler-Langrangian model implemented in CFDEM®-Coupling (Goniva et al., 2012; Kloss et al., 2012). To account for the heat transfer inside the particles, inclusion of the 1D model code PARSCALE (S. Radl, 2015) is used. Such an approach paves the way for computationally efficient, yet accurate, predictions of fluid-particles systems characterized by large temperature gradients inside and outside of the particles.

7.2 Methodology

7.2.1 DEM (particle bed generation)

In this work ANSYS FLUENT and Design Modeler are used to generate the packed bed using the DEM (Discrete Element Method) approach according to Table 24. The particles are injected in the reactor geometry without the gravity force with a high degree of overlap. Large repulsive forces are generated because of these overlapping particles, thus initiating random particle motions. After 20 s of random translation and collision of the particles in the DEM simulation, the resulting random packed bed of the particles is obtained. Particle positions are exported to Design Modeler and particles which are very close to each other are cut with a small cylindrical geometry to ensure at least $d_p/25$ m of space between all particles. This results in a geometry which can be meshed with a good quality mesh.

Table 24. DEM simulation setup

Parameters	Law	Value
Number of particles		350
Diameter of the particles (d_P) (m)		0.001
Particle normal force Spring Dashpot for DEM	Spring dashpot	*K* = 1250 *Eta* = 0.9
Particle tangential force parameter for DEM	Friction-dshf	*mu-stick* = 0.5 *mu-glide* = 0.2 *mu-limit* = 0.1
Time step (s)		$5x10^{-05}$

7.2.2 Mesh

The packed bed reactor geometry is meshed with refined cutcell mesh using ANSYS Meshing both inside and outside the particles.

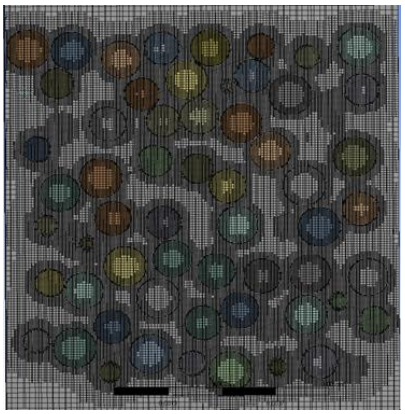

Figure 7.1. The section (y=0) of the reactor geometry with cutcell mesh

Table 25. Mesh sizing details

Parameters	Value
The cell size of surface mesh on the particles (m)	$4e^{-05}$
Maximum face size for the mesh (m)	$2e^{-04}$
Resolution of mesh on particles for DNS	$d_p/25$
Growth rate of mesh	1.2

7.2.3 CFD (DNS)

ANSYS FLUENT is used to perform the DNS in the resulting geometry. The SIMPLE algorithm with 2nd order spatial discretization is used for the DNS simulations. Further details of the simulation are given below.

7.2.3.1 Model equations

The conservation equations of continuity, momentum, and energy for the incompressible, steady state, Newtonian fluid solved for the DNS in this paper are given by

$$\nabla.\vec{u} = 0 \tag{85}$$

$$\nabla.(\rho\vec{u}\vec{u}) = -\nabla p - \mu\nabla^2\vec{u} + \rho\vec{g} \tag{86}$$

$$\rho C_p \nabla.(T\vec{u}) = K_f \nabla^2 T \tag{87}$$

Steady DNS was found to be sufficient as transient fluctuations were not forming in the channels between particles at the Reynolds numbers investigated in this work. Rotational particle motion was not solved as this was not necessary to obtain a randomly dispersed particle array.

7.2.3.2 Boundary conditions

The reactor is contained with a velocity inlet and pressure outlet. While the reactor walls are maintained at a condition of zero heat flux with no-slip condition. The particles contain a constant heat source of $1e^{07}$ W/m^3 integrated in the centre of all the cells inside the particles to obtain the correlation with heat source. In order to obtain the correlation with constant temperature, particles are maintained at a fixed temperature of 573 K.

$$\varphi_{P\to f} = h \times (av.(T_P) - T_{bulk})$$
$$\varphi_{P\to f} = h \times (av.(T_P) - T_{av}) \quad (88)$$

The heat transfer coefficient *(h)* is computed using the Eqn. (88), where (T_P) is the average for all the particle surface temperatures and (T_{bulk}) is the bulk fluid temperature and (T_{av}) is the average fluid temperature. Two different averaging procedures for T_{bulk} and T_{av} are discussed in Section 7.2.4.

7.2.4 Average procedure

The exact procedure for computing the locally-averaged fluid temperature experienced by the particles in the reactor is relevant, since it directly impacts the local heat transfer coefficient. Therefore, the concept of the bulk fluid temperature (T_{bulk}) used by (Deen et al., 2012) can be followed, suggesting that the fluid temperature should be computed in several planes perpendicular to the flow direction. Deen et al.'s approach is based on the so-called cup-mixing temperature, i.e., a flux-weighted temperature. In contrast, (Sun et al., 2015) used the average fluid temperature (T_{av}) to obtain the heat transfer predictions. In this paper both approaches are evaluated, and bulk as well as the average fluid temperatures are calculated. These temperatures are then used to formulate correlations, which are then verified against the unresolved model to obtain the correct averaging procedure.

The averaging procedures are given in Eq. (89) showing the bulk fluid temperature and average temperatures respectively; where T is the static fluid temperature.

$$T_{bulk} = \frac{\int (u.e_z) T \, dV}{\int (u.e_z) \, dV}$$
$$T_{av} = \frac{\int T \, dV}{\int dV} \quad (89)$$

7.2.5 Non resolved Eulerian-Lagrangian simulations

The non-resolved simulations involve the usage of the DEM open source package LIGGGHTS (Kloss et al., 2012) for generation of the packed bed and CFDEM-Coupling (Goniva et al., 2012) for the CFD simulations. The CFD and DEM codes generally perform their calculations separately in parallel and exchange data in accordance with the coupling intervals specified.

In non-resolved Eulerian-Lagrangian simulations the particles are not resolved, which means that particle sizes should be smaller than the computational grid (Figure 7.2), making this simulation much less computationally costly than the resolved simulations. The interaction of the particle phase with the fluid phase in terms of the momentum, energy and mass transfer is considered. This is facilitated by using the appropriate correlations to account for the transfer. The correlations obtained in this work are applied to model heat transfer, while momentum transfer is modelled via the KochiHill drag model.

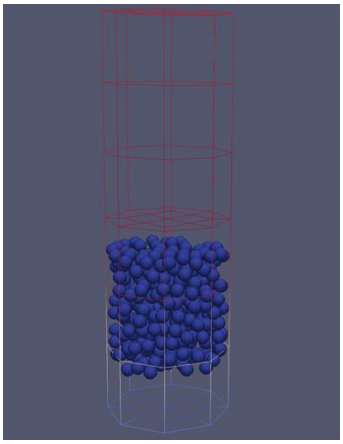

Figure 7.2. Non-resolved Euler-Lagrangian grid setup

7.3 Results

A consistent correlation to predict the heat transfer in the packed bed is obtained using three different randomly packed beds over a range of porosity values and Reynolds numbers. The effect of change in the Prandtl number is not considered currently as the Prandtl number does not vary a great deal for gaseous flows. The details of the different cases simulated to obtain the correlation are given in Table 26.

Table 26. Representation of the cases simulated

Parameters	Value
Number of particles in the reactor	350
Particle diameter size (m)	10^{-3}
Bed Porosities (ε)	0.42; 0.62; 0.87
Reynolds numbers simulated	10; 40; 70; 100

7.3.1 Heat transfer in randomly arranged packed beds

The results for the heat transfer coefficient from spherical particles (with a non-homogenous particle surface temperature) in the packed bed is simulated for different Reynolds numbers and bed porosities as shown in Table 25. This data is then benchmarked against the correlations of Gunn et al., Deen et al. and Sun et al. (Deen et al., 2014; Gunn, 1978; Sun et al., 2015). Figure 7.3 shows the temperature variations with the change in Reynolds numbers and the bed porosity. Temperature gradients inside the particle are observed, which depend on the Reynolds number. The plots for the convective heat transfer inside the region of interest (which is located far from the wall, as well as the inlet and the outlet to avoid effects due to an inhomogeneous bed structure) are shown in Figure 7.4. It is seen that the results agree with the correlations in case the bulk fluid temperature (T_{bulk}) is considered when computing the heat transfer coefficient. In contrast, the heat transfer coefficient that relies on the average fluid temperature (T_{av}) significantly differs from literature correlations. We can only speculate the origin of this difference, which has been also observed by (Sun et al., 2015). Certainly, one argument is that existing correlations are limited by the assumption of a fixed particle surface temperature, which is not the case in simulations using a fixed volumetric heat source. Clearly, a more detailed analysis of the variation of the particle surface temperature is needed in order to probe the exact origin for the observed differences.

7.3.2 Heat transfer correlations

Nusselt number correlations for the fluid-particle heat transfer in the random particle array with non-homogenous particle surface temperature and homogenous particle surface temperature are obtained by fitting the data obtained over different porosities and Reynold numbers.

The effect of the change in Prandtl number is not considered in this current correlation (i.e., we assume $Pr = 1$). The correlation is valid over a porosity range ($0.4 < \varepsilon < 0.9$) and particle Reynolds number (Re_p<100).

The correlation is fitted in the structure of the Gunn correlation. Two different methods to compute the fluid temperature described in Section 7.2.4 are used to obtain different correlations according to the method of computing fluid temperature.

The correlations for non-homogeneous particle surface temperature are as follows for bulk (Eq. (90)) and volume averaged (Eq. (91)) fluid temperatures. The same correlations are given for the case with constant particle surface temperature in Eqns. (92) and (93).

$$Nu_{bulk} = (0.455 + 5.09\varepsilon - 5.05\varepsilon^2)(0.67 + 0.35Re^{0.2}) + (1.73 - 3.38\varepsilon + 1.95\varepsilon^2)(Re^{0.7}) \quad (90)$$

$$Nu_{av} = (-1.42 + 6.43\varepsilon - 5.12\varepsilon^2)(3.2 + 2.54Re^{0.2}) + (2.9 - 6.13\varepsilon + 3.59\varepsilon^2)(Re^{0.7}) \quad (91)$$

$$Nu_{bulk} = (2.844 - 3.49\varepsilon + 2.36\varepsilon^2)(-0.71 + 1.17Re^{0.2}) + (1.4 - 2.35\varepsilon + 1.12\varepsilon^2)(Re^{0.7}) \quad (92)$$

$$Nu_{av} = (-0.3 + 6.87\varepsilon - 6.31\varepsilon^2)(-1.08 + 2.60Re^{0.2}) + (2.28 - 4.58\varepsilon + 2.51\varepsilon^2)(Re^{0.7}) \quad (93)$$

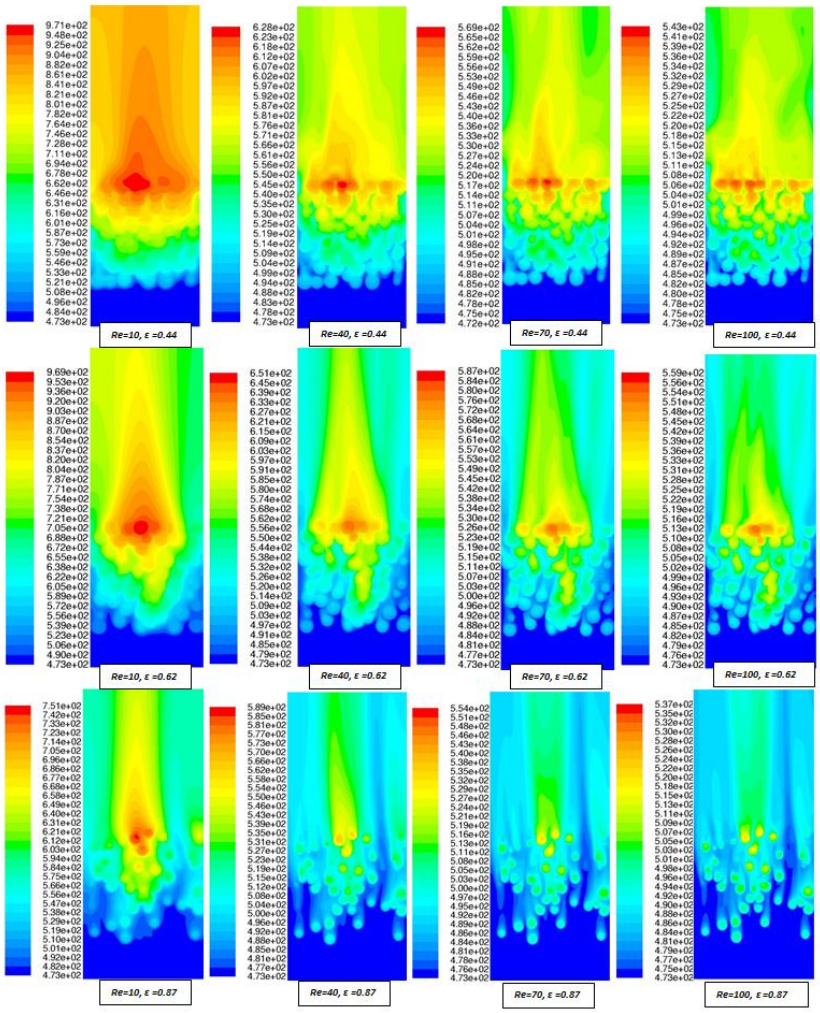

Figure 7.3. Temperature distribution profiles with temperature gradients inside the particles at plane y=0, through the reactor geometries with different bed porosities and Reynolds numbers for the case with a fixed volumetric heat source inside the particles**.**

7.3.3 Comparison of the correlations with non-homogenous vs homogenous particle temperature

Figure 7.5 compares the four different correlations described in Section 7.3.2 over a range of Reynolds numbers. It is immediately clear that a large difference between the correlations using bulk and average temperatures exists. The difference in the correlations using uniform and non-uniform particle surface temperatures is smaller, but does become

significant for the highest porosity considered. It is reasoned that higher porosities create sufficient space between particles to allow a wake region to be established behind the majority of particles. As a result, the convective heat transfer behind the particle is slower than at the front, leading to an asymmetric temperature profile in the particle with higher surface temperatures behind the particle. The hottest part of the particle surface is therefore exposed to the slowest moving fluid and vice versa, thus creating a heat transfer limitation which requires a higher average particle surface temperature to attain a given surface heat flux.

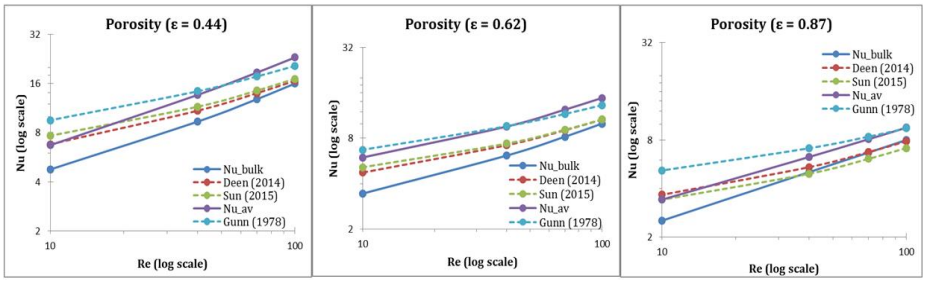

Figure 7.4. Comparison of the heat transfer coefficient in the region of interest (no wall, inlet and outlet effects) over different porosity and Reynolds number values for the case with integrated heat source inside the particles.

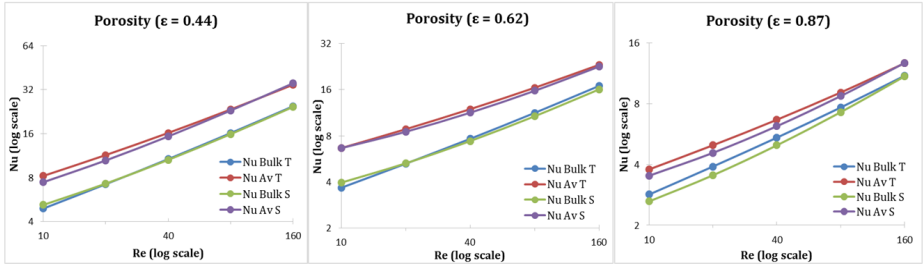

Figure 7.5. Comparison of the prediction of heat transfer from the correlations obtained in this work. T = constant temperature (homogenous particle surface temperature); and S = integrated heat source (non-homogenous particle surface temperature.

7.3.4 Comparison between resolved and unresolved models

The correlation obtained with homogenous particle surface temperature is used to account for the external heat transfer in the non-resolved Euler-Langrangian simulations. The particle bed with a porosity of 0.62 is replicated in LIGGGHTS® + CFDEM® + PARSCALE® simulation, with identical flow properties as in the PR-DNS using FLUENT.

i) Mean particle surface temperature

This is the comparison of mean particle surface temperatures over different Reynolds number (Figure 7.6). The approximation is quite reasonable. Only at low Reynolds number the difference can be observed which we can be speculated looking into the later results.

ii) Fluid temperature profiles

This is the comparison of the fluid temperature profiles obtained from CFDEM and FLUENT, the temperature profile match quite well and the CFDEM approach is able to predict fluid temperature reasonable well when compared with PR-DNS results from FLUENT. The grid for the unresolved setup was refined to the point to obtain a grid independent result and to be able to capture the effects to the level of particle scale.

The results in Figure 7.7 show the overall temperature for Re10 is higher and the prediction is not in agreement with FLUENT result, which is seen in the mean particle surface temperature predictions as well.

iii) Intra-particle temperature distributions

With the presence of PARSCALE coupled to our unresolved simulation we can obtain the 1D profile for the variation of temperature inside the particle (radial). In here we compare the distribution inside the particle given by 1D code PARSCALE® (symmetric profile) and FLUENT (asymmetric profiles).

For the comparison the particles chosen for the study are seen in the Figure 7.8. One particle is chosen from the top of the bed, while one from the bottom of the bed. Three different particles are considered in the middle of the bed, each representing different temperature zones.

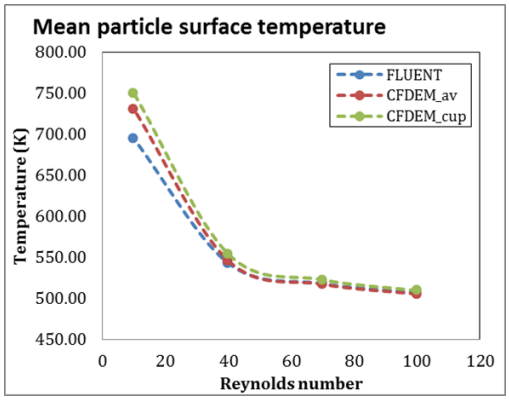

Figure 7.6. Comparison of the prediction of mean particles surface temperature from PR-DNS and non-resolved simulations. (Where, FLUENT= Prediction from PR-DNS; and CFDEM_av and CFDEM_cup are predictions from non-resolved simulations with averaged fluid temperature and bulk fluid temperature respectively).

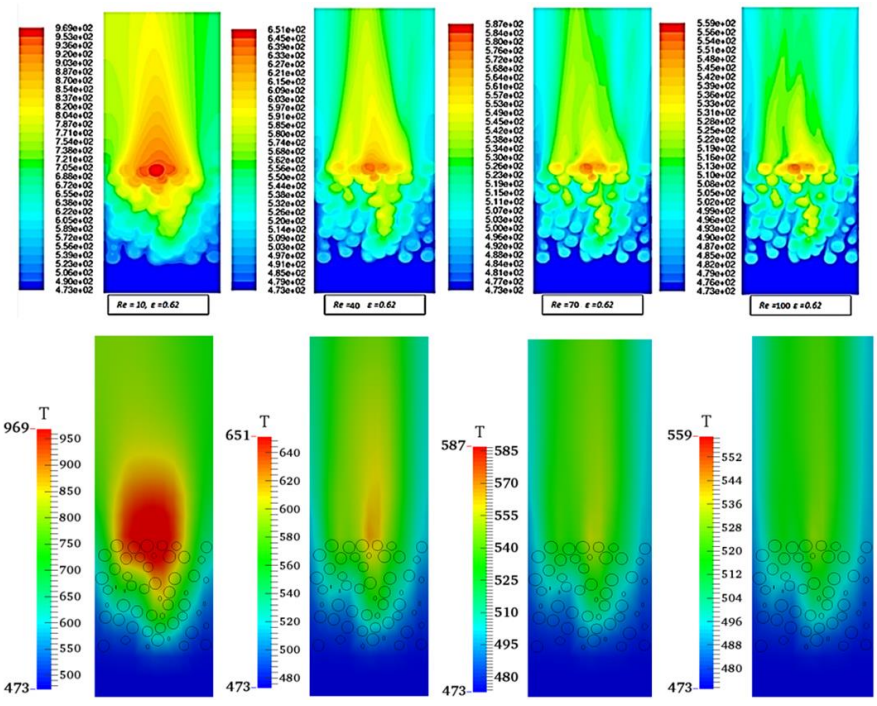

Figure 7.7. Temperature distribution profiles at plane y=0, through the reactor geometries with different and Reynolds numbers for the case with a fixed volumetric heat source inside the particles. FLUENT (above) and CFDEM (below).

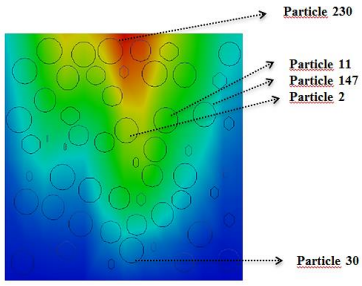

Figure 7.8. Approx. location of the particles studied for the intra particle temperature distribution comparison**.**

In the plots shown in Figure 7.9, the intra particle temperature distributions obtained for particles represented in Figure 7.8 can be seen for Re100. The predictions at Re100, suggests really good match with the results from PARSCALE®, considering the fact that the results obtained with FLUENT are asymmetric in nature.

Similar predictions are observed for Re70 and 40 shown in Figure 7.9. The variation in prediction of intra particle temperature is similar to PR-DNS results from FLUENT. The predictions with average and bulk fluid temperatures don't show a huge difference. Both the correlations predict the temperatures equally well

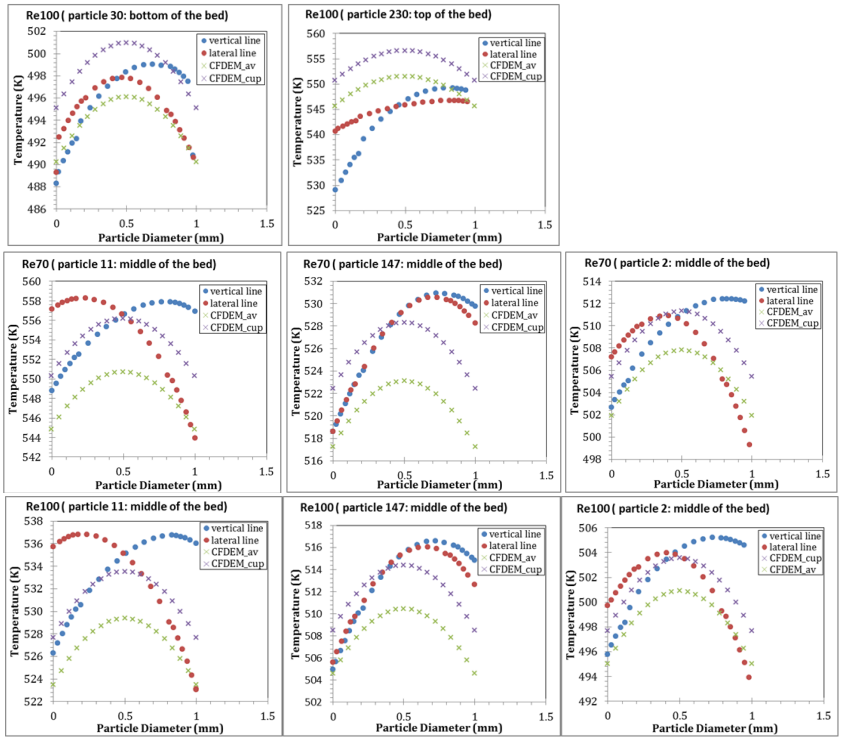

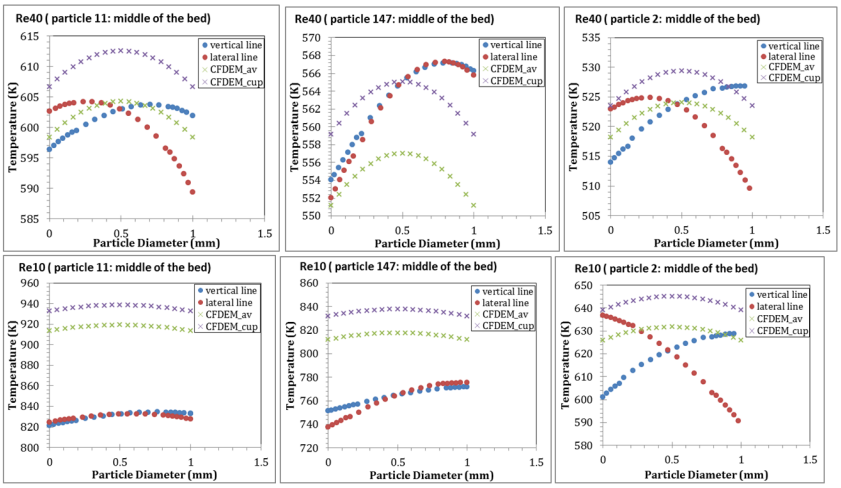

Figure 7.9. Intra particle Temperature distribution profiles at Re100, Re70, Re40 and Re10 obtained from FLUENT (asymmetric) and PARSCALE (symmetric). [Vertical line = prediction in the direction of flow (FLUENT), Lateral line= prediction perpendicular to the flow (FLUENT); CFDEM_av and CFDEM_cup = PARSCALE predictions in a non-resolved coupled simulation using different fluid averaged temperatures (average and bulk fluid respectively).

At Re10, the heat transfer will be very fast therefore there will not be a gradient between the surface temperature and the center temperature of the particle. The deviation is observed at Re10, which was seen in Figure 7.6, Figure 7.7 and also in Figure 7.9. But at low-Reynolds number the mean particle temperature will be generally higher. Moreover models at low-Reynolds number and Pr ~ 1 are difficult to determine, because the heat transfer is very fast. It is clear that any model for this regime has more inaccuracies than models for larger Re. Therefore having a heat transfer model for such low Re might not be necessary and industrial scale packed bed reactors doesn't operate at such low Reynolds number.

iv) Nusselt number with wall distance

To obtain a clear picture of the presence of wall effects, a Nusselt number with wall distance variation plot is obtained as shown in Figure 7.10 at Reynolds number (Re100) with the unresolved approach mentioned above. The cluster plot shows the presence of high Nusselt number near the wall of the reactor and then becomes quite stabilized within $d_p/2$ distance. For now we can only report from the unresolved approach (COSI platform) because FLUENT imposes the current limitation in extracting the per particle Nusselt number.

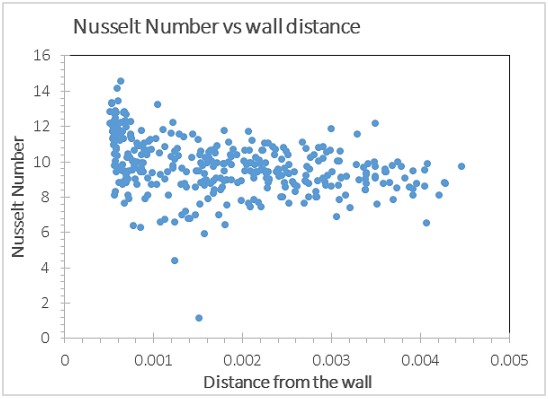

Figure 7.10. Nusselt number variation with the wall distance for Re100 obtained from the unresolved simulation approach.

7.4 Summary and conclusions

This work presented two different approaches for predicting heat transfer in narrow packed bed reactors that are confined by cylindrical walls. First, using resolved DNS, heat transfer rates are directly computed for both (i) a fixed particle surface temperature, and (ii) a fixed volumetric heat source inside the particles. This exercise allowed us to establish in total four heat transfer correlations. Second, non-resolved simulations are performed, which are computationally cheaper, and hence more efficient. Heat transfer rates are predicted using the developed correlations, and agreement analysed between the two approaches were quite satisfactory except at lower Reynolds numbers.

Author Contributions: *Arpit, Stefan and Schalk conceived the idea. Arpit designed, and performed the simulations; Rosa Quinta-Ferreira and Shahriar Amini supervised the work; Arpit wrote the paper.*

Arpit Singhal (Sign)

8 CONCLUSION AND FUTURE OUTLOOK

This thesis focused on the development of new external heat and mass transfer models for gas-solid systems in densely packed bed reactors. These gas-solid systems are of great interest and has been limited to more fluidized bed applicable models in literature. Here in this thesis realistically packed particle packings were considered (which are approximately similar to the packings obtained experimentally). Thus, the models developed in this work using particle resolved direct numerical simulations (PR-DNS) are fundamentally accurate and more applicable to packed bed applications. The PR-DNS has been proved in literature to be more accurate than experiments in terms of obtaining detailed information on the local scale inside the reduced-length heterogeneous reactors.

The development of realistic packings through discrete element method (DEM) leads to an overlap of particle surfaces, and consequently, to the problem in creation of mesh for computational fluid dynamics (CFD) study. Initial investigations revealed the limitations with the most followed approach of shrinking the particles to deal with the aforementioned problem. The packed beds reproduced by shrinking the particles creates equally spaced particles and can neither be classified as random nor realistic packings.

A new method was developed to deal with the particle overlaps in spherical particle beds and also to obtain the rendered geometry used in this work. This geometry was proved to be free from any wall effects when studying external heat transfer. It was found that the steady state direct numerical simulations (DNS) can provide accurate solution for the particle Reynolds number under consideration. Overall, a new methodology was developed for studying external heat and mass transfer using particle resolved DNS in densely packed beds. The numerical accuracy of the developed methodology was backed by thorough deep sensitivity analysis using 95% confidence intervals (in order to quantify the uncertainties). The simulated data suggested the loopholes in the correlations from

literature to study external heat transfer in densely particle beds. Hence, a new external heat and mass transfer model is developed. The new model is applicable to packed beds of mono-disperse spherical particles in gas-solid system and is valid till particle Reynolds number of 200.

The study of gas-solid heat transfer in packed beds was extended for cylindrical particle packings. The particle packings with cylindrical particles of different aspect rations (2, 4 and 6), depending on their applications in the industries are studied and the first external heat and mass transfer model in densely packed beds of cylindrical particles was developed using PR-DNS. In addition, new improved Ergun constants were refitted for pressure drop in cylindrical particle beds. The heat transfer phenomena in packed beds vary with the location, hence an attempt was made to fit a generic external heat and mass transfer model valid for dense packings (of either mono-disperse spherical or cylindrical particles). The presented model was found to be accurate (with R^2 value = 0.978) and lays foundation for the possibility of fitting more accurate external heat transfer models for different shaped particles.

The existing intra particle diffusion models were verified and improved for several levels of complexities in internal mass transfer and reaction kinetics on a reduced scale of computationally cheap 1D model. The developed external heat and mass transfer models along with the PR-DNS data for intra particle diffusion simulations helped to ascertain the industrially viable 1D packed bed model.

The reforming step of steam methane reforming studied on a smaller scale reactors argued the need for enhancements in the 1D model to correctly simulate steam methane reforming on a larger scale. The enhanced 1D model presented promising results for maximizing process efficiency by feeding off-gas fuel from the pressure swing adsorption (PSA) unit back to the fuel stage of the packed bed chemical looping reforming (PBCLR) reactor, thus ensuring complete fuel conversion on an industrial scale PBCLR reactor.

This thesis has covered various theoretical and numerical analysis for external heat and mass transfer and internal mass transfer models in packed beds. In the last chapter, PR-DNS was used to formulate a non-resolved Euler-Lagrange simulation structure. The in-depth comparison of adaption from the resolved simulations to non-resolved simulations presented with a good comparison between the two approaches using the closure models

from the resolved simulations for external heat and mass transfer. The discrepancy between the two approaches was found to be at extremely low particle Reynolds numbers (Re_p = 10), which doesn't affect the practical implementation of the method (as the application of the packed beds operating at such a low Reynolds number is quite unusual).

The thesis has laid foundation for taking a closer look at the available external heat and mass transfer closure models in literature for densely packed bed packings. In the current work, closure models for external heat and mass transfer were presented for gas-solid systems, hence extending this work to include liquid-solid system can be an important research topic.

The work presented the intra particle mass transfer analysis based on the catalytic reaction system, modelling non-catalytic reactions with PR-DNS would be quite a novel approach, as they are extremely complex simulations, but with the methodology already in place from this thesis, this can be a major step forward.

The 1D model framework presented in this thesis can be coupled with full plant scale simulations to carry out the techno-economic analysis of the packed bed chemical looping reforming (PBCLR) reactor integrated with combined cycle power plants. This will help us get detailed insight about the performance of the PBCLR process when compared to tradition GSR, steam methane reforming and auto thermal reforming.

REFERENCES

Abad, A., Adánez, J., García-Labiano, F., de Diego, L.F., Gayán, P., Celaya, J., (2007). ''Mapping of the range of operational conditions for Cu-, Fe-, and Ni-based oxygen carriers in chemical-looping combustion''. *Chemical Engineering Science* **62**, 533-549.

Achenbach, E., (1995). ''Heat and flow characteristics of packed beds''. *Experimental Thermal and Fluid Science* **10**, 17-27.

ANSYS, (November 2013). ''ANSYS Fluent Theory Guide, Release 15.0, Section 16.12.1.3''.

Atmakidis, T., Kenig, E.Y., (2009). ''CFD-based analysis of the wall effect on the pressure drop in packed beds with moderate tube/particle diameter ratios in the laminar flow regime''. *Chemical Engineering Journal* **155**, 404-410.

Augier, F., Idoux, F., Delenne, J.Y., (2010). ''Numerical simulations of transfer and transport properties inside packed beds of spherical particles''. *Chemical Engineering Science* **65**, 1055-1064.

Bai, H., Theuerkauf, J., Gillis, P.A., Witt, P.M., (2009). ''A Coupled DEM and CFD Simulation of Flow Field and Pressure Drop in Fixed Bed Reactor with Randomly Packed Catalyst Particles''. *Industrial and Engineering Chemistry Research* **48**, 4060-4074.

Blais, B., Lassaigne, M., Goniva, C., Fradette, L., Bertrand, F., (2016). ''A semi-implicit immersed boundary method and its application to viscous mixing''. *Computers & Chemical Engineering* **85**, 136-146.

Boccardo, G., Augier, F., Haroun, Y., Ferré, D., Marchisio, D.L., (2015). ''Validation of a novel open-source work-flow for the simulation of packed-bed reactors''. *Chemical Engineering Journal* **279**, 809-820.

Bonefacic, I., Frankovic, B., Kazagic, A., (2015). ''Cylindrical particle modelling in pulverized coal and biomass co-firing process''. *Applied Thermal Engineering* **78**, 74-81.

Calis, H.P.A., Nijenhuis, J., Paikert, B.C., Dautzenberg, F.M., van den Bleek, C.M., (2001). ''CFD modelling and experimental validation of pressure drop and flow profile in a novel structured catalytic reactor packing''. *Chemical Engineering Science* **56**, 1713-1720.

Carman, P.C., (1956). ''Flow of gases through porous media''. Butterworths, London.

Caulkin, R., Jia, X., Xu, C., Fairweather, M., Williams, R.A., Stitt, H., Nijemeisland, M., Aferka, S., Crine, M., Léonard, A., Toye, D., Marchot, P., (2009). ''Simulations of Structures in Packed Columns and Validation by X-ray Tomography''. *Industrial & Engineering Chemistry Research* **48**, 202-213.

Chhabra, R.P., Agarwal, L., Sinha, N.K., (1999). ''Drag on non-spherical particles: an evaluation of available methods''. *Powder Technology* **101**, 288-295.

Cloete, S., Gallucci, F., van Sint Annaland, M., Amini, S., (2016). ''Gas Switching as a Practical Alternative for Scaleup of Chemical Looping Combustion''. *Energy Technology* **4**, 1286-1298.

Collier, A.P., Hayhurst, A.N., Richardson, J.L., Scott, S.A., (2004). ''The heat transfer coefficient between a particle and a bed (packed or fluidised) of much larger particles''. *Chemical Engineering Science* **59**, 4613-4620.

Cundall, P.A., Strack, O.D.L., (1979). ''A discrete numerical model for granular assemblies''. *Géotechnique* **29**, 47-65.

Deen, N.G., Kriebitzsch, S.H.L., van der Hoef, M.A., Kuipers, J.A.M., (2012). ''Direct numerical simulation of flow and heat transfer in dense fluid–particle systems''. *Chemical Engineering Science* **81**, 329-344.

Deen, N.G., Peters, E.A.J.F., Padding, J.T., Kuipers, J.A.M., (2014). ''Review of direct numerical simulation of fluid–particle mass, momentum and heat transfer in dense gas–solid flows''. *Chemical Engineering Science* **116**, 710-724.

Derksen, J.J., (2014). ''Simulations of solid–liquid mass transfer in fixed and fluidized beds''. *Chemical Engineering Journal* **255**, 233-244.

Dixon, A.G., (1988). ''Correlations for wall and particle shape effects on fixed bed bulk voidage''. *The Canadian Journal of Chemical Engineering* **66**, 705-708.

Dixon, A.G., (1997). ''Heat Transfer in Fixed Beds at Very Low (<4) Tube-to-Particle Diameter Ratio''. *Industrial and Engineering Chemistry Research* **36**, 3053-3064.

Dixon, A.G., (2017). ''Local transport and reaction rates in a fixed bed reactor tube: Endothermic steam methane reforming''. *Chemical Engineering Science* **168**, 156-177.

Dixon, A.G., Boudreau, J., Rocheleau, A., Troupel, A., Taskin, M.E., Nijemeisland, M., Stitt, E.H., (2012). ''Flow, Transport, and Reaction Interactions in Shaped Cylindrical Particles for Steam Methane Reforming''. *Industrial & Engineering Chemistry Research* **51**, 15839-15854.

Dixon, A.G., Ertan Taskin, M., Hugh Stitt, E., Nijemeisland, M., (2007). ''3D CFD simulations of steam reforming with resolved intraparticle reaction and gradients''. *Chemical Engineering Science* **62**, 4963-4966.

Dixon, A.G., Nijemeisland, M., (2001). ''CFD as a Design Tool for Fixed-Bed Reactors''. *Industrial and Engineering Chemistry Research* **40**, 5246-5254.

Dixon, A.G., Nijemeisland, M., Stitt, E.H., (2013). ''Systematic mesh development for 3D CFD simulation of fixed beds: Contact points study''. *Computers and Chemical Engineering* **48**, 135-153.

Dixon, A.G., Nijemeisland, M., Stitt, H., (2003). ''CFD Simulation of Reaction and Heat Transfer Near the Wall of a Fixed Bed'', International Journal of Chemical Reactor Engineering.

Dixon, A.G., Taskin, M.E., Nijemeisland, M., Stitt, E.H., (2010). ''CFD Method To Couple Three-Dimensional Transport and Reaction inside Catalyst Particles to the Fixed Bed Flow Field''. *Industrial & Engineering Chemistry Research* **49**, 9012-9025.

Dorai, F., Moura Teixeira, C., Rolland, M., Climent, E., Marcoux, M., Wachs, A., (2015). ''Fully resolved simulations of the flow through a packed bed of cylinders: Effect of size distribution''. *Chemical Engineering Science* **129**, 180-192.

Doraia, F., Rolland, M., Wachs, A., Marcoux, M., Climent, E., (2012). ''Packing Fixed Bed Reactors with Cylinders: Influence of Particle Length Distribution''. *Procedia Engineering* **42**, 1335-1345.

Eppinger, T., Seidler, K., Kraume, M., (2011). ''DEM-CFD simulations of fixed bed reactors with small tube to particle diameter ratios''. *Chemical Engineering Journal* **166**, 324-331.

Eppinger, T., Wehinger, G.D., Jurtz, N., Aglave, R., Kraume, M., (2016). ''A numerical optimization study on the catalytic dry reforming of methane in a spatially resolved fixed-bed reactor''. *Chemical Engineering Research and Design* **115, Part B**, 374-381.

Ergun, S., (1952). ''Fluid flow through packed columns''. *Chem. Eng. Prog.* **48**, 89-94.

Francisco Morgado, J., Cloete, S., Morud, J., Gurker, T., Amini, S., (2016). ''Modelling study of two chemical looping reforming reactor configurations: looping vs. switching''. *Powder Technology* **316**, 599-613.

Ganser, G.H., (1993). ''A rational approach to drag prediction of spherical and nonspherical particles''. *Powder Technology* **77**, 143-152.

Gnielinski, V., (1978). ''Gleichungen zur Berechnung des Wärmeübergangs in querdurchströmten einzelnen Rohrreihen und Rohrbündeln''. *Forschung im Ingenieurwesen A* **44**, 15-25.

Goniva, C., Kloss, C., Deen, N.G., Kuipers, J.A.M., Pirker, S., (2012). ''Influence of rolling friction on single spout fluidized bed simulation''. *Particuology* **10**, 582-591.

Guardo, A., Coussirat, M., Larrayoz, M.A., Recasens, F., Egusquiza, E., (2004). ''CFD Flow and Heat Transfer in Nonregular Packings for Fixed Bed Equipment Design''. *Industrial and Engineering Chemistry Research* **43**, 7049-7056.

Gunjal, P.R., Ranade, V.V., Chaudhari, R.V., (2005). ''Computational study of a single-phase flow in packed beds of spheres''. *AIChE Journal* **51**, 365-378.

Gunn, D.J., (1978). ''Transfer of heat or mass to particles in fixed and fluidised beds''. *International Journal of Heat and Mass Transfer* **21**, 467-476.

Guo, G., Thompson, K.E., (2001). ''Experimental analysis of local mass transfer in packed beds''. *Chemical Engineering Science* **56**, 121-132.

Gupta, S.N., Chaube, R.B., Upadhyay, S.N., (1974). ''Fluid—particle heat transfer in fixed and fluidized beds''. *Chemical Engineering Science* **29**, 839-843.

Handley, D., Heggs, P.J., (1968). ''Momentum and heat transfer mechanisms in regular shaped packings''. *Trans. Inst. Chem. Eng.* **46**, T251-T264.

Hölzer, A., Sommerfeld, M., (2009). ''Lattice Boltzmann simulations to determine drag, lift and torque acting on non-spherical particles''. *Computers & Fluids* **38**, 572-589.

Inaba, H., Fukuda, T., Saito, H., Mayinger, F., (1988). ''Transient behavior of heat removal from a cylindrical heat storage vessel packed with spherical porous particles''. *Wärme - und Stoffübertragung* **22**, 325-333.

Ishida, M., Wen, C.Y., (1968). ''Comparison of kinetic and diffusional models for solid-gas reactions''. *AIChE Journal* **14**, 311-317.

Jafari, A., Zamankhan, P., Mousavi, S.M., Pietarinen, K., (2008). ''Modeling and CFD simulation of flow behavior and dispersivity through randomly packed bed reactors''. *Chemical Engineering Journal* **144**, 476-482.

Jakobsen, H.A., 2014. Packed Bed Reactors, Chemical Reactor Modeling. Springer International Publishing, pp. 1057-1088.

Karthik, G.M., Buwa, V.V., (2017). ''Effect of particle shape on fluid flow and heat transfer for methane steam reforming reactions in a packed bed''. *AIChE Journal* **63**, 366-377.

Khan, J.A., Beasley, D.E., Alatas, B., (1991). ''Evaporation from a packed bed of porous particles into superheated vapor''. *International Journal of Heat and Mass Transfer* **34**, 267-280.

Kloss, C., Goniva, C., Hager, A., Amberger, S., Pirker, S., (2012). ''Models, algorithms and validation for opensource DEM and CFD–DEM''. *Progress in Computational Fluid Dynamics, an International Journal* **12**, 140-152.

Kuroki, M., Ookawara, S., Ogawa, K., (2009). ''A High-Fidelity CFD Model of Methane Steam Reforming in a Packed Bed Reactor''. *JOURNAL OF CHEMICAL ENGINEERING OF JAPAN* **42**, s73-s78.

Lee, J.J., Yoon, S.J., Park, G.C., Lee, W.J., (2007). ''Turbulence-induced Heat Transfer in PBMR Core Using LES and RANS''. *Journal of Nuclear Science and Technology* **44**, 985-996.

Levenspiel, O., (1999). ''Chemical Reaction Engineering, 3rd ed''. John Wiley & Sons, New York.

Lopes, R.J.G., Quinta-Ferreira, R.M., (2009). ''Numerical Simulation of Trickle-Bed Reactor Hydrodynamics with RANS-Based Models Using a Volume of Fluid Technique''. *Industrial and Engineering Chemistry Research* **48**, 1740-1748.

Maestri, M., Cuoci, A., (2013). ''Coupling CFD with detailed microkinetic modeling in heterogeneous catalysis''. *Chemical Engineering Science* **96**, 106-117.

Magnico, P., (2009). ''Pore-scale simulations of unsteady flow and heat transfer in tubular fixed beds''. *AIChE Journal* **55**, 849-867.

Mehrabian, R., Shiehnejadhesar, A., Scharler, R., Obernberger, I., (2014). ''Multi-physics modelling of packed bed biomass combustion''. *Fuel* **122**, 164-178.

Mirhashemi, F.S., Hashemabadi, S.H., (2012). ''Experimental and CFD study of wall effects on orderly stacked cylindrical particles heat transfer in a tube channel''. *International Communications in Heat and Mass Transfer* **39**, 449-455.

Mirhashemi, F.S., Hashemabadi, S.H., Noroozi, S., (2011). ''CFD simulation and experimental validation for wall effects on heat transfer of finite cylindrical catalyst''. *International Communications in Heat and Mass Transfer* **38**, 1148-1155.

Motlagh, A.H.A., Hashemabadi, S.H., (2008). ''3D CFD simulation and experimental validation of particle-to-fluid heat transfer in a randomly packed bed of cylindrical particles''. *International Communications in Heat and Mass Transfer* **35**, 1183-1189.

Mousazadeh, F., van Den Akker, H.E.A., Mudde, R.F., (2013). ''Direct numerical simulation of an exothermic gas-phase reaction in a packed bed with random particle distribution''. *Chemical Engineering Science* **100**, 259-265.

Nemec, D., Levec, J., (2005). ''Flow through packed bed reactors: 1. Single-phase flow''. *Chemical Engineering Science* **60**, 6947-6957.

Nijemeisland, M., Dixon, A.G., Hugh Stitt, E., (2004). ''Catalyst design by CFD for heat transfer and reaction in steam reforming''. *Chemical Engineering Science* **59**, 5185-5191.

Noorman, S., van Sint Annaland, M., Kuipers, (2007). ''Packed Bed Reactor Technology for Chemical-Looping Combustion''. *Industrial & Engineering Chemistry Research* **46**, 4212-4220.

Oliveira, E.L.G., Grande, C.A., Rodrigues, A.E., (2010). ''Methane steam reforming in large pore catalyst''. *Chemical Engineering Science* **65**, 1539-1550.

Ortiz, M., de Diego, L.F., Abad, A., García-Labiano, F., Gayán, P., Adánez, J., (2012). ''Catalytic Activity of Ni-Based Oxygen-Carriers for Steam Methane Reforming in Chemical-Looping Processes''. *Energy & Fuels* **26**, 791-800.

Oschmann, T., Hold, J., Kruggel-Emden, H., (2014). ''Numerical investigation of mixing and orientation of non-spherical particles in a model type fluidized bed''. *Powder Technology* **258**, 304-323.

Oschmann, T., Schiemann, M., Kruggel-Emden, H., (2016). ''Development and verification of a resolved 3D inner particle heat transfer model for the Discrete Element Method (DEM)''. *Powder Technology* **291**, 392-407.

Partopour, B., Dixon, A.G., (2017). ''Resolved-particle fixed bed CFD with microkinetics for ethylene oxidation''. *AIChE Journal* **63**, 87-94.

Ramachandran, P.A., Doraiswamy, L.K., (1982). ''Modeling of noncatalytic gas-solid reactions''. *AIChE Journal* **28**, 881-900.

Rawlings, J.B.a.E., John G, (2002). ''Chemical reactor analysis and design fundamentals (Chapter 7)''. Nob Hill Pub, Madison, Wis.

Rebughini, S., Cuoci, A., Maestri, M., (2016). ''Handling contact points in reactive CFD simulations of heterogeneous catalytic fixed bed reactors''. *Chemical Engineering Science* **141**, 240-249.

Reddy, R.K., Joshi, J.B., (2008). ''CFD modeling of pressure drop and drag coefficient in fixed and expanded beds''. *Chemical Engineering Research and Design* **86**, 444-453.

Robie, R.A., Hemingway, B.S., (1995). ''Thermodynamic properties of minerals and related substances at 298.15 K and 1 bar (10^5 pascals) pressure and at higher temperatures'', Bulletin, - ed.

Romkes, S.J.P., Dautzenberg, F.M., van den Bleek, C.M., Calis, H.P.A., (2003). ''CFD modelling and experimental validation of particle-to-fluid mass and heat transfer in a packed bed at very low channel to particle diameter ratio''. *Chemical Engineering Journal* **96**, 3-13.

S. Radl, T.F., A. Aigner, and C. Kloss., (2015). ''An Open-Source Library for the Simulation of Intra-Particle Heat and Mass Transport Processes in Coupled Simulations.'', IV International Conference on Particle-based Methods Fundamentals and Applications (PARTICLES 2015),, Barcelona, Spain, pp. pages 46–55, 2015.

Scott, S.A., Davidson, J.F., Dennis, J.S., Hayhurst, A.N., (2004). ''Heat Transfer to a Single Sphere Immersed in Beds of Particles Supplied by Gas at Rates above and below Minimum Fluidization''. *Industrial and Engineering Chemistry Research* **43**, 5632-5644.

Singhal, A., Cloete, S., Quinta-Ferreira, R., Amini, S., (2017a). ''Comparison of particle-resolved direct numerical simulation and 1D modelling of catalytic reactions in a cylindrical particle bed'', V International Conference on particle-based methods. Fundamentals and Applications, 2017 ed. International Center for Numerical Methods in Engineering (CIMNE), Hannover, Germany, pp. 802-812.

Singhal, A., Cloete, S., Quinta-Ferreira, R., Amini, S., (2017b). ''Multiscale Modeling of a Packed Bed Chemical Looping Reforming (PBCLR) Reactor''. *Energies* **10**, 2056.

Singhal, A., Cloete, S., Quinta-Ferreira, R., Amini, S., (2017c). ''Multiscale modelling of packed bed chemical looping reforming''. *Energy Procedia* **136**, 349-355.

Singhal, A., Cloete, S., Radl, S., Quinta-Ferreira, R., Amini, S., (2016a). ''CFD-DEM predictions of heat transfer in packed beds using commercial and open source codes''. *MAYFEB Journal of Chemistry and Chemical Engineering* **1**, 10-26.

Singhal, A., Cloete, S., Radl, S., Quinta-Ferreira, R., Amini, S., (2016b). ''Multiscale modelling of heat transfer from arrays of spherical particles'', 9th International Conference on Multiphase Flow (ICMF). ICMF, Firenze, Italy.

Singhal, A., Cloete, S., Radl, S., Quinta-Ferreira, R., Amini, S., (2017d). ''Comparison of Particle-Resolved Direct Numerical Simulation and 1D modelling of catalytic reactions in a packed bed'', 12th International Conference on CFD in Oil & Gas, Metallurgical and Process Industries. Progress in Applied CFD – CFD2017, Trondheim, Norway, pp. 667-674.

Singhal, A., Cloete, S., Radl, S., Quinta-Ferreira, R., Amini, S., (2017e). ''Heat transfer to a gas from densely packed beds of cylindrical particles''. *Chemical Engineering Science* **172**, 1-12.

Singhal, A., Cloete, S., Radl, S., Quinta-Ferreira, R., Amini, S., (2017f). ''Heat transfer to a gas from densely packed beds of monodisperse spherical particles''. *Chemical Engineering Journal* **314**, 27-37.

Smirnov, E.I., Muzykantov, A.V., Kuzmin, V.A., Kronberg, A.E., Zolotarskii, I.A., (2003). ''Radial heat transfer in packed beds of spheres, cylinders and Rashig rings: Verification of model with a linear variation of λer in the vicinity of the wall''. *Chemical Engineering Journal* **91**, 243-248.

Soleymani, A., Turunen, I., Yousefi, H., Bastani, D., (2007). ''Numerical Investigations of Fluid Flow and Lateral Fluid Dispersion in Bounded Granular Beds in a Cylindrical Coordinates System''. *Chemical Engineering and Technology* **30**, 1369-1375.

Sun, B., Tenneti, S., Subramaniam, S., (2015). ''Modeling average gas–solid heat transfer using particle-resolved direct numerical simulation''. *International Journal of Heat and Mass Transfer* **86**, 898-913.

Szekely, J., Evans, J.W., Sohn, H.Y.,, (1976). ''Gas-solid reactions''. Academic Press, New York.

Tavassoli, H., Peters, E.A.J.F., Kuipers, J.A.M., (2015). ''Direct numerical simulation of fluid–particle heat transfer in fixed random arrays of non-spherical particles''. *Chemical Engineering Science* **129**, 42-48.

Tenneti, S., Sun, B., Garg, R., Subramaniam, S., (2013). ''Role of fluid heating in dense gas–solid flow as revealed by particle-resolved direct numerical simulation''. *International Journal of Heat and Mass Transfer* **58**, 471-479.

Thiele, E.W., (1939). ''Relation between Catalytic Activity and Size of Particle''. *Industrial & Engineering Chemistry* **31**, 916-920.

Tsotsas, E., Martin, H., (1987). ''Thermal conductivity of packed beds: A review''. *Chemical Engineering and Processing: Process Intensification* **22**, 19-37.

Uhlmann, M., (2005). ''An immersed boundary method with direct forcing for the simulation of particulate flows''. *Journal of Computational Physics* **209**, 448-476.

W. E. Ranz and W. R. Marshall, J., (1952). '"Vaporation from Drops, Part I"'. *Chem. Eng. Prog.* **48(3)**, 141–146.

Wakao, N., Kaguei, S., Funazkri, T., (1979). ''Effect of fluid dispersion coefficients on particle-to-fluid heat transfer coefficients in packed beds: Correlation of nusselt numbers''. *Chemical Engineering Science* **34**, 325-336.

Wassie, S.A., Gallucci, F., Zaabout, A., Cloete, S., Amini, S., van Sint Annaland, M., (2017). ''Hydrogen production with integrated CO_2 capture in a novel gas switching reforming reactor: Proof-of-concept''. *International Journal of Hydrogen Energy* **42**, 14367-14379.

Wehinger, G.D., Eppinger, T., Kraume, M., (2015). ''Evaluating Catalytic Fixed-Bed Reactors for Dry Reforming of Methane with Detailed CFD''. *Chemie Ingenieur Technik* **87**, 734-745.

Wehinger, G.D., Fütterer, C., Kraume, M., (2017). ''Contact Modifications for CFD Simulations of Fixed-Bed Reactors: Cylindrical Particles''. *Industrial & Engineering Chemistry Research* **56**, 87-99.

Wehinger, G.D., Kraume, M., Berg, V., Korup, O., Mette, K., Schlögl, R., Behrens, M., Horn, R., (2016). ''Investigating dry reforming of methane with spatial reactor profiles and particle-resolved CFD simulations''. *AIChE Journal* **62**, 4436-4452.

Wen, C.Y., Yu, Y.H., (1966). ''A generalized method for predicting the minimum fluidization velocity''. *AIChE Journal* **12**, 610-612.

Xu, J., Froment, G.F., (1989). ''Methane steam reforming, methanation and water-gas shift: I. Intrinsic kinetics''. *AIChE Journal* **35**, 88-96.

Yang, J., Wang, Q., Zeng, M., Nakayama, A., (2010). ''Computational study of forced convective heat transfer in structured packed beds with spherical or ellipsoidal particles''. *Chemical Engineering Science* **65**, 726-738.

Yang, W., Cloete, S., Morud, J., Amini, S., (2016). ''An Effective Reaction Rate Model for Gas-Solid Reactions with High Intra-Particle Diffusion Resistance'', International Journal of Chemical Reactor Engineering, pp. 331-342.

Zare, M., Hashemabadi, S.H., (2013). ''Experimental study and CFD simulation of wall effects on heat transfer of an extrudate multi-lobe particle''. *International Communications in Heat and Mass Transfer* **43**, 122-130.

Zhou, X., Duan, Y., Huai, X., Li, X., (2013a). ''3D CFD modeling of acetone hydrogenation in fixed bed reactor with spherical particles''. *Particuology* **11**, 715-722.

Zhou, Z., Han, L., Bollas, G.M., (2013b). ''Model-based analysis of bench-scale fixed-bed units for chemical-looping combustion''. *Chemical Engineering Journal* **233**, 331-348.

LIST OF PUBLICATIONS

The thesis is based on the list of following research articles and deliverables.

Journal papers

Arpit Singhal, Schalk Cloete, Stefan Radl, Rosa Quinta-Ferreira, Shahriar Amini, *CFD-DEM predictions of heat transfer in packed beds using commercial and open source codes.* MAYFEB Journal of Chemistry and Chemical Engineering. 2016. 1: p. 10-26. (Singhal et al., 2016a)

Arpit Singhal, Schalk Cloete, Stefan Radl, Rosa Quinta-Ferreira, Shahriar Amini, *Heat transfer to a gas from densely packed beds of monodisperse spherical particles.* Chemical Engineering Journal. 2017. 314: p. 27-37. (Singhal et al., 2017f)

Arpit Singhal, Schalk Cloete, Stefan Radl, Rosa Quinta-Ferreira, Shahriar Amini, *Heat transfer to a gas from densely packed beds of cylindrical particles.* Chemical Engineering Science. 2017. 172: p. 1-12. (Singhal et al., 2017e)

Arpit Singhal, Schalk Cloete, Rosa Quinta-Ferreira, Shahriar Amini, *Multiscale Modeling of a Packed Bed Chemical Looping Reforming (PBCLR) Reactor.* Energies. 2017. 10 (12): 2056. (Singhal et al., 2017b)

Arpit Singhal, Schalk Cloete, Rosa Quinta-Ferreira, Shahriar Amini, *Verification of heat and mass transfer closures for industrial scale packed bed reactor simulations.* Energies. 2018. 11 (4): 805

Presentations and conference proceedings

Arpit Singhal, Schalk Cloete, Stefan Radl, Shahriar Amini, *ECCOMAS Thematic Conferences: IV International Conference on Particle-based Methods, PARTICLE (2015)*, 28 – 30 September, Barcelona, Spain. **Oral Presentation**, "*CFD-DEM predictions of heat transfer in packed beds using commercial and open source codes".*

Arpit Singhal, Schalk Cloete, Stefan Radl, Shahriar Amini, ***proceedings*** *of 9th International Conference on Multiphase Flow, ICMF (2016)*, 22 – 27 May, Firenze, Italy. **Oral Presentation and Paper**, "*Multiscale modelling of heat transfer from arrays of spherical particles".*

Arpit Singhal, Schalk Cloete, Stefan Radl, Rosa Quinta-Ferreira, Shahriar Amini, **Progress in Applied CFD—CFD2017***, proceedings of 12th International Conference on CFD in Oil & Gas, Metallurgical and Process Industries, CFD (2017)*, 30 May – 1 June, Trondheim, Norway, SINTEF Academic Press: p. 667-674. **Oral Presentation and Paper**, "*Comparison of Particle-Resolved Direct Numerical Simulation and 1D modelling of catalytic reactions in a packed bed".*

Arpit Singhal, Schalk Cloete, Rosa Quinta-Ferreira, Shahriar Amini, **Energy Procedia** 2017. 136. p. 349-355*, in 4th International Conference on Energy and Environment Research, ICEER (2017)*, 17 – 20 July, Porto, Portugal. **Oral Presentation and Paper**, "*Multiscale modelling of packed bed chemical looping reforming".*

Arpit Singhal, Schalk Cloete, Rosa Quinta-Ferreira, Shahriar Amini, **proceedings** of *ECCOMAS Thematic Conferences: V International Conference on Particle-based Methods, PARTICLE (2017)*, 26 – 28 September, Hannover, Germany. **Oral Presentation and Paper**, "*Comparison of Particle-Resolved Direct Numerical Simulation and 1D modelling of catalytic reactions in a cylindrical particle bed".*

Deliverable reports - NanoSim

Arpit Singhal, Schalk Cloete, Stefan Radl. **Deliverable D4.4**, "Models for 1D Simulations of Packed beds".

Arpit Singhal, Schalk Cloete, Pascal Fede, **Deliverable D5.5**, "Fully functional 2D axis-symmetric and 3D model for fixed bed reactors".

APPENDICES

APPENDIX 1 COMPARISON OF PARTICLE RESOLVED DIRECT NUMERICAL SIMULATION AND 1D MODELING OF CATALYTIC REACTIONS IN A PACKED BED.

APPENDIX 2 COMPARISON OF PARTICLE RESOLVED DIRECT NUMERICAL SIMULATION AND 1D MODELLING OF CATALYTIC REACTIONS IN A CYLINDRICAL PARTICLE BED.

APPENDIX 1 COMPARISON OF PARTICLE RESOLVED DIRECT NUMERICAL SIMULATION AND 1D MODELING OF CATALYTIC REACTIONS IN A PACKED BED

COMPARISON OF PARTICLE-RESOLVED DIRECT NUMERICAL SIMULATION AND 1D MODELLING OF CATALYTIC REACTIONS IN A PACKED BED

Arpit Singhal [a, b*], Schalk Cloete [c], Stefan Radl [d], Rosa Quinta-Ferreira [b] and Shahriar Amini [a, c]

[a] NTNU (Norwegian University of Science and Technology), Department of Energy and Process Engineering, Kolbjørn hejes v 1B, NO-7491, Trondheim, Norway
[b] University of Coimbra, Department of Chemical Engineering, Rua Sílvio Lima, Polo II, 3030-790 Coimbra, Portugal
[c] SINTEF Materials and Chemistry, Flow Technology Department, S. P. Andersens veg 15 B, NO-7031, Trondheim, Norway
[d] TU Graz, Institute of Process and Particle Engineering, 8010 Graz, Inffeldgasse 13/III, Austria

Corresponding author's e-mail: arpit.singhal@ntnu.no

ABSTRACT

The work presents a comparison of catalytic gas-solid reactions in a packed bed as simulated on two widely different scales: direct numerical simulation (capable of accurately predicting transfer phenomena in and around a few particles) and 1D modelling (capable of engineering simulations of industrial scale reactors).

Particle-resolved direct numerical simulation (PR-DNS) is performed on a small geometry containing ~100 realistically packed monodisperse spherical particles generated via the discrete element method (DEM). These results are compared to a 1D packed bed reactor model using the effectiveness factor approach to account for intra-particle mass transfer and a suitable closure for gas-particle heat transfer.

The differences between the results from the two modelling approaches are quantified over a range of Thiele moduli, Prandtl numbers and reaction enthalpies. Results showed that existing 1D-model closures perform well for a simple first order catalytic reaction. Heat transfer completely dominates the overall reaction system when large reaction enthalpies are simulated, while mass transfer limitations dominate at low reaction enthalpies. Future work will extend this comparative approach to packings with more complex particle shapes and complex reactions.

Keywords: Direct numerical simulation (DNS), CFD-DEM, packed bed, catalytic gas-solid reaction, reaction rate, heat transfer, multiscale.

NOMENCLATURE

Greek Symbols

α	Volume fraction
ε	Void fraction
ϕ	Thiele modulus (Th)
η	Effectiveness factor

Latin Symbols

C_p	Specific heat capacity of fluid [J/kg.K]
C_A	Concentration of species A [mol/m^3]
D	Molecular diffusivity [m^2/s]
d_p	Diameter of the cylindrical particle [m]
E	Activation energy [J/mol]
h	Heat transfer coefficient [W/m^{2}K]
k_0	Arrhenius constant [1/s]
K_f	Thermal Conductivity of fluid [W/m.K]
Nu	Nusselt number (hd_p/K_f)
Pr	Prandtl number ($\mu C_p/K_f$)
R	Gas constant [8.314 J/mol/K]
R_{cat}	Catalytic reaction rate [mol/m^{3}s]
r	Radius [m]
Re	Reynolds number ($\rho u_s d_p/\mu$)
T	Temperature [K]
u_s	Superficial velocity of the fluid [m/s].

Sub/superscripts

f	Fluid
s	Solid.
p	Particle.

INTRODUCTION

Gas-solid reaction systems in packed beds are of great industrial influence, with the application widespread from process to metallurgical industries. The catalytic or non-catalytic role of the solid defines the complexity involved in the gas-solid reactions.

There are several advanced models available in literature for gas-solid reaction systems. The non-catalytic reaction systems are considered more complicated as they are transient in nature. The detailed review of such systems is described by (Ramachandran and Doraiswamy, 1982) and more recently by (Nashtaee and Khoshandam, 2014). Meanwhile, (Ishida and Wen, 1968) have described the effectiveness factor (η) in catalytic reactions for gas-solid systems. The effectiveness factor in heterogeneous catalyst reaction to obtain the intra particle diffusion in porous particles is suggested in (Levenspiel, 1999).

The recent work from (Yang et al., 2016) described an effectiveness factor for general reaction forms. They presented an analytical expression, which is applicable to wide range of reaction rate forms and provides a direct and computationally efficient approach of obtaining effectiveness factor in packed bed reactors. The validity of such a simplified model when added with heat transfer limitations motivates the current work. Hence, the objective of the work is to obtain a comparison in prediction of effectiveness factor for a catalytic gas-solid reaction on two distinct scales. Firstly, a PR-DNS study of a packed bed of ~100 spherical particles now involving a catalytic reaction based on our previously published work (Singhal et al., 2017) gives insight into a phenomenon of intra particle diffusion along with heat transfer limitations. Secondly, a 1D packed bed reactor model coupled with the effectiveness

factor model from (Yang et al., 2016) describes the intra-particle heat and mass transfer. The results obtained from both the approaches are compared and documented.

METHODOLOGY

Thiele Modulus and Effectiveness Factor

The effectiveness factor concept in heterogonous catalytic gas-solid reactions can be explained as the effect of intra particle diffusion on the reaction rate (Ishida and Wen, 1968; Levenspiel, 1999).

$$\eta = \frac{\text{actual reaction rate}}{\text{reaction rate without diffusion limitations}}$$

Thus, the effectiveness factor in catalytic reactions is directly linked with the Thiele modulus (Thiele, 1939). Thiele modulus is explained as:

$$\phi \approx \frac{\text{reaction rate}}{\text{diffusion rate}}$$

PR-DNS Simulation Setup

The spherical particle bed is generated using DEM (Discrete Element Method) integrated in ANSYS FLUENT following the procedure described in the paper (Singhal et al., 2017). The geometry is meshed with fine body-fitted polyhedral elements both inside and outside the particles with resolution of dp/30 on the particle surfaces and the growth rate of 20% (Figure 1).

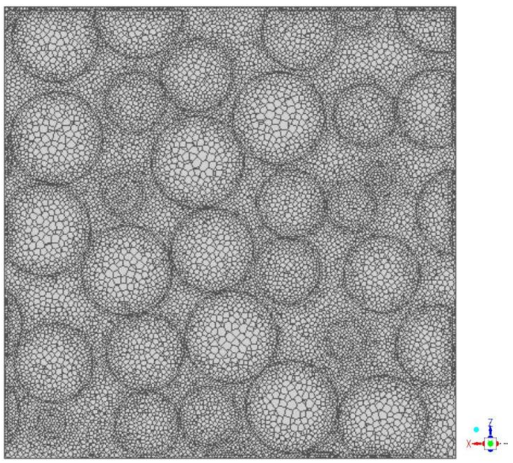

Figure 1: A section (y = 0) through the geometry meshed with polyhedral elements.

ANSYS FLUENT is used to complete steady state DNS using the SIMPLE algorithm for pressure-velocity coupling with 2nd order spatial discretization of other equations. Steady state DNS was found to be sufficient for this case since no transient fluctuations occurred in the small spaces between particles (Singhal et al., 2017). The geometry incorporates a velocity inlet, a pressure outlet and a no-slip condition on the wall. The reaction takes place in the porous solid particles (grain model (Szekely, 1976)) modelled by the Eq. (1). The simulation parameters used in the DNS simulations are describe in the Table 1.

$$A\,(g) + B\,(s) \rightarrow C\,(g) + B\,(s) \quad \textbf{(1)}$$

The reaction rate is described in the conventional way:

$$R_{cat} = \alpha_s k C_A \quad \textbf{(2)}$$

$$k = k_0 exp\left(\frac{-E}{RT}\right) \quad \textbf{(3)}$$

Simulations were completed at three different levels of mass transfer resistance (Thiele modulus), heat transfer resistance (Prandtl number) and reaction enthalpy as outlined in Table 1. Mass and heat transfer was adjusted by setting the molecular diffusivity and gas-phase thermal conductivity according to the Th and Pr numbers specified in Table 1. No solids phase thermal conductivity was included in order to accentuate heat transfer resistances in the particle. For the reaction rate, the pre-exponential factor in Eq. (3) was chosen to result in a reaction rate constant of 10000 1/s at a temperature of 1000 K. A large activation energy is selected to accentuate coupling between heat and mass transfer.

Table 1: Simulation parameters for PR-DNS

Parameters	Value	
Particle diameter (d_p) (m)	0.001	
Packed bed voidage	0.355	
Particle void fraction (internal)	0.3	
Density (kg/m^3)	*Fluid* :1	*Particles* :2500
Fluid velocity (m/s)	1	
Inlet mole fraction (A)	0.1	
Specific heat capacity (C_p) (J/kg/k)	1000	
Thiele moduli (Th)	5, 10, 20	
Prandtl numbers (Pr)	0.4, 1.6, 6.4	
Heat of reaction (kJ/mol)	100, 10, 0	

1D Packed Bed Model

A detailed outline of the setup of the 1D model used in this work can be viewed in a recent work by the authors (Cloete et al., 2016). The model is solved in the commercial CFD code, ANSYS FLUENT 16.2, on a domain with 100 cells arranged in only one direction. In order to simulate a packed bed, the Eulerian Two Fluid Model approach is followed and the velocity of the solids phase is fixed to zero in all cells. Conservation equations for mass, momentum, species and energy are then solved in the conventional manner.

In the present study, the most important closures are the effectiveness factor for modelling intra-particle mass transfer limitations (Levenspiel, 1999) and the gas-particle heat transfer coefficient for modelling external heat transfer limitations (Gunn, 1978). The effectiveness factor for the simple first order catalytic reaction considered in this study is written as follows:

$$\eta = \frac{3}{\phi^2}(\phi \coth(\phi) - 1) \quad \textbf{(4)}$$

$$\phi = r_p \sqrt{\frac{k}{D_e}} \quad \textbf{(5)}$$

$$D_e = \frac{D\varepsilon}{\tau} \quad \textbf{(6)}$$

The Thiele modulus (ϕ) represents the ratio of kinetic rate to diffusion rate, so higher values represent greater mass transfer limitation. The effective diffusivity (D_e) is composed of the molecular diffusivity (D), the void fraction of porous particles $(\varepsilon = 0.3)$ and the tortuosity $(\tau = 1)$.

The classical Gunn correlation for gas-particle heat transfer is written as follows:

$$Nu = (7 - 10\varepsilon + 5\varepsilon^2)\left(1 + 0.7Re^{0.2}Pr^{\frac{1}{3}}\right) + (1.33 - 2.44\varepsilon + 1.2\varepsilon^2)Re^{0.7}Pr^{\frac{1}{3}} \quad \textbf{(7)}$$

Inlet and outlet boundary conditions as well as the domain length are set to identical values as the PR-DNS simulations. The solids volume fraction in the bed is taken as the product of the mean solids volume fraction in the PR-DNS domain (0.645) and the solids volume fraction in the particles (0.7).

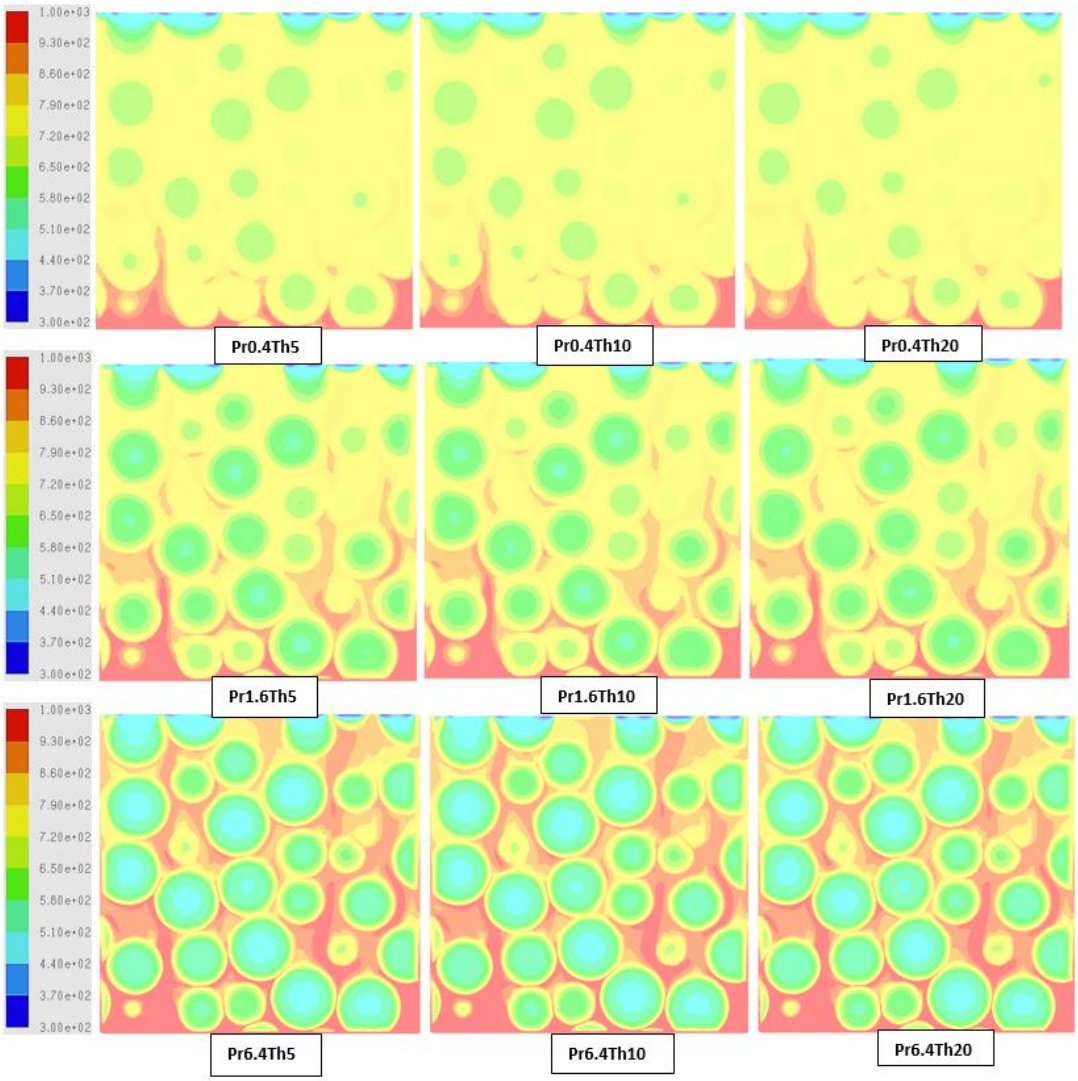

Figure 2: The PR-DNS results for the temperature variation in the packed bed of spherical particles for different Prandtl numbers (Pr) and Thiele moduli (Th)

RESULTS AND DISCUSSIONS

Heat and Mass Transfer in Densely Packed Bed

PR-DNS results for simulations completed with different Thiele moduli and Prandtl numbers for the highly endothermic reaction ($dH_{rxn} = 100$ kJ/mol) are shown in Figure 2 and Figure 3. The temperature variation in Figure 2 illustrates the increasing effect of the heat transfer resistance as Pr is increased by decreasing the gas-phase thermal conductivity. Even though the thermal conductivity is also very low inside the particle, it is clear that external gas-particle heat transfer still dominates. This is most clearly visible in the Pr6.4 cases in Figure 2 where the temperature gradient inside the particles is small relative to the temperature gradient in the fluid film around the particles. Figure 3 illustrates the mass transfer resistances. It is immediately evident that mass transfer resistances are much less influential in this case than heat transfer resistances because the species concentration gradients are small relative to the temperature gradients in Figure 2. The Pr0.4Th20 case shows some intra-particle mass transfer resistance as a clear species gradient within the particles. The importance of heat transfer resistance relative to mass transfer resistance for this particular case will be further discussed in the next sections.

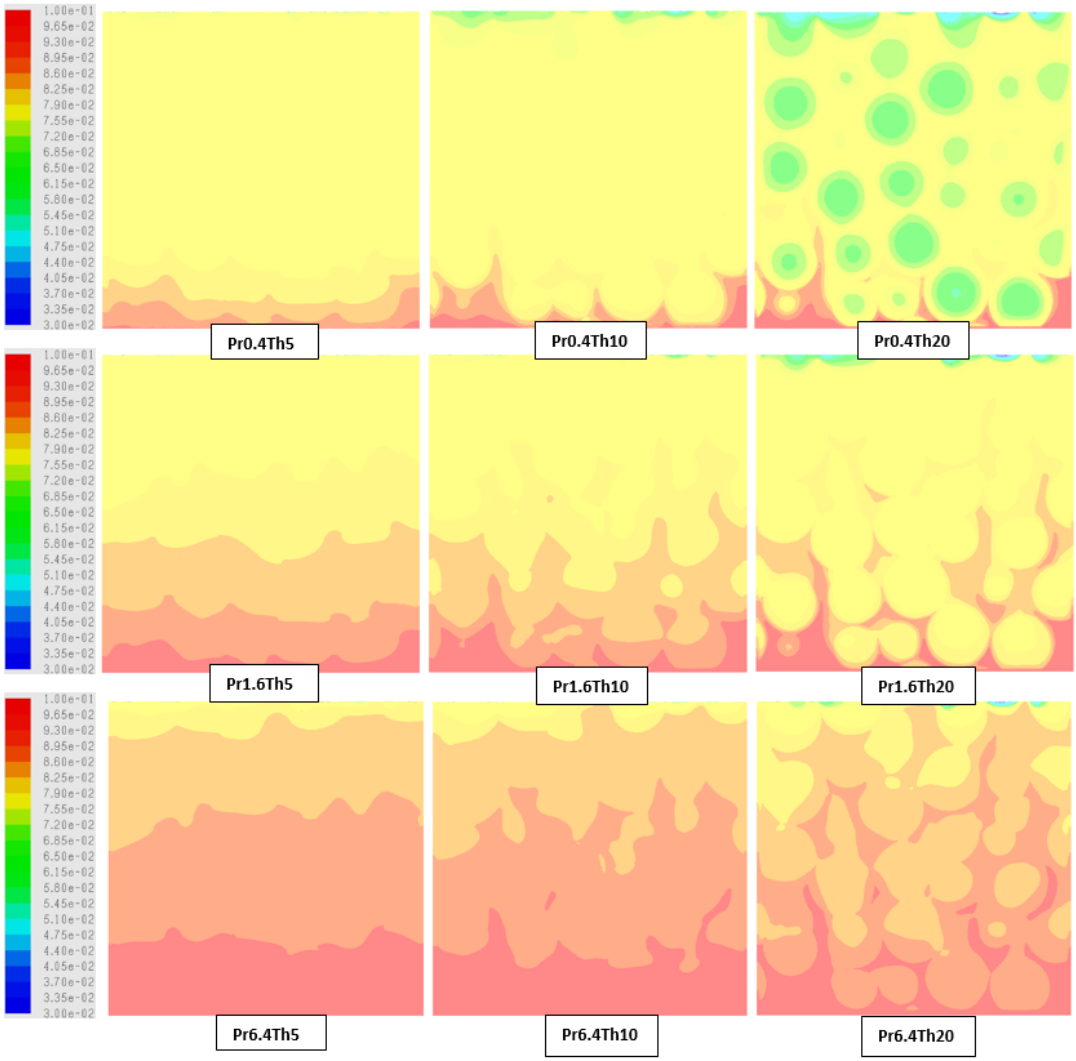

Figure 3: The PR-DNS results for the reactant (A) mole fraction in the packed bed of spherical particles for different Prandtl numbers (Pr) and Thiele moduli (Th).

Individual Particle Data

The PR-DNS approach allows for extraction of detailed data from individual particles within the domain. In this way, the effectiveness factor for individual particles can be extracted and compared. This will be done for the case with the largest heat and mass transfer limitations (Th20-Pr6.4). The definition of the effectiveness factor becomes very important in this case. Three different approaches will be followed (Figure 4):

- **Species:** Comparing the species concentration on the particle surface to the average concentration in the particle (the effectiveness factor for an isothermal first order reaction)
- **Surface:** Comparing the average reaction rate in the particle to the reaction rate that would occur using species concentration and temperature on the particle surface.
- **Volume:** The same as the previous point, only using data averaged over the volume of the particle.

The fact that the "species" effectiveness factor is close to unity implies that mass transfer plays essentially no role in this particular case (the reactant concentration on the particle surface is essentially the same as the reactant concentration in the particle volume). This case is therefore almost exclusively controlled by heat transfer (as seen in the Th20-Pr6.4 case of Figure 2 and Figure 3).

The heat transfer limitation becomes clear when looking at the "surface" effectiveness factor. The temperature on the particle surface is a lot higher than inside the particle volume where the reaction takes place. Calculating the reaction based on the particle surface temperature would therefore result in large errors.

Interestingly, the "volume" effectiveness factor is larger than unity. This implies that there is a significant amount of temperature variation inside the particle, brought about by the assumption of zero thermal conductivity by the solid material. Naturally, this will not be the case in most catalyst particles, but it presents an interesting phenomenon. Given the exponential increase in reaction kinetics with temperature, any variation in temperature around the mean will strongly increase the average

kinetic rate inside the particle. This is what happened in this case: the actual reaction rate inside the particle was higher than the reaction rate calculated based on the average particle temperature.

1D Model Predictions

Comparisons between PR-DNS and 1D model results are discussed in this section. Firstly, the 1D model will be compared to PR-DNS results over a range of Prandtl numbers and Thiele moduli. Secondly, the reaction enthalpy will be changed and the models will be compared again. Finally, an important observation regarding the implementation of the 1D model will be presented.

Variation of Prandtl number and Thiele modulus

A comparison of axial reactant concentration is given in Figure 5 for nine combinations Prandtl number and Thiele modulus. It is clear that the 1D model successfully predicts the PR-DNS results.

In addition, the dominance of heat transfer limitations is clear in all cases because results for different Thiele moduli are essentially identical, whereas results for different Prandtl numbers differ substantially. As may be expected, the amount of reaction in this endothermic system decreases as Pr is increased by decreasing the gas phase thermal conductivity. A lower thermal conductivity implies greater gas-particle heat transfer resistance, thereby allowing less heat to enter and sustain the highly endothermic reaction.

The continued dominance of heat transfer resistance at Pr = 0.4 is interesting given the clear intra-particle species gradients that can be observed in the Th20-Pr0.4 case in Figure 2. This is because the outer shell of the particles is slightly hotter than the centre, implying that reduced species concentrations in the centre of the particle (where the temperature is lower and the kinetics is slower) does not have such a large impact on the overall reaction rate.

Figure 6 shows the axial evolution of the difference between the average gas temperature and the average particle temperature. Again, it is clear that mass transfer limitations are essentially negligible, while gas-particle heat transfer dominates the system.

In this case, there is a clear deviation between the PR-DNS and 1D-simulation results: PR-DNS consistently predicts a larger difference between the average gas and particle temperatures. This implies that the PR-DNS predicts a lower particle temperature than the 1D simulations (gas temperature reduces with gas species concentration and is almost identical between the PR-DNS and 1D simulations). As mentioned in the previous section, the temperature variation inside the particle in the PR-DNS allows the reaction rate to be higher than that implied by the average particle temperature. On the other hand, the 1D simulation inherently assumes constant temperature in all particles. For this reason, the two models predict the same overall reaction rate at different average particle temperatures.

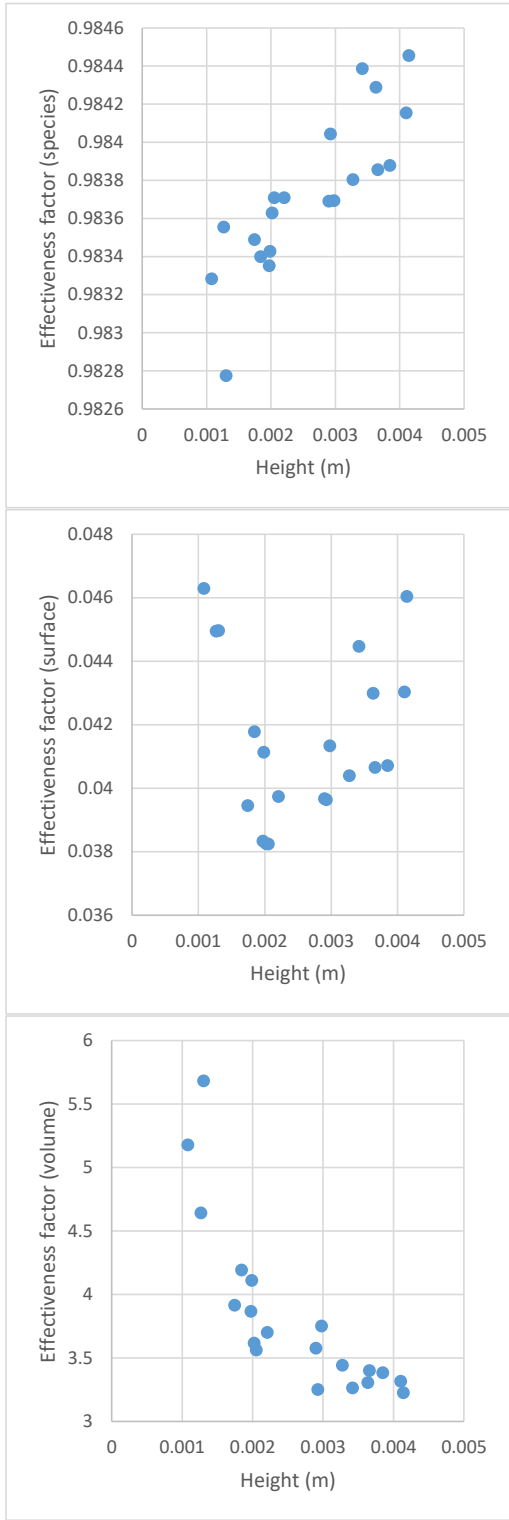

Figure 4: Three different representations of effectiveness factors for 20 particles from the Th20-P6.4 case.

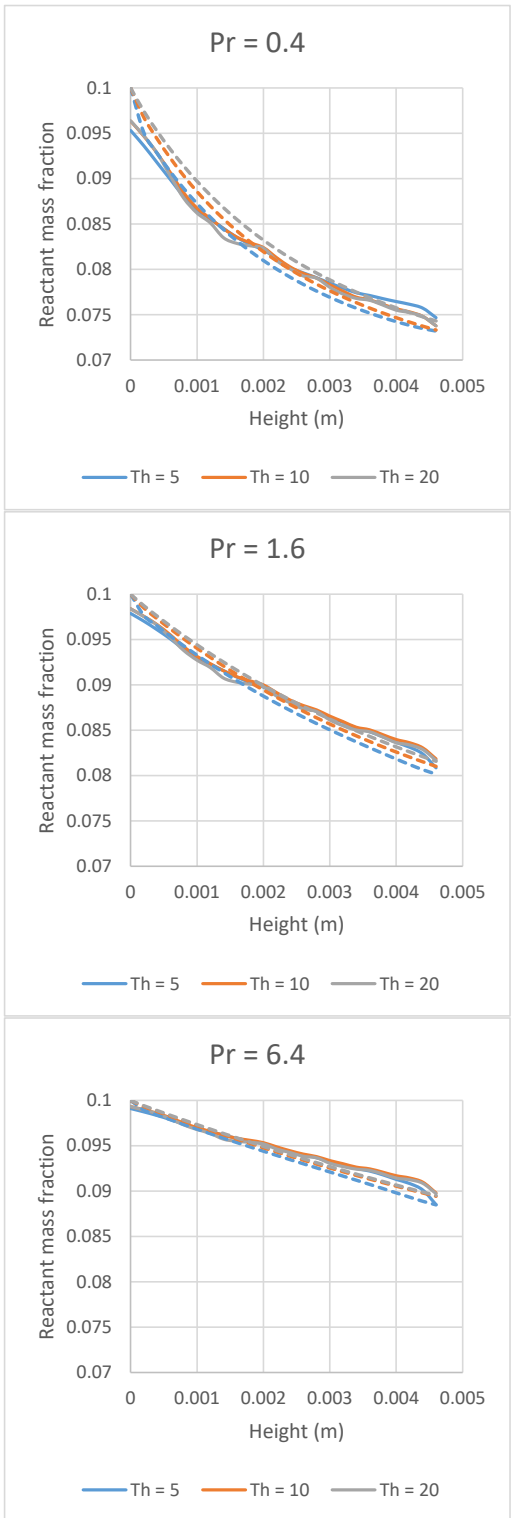

Figure 5: Comparison of axial species profiles between PR-DNS (solid lines) and 1D simulations (dashed lines) for different Prandtl numbers (Pr) and Thiele moduli (Th).

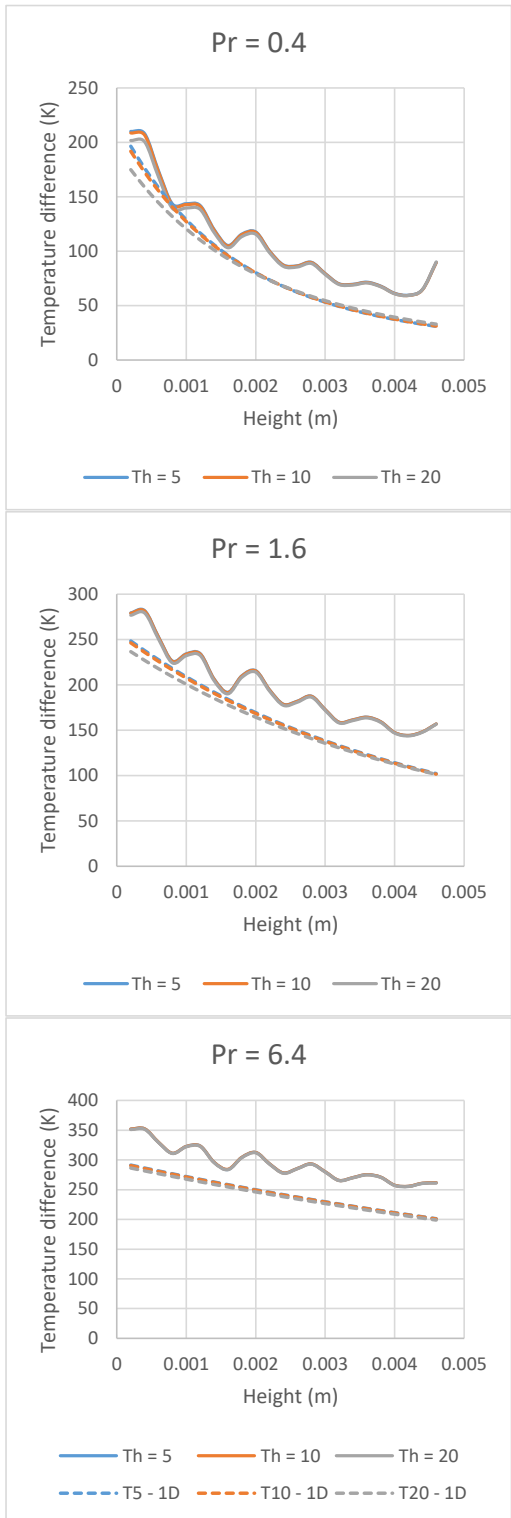

Figure 6: Comparison of axial gas-particle temperature difference between PR-DNS (solid lines) and 1D simulations (dashed lines) for different Prandtl numbers (Pr) and Thiele moduli (Th).

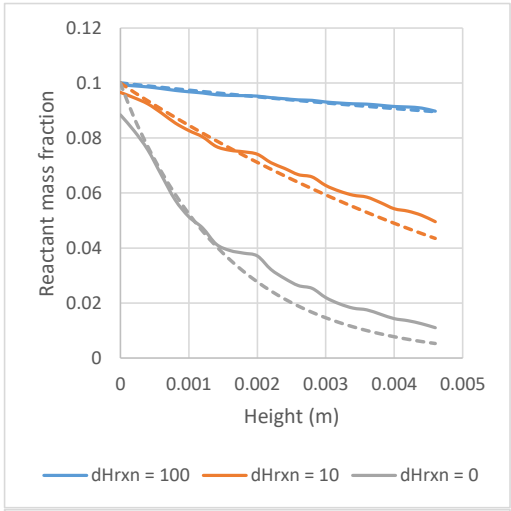

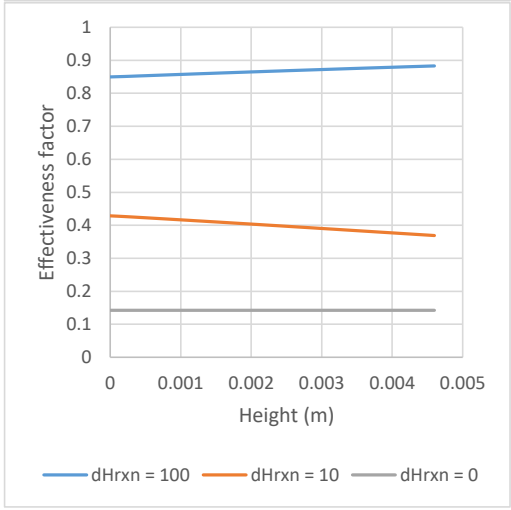

Figure 7: Comparison of axial species profiles between PR-DNS (solid lines) and 1D simulations (dashed lines) for different reaction enthalpies (dHrxn in kJ/mol). The effectiveness factor predicted by the 1D model is also shown for the different cases.

Variation of reaction enthalpy

Results in the previous section were generated with a strongly endothermic reaction ($dH_{rxn} = 100$ kJ/mol). This section will investigate three additional reaction enthalpies on the case with the greatest mass and heat transfer resistances (Th20-Pr6.4).

Figure 7 shows the effect of reaction enthalpy on the reactant conversion. It is clear that a decrease in the reaction enthalpy greatly increased reactant conversion and that the 1D model accurately predicts the results from PR-DNS.

The increase in conversion with a decrease in the endothermicity of the reaction is simply due to the large heat transfer resistances included in this case. As the reaction becomes less endothermic, the requirement for heat flow into the particle reduces, thereby lessening the impact of this limitation. As a result, mass transfer becomes the controlling phenomenon, as can be seen from the reduction in the effectiveness factor in Figure 7.

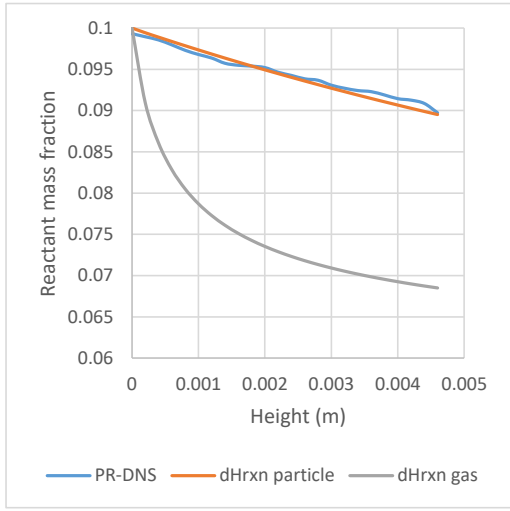

Figure 8: Comparison of the 1D simulations to the PR-DNS results illustrating the importance of assigning the reaction heat to the particle phase.

Importance of the reaction enthalpy source term

Finally, an important observation regarding the 1D-modelling of gas-solid reaction systems with significant reaction enthalpies can be shared. It is intuitive to add the energy source term related to a reaction involving gas species to the gas phase, but this results in large errors if significant gas-particle heat transfer limitations exist. To get accurate predictions, all reaction enthalpy must be assigned to the particle phase in the 1D simulation. This practice mimics the real case where all reaction heat is released or consumed within the particle, even if only gas species is involved in the reaction.

As an illustration of the importance of this observation, the axial species profiles from the Th20-Pr6.4 case with $dH_{rxn} = 100$ kJ/mol are presented in Figure 8. It is clear that assigning the reaction heat to the gas phase completely over-predicts the reaction. This is because the large gas-particle heat transfer limitation observed in earlier sections is essentially eliminated if the heat is not extracted in the particle phase.

CONCLUSION

This work presented a comparison of particle-resolved direct numerical simulations (PR-DNS) results with 1D modelling of a reactive gas-particle system with large heat and mass transfer limitations. Existing 1D model closures for intra-particle mass transfer and gas-particle heat transfer compared well to the PR-DNS results. However, it was shown that it is vitally important that all reaction heat must be assigned as a source term in the particle phase, even if only gas species are reacting.

When a highly endothermic reaction ($dH_{rxn} = 100$ kJ/mol) is simulated, gas-particle heat transfer completely dominates the reaction phenomena in the particle assembly. Large heat consumption in the particle requires large quantities of heat to enter the particle from the gas phase. Mass transfer resistances become increasingly important as the reaction enthalpy becomes smaller until the system becomes exclusively mass transfer controlled when no reaction heat is simulated.

It was also interesting to observe that the 1D model still produced good results even though significant intra-particle heat transfer limitations were included to generate some temperature gradients inside the particles. This finding, combined with the knowledge that a constant particle temperature is normally a safe assumption, suggests that good models for external gas-particle heat transfer and internal mass

transfer are sufficient for accurate 1D model predictions of packed bed reactors.

ACKNOWLEDGEMENT

This work is a part of a European Union project under Seventh research framework program (FP7/2007-2013) under grant agreement n° 604656 - A multi-scale Simulation based design platform for Cost effective CO_2 capture Processes using Nano-structured materials (NanoSim). The authors are grateful to European Research Council for its support. Additionally, the computational resources at NTNU provided by NOTUR, http://www.notur.no, were used during this project.

REFERENCES

Cloete, S., Gallucci, F., van Sint Annaland, M., Amini, S., (2016). "Gas Switching as a Practical Alternative for Scaleup of Chemical Looping Combustion". *Energy Technology* **4**, 1286-1298.

Gunn, D.J., (1978). "Transfer of heat or mass to particles in fixed and fluidised beds". *International Journal of Heat and Mass Transfer* **21**, 467-476.

Ishida, M., Wen, C.Y., (1968). "Comparison of kinetic and diffusional models for solid-gas reactions". *AIChE Journal* **14**, 311-317.

Levenspiel, O., (1999). "Chemical Reaction Engineering, 3rd ed". John Wiley & Sons, New York.

Nashtaee, P.S.b., Khoshandam, B., (2014). "Noncatalytic gas-solid reactions in packed bed reactors: a comparison between numerical and approximate solution techniques". *Chemical Engineering Communications* **201**, 120-152.

Ramachandran, P.A., Doraiswamy, L.K., (1982). "Modeling of noncatalytic gas-solid reactions". *AIChE Journal* **28**, 881-900.

Singhal, A., Cloete, S., Radl, S., Quinta-Ferreira, R., Amini, S., (2017). "Heat transfer to a gas from densely packed beds of monodisperse spherical particles". *Chemical Engineering Journal* **314**, 27-37.

Szekely, J., Evans, J.W., Sohn, H.Y.,, (1976). "Gas-solid reactions". Academic Press, New York.

Thiele, E.W., (1939). "Relation between Catalytic Activity and Size of Particle". *Industrial & Engineering Chemistry* **31**, 916-920.

Yang, W., Cloete, S., Morud, J., Amini, S., (2016). "An Effective Reaction Rate Model for Gas-Solid Reactions with High Intra-Particle Diffusion Resistance", International Journal of Chemical Reactor Engineering, p. 331.

Appendix 2 Comparison of particle resolved direct numerical simulation and 1D modeling of catalytic reactions in a Cylindrical particle bed

V International Conference on Particle-based Methods – Fundamentals and Applications
PARTICLES 2017
P. Wriggers, M. Bischoff, E. Oñate, D.R.J. Owen, & T. Zohdi (Eds)

COMPARISON OF PARTICLE-RESOLVED DIRECT NUMERICAL SIMULATION AND 1D MODELLING OF CATALYTIC REACTIONS IN A CYLINDRICAL PARTICLE BED

ARPIT SINGHAL[1, 2*], SCHALK CLOETE[3], ROSA QUINTA-FERREIRA[2] AND SHAHRIAR AMINI[1, 3]

[1] NTNU: Norwegian University of Science and Technology
Department of Energy and Process Engineering,
Kolbjørn hejes v 1B, NO-7491,
Trondheim, Norway
arpit.singhal@ntnu.no

[2] University of Coimbra
Department of Chemical Engineering
Rua Sílvio Lima, Polo II, 3030-790
Coimbra, Portugal
rosaqf@eq.uc.pt

[3] SINTEF Materials and Chemistry
Flow Technology Department
S. P. Andersens veg 15 B, NO-7031
Trondheim, Norway
schalk.cloete@sintef.no and
shahriar.amini@sintef.no

Key words: Direct numerical simulation (DNS), CFD-DEM, packed bed, catalytic gas-solid reaction, reaction rate, heat transfer, multiscale.

Abstract. This work presents a comparative study of reactive flow in a realistically packed array of cylindrical particles on two widely different scales: particle-resolved direct numerical simulation (PR-DNS) and 1D modelling. PR-DNS directly simulates all transfer phenomena in and around the cylindrical particles, while 1D modelling utilizes closure models to predict system behaviour at a computational cost several orders of magnitude lower than PR-DNS.

PR-DNS is performed on a geometry of ~100 realistically packed cylindrical particles generated using the discrete element method (DEM). Simulations are performed over a range of Thiele moduli, Prandtl numbers and reaction enthalpies. The geometry with particles of aspect ratio four is meshed with fine polyhedral elements both inside and outside the particles. Hence, we obtain accurate results for combined internal and external heat and mass transfer in the cylindrical particle array.

These results are compared with a 1D packed bed reactor model incorporating appropriate models for intra particle diffusion and for external heat and mass transfer (applicable to cylindrical particles). Results document a good comparison for the heterogeneous first order

catalytic simple reaction. Therefore, recommendations are made to guide future 1D modelling works involving reactive flows in packed beds of cylindrical particles.

NOMENCLATURE

Greek Symbols

α	Volume fraction
ε	Void fraction
ϕ	Thiele modulus (Th)
η	Effectiveness factor

Latin Symbols

a	Characteristic length of cylinder particle ($r_p/2$)
C_p	Specific heat capacity of fluid [J/kg.K]
C_A	Concentration of species A [mol/m^3]
D	Molecular diffusivity [m^2/s]
d_p	Diameter of the cylindrical particle [m]
E	Activation energy [J/mol]
h	Heat transfer coefficient [W/m^{2}K]
k_0	Arrhenius constant [1/s]
K_f	Thermal Conductivity of fluid [W/m.K]
Nu	Nusselt number (hd_p/K_f)
Pr	Prandtl number ($\mu C_p/K_f$)
R	Gas constant [8.314 J/mol/K]
R_{cat}	Catalytic reaction rate [mol/m^{3}s]
r	Radius [m]
Re	Reynolds number ($\rho u_s d_p/\mu$)
Sc	Schmidt number ($\mu/\rho D$)
Sh	Sherwood number (hd_p/D)
T	Temperature [K]
u_s	Superficial velocity of the fluid [m/s].

Sub/superscripts

f	Fluid
p	Particle.

1 INTRODUCTION

Cylindrical particles are often utilized in gas-solid packed bed systems, with application from process to pharmaceutical industry. Therefore, a wide range of closure models is available for gas-solid reaction systems. The closure models are segregated depending upon the application of the particles in either catalytic or non-catalytic role.

There are several important works describing the non-catalytic gas-solid systems [1, 2]. While, for the heterogeneous catalytic system the most important parameter of effectiveness factor is given for intra particle diffusion in spherical porous particle by [3]. The correct expression for the effectiveness factor with the cylindrical particle can be found in [4-6].

The recent work from the authors [7, 8] used the analytical expressions for effectiveness factor of general catalytic reaction forms in 1D packed bed models. The validity of these 1D packed bed models when combined with appropriate closure models for external heat and mass transfer in dense packed beds of cylindrical particle motivates the current work.

The objective of our work is to evaluate the predictions of gas-solid reaction systems on two distinct scales. Firstly, a PR-DNS on a geometry of ~100 densely packed cylindrical particles (aspect ratio four; $\varepsilon = 0.468$) [9] is used to give insight into the intra-particle diffusion and heat transfer phenomenon. Then the 1D packed bed model based on the closure for effectiveness factor [6] and external heat and mass transfer [9] is used to approximate this solution at a much lower computational cost. The comparison of the results for species concentration and temperature variation from both approaches are then documented.

2 METHODOLOGY

2.1 PR-DNS Simulation Setup

The realistically packed cylindrical particle bed of aspect ratio four ($\varepsilon = 0.468$) is generated using discrete element method (DEM) integrated in Star CCM+ 11.02. It is explained in more detail in Singhal et al. [9]. Such a geometry obtained is free from wall effects, which has been proved in [10]) hence giving confidence in the numerical accuracy of the methodology. The geometry is meshed with polyhedral elements with resolution $d_e/30$ using FLUENT meshing on particle surfaces both inside and outside the particle to account for intra particle diffusion. Subsequently a growth rate of 20% is allowed from the particle surface to fill up the void (Figure 1).

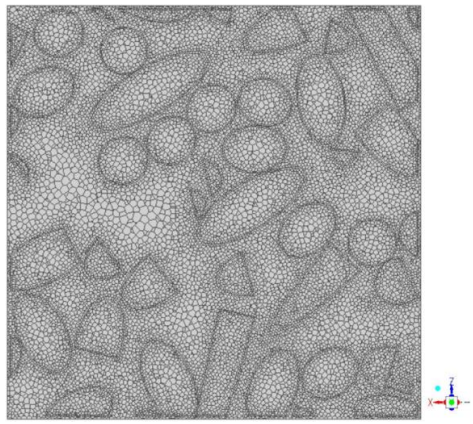

Figure 1: A section (y = 0) through the geometry of cylindrical particles meshed with polyhedral elements.

Steady state DNS with SIMPLE algorithm for pressure-velocity coupling and 2nd order spatial discretization for solver equations using ANSYS FLUENT is used to provide solution to the problem at hand. Steady state DNS is found to be accurate for the type of geometry solved, as transient fluctuations in the small spaces are negligible [10]. The final rendered geometry has a velocity inlet, pressure outlet and a non-slip condition on the wall. The solid particles are considered to be porous (the grain model [11]), where the reaction modelled by Eq. (1) takes place. Table 1 describes the simulation parameters used in the DNS.

$$A\ (g) + B\ (s) \rightarrow C\ (g) + B\ (s) \tag{1}$$

The reaction rate is defined by Eq. (2) and (3):

$$R_{cat} = \alpha_s k C_A \tag{2}$$

$$k = k_0 exp\left(\frac{-E}{RT}\right) \tag{3}$$

PR-DNS was performed for different combinations of heat transfer resistance (Prandtl number) and mass transfer resistance (Thiele modulus). In total, nine combinations of Thiele modulus and Prandtl number were used to obtain the results (Table 1). Different mass and heat transfer mechanisms are obtained by varying the molecular diffusivity and thermal conductivity of the gas phase using Thiele modulus (Th) and Prandtl number (Pr) definition given in Table 1. Using an appropriate pre-exponential factor (Eq. (3)), the value for reaction rate constant of 10000 1/s at temperature 1000 K is obtained. Similarly, a high value for activation energy is assumed to create a strong coupling between heat and mass transfer.

Table 1: Simulation parameters for PR-DNS

Parameters	**Value**
Eq. Particle diameter (d_e) (m)	0.001
Packed bed voidage	0.468
Particle void fraction (internal)	0.3
Density (kg/m^3)	*Fluid* :1 *Particles* :2500
Fluid velocity (m/s)	1
Inlet mole fraction (A)	0.1
Specific heat capacity (C_p) (J/kg/k)	1000
Arrhenius constant (k_0) (1/s)	1673603814
Activation energy (E) (J/mol)	100000
Thermal conductivity (Solid) (W/m.K)	0.1
Thiele moduli (Th)	5, 10, 20
Prandtl numbers (Pr)	0.50, 0.75, 1
Heat of reaction (kJ/mol)	100, 10, 0, -10

2.2 Thiele Modulus and Effectiveness Factor

The effectiveness factor and Thiele modulus [12] definition is similar to the previous work with spherical particle [8] defined for heterogeneous catalytic gas-solid reactions of first order. It is defined as the effect of intra particle diffusion on reaction rate [3, 13].

$$\eta = \frac{actual\ reaction\ rate}{reaction\ rate\ without\ diffusion\ limitations} \tag{4}$$

$$\phi \approx \frac{reaction\ rate}{diffusion\ rate} \tag{5}$$

2.3 1D Packed Bed Model

An outline of the 1D model setup can be seen in detail in the earlier work of the authors [7, 8]. The 1D packed bed model domain consists of 100 cells in one direction. The model is simulated using a Two Fluid Model approach in ANSYS FLUENT 17.2. The velocity of the solid phase in all 100 cells is fixed to zero. Subsequently, the conservation for mass, momentum, energy and specie are solved to obtain the solution.

In the 1D-model approach, appropriate closure models applicable to cylindrical particle beds have to be used to account for heat and mass transfer limitations. The closure models for effectiveness factor to model intra particle mass transfer limitations are given by Levenspiel [3], these closures are modified as suggested by [6], to be now applicable for cylindrical particles. Moreover, the external heat and mass transfer limitations are modelled using the closure models developed for cylindrical particles [9]. The effectiveness factor closures considered in this work are given below in Eq. (6)-(8):

$$\eta = \frac{1}{\phi}\left(\frac{1}{tanh(3\phi)} - \frac{1}{3\phi}\right) \tag{6}$$

$$\phi = a\sqrt{\frac{k}{D_e}} \tag{7}$$

$$D_e = \frac{D\varepsilon}{\tau} \tag{8}$$

The Thiele modulus (ϕ) represents the ratio of kinetic rate to diffusion rate, so higher values represent greater mass transfer limitation. The effective diffusivity (D_e) is composed of the molecular diffusivity (D), the void fraction of porous particles $(\varepsilon = 0.3)$ and the tortuosity $(\tau = 1)$. The correlation for external heat (Pr) and mass transfer (Sc) from Singhal et al. [9] is written as shown in Eq. (9).

$$\begin{aligned} Nu &= (0.81 + 0.0652\varepsilon^{-3.55}Re^{0.644}Pr^{0.456}) \\ Sh &= (0.81 + 0.0652\varepsilon^{-3.55}Re^{0.644}Sc^{0.456}) \end{aligned} \tag{9}$$

The domain dimensions and the boundary conditions are identical to the PR-DNS simulations. In addition, the solid volume fraction is set as the mean volume fraction of the solid in the PR-DNS domain (0.532) times the solid volume fraction in the particles (0.7).

3 RESULTS AND DISCUSSIONS

3.1 Heat and Mass Transfer in Densely Packed Cylinders

PR-DNS is performed over a range of Thiele moduli (Th 5-20) and Prandtl numbers (Pr 0.5-1) for a densely packed bed of cylindrical particles of aspect ratio four (ε = 0.468). The results for typical variation of gas temperature and specie concentration (of specie A) for an

endothermic reaction (at dH_{rxn} = 10 kJ/mol) are shown in Figure 2 and Figure 3. Figure 2 shows temperature variation over Pr 0.50 to Pr 1 (top to bottom). As the gas thermal conductivity decreases, the particle temperature decreases (Pr 1 has colder particles than at Pr 0.50). This is due to increase in heat transfer resistance with increasing Prandtl number that limits the influx of heat consumed by the endothermic reaction. Also, for a fixed heat transfer resistance (Figure 2 (right to left)), a lower mass transfer resistance results in colder particles due to a faster endothermic reaction.

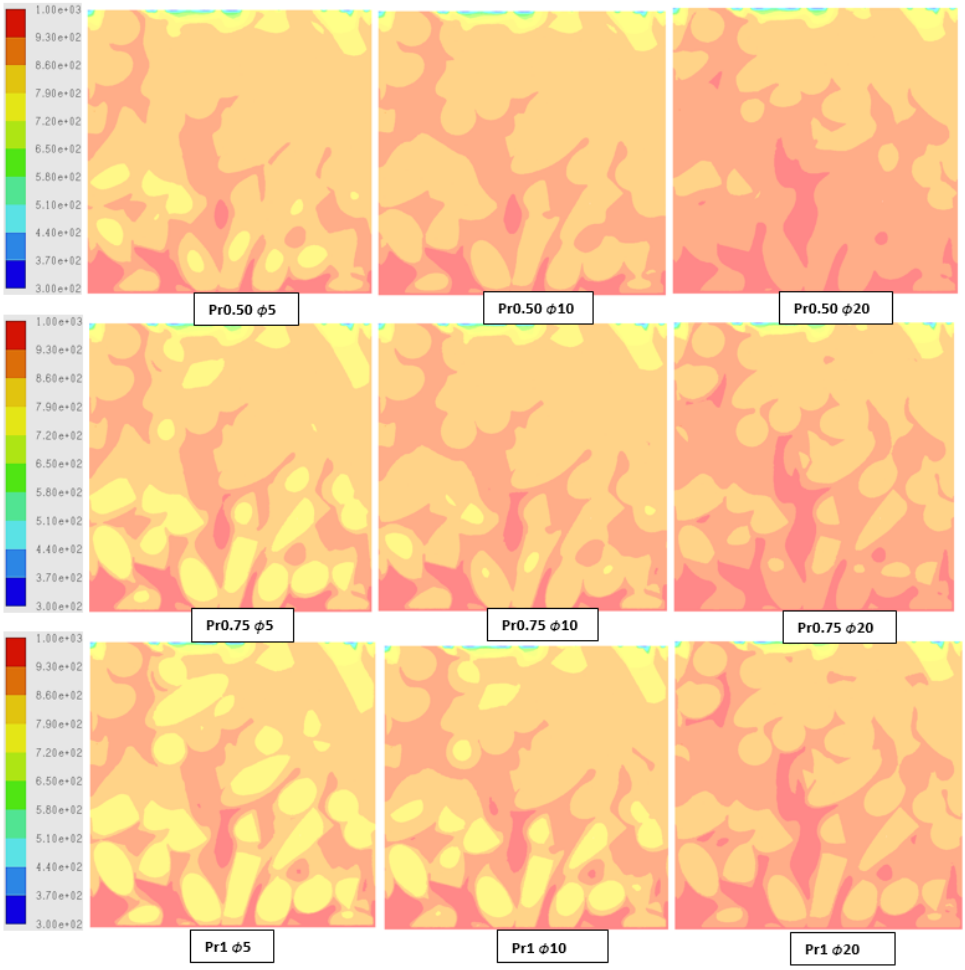

Figure 2: PR-DNS results (plane y= 0) for the temperature variation in the packed bed of cylindrical particles of aspect ratio four for different Prandtl numbers (Pr) and Thiele moduli (Th) at dHrxn = 10 KJ/mol.

The mass transfer limitations can be seen appropriately in Figure 3. It is evident from Figure 3 (left to right), that the concentration of specie A inside the particle decreases. This is because

of the increase in the mass transfer resistance, i.e. the gas mass diffusivity decreases with increase in Thiele modulus. More details are given in the subsequent sections.

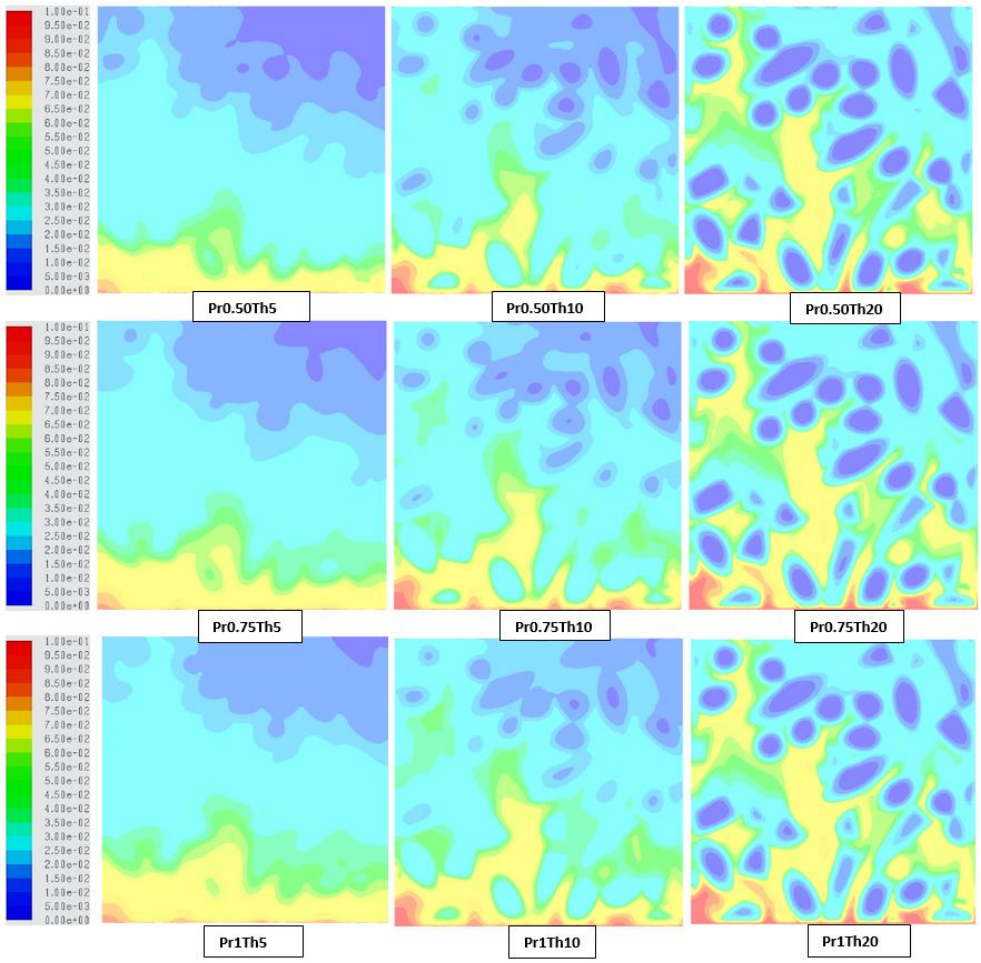

Figure 3: PR-DNS results for the reactant (A) mole fraction in the packed bed of cylindrical particles of aspect ratio four for different Prandtl numbers (Pr) and Thiele moduli (Th) at dHrxn = 10 KJ/mol.

The effect of heat of reactions (dH_{rxn}) on specie concentration (of A) is shown in Figure 4. Four different dH_{rxn} (= 100, 10, 0, -10 kJ/mol) are assessed for the Pr1T20 case, including one exothermic reaction. The specie concentration (of specie A) inside the particle decreases as we decrease the dH_{rxn}. This is because an exothermic reaction is self-strengthening (faster reaction ➔ higher temperature ➔ faster reaction), whereas the opposite is true for an endothermic reaction. The exothermic reaction strengthens itself by increasing the temperature, while the endothermic reaction extinguishes itself by decreasing the temperature.

3.2 1D Model Predictions

The comparison between the PR-DNS data and the 1D model predictions are presented in this section. In the first comparison, the 1D model data is compared with the PR-DNS data for bulk fluid specie concentration and temperature (over a range of Prandtl number and Thiele modulus). The bulk fluid [9, 10, 14-16] properties are used for PR-DNS data to generalise any effect of the location of the planes [9, 10] in the geometry in the calculation of the temperature and specie concentration. Secondly, the effect of change in reaction enthalpies are compared. Also note that for the 1D model all the heat of reaction source term is implemented in the solid phase as suggested in our previous work [8].

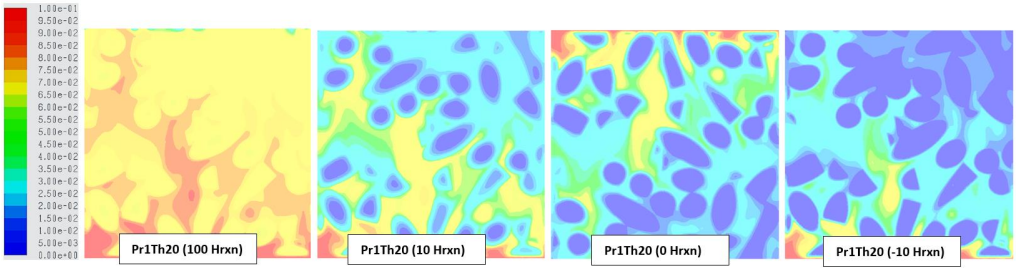

Figure 4: PR-DNS results for the reactant (A) mole fraction for (Pr = 1; Th = 20) case. The variation in specie concentration with different heat of reactions (dH_{rxn} = 100, 10, 0, -10) is shown from left to right.

3.2.1 Variation of Prandtl number and Thiele modulus

Figure 5 shows the axial specie concentration (for specie A) profiles for nine combinations of Thiele modulus and Prandtl number. The results agree well with the PR-DNS results suggesting that mass transfer limitations are defined with appropriate closures for 1D model. Figure 6 shows the axial profiles for the difference between the bulk gas temperature and the average particle temperature. The amount of reaction in an endothermic system decreases as Pr is increased by decreasing the gas phase thermal conductivity. A lower thermal conductivity implies greater gas-particle heat transfer resistance, thereby allowing less heat to enter and sustain the highly endothermic reaction. The temperature variation inside each particle should be very small given the solids phase thermal conductivity (Table 1) implemented. In general, good agreement between PR-DNS and 1D results is obtained with a moderate discrepancy at Pr = 1.

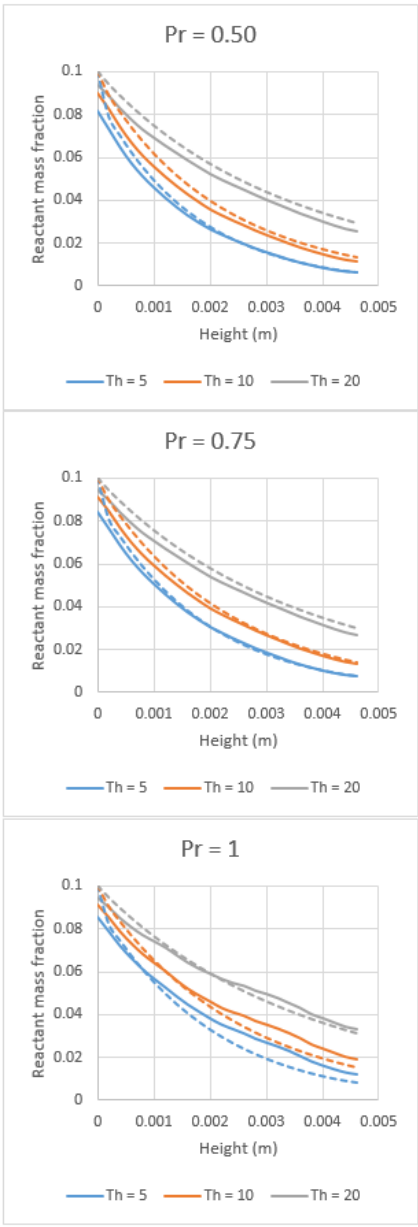

Figure 5: Comparison of axial species profiles (for specie A) between PR-DNS (solid lines) and 1D simulations (dashed lines) for different Prandtl numbers (Pr) and Thiele moduli (Th) at dHrxn = 10 kJ/mol..

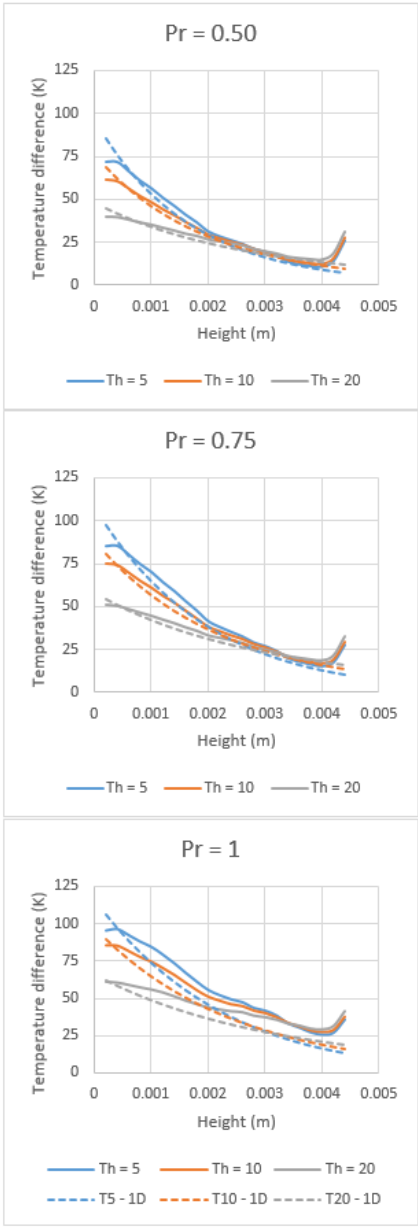

Figure 6: Comparison of axial gas-particle temperature difference between PR-DNS (solid lines) and 1D simulations (dashed lines) for different Prandtl numbers (Pr) and Thiele moduli (Th) at dHrxn = 10 kJ/mol.

3.2.2 Variation of reaction enthalpy

In the previous sections, the heat of reactions used is ($dH_{rxn} = 10$ kJ/mol) signifying an endothermic reaction. In order to monitor the effect of dH_{rxn} on the reactant conversion, three additional heat of reactions (including an exothermic reaction) are evaluated for the case (Pr1T20) with greatest heat and mass transfer limitations.

It can be seen from Figure 7 that the 1D model predicts PR-DNS results accurately and the reactant conversion increases with a decrease in the reaction enthalpies. In the two cases with the fastest reaction rates, the inclusion of the external mass transfer limitation becomes important to achieve a good match with PR-DNS results.

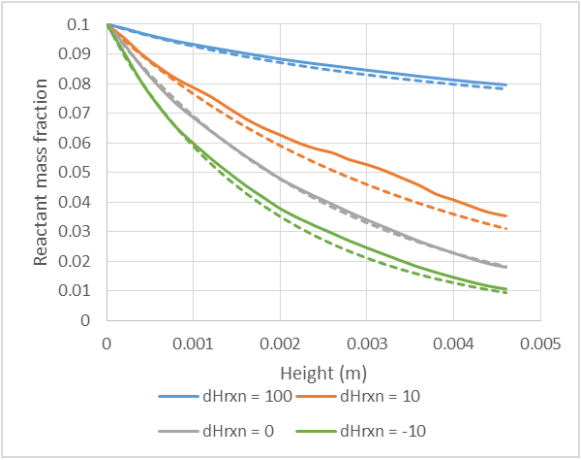

Figure 7: Comparison of axial species profiles (for specie A) between PR-DNS (solid lines) and 1D simulations (dashed lines) for Pr1T20 case and different reaction enthalpies (dH_{rxn} in kJ/mol).

11 CONCLUSIONS

This work presented a comparison of particle-resolved direct numerical simulations (PR-DNS) with 1D packed bed model for a densely packed bed of cylindrical particles of aspect ratio four ($\varepsilon = 0.468$) in a gas-solid first order catalytic reaction system.

Existing closures for 1D packed bed model for spherical particles modified appropriately for cylindrical particles predicts well against the result for resolved simulations (PR-DNS) over a range of Thiele moduli, Prandtl numbers and reaction enthalpies. Recently proposed closures for external heat and mass transfer from cylindrical particles were important to ensure good performance of the 1D model. Future works will assess whether this good performance is maintained in systems with multiple reactions with different reaction orders.

12 ACKNOWLEDGEMENT

This work is a part of a European Union project under Seventh research framework program (FP7/2007-2013) under grant agreement n° 604656 - A multi-scale Simulation based design platform for Cost effective CO_2 capture Processes using Nano-structured materials (NanoSim).

The authors are grateful to European Research Council for its support. Additionally, the computational resources at NTNU provided by NOTUR, http://www.notur.no, were used during this project.

REFERENCES

[1] Nashtaee, P.S.b. and B. Khoshandam, Noncatalytic gas-solid reactions in packed bed reactors: a comparison between numerical and approximate solution techniques. *Chemical Engineering Communications*, 2014. **201**(1): p. 120-152.

[2] Ramachandran, P.A. and L.K. Doraiswamy, Modeling of noncatalytic gas-solid reactions. *AIChE Journal*, 1982. **28**(6): p. 881-900.

[3] Levenspiel, O., *Chemical Reaction Engineering, 3rd ed*. Vol. 3rd ed. 1999: John Wiley & Sons, New York.

[4] Asif, M., Efficient Expressions for Effectiveness Factor for a Finite Cylinder. *Chemical Engineering Research and Design*, 2004. **82**(5): p. 605-610.

[5] Gunn, D.J., Diffusion and chemical reaction in catalysis and absorption. *Chemical Engineering Science*, 1967. **22**(11): p. 1439-1455.

[6] Rawlings, J.B.a.E., John G, *Chemical reactor analysis and design fundamentals (Chapter 7)*. 2002: Nob Hill Pub, Madison, Wis.

[7] Cloete, S., et al., Gas Switching as a Practical Alternative for Scaleup of Chemical Looping Combustion. *Energy Technology*, 2016. **4**(10): p. 1286-1298.

[8] Singhal, A., et al. *Comparison of Particle-Resolved Direct Numerical Simulation and 1D modelling of catalytic reactions in a packed bed*. in *12th International Conference on CFD in Oil & Gas, Metallurgical and Process Industries*. 2017. Trondheim, Norway: Progress in Applied CFD – CFD2017.

[9] Singhal, A., et al., Heat transfer to a gas from densely packed beds of cylindrical particles. *Chemical Engineering Science*, 2017. **172**: p. 1-12.

[10] Singhal, A., et al., Heat transfer to a gas from densely packed beds of monodisperse spherical particles. *Chemical Engineering Journal*, 2017. **314**: p. 27-37.

[11] Szekely, J., Evans, J.W., Sohn, H.Y.,, *Gas-solid reactions*. 1976: Academic Press, New York. 612-612.

[12] Thiele, E.W., Relation between Catalytic Activity and Size of Particle. *Industrial & Engineering Chemistry*, 1939. **31**(7): p. 916-920.

[13] Ishida, M. and C.Y. Wen, Comparison of kinetic and diffusional models for solid-gas reactions. *AIChE Journal*, 1968. **14**(2): p. 311-317.

[14] Deen, N.G., et al., Direct numerical simulation of flow and heat transfer in dense fluid–particle systems. *Chemical Engineering Science*, 2012. **81**: p. 329-344.

[15] Deen, N.G., et al., Review of direct numerical simulation of fluid–particle mass, momentum and heat transfer in dense gas–solid flows. *Chemical Engineering Science*, 2014. **116**: p. 710-724.

[16] Sun, B., S. Tenneti, and S. Subramaniam, Modeling average gas–solid heat transfer using particle-resolved direct numerical simulation. *International Journal of Heat and Mass Transfer*, 2015. **86**: p. 898-913.